AN INVESTIGATION OF THE GROWTH OF SILVER AND COPPER FILMS ON NICKEL SURFACES

A thesis submitted for the Degree of Doctor of Philosophy of the University of York

D. C. JACKSON

Department of Physics
University of York
Heslington
York

March 1974

BEST COPY AVAILABLE.

VARIABLE PRINT QUALITY

An Investigation of the Growth of Silver and Copper Films on Nickel Surfaces

D C Jackson March 1974

Abstract

A Knudsen source has been built to enable the controlled deposition of silver and copper on nickel surfaces in ultra-high vacuum.

The deposition of silver was monitored by Auger electron spectroscopy and the dependence of the Auger signal strength with deposition time compared with a simple model. The data enabled the occurrence of layer by layer growth to be ascertained together with mean escape depths for the relevant Auger electrons and a value for the sticking coefficient.

The affect of heat treatment on silver-nickel bicrystals was studied by Auger electron spectroscopy and electron microscopy and it was found that heating to 300°C caused a change of deposit morphology to occur. There was no evidence that alloying occurs between silver and nickel films at either room temperature or 300°C.

Pseudomorphism of copper on nickel was studied at both room temperature and 300°C. A graph of elastic strain against average thickness for copper on nickel at room temperature was in reasonable agreement with theoretical predictions. Contamination of the nickel substrate by prolonged exposure to the residual gas resulted in a copper film showing an abnormally high value of elastic strain. It is thought that the presence of oxygen on the nickel surface may have caused the increased elastic strain but it was not possible to obtain the structure of the contaminant.

For depositions at 300°C the copper formed islands which were frequently rectangular in shape. A study was made of the number of misfit dislocations in small islands and it was found that the number was generally less than predicted by theory. This was attributed to the small value for the ratio of the height to the width of most of the islands.

CONTENTS

CHAPTER 1

INTRODUCTORY REVIEW

1.1 Introduction

Industrial applications of thin solid films are now widespread, ranging from anti-reflection coatings, front surface mirrors, interference filters to magnetic and electronic devices. Films used in optical devices normally have a low state of order, but this is not the case for thin film semiconducting devices. In such devices it is essential that the film be a good single crystal, and hence the problem arises of producing single crystal films.

The production of a thin film involves the arrival of material at the surface of a supporting solid, called the substrate, where the material builds up into a thin layer. The methods of producing thin films are numerous, ranging from electro-deposition, chemical reaction, sputtering and vacuum deposition (1). Attention here will be focused entirely on vacuum deposition since it is the method which offers greatest control and is also most widely used. In vacuum deposition the deposit material is heated until evaporation occurs, the vapour then traverses the space between source and substrate at substantially reduced gas pressure, and finally condenses on the substrate. Initial condensation normally results in the formation of small three dimensional islands, and additional material causes growth of these islands until they eventually coalesce and a continuous film is formed (2). There are however examples in which the deposit material is distributed evenly and growth is two-dimensional or layer-like. Such systems will be discussed in detail in section 1.2.3 and chapter 2.

If the deposited film is to form into a single crystal then the substrate itself is usually a single crystal, although there are experiments in which this has not been the case (3). The process of oriented growth of deposit material on top of a single crystal substrate is known as epitaxy. There are many important factors which determine whether or not epitaxy will occur and it is a process which is not yet fully understood. Thus the occurrence of epitaxy is found to be dependent upon the relative lattice spacing, the substrate temperature, the arrival rate of deposit material, the deposit thickness and the deposition conditions, including the condition of

the substrate surface.

In early work (4) it was concluded that epitaxy was possible only for small values of misfit between the substrate and deposit lattices, where the misfit may be defined as

$$M = \frac{a - b}{\frac{1}{2}(a + b)} \qquad (1.1)$$

a and b being the lattice spacings of deposit and substrate respectively. Subsequent investigations have shown that this is not the case and epitaxy has been observed in many systems where the misfit is large (5,6,7,8). Thus epitaxy has been observed for depositions of LiF on KBr (6) where the misfit is -39%.

The affect of substrate temperature was investigated extensively and it was thought at one time that there existed a particular temperature for a given system such that film growth above this temperature resulted in perfect epitaxy, whilst lower temperatures gave imperfect epitaxy (9). The experimental values of epitaxial temperature were in poor agreement and this is most likely a result of failure to consider other important parameters. In general epitaxy is improved by a higher substrate temperature because deposit atoms have more thermal energy and are able to migrate to positions of minimum potential energy.

The affect of arrival rate on epitaxy is interesting in that for some systems a high arrival rate results in good epitaxy (10), whereas in other cases the reverse is true (11). Closely linked to the affect of arrival rate is the thickness of the deposit and it is found that in some cases epitaxy improves as the deposit thickness increases whereas in other cases the film becomes polycrystalline (12). Thus in the case of silver on mica (13) or gold on molybdenite (14) epitaxy improves as deposition proceeds. One of the mechanisms causing this was shown by Jacobs et al. (14) to be coalescence of deposit islands. In the early stages of deposition islands of more than one orientation were present, but on coalescing one orientation dominates and other orientations are eliminated. It has also been observed that two nuclei in almost parallel orientation may rotate upon coalescence so that perfect orientation is obtained (15).

The affect of deposition conditions has until recently been beyond experimental control. In early work depositions were often

performed in relatively poor vacua and even with the achievement of pressures in the 10^{-6} torr range it was still impossible to maintain a clean substrate surface. A related problem was the inclusion of residual gas into the growing film, since at pressures of 10^{-6} torr the rate of impingement of gas molecules on the specimen surface is comparable with typical arrival rates of deposit atoms. Nevertheless it was found in many cases that improvement in epitaxy was obtained if the substrate surface was cleaved in vacua immediately prior to deposition (16,17,18,19).

The advent of ultra high vacuum (UHV) in which residual gas pressures below 10^{-9} torr can be obtained has made it possible to control deposition conditions with much greater certainty. Thus a freshly cleaved surface in UHV will remain uncontaminated for sufficient time to enable most experimental observations to be carried out. The improved cleanliness of experimental conditions has not always resulted in better epitaxy and for the case of gold deposits on sodium chloride improved epitaxy has been observed if the salt surface is exposed to air prior to deposition (11).

Another factor related to the substrate is the presence of defects on the substrate surface and preferred nucleation has been observed at surface steps and point defects (20,21,22,23,24,25). Of particular importance in this respect is electron bombardment of the substrate either prior to or during deposition (26,27). It has been shown by Gallon et al. (28) and by Lord (29) that electron bombardment of alkali halide crystals can cause extensive damage and may even result in non-stoichiometric dissociation of the surface. The damaged areas act as preferred nucleation sites for deposit material and also favour the epitaxial configuration (29), although no explanation of this has yet been given.

In summary the process of epitaxial deposition of thin films is complicated involving many variables. The advent of UHV, whilst not reducing the number of variables does at least offer greater control, and such experiments should lead to a better understanding of epitaxy.

1.2 Vacuum Deposition of Thin Films

1.2.1 Evaporation Sources

The vacuum deposition of thin films involves three stages, namely the transition of a condensed phase (solid or liquid) into a vapour, the passage of this vapour from source to substrate at reduced

gas pressure, and finally its condensation on the surface of the substrate. In this section attention will be focused entirely on the vapour source itself. Stage two is simply a geometrical problem of arranging shutters and apertures to define the vapour beam and also ensuring that substantially reduced gas pressure is maintained in the system. Stage three is very complex and some of the factors influencing nucleation and growth of the deposit have been briefly mentioned in section 1.1. A comprehensive review of condensation and nucleation of thin films is given by Neugebauer (30).

The principal requirement of an evaporation source is a method of heating the evaporant to a temperature at which the vapour pressure is sufficiently high to produce usable condensation rates on the distant substrate. Vapour pressures of about 10^{-2} torr are normally required and for most common evaporant materials this entails heating to temperatures in the range 1000 to 2000°C. Another important requirement is that the method of heating or support of the evaporant must not cause contamination of the vapour. In practice this is one of the most serious limitations on source design.

The simplest type of evaporation source consists of a bent wire or dimpled boat which is resistively heated. The wire or boat is normally constructed from tungsten or tantalum because these metals have very low vapour pressures in the temperature range required. The only limitation to their use is that some metals e.g. nickel and cobalt, rapidly alloy causing destruction of the source. The problem of alloying can be overcome in some instances by employing an alumina or beryllia lining to the boat.

The need to overcome reaction between the support and molten evaporant has led to many designs of evaporation source employing electron bombardment heating. This entails focusing a beam of energetic electrons on the evaporant material, where the electrons lose kinetic energy and cause heating. The simplest arrangement of this type is the pendant drop source (31,32), and it is also the most satisfactory with regard to contamination because the support and evaporant are of the same material. Figure 1.1a shows a typical pendant drop source. Electrons from the hot filament are accelerated on to the tip of the rod causing it to melt. Evaporation then takes place from the molten drop which is held in position by surface tension.

A similar type of source is the design due to Unvala (33)

in which the evaporant material is placed on a water cooled copper hearth. The electron beam is focused on a small region of the upper surface of the evaporant and the material in contact with the copper hearth remains cool. There are various alternative designs of electron bombardment source but in all cases the aim is to focus the electrons on a small region of the evaporant so that the evaporant forms its own crucible and contamination is reduced. Comprehensive reviews of electron bombardment sources are given in references (34,35).

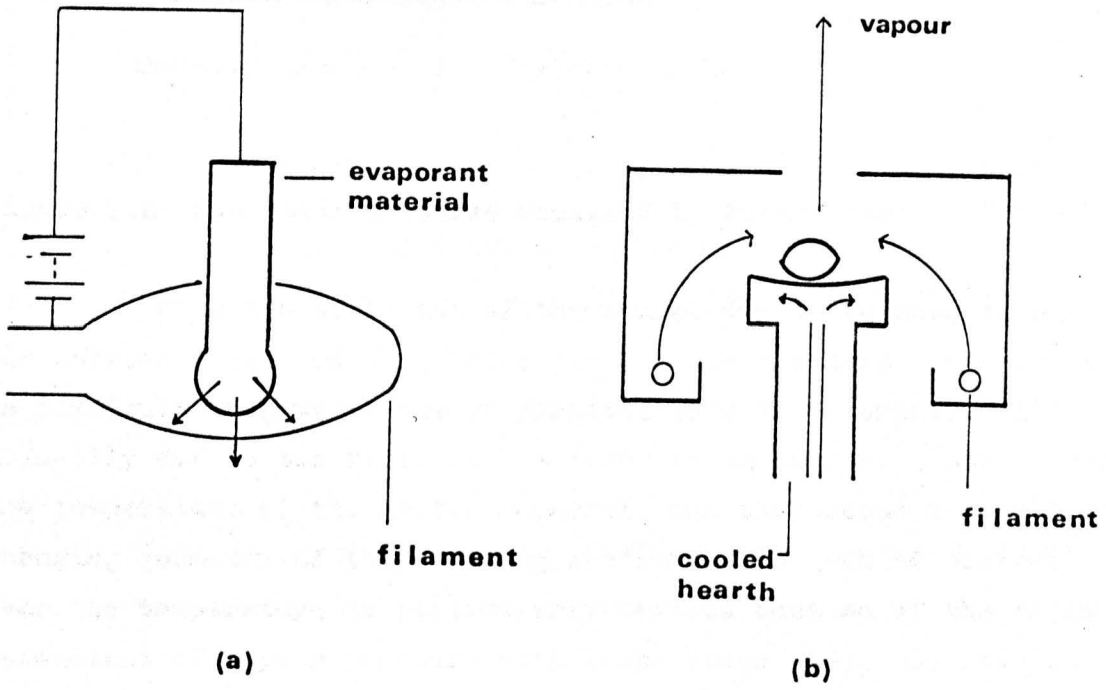

Figure 1.1 Electron bombardment sources a) pendant drop b) Unvala

There are materials such as nickel and cobalt which have appreciable vapour pressures at temperatures below their melting points. This enables material to be sublimed from the solid and hence reduction of contamination is possible. Various types of sublimation source have been used, the simplest being due to Matthews (36) in which the material in the form of a wire is wound into a tight helix. The wire is then heated resistively until usable sublimation rates are obtained. Another type used by Farnsworth (37) employed electron bombardment of a nickel slug, Figure 1.2. A thermocouple attatched to the slug enables the temperature to be monitored and constant deposition rates may be obtained.

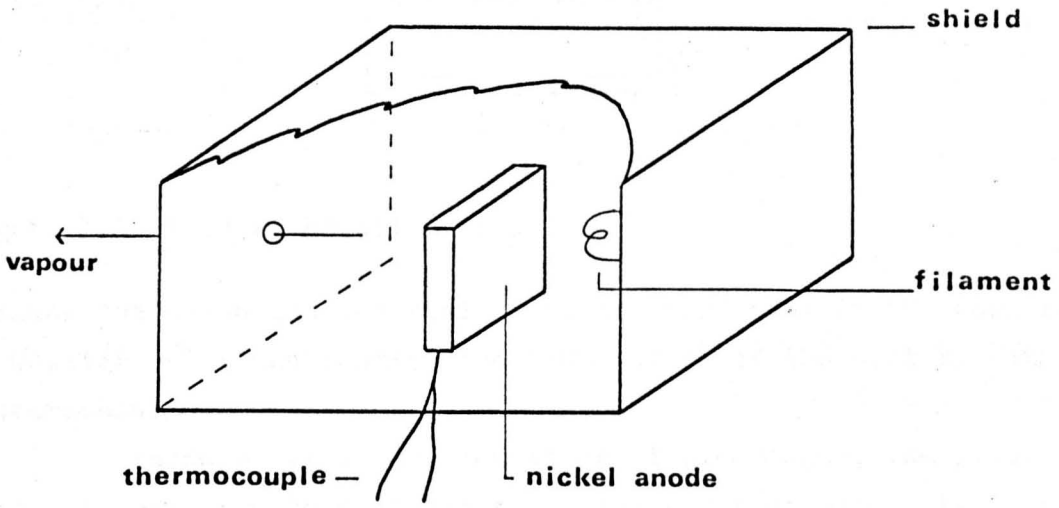

Figure 1.2 Sublimation source designed by Farnsworth

With the exception of the source due to Farnsworth all the sources described above have the serious disadvantage that it is difficult to control the evaporation rate of material. This is primarily due to two factors, the first being lack of control over the temperature of the molten material, and the second a result of changing geometry of the emitting surface. The lack of control over the temperature is particularly serious because of the rapid dependence of vapour pressure with temperature (38). In practice this is often overcome by employing a device to measure the arrival rate of material at a detector close to the substrate. The power input to the source is then adjusted until the required arrival rate is obtained. Nevertheless there are experiments in which it is desirable to have a vapour source with which a constant and reproducible arrival rate can be maintained for long periods. Evaporation sources of the Knudsen type fulfil this requirement (35). Knudsen sources generally consist of a closed crucible with a small hole in the top or side. The evaporant material is placed in the crucible and heated until the vapour inside the crucible is in equilibrium, Figure 1.3. Some of the vapour effuses through the small hole in the cell, and if the temperature of the cell is kept constant the rate of effusion is also constant.

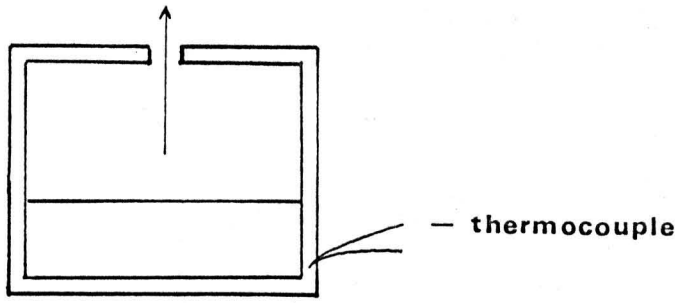

Figure 1.3 Knudsen Effusion Cell

Because the evaporant material is in a closed cell it is possible to monitor and hence control the temperature of the cell by attatching a thermocouple.

Knudsen cells have two major disadvantages, the first being that they can only be used for a limited range of materials. This is because the molten evaporant is in contact with the cell and hence materials which alloy are excluded. The second reason is that practical cells have a limited capacity and are not suitable for repeated depositions of thick films at typical source to substrate distances. The limitation on size is primarily a result of keeping the volume of hot metal to a minimum to reduce outgassing problems. Nevertheless the ability to obtain constant and reproducible deposition rates is essential for some experiments and a major part of the present work has been has been concerned with developing a Knudsen source for deposition of silver and copper in UHV. Details of the source are given in chapter 4, together with a higher capacity sublimation source for the deposition of thick films.

1.2.2 Deposit Thickness Calibration

Methods of measuring film thickness or monitoring deposition are numerous, involving many different physical properties. They can however be divided into two general categories, the first including methods which measure the arrival rate of material, and the second involving methods which determine the total film thickness after deposition. A comprehensive review of techniques is given in reference (39).

(a) Rate Measurement

A widely used method of thickness calibration which falls into either category given above is the use of a quartz crystal oscillator. This involves utilizing a thin crystal wafer which is

made part of an oscillatory circuit. The crystal is placed so as to intercept part of the vapour beam and hence the vapour condenses on one face of the crystal. The mass loading of the crystal causes a change in the resonant frequency, which can be measured and the deposited mass obtained, hence the film thickness. Electronic differentiation of the frequency change enables the arrival rate to be determined. The major disadvantage with crystal ratemeters is that it is necessary to make some subsidiary assumption about the sticking coefficient on the specimen and the ratemeter; where the sticking coefficient is the ratio of material condensing into the film to the material actually arriving at the surface. It is frequently assumed that the sticking coefficient on the ratemeter and the sample are the same, although it is possible to determine the mean sticking coefficient for the ratemeter by subsidiary experiments (40). However, uncertainty about sticking coefficient is a disadvantage common to all rate measurement techniques.

Other less widely used methods of monitoring the vapour stream are ionization cells and momentum balances. In ionization cells some of the vapour is ionized by collision with an electron beam, the ions are then collected and constitute an ion current. The ion current is proportional to the arrival rate, but independent calibration is necessary before the ion current and arrival rate can be directly related. Momentum balances (41) consist of a light aluminium cylinder mounted on a torsion fibre. The vapour beam is allowed to impinge on part of the cylinder and momentum transfer causes the cylinder to rotate. The rotation of the cylinder can be related to the arrival rate providing the torsional constant of the suspension and the average velocity of the molecules are known.

(b) Thickness Measurement

Methods of measuring the thickness of a film following deposition are numerous and it is not possible to cover them all. Reviews of some of the methods available are given in references (34,35,1,42). The most direct methods involve weighing or measurement of the height of a step at the edge of the film using a stylus (43). Methods involving optical interferometry are commonly used (42), in which the optical path difference for light reflected from the film surface and from the substrate causes displacement of interference fringes. Measurement of the displacement can be related to the thickness of the film. An optical method which is capable of

high accuracy is that of ellipsometry, which is based on the change in state of polarization of light reflected from the sample. The computation involved is laborious, although there are now standard computer programs available and the method is becoming more widely used (39).

Film thickness may be determined by X-ray flourescence analysis and this can be usefully combined with electron microscopy. Energetic electrons incident on the sample give rise to X-rays which are separated and collected. The film thickness can be related to the intensity of X-rays originating from the film.

Chemical methods have not been widely used although they are relatively simple and accuracy is comparable with other techniques (44,45). The best chemical method is probably that of photometric analysis, in which the material of the film is combined chemically with compounds giving rise to distinct colouration of resulting solutions. The optical absorption of the solution at a particular wavelength is then determined and from this the mass of deposit may be found. This method was used in the present work for calibrating vapour sources and is described in detail in chapter 4. The method was chosen because of its simplicity and also because a single beam spectrophotometer was available, enabling accurate optical absorption measurements to be made. One serious disadvantage of the method is that it is destructive.

The methods of thickness calibration described above have one feature in common in that they are not suitable in cases where the deposit is only a few layers thick. There are microbalances which can detect a few atomic layers of deposit, but this method of detection involves assuming bulk density values which may not be valid for such thin films. Microbalance techniques have been shown to be reliable to within a few per cent for film thicknesses down to about 100 Å (46). In principle a knowledge of the arrival rate should enable films of any required thickness to be deposited, since for constant arrival rate the film thickness is a function of time, which can be very accurately controlled. However a knowledge of the sticking coefficient is required and this is difficult to obtain for the very early stages of deposition i.e. the first layer or two.

In many experiments, such as nucleation and gas adsorption experiments, it is necessary to know the quantity of deposit material on the substrate surface when this quantity may be a few atomic layers

or less. The methods described above are not suitable for such measurements, particularly in the case of gas adsorption.
A technique which in many ways is similar to X-ray flourescence analysis and which is sensitive to very small amounts of material is that of Auger electron spectroscopy (AES). Auger electrons arise when an atom ionized in an inner level relaxes to a state of lower energy. The energy released by this process may be emitted as an X-ray photon, or alternatively be transferred to another electron which is ejected from the atom: the Auger electron. The energy of this ejected electron is characteristic of the atom from which it originated and hence energy analysis of the Auger electrons enables identification of different chemical species. At the present little work has been done relating observed Auger spectra to the amount of material present, AES being used primarily for chemical identification. Part of the work reported in this thesis was concerned with investigation of AES as a quantitative tool for surface analysis.
A more detailed description of the Auger process is given in section 1.5 and a model relating observed Auger electron currents to deposited material (47) is described in chapter 3.

1.3 Mode of Growth

1.3.1 Introduction

In the majority of deposit-substrate combinations the initial growth of the film consists of the generation of three dimensional islands. Film growth is expected to begin with three dimensional islands if the contact angle θ between deposit and substrate is greater than zero (48). At equilibrium the contact angle is given by the equation

$$\sigma_s = \sigma_i + \sigma_o \cos\theta \qquad (1.2)$$

where σ_s, σ_o and σ_i are the surface free energies of substrate, overgrowth and interface respectively. Hence the condition for monolayer growth to occur is

$$\sigma_s \geq \sigma_i + \sigma_o \qquad (1.3)$$

This condition is not the only one for which monolayer growth may be observed, thus a low substrate temperature or high deposition rate may also lead to layer growth by inhibiting attainment of equilibrium

conditions.

The possibility of the initial deposit atoms forming a single layer is interesting from the theoretical viewpoint, since the single layer may elastically strain to fit the substrate lattice. Frank and Van der Merwe (49,50,51) developed a model for epitaxy in which the first layer of an oriented deposit was strained to fit the substrate. This concept of elastic strain in the deposit to reduce the misfit was termed pseudomorphism, and the first observations of the affect were reported in 1933 by Finch and Quarrell (52). These observations were generally discredited and it was not until 1961 that Matthews (53) showed the affect to be real.

The model of an elastically strained initial deposit layer is not of general validity for epitaxial growth because the majority of systems exhibit three dimensional island growth. Nevertheless it is a system which is relatively amenable to theoretical analysis and for this reason a considerable amount of experimental and theoretical work has been carried out.

1.3.2 Pseudomorphism

The theory of Frank and Van der Merwe predicted that for deposit-substrate systems with small misfit the first monolayer would elastically strain to fit the substrate. Subsequent layers would also strain by the same amount until a critical thickness is reached at which it is energetically favourable for the deposit to relax by the introduction of a dislocation. The dislocations are at the deposit-substrate interface and are called misfit dislocations because they accommodate some of the lattice misfit. The thickness of deposit at which relaxation occurs depends upon the lattice misfit and the elastic constants of overgrowth and interface.

The theory of Frank and Van der Merwe was extended by Cabrera (54) and Jesser and Kuhlmann-Wilsdorf (55) to the case of island deposits. They assumed hemispherical islands with radial strains which decreased from the base to the top of the island. The theory predicted that islands up to a critical radius would be strained to match the substrate exactly, but beyond this radius dislocations would be introduced to accommodate some of the misfit. In the cases of layer and island deposits the theories predict that systems likely to exhibit pseudomorphism are those for which the lattice misfit is small, the interfacial bonding is strong and the elastic constant of the overgrowth is small. If the values for the elastic constants are

known it is possible to predict the critical thickness of deposit at which complete pseudomorphism is lost. The predictions of theory are generally in reasonable agreement with experiment, although there are some major discrepancies which will be discussed later.

The theory of Frank and Van der Merwe can be extended to cases in which the substrate is also thin and undergoes elastic strain. In this case the thickness of overgrowth which should be totally pseudomorphic is considerably increased, but at present this type of system has not been investigated because of difficulties in producing thin, continuous substrate films.

The introduction of misfit dislocations into the growing film is of crucial importance to pseudomorphism and hence it is worthwhile to consider the types of dislocation observed and the way in which they are formed. If one considers two crystals with slightly different lattice spacings, the difference in lattice spacing can be accommodated most efficiently by pure edge dislocations at the interface, Figure 1.4.

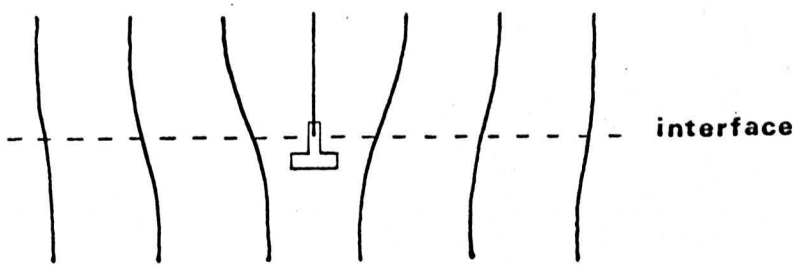

Figure 1.4 A pure edge misfit dislocation

This type of dislocation is the most efficient because the Burgers vector is in the plane of the interface. It might therefore be expected that all misfit dislocations would be of this type, but this is not observed. In the case of f.c.c. crystals with an (001) interface the plane of the interface is not a glide plane for pure edge dislocations (56). As the deposit thickness builds up more and more misfit dislocations have to be introduced. It is not possible under normal conditions to nucleate dislocations at the interface because the stress required is very high (56), and hence dislocations that can glide into the interface are favoured.

Several mechanisms for the introduction of misfit dislocations have been proposed by Matthews (48). The first method involves dislocations which extend through the substrate and overgrowth and

have Burgers vectors inclined to the interface. The stresses in overgrowth and substrate cause the section of dislocation in the overgrowth to separate from that in the substrate, leaving a long length of dislocation line trapped at the interface. This mechanism is thought to operate in many pseudomorphic systems and is described in more detail in chapter 2. The second mechanism involves nucleation of a dislocation at the specimen surface. The dislocation then extends under the action of the stress in the overgrowth and glides into the interface. This mechanism is expected to operate in bicrystal systems in which there is a fairly large misfit, since a large stress is required to nucleate a dislocation. The mechanism is shown schematically in Figure 1.5

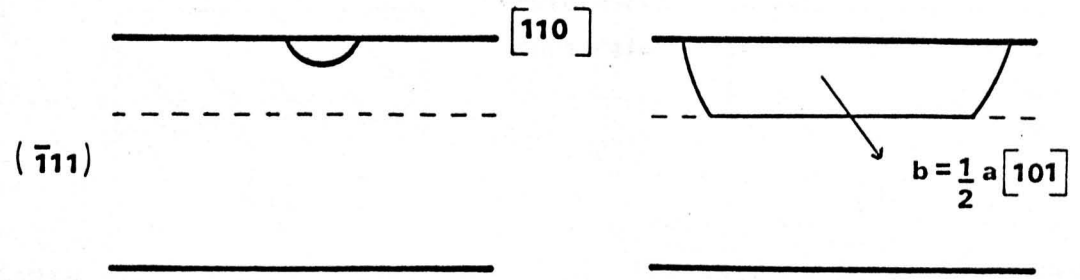

Figure 1.5 Nucleation and subsequent extension of a dislocation in a strained film. The diagram represents the (1̄11) plane, the two bold lines being the upper and lower specimen surfaces and the dotted line the overgrowth-substrate interface.

In both the mechanisms described the misfit dislocations formed are not of the pure edge type.

The introduction of a misfit dislocation into a growing island should not require the same amount of strain as in the case of a continuous film, since dislocations can be readily formed at the edge of the island. The relative ease of formation means that dislocations in islands should frequently be of the pure edge type, which has been observed for gold islands on platinum (48) and gold islands on palladium (57). However not all island deposits reveal pure edge dislocations, thus in the system of iron on hot (100) copper Jesser and Matthews (58) observed dislocations with inclined Burgers vectors. A mechanism involving extension of existing dislocations was proposed, operating in the same way as for continuous deposits. Jesser and Matthews suggested that in some systems, such as iron on copper, less energy is required to extend existing dislocations than

to nucleate new ones, despite the fact that dislocations so formed are inefficient.

1.3.3 Experimental Techniques

The experimental methods used in the study of pseudomorphism generally involve the preparation of a substrate followed by deposition of a uniform layer of overgrowth, Figure 1.6a. The misfit is then determined in situ, or the specimen is removed from the vacuum chamber and examined in the electron microscope.

An alternative technique introduced by Matthews (57) involves the use of a shutter during deposition of the over-layer, so that a thickness gradient or wedge is obtained, Figure 1.6b.

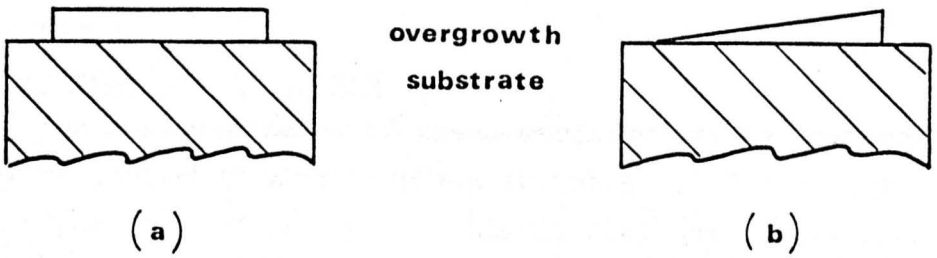

Figure 1.6 Schematic diagrams of a) the uniform layer technique and b) the wedge technique

The experimental investigation of pseudomorphism involves obtaining a series of values of misfit against deposit thickness so that elastic strain as a function of deposit thickness may be examined and compared with theory. Using the first technique several experimental runs are required to obtain sufficient data, whereas the wedge technique contains all the information required in a single experiment. However it is necessary to be able to obtain the deposit thickness at various stations along the wedge. Matthews achieved this with the use of an X-ray microanalysis attatchment to the electron microscope, so that microscopy of a given region of the sample could be coupled with a thickness determination.

There are a number of disadvantages with the wedge technique, the most important is probably the necessity of expensive X-ray microanalysis equipment before misfit against thickness data can be obtained. Secondly the theory of pseudomorphism assumes a deposit of constant thickness uniformly strained, which is not the case for a wedge. This objection is probably unimportant if the angle of the wedge is kept small so that the elastic strain does not change rapidly across the sample. Finally the wedge technique does not allow in-situ

measurements in the vacuum chamber to be carried out, because it is not possible to determine accurately the region of the sample from which the information is obtained. Thus a misfit measurement by reflection high energy electron diffraction (RHEED) may be obtained, but the thickness of deposit giving rise to this misfit would be unknown.

The deposition of a uniform layer does not suffer from any of the above disadvantages but it is a considerably more time-consuming procedure. The uniform layer technique was used in the present work because of the absence of X-ray microanalysis equipment. If the microanalysis equipment had been available then the wedge technique would have been used, since there is always the possibility of cross-checking results with a few samples prepared by the uniform layer technique.

1.3.4 Previous Investigations

The reported cases of pseudomorphism are not numerous and a summary of published work is given in Table I. It is only recently that the importance of the type of misfit dislocation has been realised and hence in many of the earlier investigations Burgers vector determinations were not carried out. Experimentally determined values of the critical thickness h_c for two dimensional deposits, or the critical radius R_c for island deposits are shown. It is noticeable that for misfits greater than about 5% critical thickness data were not obtained. This probably means that for misfits greater than 5% the critical thickness would be less than one monolayer and hence would not be observed. The observed values of critical thickness for different values of misfit follow the general predictions of theory, h_c varying from a few Ångstroms for misfits of about 4%, up to several microns for misfits considerably less than 1%.

With the advent of UHV the values of h_c obtained by different workers for the same system are in good agreement e.g. cobalt on copper and iron on copper. Experiments performed in technical vacuum whilst not showing the same consistency are however interesting. Of particular importance are the results obtained by Kuntze et al. (59) and Gradmann (60) for nickel on copper. For the system nickel on copper the value of h_c predicted by theory (chapter 2) is about 10 Å, which is in agreement with the experimental values obtained in UHV. The value of 80 Å obtained by Kuntze is in serious disagreement and it seems likely that the poorer vacuum conditions contributed to this disagreement. It is particularly interesting that the value of h_c was increased and

hence evaluation of the factors causing this disagreement might lead to a method of producing very thick pseudomorphic films. Such films might show unusual and useful magnetic or electronic properties. In the experiment performed by Gradmann the deposition of nickel was carried out in the presence of 5×10^{-6} torr of oxygen and pseudomorphism was completely inhibited. Thus it would seem that while some contamination can enhance pseudomorphism the oxygen contamination in Gradmann's experiment had the opposite effect. The possible role of contamination in pseudomorphic systems is discussed further in chapter 2.

The experiment performed by Haque and Farnsworth (37) on nickel-copper is relevant in that it is in complete disagreement with other UHV examinations. The analytical technique used was low energy electron diffraction (LEED) and the application of LEED to pseudomorphism is the subject of some controversy and will be discussed further in section 1.4.2.

Finally it is worth noting that in experiments reported to date the possibility of alloying at the interface between deposit and overgrowth has not been examined. This is of particular importance in systems such as copper-nickel where alloying is likely, since an interfacial alloy could have a considerable affect on subsequently deposited material. This omission was primarily due to lack of a suitable technique to detect rearrangement of different atomic species on a surface. However Auger electron spectroscopy is a surface sensitive technique which ought to enable alloying or surface rearrangement to be detected and this application of AES to bicrystal systems is reported in this thesis.

1.4 Techniques for the Examination of Films and Surfaces

1.4.1 Introduction

In the following section the experimental techniques used in the present work are described and their relevance to surface studies and pseudomorphism outlined. Finally other relevant techniques which were not available will be briefly described and a comparison made between these and the techniques employed.

1.4.2 Low Energy Electron Diffraction (LEED)

LEED involves directing a beam of monoenergetic electrons towards the surface of a crystal and then detecting the electrons which are elastically back-scattered. The energy of the primary electron beam is typically in the region of 10 - 500 eV.

TABLE I

system	misfit %	mode of growth	experimental conditions	h_c or R_c Å	analytical technique	Burgers vector	reference
Au-Pd	4.6	3D(001)Au//(001)Pd	UHV		EM	$\frac{1}{2}a[110]$	57
Au-Pd	4.6	2D(001)Au//(001)Pd	UHV	>1 layer	LEED		61
Au-Pd	4.6	2D(111)Au//(111)Pd	10^{-7} torr		EM	$\frac{1}{2}a[1\bar{1}0]$	89
Au-Pd	4.6	2D(001)Au//(001)Pd	UHV		EM	$\frac{1}{2}a[110]$	89
Au-Ag	0.19	2D(001)Au//(001)Ag	UHV	250	EM	$\frac{1}{2}a[\bar{1}0\bar{1}]$	57
Au-Pt	4.0	2D(001)Au//(001)Pt			EM	$\frac{1}{2}a[110]$	48
Pt-Au	4.0	2D(001)Pt//(001)Au	UHV		EM		57
Pt-Au	4.0	3D(001)Pt//(001)Au	electrodeposit		EM	$\frac{1}{2}a[110]$	63
Pt-Au	4.0	2D(001)Pt//(001)Au	UHV	10	EM	$\frac{1}{2}a[101]$	62
Pd-Au	4.6	2D(111)Pd//(111)Au	10^{-5} torr		EM		64
Pd-Au	4.6	2D(111)Pd//(111)Au	10^{-7} torr		EM		89
Fe-Au	8	2D(110)Fe//(111)Au	UHV		EM		65
Fe-Au	8	2D(110)Fe//(111)Au	UHV	0	EM	$\frac{1}{2}a[110]$	66
Au-Cu	13	2D(001)Au//(001)Cu	UHV	alloy	LEED		61
Au-MoS_2		3D	10^{-7} torr		EM		67,68
Ag-Cu	12.2	2D(111)Ag//(111)Cu	UHV		RHEED	$\frac{1}{6}a[\bar{1}\bar{1}2]$	60
Ag-Cu	12.2	2D(001)Ag//(001)Cu	UHV	<1 layer	LEED		61
Ag-Cu	12.2	spherical substrate	10^{-6} torr		RHEED	$\frac{1}{6}a[112]$	70
Cu-Ag	12.2	2D(001)Cu//(001)Ag	UHV		RHEED		126
Cu-Ag	12.2	2D(111)Cu//(111)Ag	10^{-7} torr	<15	RHEED		127

Ni-Ag	14.7	3D(001)Ni//(001)Ag	UHV		RHEED		126
Co-Ag	13	3D(001)Co//(001)Ag	UHV		RHEED		126
Ag-Ge	28	(001)Ag//(110)Ge	UHV		LEED		71
Pb-Ag	21	2D(111)Pb//(111)Ag	10^{-5} torr		RHEED		72
Co-Cu	1.5	2D(001)Co//(001)Cu	UHV	18.5	EM	$\frac{1}{6}a[\bar{1}12]$ $\frac{1}{2}a[101]$	73
Co-Cu	1.5	2D(001)Co//(001)Cu	UHV	20	EM	$\frac{1}{6}a[\bar{1}12]$ $\frac{1}{2}a[101]$	74
Co-Cu	1.5	2D(001)Co//(001)Cu	UHV	13	EM	$\frac{1}{6}a[\bar{1}12]$ $\frac{1}{2}a[101]$	75
Fe-Cu	0.9	3D(001)Fe//(001)Cu	UHV	750	EM	$\frac{1}{2}a[101]$	76
Fe-Cu	0.9	2D(001)Fe//(001)Cu	UHV	20	EM	$\frac{1}{2}a[101]$	77
Fe-Cu	0.9	2D(001)Fe//(001)Cu	UHV	20	EM		78
Ni/Fe-Cu		2D(111)Ni/Fe//(111)Cu	10^{-6} torr	20	RHEED		79
Ni-Cu	2.5	2D(001)Ni//(001)Cu	UHV	15	EM	$\frac{1}{2}a[101]$	36
Ni-Cu	2.5	2D(111)Ni//(111)Cu	UHV	10	RHEED		80,81
Ni-Cu	2.5	2D(001)Ni//(001)Cu	5×10^{-6} torr oxygen	0	RHEED		60
Ni-Cu	2.5	2D(001)Ni//(001)Cu	10^{-6} torr	80	THREED		59

Ni-Cu	2.5	2D(111)Ni//(111)Cu	UHV	0	LEED		37
Ni-Cu	2.5	2D(001)Ni//(001)Cu	electrodeposit		EM	$\frac{1}{2}a[011]$	82
Ni-Cu	2.5	2D(111)Ni//(111)Cu	electrodeposit		EM		82
Cu-Cu	0	spherical substrate	10^{-6} torr		RHEED		83
Cu_2O-Cu	17	spherical substrate	10^{-6} torr		RHEED		83
Cu_2O-Cu	17		1 atmosphere of oxygen		X		84
Cu-Ni	2.6	2D(001)Cu//(001)Ni	10^{-6} torr		THREED		59
Cu-Ni	2.6	3D(001)Cu//(001)Ni	10^{-6} torr		THREED		59
Cu-Ni	2.6	3D(001)Cu//(001)Ni	UHV		EM	$\frac{1}{2}a[110]$	85
Fe-Ni	3.5	2D(001)Fe//(001)Ni	UHV	15	EM		86
Cr-Ni	18	2D(001)Cr//(001)Ni	UHV	10	EM	$\frac{1}{2}a[101]$	76
Co-Ni	1.05	2D(001)Co//(001)Ni	UHV	50	EM	$\frac{1}{6}a[\bar{1}12]$	87
FeO-Fe	17			2 - 3 layers	LEED		88
PbSe-PbS	3	2D(001)PbSe//(001)PbS	10^{-7} torr		EM	$\frac{1}{2}a[110]$	89
PbSe-PbS	3	2D(001)PbSe//(001)PbS	10^{-6} torr		EM	$\frac{1}{2}a[110]$	53
Sn-SnTe	0.5	3D β-Sn (b.c.c.)	UHV	10	EM		90
Si-doped Si	≥ 0.003			1 micron	X		91
Ge-GaAs	0.07	2D(110)Ge//(110)GaAs	chemical decomposition	2000	EM		92
GaAs-Ge	0.07	(100)GaAs//(100)Ge	chemical reduction		X		93

$NiBr_2$-$CrBr_3$	0.3	(0001)$NiBr_2$//(0001)$CrBr_3$	sublimation in argon		RHEED		94
Co-Ni/Pd	0	2D(001)Co//(001)Ni/Pd	UHV	200	EM	$\frac{1}{6}a[112]$	158

KEY

EM	electron microscopy
LEED	low energy electron diffraction
RHEED	reflection high energy electron diffraction
THREED	transmission high resolution high energy electron diffraction
X	X-ray topography

LEED systems of several different designs are in use and Figure 1.7 shows the main components of the two most commonly used systems. The most important difference between the two types of system is in the method of detecting the scattered electrons. In the first system a double walled Faraday cup is employed which can be moved about to detect the diffracted beams. This method gives a direct and accurate measurement of the diffracted intensity at a particular angle. It is however comparitively slow, although using suitable electronics an oscilloscope display of the diffraction pattern may be obtained in a few minutes (95). In the post-diffraction acceleration method a series of hemispherical grids and a flourescent screen are used. The first grid is grounded so that the diffracted electrons travel in field free space, and the second grid is held at a negative potential to reduce the background intensity. A high

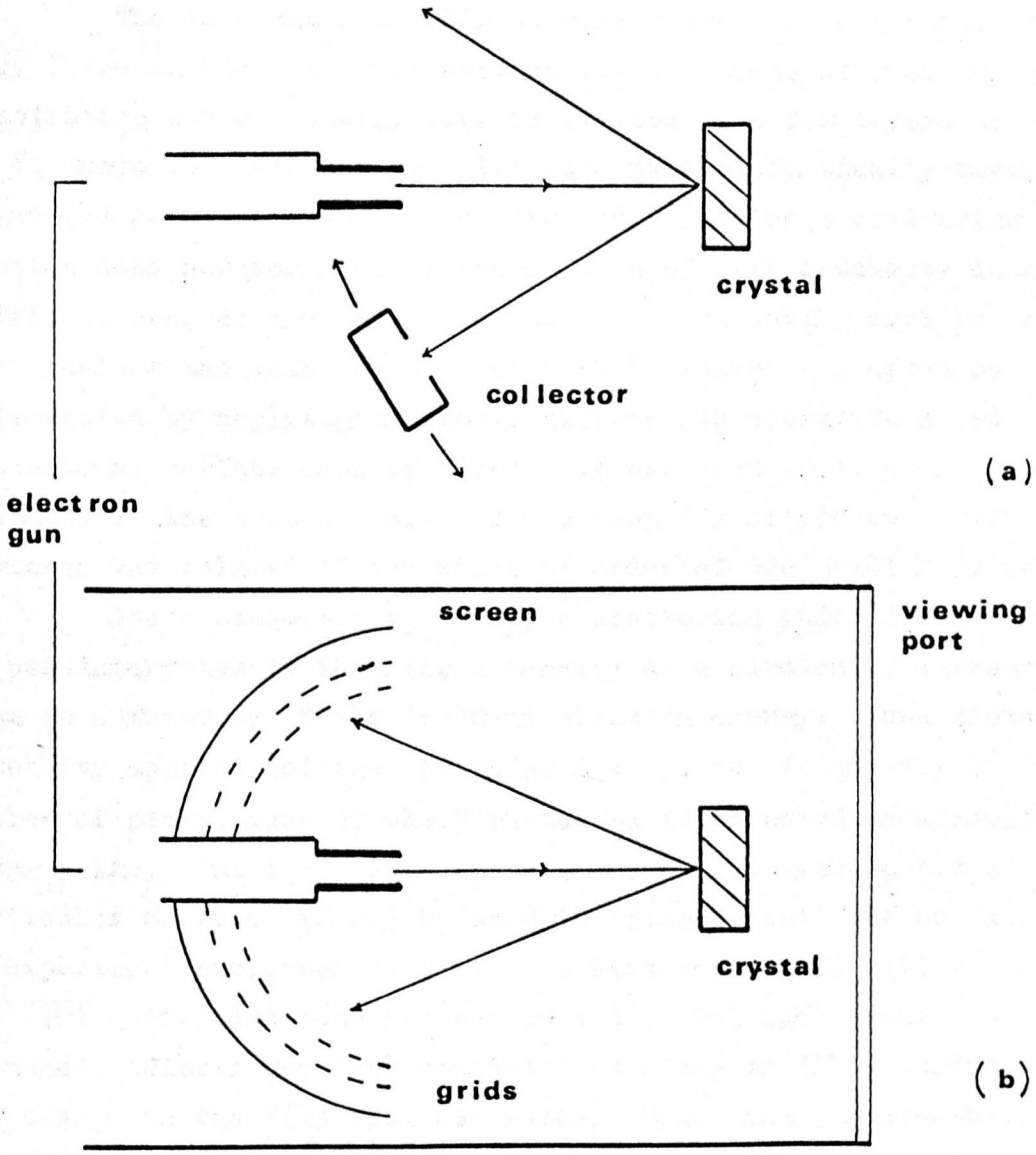

Figure 1.7 Schematic diagram of a LEED chamber a) Faraday cup system
b) Display system

positive voltage is maintained on the screen so that electrons are accelerated and given sufficient energy to cause flourescence in the coating. Each diffracted beam gives rise to a bright spot on the screen and the spot pattern may be observed through a suitable viewing port. Most modern LEED systems have an additional grid to reduce the penetration of the high positive potential to grid 2, resulting in much better cut off of inelastically scattered electrons. Beam intensity measurements may be made using a spot photometer mounted outside the vacuum chamber. This method gives less accurate intensity data but has the advantage that many diffracted beams may be viewed at once and rapid changes in the diffraction pattern followed. One other considerable advantage of this system is that it may be converted relatively simply to an Auger electron spectrometer and hence this type of LEED apparatus is much more widely used.

The importance of LEED to surface studies is a result of the very large scattering cross-section for electrons at such low energies. Penetration without energy loss is limited to a few layers and hence it is these few layers which give rise to the elastically back scattered components which are detected. The large scattering cross-section does however make interpretation of LEED intensity data difficult because the effects of multiple scattering must be included. Nevertheless the main features of a LEED pattern can often be interpreted by applying kinematic diffraction theory to a two dimensional surface mesh of atoms. It was this feature of LEED that was used in the present work and the geometry of observed diffraction patterns was related to the state of order of the crystal surface.

One consequence of multiple scattering which is of importance to pseudomorphism is that the intensity of a particular diffracted beam is a function of the incident electron energy. Such plots of intensity against voltage, known as I(V) plots, frequently show a large number of peaks, many of which cannot be interpreted as kinematical Bragg peaks. The I(V) plots are however characteristic for a particular surface and may be used to 'fingerprint' the surface. In an experiment performed by Haque and Farnsworth (37) I(V) plots for the $(\bar{1}0)$ diffracted beam for copper and nickel bulk specimens were obtained. Nickel was then condensed on a copper (111) surface and the change in the I(V) plot monitored. Haque and Farnsworth found that the I(V) plot from the specimen very rapidly became identical to the I(V) plot for pure nickel and concluded that the nickel was

growing with its bulk lattice parameter. This interpretation was challenged by Gradmann(81), although Gradmann's arguments were based on kinematical reasoning. The matter remains unresolved. However it is interesting that nickel on copper is a system which many observers have found to be pseudomorphic (Table I).

Recent reviews of LEED have been given by Prutton (96) and Estrup (97).

1.4.3 Auger Electron Spectroscopy

When an atom is ionized in an inner level it can relax to a state of lower energy by one of two processes. In the first process an electron from a higher level fills the vacancy and the excess energy is emitted as a photon. Alternatively an electron from a higher level may fill the vacancy and the excess energy is transferred by a radiationless process to another electron which is emitted from the atom. This emitted electron is the Auger electron and the net result is to leave the atom doubly ionized. In both the above processes the energy of the photon and of the Auger electron is characteristic of the energy levels of the atom from which they originate. Energy analysis of the photon or Auger electron can therefore be used as a method of chemical identification. Collection and energy analysis of the emitted photon is the basis of X-ray flourescence spectroscopy whereas the same process applied to the Auger electrons forms the basis of Auger electron spectroscopy (AES). The importance of AES as a method of surface chemical analysis is a result of the very large scattering cross-section for electrons in the range 0 - 1 keV normally used. Hence only Auger electrons produced within a few layers of the surface can escape without significant energy loss and be detected as Auger electrons.

The emission of an Auger electron is a result of an atom being ionized but is not dependent upon the method used to produce ionization. Hence any ionization mechanism may be used to create the initial vacancy in the sample. The majority of work on AES of solids has used an electron beam to produce the initial ionization because electrons have several advantages as sources of ionization. The cross-section for ionization of a given level is greater for electrons than for X-rays of similar energy, also the electron guns are fairly cheap, simple pieces of equipment and can produce well focused high density beams. There is one serious disadvantage of using electrons to produce the primary ionization; the emitted Auger electrons have to be separated from the background of secondary electrons. The background

is typically several orders of magnitude greater than the Auger current being analysed and hence this leads to problems of detection.

Instruments used for detection of Auger electrons may be divided into two types, dispersive analysers and retarding field analysers normally based on LEED optics. In the dispersive analysers only electrons within a certain energy range can pass through the analyser and be collected and hence a very large part of the background intensity is eliminated. Dispersive analysers using either cylindrical mirrors (98,99) or concentric hemispheres (100) for electron separation can obtain resolutions of about 0.1%, although a resolution of 0.01% has been obtained (101). (Resolution is defined as $\Delta E/E \times 100\%$ where ΔE is the width of the peak recorded by the spectrometer when a monoenergetic beam of electrons of energy E is passed through the analyser.)

In the retarding field analyser based on LEED optics a negative potential is applied to the centre grid so that electrons with energies below this potential are rejected. Hence all electrons with energies above this cut off potential are accepted and this leads to the much poorer signal to noise ratios of this type of analyser. Operated in this mode the retarding grid analysers would be very insensitive and it was not until Harris (102) showed that electronic differentiation of the electron energy distribution greatly enhanced the sensitivity that AES became widely used.

At present the major application of AES has been as a method of chemical identification. In this respect it has been extremely successful allowing surface contaminants to be detected at concentrations of 2% of a monolayer (103). However the strength of a detected Auger signal must be a function of the amount of material present and hence AES ought to be quantitative as well as qualitative. Until recently this aspect of AES had received very little consideration, but probably as a result of increased reliability of Auger electron spectrometers this is no longer the case. Nevertheless in the experiments reported so far some subsidiary assumption, e.g. a value of sticking coefficient, has been made in order to calibrate the observed Auger intensities. In chapter 3 a model proposed by Gallon (47) is described which relates observed Auger intensities to amount of deposited material without the necessity of such assumptions. The only requirements of this model being a substrate-deposit system which grows in layer by layer fashion and a constant rate source for the deposit material.

The application of AES to pseudomorphism is important with respect to rearrangement of deposited atoms on the surface. In any investigation of pseudomorphism the possibility of alloying at the interface must be considered and so far no experimental investigation of this has been possible. AES should fulfil this need, since if alloying does occur between deposit and substrate, Auger traces of a given amount of deposited material should show time dependence, which otherwise would not be the case. Quantitative development of AES could also be of importance in pseudomorphism since it would allow in situ misfit measurement to be related to deposit thickness. This could be particularly useful in the very early stages of deposition for systems with a critical thickness of only a few layers. Finally AES should enable the detection of oxide layers or impurities which could affect pseudomorphism of the deposited film.

A comprehensive review of AES has been given by Gallon and Matthew (104).

1.4.4 Reflection High Energy Electron Diffraction (RHEED)

In reflection high energy electron diffraction a narrow beam of monoenergetic electrons is directed at the surface at glancing incidence and the elastically scattered electrons are viewed on a distant screen, Figure 1.8.

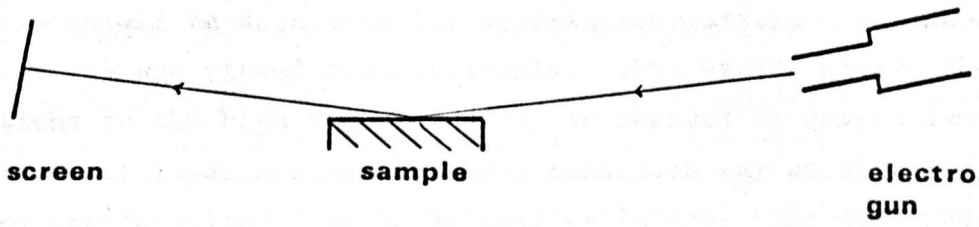

Figure 1.8 Schematic diagram of a RHEED system.

Because of the grazing incidence of the electron beam the penetration normal to the surface is small and hence RHEED is a surface analytical technique. In addition the grazing incidence makes the technique particularly sensitive to small asperities on the surface of the sample, which is not normally a feature of LEED; see Figure 1.9.

The small penetration normal to the surface means that the reciprocal lattice consists of a set of parallel rods perpendicular to the crystal surface. As a result of the high energies used (typically 10 - 30 keV) the radius of the Ewald sphere is large and hence the

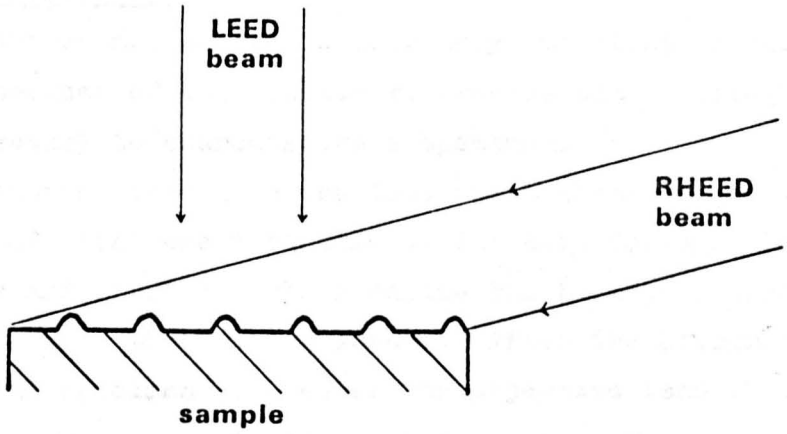

Figure 1.9 Relative illuminating conditions of LEED and RHEED.

diffraction pattern from a flat single crystal consists of a set of parallel streaks. However, if the beam passes through islands or undulations on the surface then a transmission diffraction pattern is obtained with characteristic sharp spots, this being one of the most useful properties of RHEED. In addition the high energies used lead to a small coherence length for the electrons and hence RHEED is applicable to polycrystalline samples.

RHEED is a technique which is applicable to studies of pseudomorphism and a number of investigations using RHEED have been performed (see Table I). For greatest reliability the experimental conditions should be such that the diffraction patterns from substrate and overgrowth are viewed simultaneously. This avoids errors due to fluctuations in the high voltage supply or changes in camera length. For the case of layer growth the above condition may be obtained by arranging the deposited film to be smaller in area than the substrate. The condition is automatically achieved in cases where the deposit nucleates, but in this situation the diffracted beam does not necessarily come from a region of deposit close to the interface. The elastic strain in an island is not uniform (67) as in the case of layer growth and hence uncertainties arise in measurement of misfit. In the case of layer deposits with non-zero misfit the diffracted streaks are doublets and the separation of the streaks enables determination of the misfit. The limitation of the technique is simply the width of the diffracted streaks which governs the resolution possible, and for this reason misfit measurements of less than a few per cent cannot be made with RHEED.

1.4.5 Electron Microscopy

The electron microscope is extremely important in thin film investigations because of its ability to provide almost all the information necessary to characterise a specimen.

The electron microscope consists of an electron gun (which produces a beam of electrons typically at 100 keV) followed by a system of lenses and apertures which define the beam path through the specimen and on to the viewing screen. After the electrons have passed through the specimen they enter the objective lens which focuses them to form the first intermediate image. This image is then further magnified in two stages by the intermediate and projector lenses, the projector lens forming the final image on the screen. However, magnetic lenses suffer from considerable spherical aberration and if all the diffracted beams leaving the specimen were allowed to reach the final image a low resolution, poor contrast image would result. This is overcome by the introduction of an aperture near the back focal plane of the objective lens (Figure 1.10) so that only the undeflected beam passes on to the other lenses. Image contrast is therefore a result of diffraction out of the straight-through beam and is known as diffraction contrast.

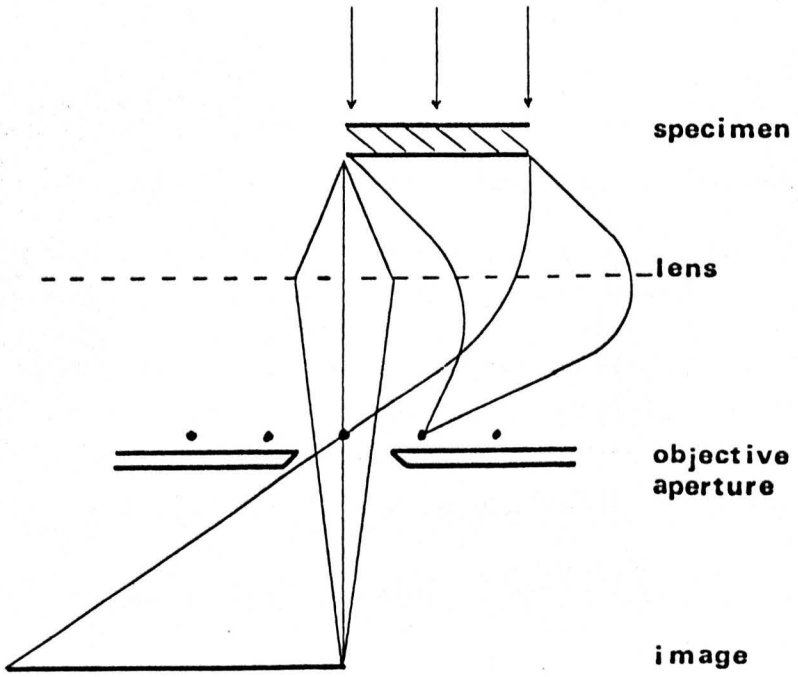

Figure 1.10 Use of the objective aperture to obtain diffraction contrast.

One particularly useful application of this method of image formation is that a final image can be produced with any diffracted beam. The brightest image is normally formed with the undeflected beam and is

called the bright field image. However, by displacing the objective aperture or tilting the beam, any diffracted beam may be made to pass down the axis of the microscope, producing a dark field image. Dark field microscopy is particularly useful since it reveals which regions of the specimen are contributing to a particular diffracted beam. It also enables the identification of defects such as dislocations, since these defects become invisible under certain diffraction conditions (105).

The power of the electron microscope is that microscopy of a given specimen can always be combined with diffraction and hence a great deal of information may be obtained. In addition most electron microscopes are fitted with an aperture in the first intermediate image plane which enables a small area of the image to be selected. If the intermediate lens is then defocused to the diffraction condition only the diffraction pattern from the selected area will be observed. This technique, known as selected area diffraction, enables close correlation between the diffraction pattern and the image.

Finally the addition of an X-ray flourescence attatchment to the electron microscope enables chemical identification to be coupled with normal microscopy and diffraction. The electron beam incident upon the sample generates X-rays which have energies characteristic of the atom from which they originated. Hence detection and energy separation of the emitted X-rays enables chemical identification.

The electron microscope has been extensively used in the study of pseudomorphism because of the ability to obtain misfit measurements from a sample, as well as structural or crystallographic information. The following methods have been used to obtain misfit measurements:

(i) Measurement of the spacing of Moiré fringes. When an electron beam passes through two crystals it is possible that a diffracted beam from the first crystal will be diffracted again in the second crystal. If such a doubly diffracted beam combines with an undiffracted beam interference may occur, resulting in a pattern of fringes known as Moiré fringes. For the case of parallel lattice planes the spacing of the Moiré fringes is given by (105)

$$D_m = \frac{d_1 d_2}{d_1 - d_2} \qquad (1.3)$$

where d_1 and d_2 are the spacings of the two lattices. Therefore in a

specimen consisting of one crystal grown epitaxially on another with a different lattice spacing, a set of Moiré fringes may be obtained, the spacing of which will depend upon the two lattice constants. For the case in which $d_1 \simeq d_2$ the misfit may be written as

$$M = \frac{d_2 - d_1}{d_2} \qquad (1.4)$$

and hence the separation of the Moire fringes is given by

$$D_m = \frac{d_1}{M} \qquad (1.5)$$

Thus measurement of the separation of Moiré fringes enables a value for misfit to be obtained.

(ii) Measurement of the spacing between dislocation lines. In the case of a pseudomorphic specimen the spacing between dislocation lines depends upon the misfit. For large values of misfit the dislocations are close together, whereas for small misfit the dislocations are well separated. The spacing between the dislocations is given by the Brooks formula (106)

$$D_d = \frac{|\underline{b}|}{M} \qquad (1.6)$$

where $|\underline{b}|$ is the magnitude of the Burgers vector and M is the misfit. The spacing between dislocations may be measured from electron micrographs and hence determination of the Burgers vector (105) enables the misfit to be calculated.

(iii) Measurement of the spacing between diffracted spots. When an electron beam passes into a bicrystal specimen both crystals will give rise to a diffraction pattern. The spacing between features on the diffraction pattern will depend upon the lattice constant of the crystal from which they originate. Hence measurement of the spacing between two features of the diffraction pattern from one crystal and the spacing for the same two features of the diffraction pattern from the second crystal would enable the misfit to be calculated. Under normal diffraction conditions with typical misfits of a few per cent it is not possible to resolve features from the two different diffraction patterns. However, if a high resolution diffraction facility is

available it may be possible to achieve adequate resolution and this is the basis of the transmission high resolution high energy electron diffraction (THREED) technique used by Kuntze (59,107). This technique enables very long effective camera lengths to be obtained and by adjusting the camera length only two diffraction spots, for example the (000) and (200) spots, are obtained on opposite sides of the viewing screen. If there is misfit between the bicrystal specimen the diffracted spot is split in two and the misfit is given by the ratio of the separation of the split spots to the distance between the (000) and (200) substrate spots.

It is worthwhile comparing the three techniques since they are in some measure complementary. The spacing of Moiré fringes and dislocation lines increases as the misfit decreases and hence these two techniques should be more suited to cases of very small misfit. On the other hand the separation of the split spots in THREED decreases for decreasing misfit and hence this technique cannot be used for very small misfits because the split spots cannot be adequately resolved. The dislocation and Moiré techniques give information about the misfit in the localized area where the fringes or dislocations are seen, whereas the THREED technique gives an average value of misfit for the whole area of specimen sampled by the electron beam (typically 0.5 mm across). Consequently the THREED technique is not suited to cases of island deposits where the misfit may vary considerably from one island to the next. The accuracy obtainable by the dislocation and Moiré techniques is limited mainly by the accuracy with which the magnification of the electron microscope is known. By calibrating the magnification of the microscope absolute uncertainties in misfit measurements of $\pm$ 0.6% in a misfit value of 5.3% have been obtained (90). Misfit determination by the spacing of dislocation lines should show a similar accuracy. The accuracy obtainable with the THREED technique is under most conditions considerably better than this and is typically about $\pm$ 0.02%. This is because relative measurements only are needed and hence they are not affected by uncertainties in magnification. In addition a knowledge of lattice constants is not required and another possible source of error is avoided.

The THREED technique is therefore the most accurate and is preferable in cases where it may be readily applied. It cannot be used in situations where the deposit nucleates or when the misfit is very small (typically less than 0.5%). The Moiré and dislocation techniques,

whilst being less accurate, are applicable to island deposits and cases of very small misfit. In addition they give misfit information about localized areas which may be useful in certain circumstances. The choice of technique therefore depends primarily on the bicrystal system being studied. There are many occasions however where two techniques, or even all three, may be used and hence cross-checking of results is possible.

1.4.6 Residual Gas Analysis

Residual gas analysis differs from the techniques described previously in that it does not give structural or chemical information about a surface directly. The analysis of residual gas is performed by means of a mass spectrometer, which for applications in UHV must be bakeable.

The importance of residual gas analysis has increased considerably since the advent of UHV because of the accompanying reduction in specimen contamination. As a result it is now possible to do experiments on the interaction of specific gases with a growing film. A knowledge of the gases present and their partial pressures is important and a mass spectrometer is essential if a controlled experiment is to be performed.

The mass spectrometer may also be used to identify substances desorbed from specimen surfaces. Thus adsorbed gases may be detected by removing them from the surface using techniques such as flash desorption or ion bombardment. A mass spectrometer may be used to monitor the destructive effects of certain experimental techniques, and the non-stoichiometric dissociation of a KCl crystal during electron bombardment has been observed (28).

Finally the mass spectrometer is of considerable importance in a UHV system for the detection and identification of outgassing components and for leak detection.

1.4.7 Other Techniques for Surface Structure or Chemical Analysis

Perhaps the most powerful technique of surface structure analysis is that of field ion microscopy (FIM), because it is possible to resolve individual atoms. The field ion microscope consists of a specimen in the form of a sharp point, held at a high positive potential with respect to a flourescent viewing screen. A gas such as helium is introduced to the microscope tube at a pressure of a few millitorr, and gas atoms which go near the surface of the strongly positive specimen point are ionized by quantum mechanical tunneling. The positive ions are then accelerated to the screen where they form

an image of the metal surface. One disadvantage of the field ion microscope is that the high electric fields needed to operate the microscope can cause field evaporation of the specimen surface (108). Hence FIM is only readily applicable to the refractory metals. Field ion microscopy is not applicable to pseudomorphism because only the outer layer of atoms is imaged and hence information about the interface cannot be obtained. In addition the electric field and the spherical specimen tip results in a situation which is far from that normally used in studies of pseudomorphism.

A well established method of surface chemical analysis which in many respects is similar to AES is photoelectron spectroscopy. This involves directing a monochromatic beam of radiation on a sample surface, then collecting and energy analysing the emitted electrons. The incident radiation is normally a beam of X-rays with energies between 1000 and 1500 eV. Radiation of this wavelength permits examination of the electronic structure of the inner levels of most atoms, and since the energy of the emitted electron is characteristic of the emitting species chemical identification is possible. Alternatively the incident radiation may be ultra-violet, in which case the electrons emmited are from the less tightly bound outer shells and information on the valence electrons may be obtained (109).

The technique depends upon energy analysis of an electron which has to escape from the sample to the vacuum, and hence the depth sampled is similar to that for AES, depending upon the inelastic scattering cross-section. Photoelectron spectroscopy is therefore a surface sensitive technique and for this reason most work is now being done in UHV (110). The major disadvantage of photoelectron spectroscopy compared with electron induced AES is that the ionization cross-section for photons is small and hence very long counting times are necessary. However the emitted electrons do not appear amidst a high background of secondary electrons, hence collection and energy analysis is more straightforward and very high resolution spectra have been obtained (110). The application of photoelectron spectroscopy to surface studies may therefore be considered as similar to AES.

X-ray diffraction is generally a technique which is not applicable to thin film-surface investigations because the scattering cross-section for X-rays is so small. However, it has been used to observe dislocations in a pseudomorphic specimen (91). The technique for examination of dislocations generally used is that of X-ray diffraction topography, in which the crystal is oriented with respect

to the X-ray beam so that a set of lattice planes is at a Bragg angle for strong reflection. The reflected beam is then examined photographically, and any local bending of the lattice planes associated with a dislocation causes a change in the reflection conditions and hence the dislocation is detected on the photograph. No magnification occurs in recording the photograph but use of very fine grain film enables subsequent magnification up to x500 (111). This magnification is still very small compared with that obtainable by electron microscopy and the technique is only suitable for observation of specimens with very low dislocation densities (typically $\sim 10^6$ cm^{-2}).

Work function measurements have been used to study cleanliness of sample surfaces since the energy required to eject an electron is very sensitive to surface contamination. Work function measurements can be combined with LEED, using the LEED gun as an electron source and retarding potential methods to measure the work function (112). However it is not possible to chemically identify the contaminant species which is a major disadvantage.

Comparing the techniques used in the present work with those described above it is seen that FIM, whilst enabling observation of individual atoms is not applicable to the study of an interface of the type that occurs between two pseudomorphic crystals. In addition the equipment required is specialised and the necessity of a sharply pointed specimen makes other analytical techniques such as LEED and RHEED impractical.

Photoelectron spectroscopy and AES are very similar in their range of application but the very much faster scan rates of AES make it preferable. In addition AES is readily combined with LEED. In the present context either of these techniques is preferable to work function measurements because they allow direct chemical identification.

Finally the electron microscope is superior to all other methods of observation of dislocations with the exception of dislocations in bulk specimens. The scattering cross-section for electrons does not allow penetration of samples greater than about 1500 Å in thickness (for 100 keV electrons). In circumstances where the sample is thicker it is essential to use X-ray techniques or alternatively to reduce the thickness of the sample. This problem did not arise in the present case because thin films were used as substrate crystals.

1.5 Aim of the Present Work

The reported cases of pseudomorphism described in section 1.3.4 generally show reasonable agreement with the predictions of theory. Thus systems with a very small bulk misfit show large values of h_c (the critical thickness), whereas small values of h_c are observed for systems with larger misfit. The system of nickel on copper is one that has been investigated by many workers (Table I), but in this particular case the results are not all in agreement. The value of h_c predicted by theory (chapter 2) is about 11 Å and this result has been obtained experimentally by Matthews and Crawford (36), the experiments being done in UHV. Kuntze (59) carried out a similar series of experiments in technical vacuum and obtained a critical thickness of 80 Å, whereas Haque and Farnsworth (37) failed to observe pseudomorphism at all, even though their experiment was performed in UHV. Gradmann (80) obtained results in agreement with theory when experiments were carried out in UHV, but found that exposure to oxygen prior to nickel deposition could completely inhibit pseudomorphism (60).

The nickel-copper system was therefore in need of further investigation with a view to determining the cause of the above discrepancies. The experiments of Gradmann indicated that gas contamination could play an important role and hence a means of identifying surface species was required. The AES facility available was a suitable technique and it was hoped to investigate the affect of surface contamination on pseudomorphism, the contamination being monitored by AES. In addition copper and nickel readily alloy when in bulk form (113) and the occurrence of an interfacial alloy could have a considerable affect on pseudomorphism. However rearrangement of deposited atoms on the surface should give rise to time dependent Auger traces and this possibility was investigated.

Unfortunately the experiments involving calibrated deposition of nickel on copper could not be repeated because of the difficulty of constructing a Knudsen source for nickel. Nickel alloys with all the refractory metals commonly used for crucibles and at the time a suitable crucible material could not be found. However the reverse experiment of copper on nickel was possible and this should be very similar to nickel on copper. In addition the system copper on nickel had not been investigated in UHV for deposition at room temperature and the experiment is reported in detail in chapter 6.

As a preliminary to the above experiments the quantitative application of AES was investigated using the system of silver on nickel. A means of preparing nickel substrates had been developed for the copper-nickel experiments and a suitable deposit material was required. Silver was chosen because it is comparitively easy to construct a Knudsen source for silver and in addition a vapour source for silver was required for a different series of experiments (29). Also silver has a comparitively low surface free energy (114) and hence is likely to grow in layer by layer fashion on most metal substrates. Finally silver and nickel give rise to Auger signals which are well separated in energy, making detection simpler, and nickel-silver is not a system which alloys in bulk form (113).

A simple model relating observed Auger intensities to amount of deposited material had been proposed by Gallon (47) and the application of this model to silver deposited on nickel was investigated. The results of the silver-nickel investigation are reported in detail in chapter 5.

In summary therefore the aims of the present work were:

(i) to investigate pseudomorphism for the system of copper deposited on nickel,

(ii) an investigation of the affect of contamination on pseudomorphism between copper and nickel,

(iii) to investigate the possibility that alloying may occur at the interface between metal-metal bicrystals,

(iv) as a preliminary to the above studies to investigate the quantitative application of AES to systems which exhibit layer by layer growth and the possibility of using AES to detect surface rearrangement in such systems.

CHAPTER 2

THEORETICAL TREATMENT OF PSEUDOMORPHISM

2.1 Introduction

The first theoretical consideration given to the layer growth of a single crystal of material A on a single crystal substrate of material B was by Frank and Van der Merwe (49,50). Their simple model consisted of a one dimensional chain of balls held together by springs of equal length and strength. The chain of balls rests on the bottom of a horizontal frictionless trough on which there is a sinusoidal corrugation of low amplitude, Figure 2.1.

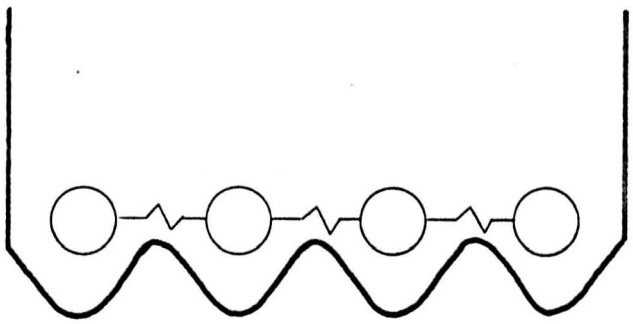

Figure 2.1 Schematic representation of the simple model of Frank and Van der Merwe.

The variables involved in the model are the length and elastic strength of the springs and the height and spacing of the corrugations. Complete pseudomorphism occurs if the springs are deformed so that each ball rests in the bottom of a trough and there are no empty troughs. On the other hand pseudomorphism does not occur if the springs remain rigid and the separation between the balls is unchanged. The intermediate case arises when partial deformation of the springs occurs so that some of the balls are in the base of a trough and the mean separation between the balls is changed. Frank and Van der Merwe were able to show mathematically using the above model that for the intermediate case there would be large regions of very good fit separated by relatively small regions of poor fit. The regions of poor fit were termed misfit dislocations.

The original theory has been considerably extended and is discussed in more detail in the next section, under the title of equilibrium theory, since the results are obtained by use of the

methods of equilibrium thermodynamics. In section 2.3 a more recent theoretical approach due to Matthews and Crawford (36) is described in which account is taken of the discrete nature of the relaxation of elastic strain.

2.2 The Equilibrium Theory

2.2.1 Two Dimensional or Layer Growth

Following the original paper in 1949 Van der Merwe and co-workers (115,116,117,118,119) have considerably extended the mathematical treatment to enable the analysis of more realistic models of pseudomorphism between two crystals. The basic procedure is to determine the sum of the elastic strain energy and the energy of the dislocations and to assume that the equilibrium configuration occurs when this sum is a minimum. This assumption is not automatically justified since crystal growth is a dynamical process and is concerned with events on a microscopic scale. The methods of equilibrium thermodynamics are not sufficient to describe a process of this kind. However the assumption is normally justified on the grounds that it leads to results which are in reasonable agreement with experiment (121).

The calculation of the energy associated with elastic strain in the film is straightforward providing the film strains uniformly throughout its thickness. For the case of elastic strain along one direction in the film plane the energy is given by (36)

$$E_\varepsilon = \frac{G_o(1-\nu)\ h\varepsilon^2}{1-2\nu} \qquad (2.1)$$

where h is the film thickness, ν is Poisson's ratio, ε is the elastic strain and G_o is the shear modulus of the overgrowth. The calculation of the interfacial energy due to the grid of misfit dislocations is not so straightforward and depends upon the model used for the tangential interfacial forces. In the original one-dimensional model of Frank and Van der Merwe the form of the interfacial potential energy was assumed sinusoidal. A refined model includes a second harmonic term in the Fourier series which allows the shape of the curve to be varied (120). Finally the simplest representation from the analytical point of view, though less realistic, is the parabolic model in which the interaction potential is obtained by joining successive parabolic arcs. The various representations are compared in Figure 2.2. The tangential interfacial shear stress is obtained from the potential

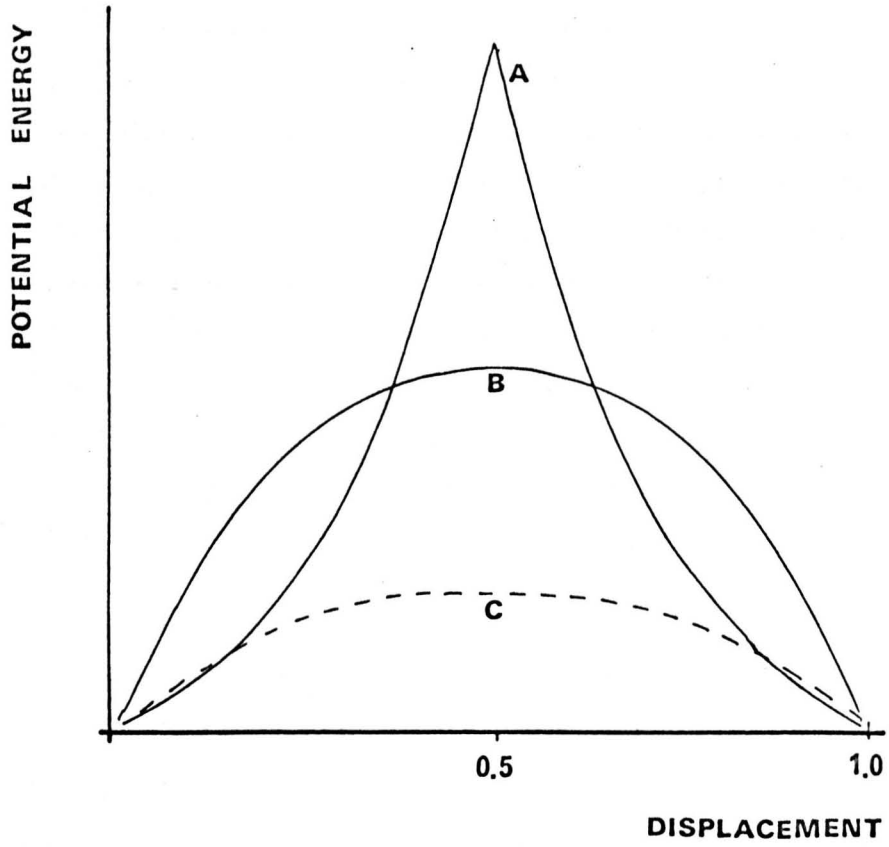

Figure 2.2 Graphs of the interfacial potential energy v relative atomic displacement.
Curve A: parabolic model; curve B: sinusoidal model; curve C: refined model.
Reference (120)

energy by differentiation.

The parabolic and sinusoidal models can be used to obtain an exact solution for the interfacial energy E_d, which for the sinusoidal representation yields

$$E_d = \frac{G_i b}{4\pi^2}\left\{1+\beta-(1+\beta^2)^{\frac{1}{2}}-\beta \ln\left[2\beta(1+\beta^2)^{\frac{1}{2}}-2\beta^2\right]\right\} \qquad (2.2)$$

where

$$\beta = \frac{2\pi(f-\varepsilon)\,G_o G_s}{(1-\nu)(G_s+G_o)\,G_i} \qquad (2.3)$$

The misfit between the unstrained lattices is represented by f, b is the magnitude of the Burgers vector of the dislocations and G_o, G_s and G_i are the shear moduli of the overgrowth, substrate and interface respectively. ν is Poisson's ratio, assumed equal for the interface, substrate and overgrowth. Three assumptions made in the derivation of equation 2.2 are that misfit exists along one direction only, that the misfit dislocations are in pure edge orientation with Burgers vectors in the interface and there is no interaction between dislocations.

If the minimum value for $E_d + E_\varepsilon$ is found then the following equation for ε in terms of the film thickness h is obtained

$$\varepsilon = \frac{-G_s b (1-2\nu)}{4\pi (1-\nu)^2 (G_s + G_o) h} \ln\left[2\beta\left(1+\beta^2\right)^{\frac{1}{2}} - 2\beta^2\right] \qquad (2.4)$$

This expression for ε predicts that if the misfit is large (greater than about 10%) then most of the misfit will be accommodated by misfit dislocations (117). If the misfit is small all of the misfit may be accommodated by elastic strain until a critical thickness h_c is reached. That complete coherency between the substrate and overgrowth is energetically possible according to this model is demonstrated by Figure 2.3. When there is no homogeneous strain the interfacial energy increases with misfit according to curve A. The elastic strain energy increases proportional to the square of the strain ε and is shown by curve B. Over the range of misfit 0 to a critical value f_c, B is below A and the coherent state is the one of lowest energy. Beyond f_c the misfit is accommodated partly by homogeneous strain and partly by misfit dislocations (121).

The equations given above can be modified to hold for systems in which there is misfit along two perpendicular interfacial directions (55) and similar predictions are obtained.

The form of equation 2.4 for the equilibrium elastic strain is interesting in that it predicts that once complete coherency is lost the overgrowth film rapidly returns to its bulk lattice parameter. This is shown schematically in Figure 2.4 for the hypothetical case of an overlayer which is completely coherent up to four monolayers. This feature is common to all the equilibrium theories of pseudomorphism and is not in general agreement with experimental results (120).

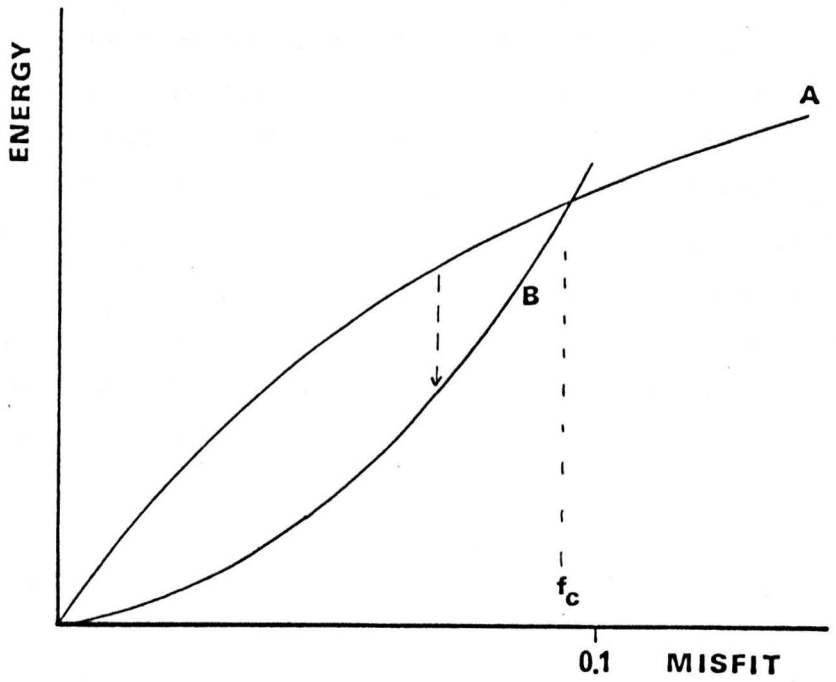

Figure 2.3 Curve B illustrates the fact that for a range of misfit 0 to f_c there is a reduction in the total energy if the film is completely coherent. The arrow represents the reduction in energy for a particular value of misfit.

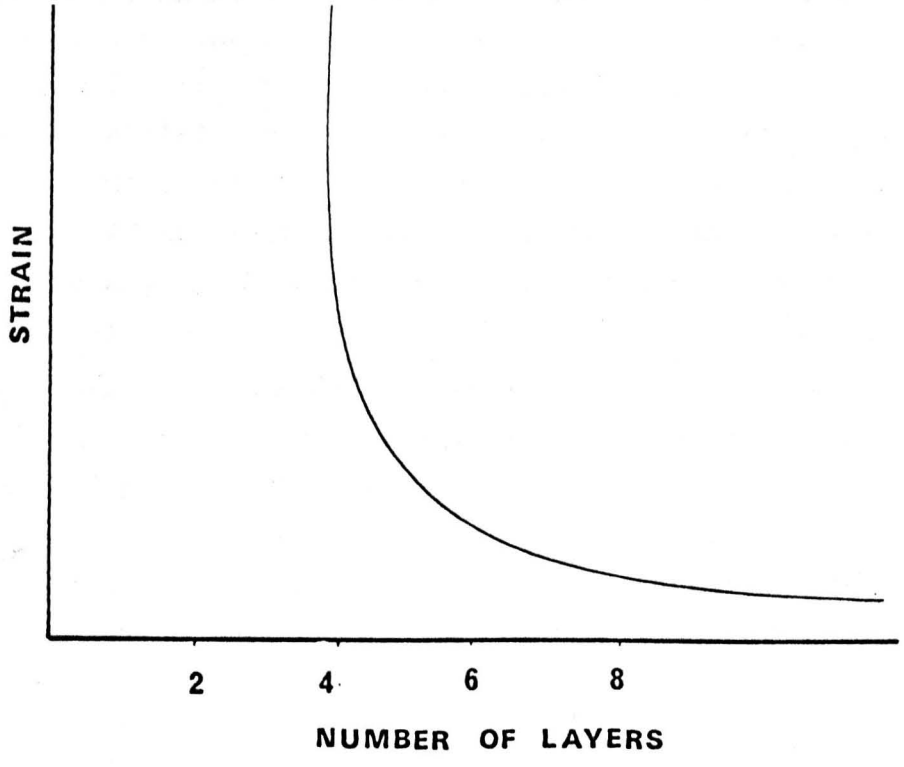

Figure 2.4 The variation in overgrowth lattice constant once complete coherency is lost.

2.2.2 Island Deposits

In the case of island deposits the elastic strains in the overgrowth are considered inhomogeneous, in that they are largest in the interface and decrease with distance along the normal to the interface. Therefore for a given strain at the interface the total elastic strain energy will be smaller for an island deposit than for a continuous film. The first analysis of the strain energy for an island was performed by Cabrera (54) who assumed that the overgrowth consisted of hemispherical islands of radius R and that the inhomogeneous elastic strains were radial strains. The total elastic strain energy associated with a radial elastic strain at the interface was found to be

$$E_\varepsilon = \frac{2 G_o R^3 \varepsilon^2}{3(1-\nu)} \qquad (2.5)$$

The interfacial energy will be the same as for the continuous overgrowth except that it must be multiplied by the contact area πR^2. The equilibrium elastic strain is found by minimising the sum of elastic strain energy and interfacial energy in the same way as for continuous deposits (55).

If the misfit is small, then in an analagous manner to a continuous deposit, the islands may initially be completely coherent. The radius of the island at which complete coherency is lost is known as the critical radius R_c, and a table of values of R_c and h_c have been calculated for various metal-metal combinations by Jesser and Kuhlmann-Wilsdorf (55). Their results are reproduced in Table II. In Table II critical values are listed for both R_c and h_c, but normally a given deposit-substrate system would display either layer growth only or island growth only, depending on the values of surface free energy. It may however be possible for the deposit morphology to change with different substrate temperatures and an example of this will be described in chapter 5.

It can be seen from Table II that the value of R_c at which an island loses coherency is much larger than the corresponding value of h_c at which the continuous film becomes non-coherent.

TABLE II

Deposit - Substrate	Misfit / %	h_c / Å	R_c / Å
Pt - Au	3.94	4	82
Au - Cu	11.35	2	24
Au - Ni	13.60	1	18
Ni - Ag	14.7	1	9
Ag - Au	0.18	243	5128
Pd - Pt	0.86	45	881
Pd - Au	4.84	4	74
Cu - Ni	2.63	11	205

2.2.3 Elastic Substrates

In the equations described so far it has been assumed that the elastic deformation occurred in the overgrowth. This is normally a good assumption, since in a typical experiment the thickness of the substrate would be an order of magnitude greater than the thickness of the deposit. If however the deposit and substrate thicknesses are comparable then the possibility of the substrate deforming cannot be ignored. This situation has been analysed by Jesser and Kuhlmann-Wilsdorf (55) and it is found that values of h_c are increased if some of the misfit is taken up by elastic strain in the substrate, as one would expect.

2.3 An Alternative Theory

2.3.1 Layer Growth

The variation of elastic strain with overgrowth thickness can be calculated by considering the forces acting on dislocations already present at the interface. It has been found (36,73) that for some systems the misfit dislocations are not pure edge type with Burgers vectors in the plane of the interface, but have Burgers vectors inclined to the interface. In the case of f.c.c. materials and an (001) interface these dislocations have Burgers vectors of the type $\frac{1}{2}a\,[011]$, which accommodate only half the misfit accommodated by a $\frac{1}{2}a\,[110]$ type of dislocation. They are therefore inefficient dislocations for accommodating misfit. They are however dislocations which are able to glide on (111) planes and can therefore move into the interface to accommodate misfit. This is not the case for the

pure edge type dislocation. Further, misfit dislocations with inclined Burgers vectors can be produced by extension of already existing dislocations whose lines extend through the substrate and overgrowth. This mechanism was first proposed and observed by Matthews (57) and the process is shown schematically in Figure 2.5. The dark outline in the figure represents a section of a glide plane in the bicrystal. The intersection of this plane and the plane of the interface is shown by the broken line. In Figure 2.5a the double outline shows an existing dislocation extending through the substrate and overgrowth. Figure 2.5b shows the same dislocation after it has undergone glide and has produced the length AB of misfit dislocation.

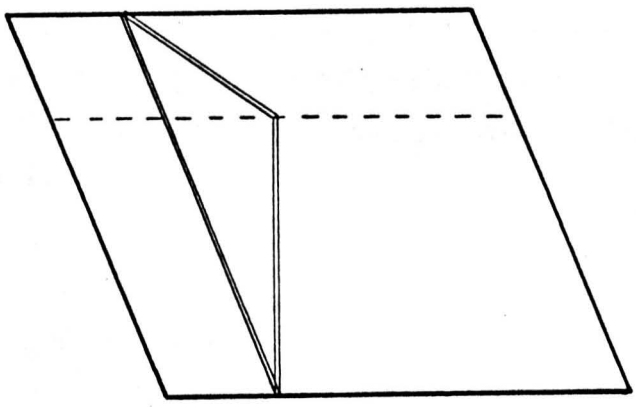

(a)

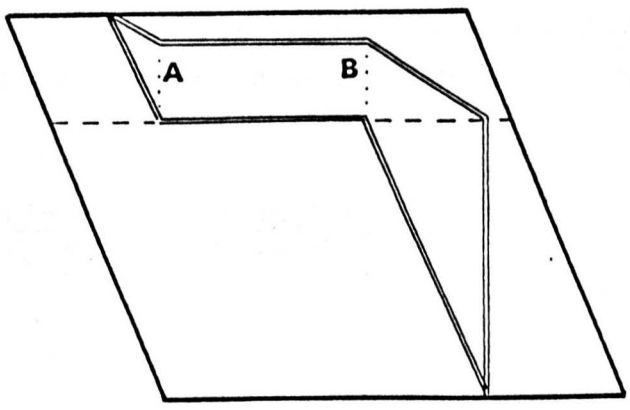

(b)

Figure 2.5 The formation of misfit dislocations by slip of existing dislocations a) before slip b) after slip.

If one considers a dislocation already present, then the length of dislocation line will only increase if a force acts upon the dislocation. This is because an increase in the length of a dislocation results in an increase in the self energy or line tension of the dislocation (56). The dependence of elastic strain with overgrowth thickness may be determined by equating the force acting on the dislocation with the tension in the misfit dislocation line (36).

The force acting on a dislocation is a result of elastic strain ε in the overgrowth and is given by

$$\frac{2 G_o \varepsilon b h (1+\nu) \cos\lambda}{(1-\nu)} \qquad (2.6)$$

where λ is the angle between the slip direction and that direction in the plane of the film which is perpendicular to the line of intersection of the slip plane and the specimen surface. The tension in a dislocation line is given by

$$\frac{G_i b^2}{10} + \frac{G_i b^2 (1-\nu \cos^2\alpha)}{4\pi (1-\nu)} \ln \frac{h}{b} \qquad (2.7)$$

where α is the angle between the line of the dislocation and its Burgers vector. The first term in equation 2.7 is the core energy of the dislocation and the second term is the elastic strain energy of a mixed dislocation. If expressions 2.6 and 2.7 are equated then the following equation for ε in terms of h is obtained.

$$\varepsilon = \frac{G_i b(1-\nu)}{20 G_o h(1+\nu) \cos\lambda}\left[1+\frac{10}{4\pi}\frac{(1-\nu\cos^2\alpha)}{(1-\nu)} \ln \frac{h}{b}\right] \qquad (2.8)$$

The form of equation 2.8 for the system nickel on copper is shown in Figure 2.6.

For the particular case of nickel on copper Matthews found that the predicted value of $h_c = 10$ Å was in reasonable agreement with his experimental results. For large deposit thicknesses the theory once again predicts a much smaller value of elastic strain

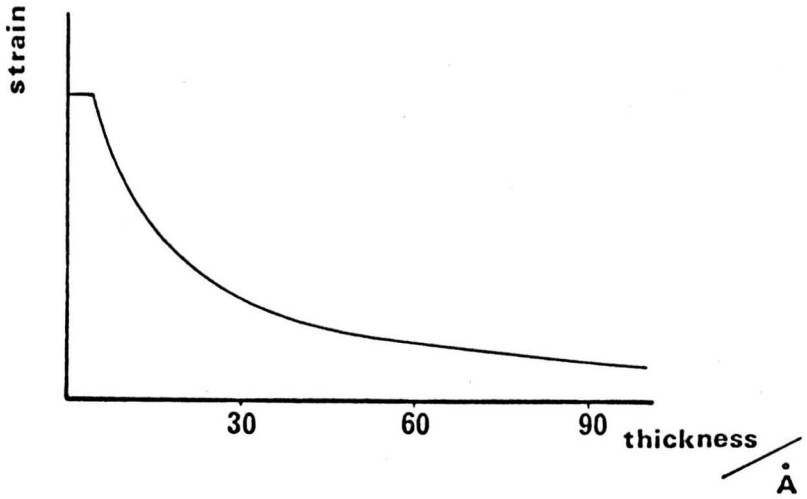

Figure 2.6 The predicted variation of elastic strain with thickness.

than was actually observed. If the possibility of interaction between dislocations was taken into account this discrepancy for thick overlayers was removed. To allow for dislocation interaction Matthews assumed that the elastic strain in the film was ε' larger than the strain predicted by equation 2.8. The additional force on dislocations as a result of this is given by

$$\frac{2G_o\varepsilon' b h(1+\nu)\cos\lambda}{1-\nu} \qquad (2.9)$$

The force of interaction between a pair of dislocations with anti-parallel Burgers vectors, a distance r apart is given by

$$\frac{G_o b^2 h}{2\pi r \cos\phi} \qquad (2.10)$$

where ϕ is the angle between the film surface and the normal to the slip plane. Thus the additional elastic strain that can be supported by interacting dislocations is

$$\varepsilon^x = \frac{1-\nu}{4\pi(1+\nu)\cos\lambda\cos\phi}\,\frac{b}{r} \qquad (2.11)$$

In order to find a value for ε^x it is necessary to consider the

probability of a given dislocation meeting another dislocation with an antiparallel Burgers vector. Matthews has estimated this for the nickel-copper system and obtains an approximate value for the additional elastic strain given by

$$\varepsilon^{*} \simeq \frac{f - \varepsilon}{10} \qquad (2.12)$$

From equation 2.12 it can be seen that the additional elastic strain is negligible in the region where most of the misfit is accommodated by elastic strain i.e. $\varepsilon \sim f$. However, when most of the misfit is accommodated by dislocations then ε is substantially less than f and ε^{*} is then significant.

It is interesting to note that in a system such as nickel-copper where misfit dislocations are formed by extension of existing dislocations, the ease with which the equilibrium number if misfit dislocations is formed will depend upon the number of dislocations already present. Therefore if a substrate were used in which there were an abnormally low number of dislocations present a much higher percentage of the misfit would have to be accommodated by elastic strain. This is because the stress needed to nucleate a new dislocation is very high (56).

Similarly, if there are impurities present which impede the motion of existing dislocations or increase the interfacial shear modulus then again a higher percentage of the misfit would have to be accommodated by elastic strain.

2.3.2 Island Growth

The alternative theory described above was initially applied to a particular situation in which the misfit dislocations were formed by glide of existing dislocations. This mechanism does not necessarily operate in the case of island growth since dislocations can be readily formed at the edges of an island. However, Matthews (85) has recently shown that the case of island growth can be analysed in terms of the dislocations present and that by doing so features not present in the analysis of Jesser and Kuhlmann-Wilsdorf are revealed.

The model is based on the elastic strain reduction in a deformed three dimensional island when a dislocation is introduced to accommodate some of the misfit, Figure 2.7.

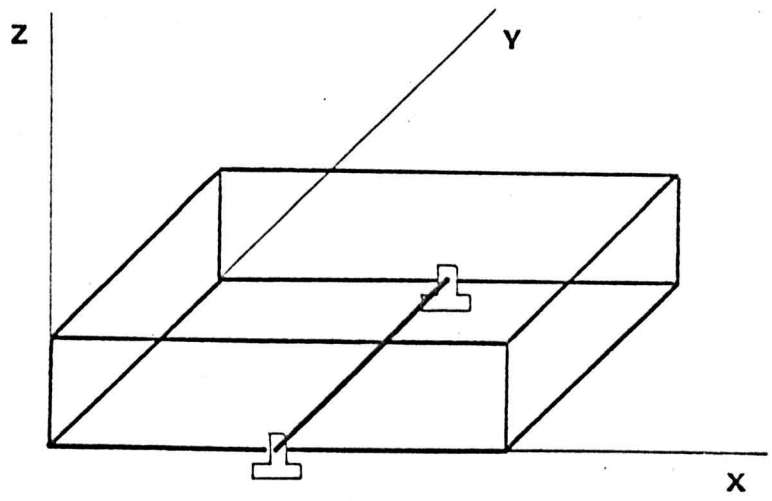

Figure 2.7 A three dimensional island containing one misfit dislocation.

If the height of the island Z is assumed to be dependent upon the width of the island X (explicitly $Z = pX$, where p is a constant) then in an island containing n dislocations in the X direction and n dislocations in the Y direction the $(2n + 1)^{th}$ dislocation will be introduced when the island dimension is given by

$$X_{2n+1} = \frac{b}{2f(1+\nu)}\left[\frac{1-\nu}{2p} + 2n + 1 + 2\nu n\right] \qquad (2.13)$$

For the system copper on nickel, assuming a value of $p = \frac{1}{4}$, Matthews obtained the dimensions of the copper islands at which dislocations should be introduced as shown in Figure 2.8. The variation of elastic strain ε with island size predicted by the above analysis is shown in Figure 2.9.

Figure 2.9 shows that the value of the elastic strain should change abruptly each time a misfit dislocation is introduced. This sawtooth behaviour of the elastic strain has been observed by Vincent (90) for small tin islands on tin telluride and is a feature not predicted by original equilibrium theories. Recent modifications to the equilibrium theory by Jesser and Van der Merwe (122,123) in which consideration was given to the discrete nature of island growth do however predict a sawtooth dependence.

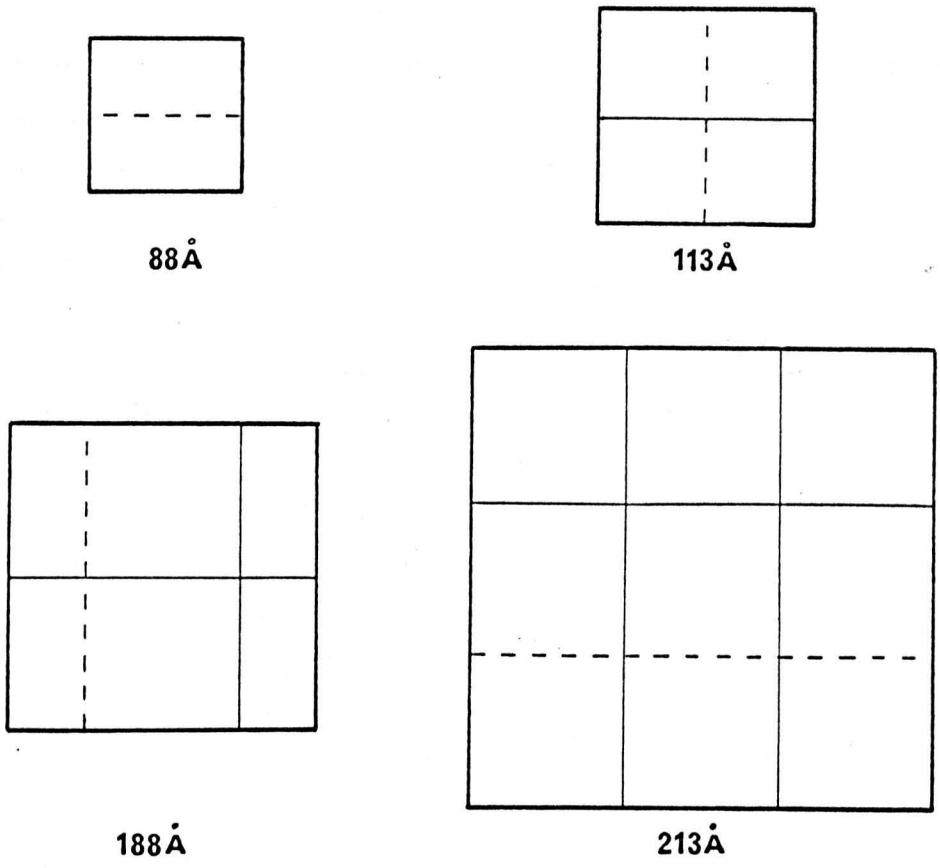

Figure 2.8 The figure shows the stages during island growth at which misfit dislocations should be introduced. The heavy continuous lines are the borders of each island, the fine continuous lines are existing dislocations and the fine broken lines are dislocations about to be formed.

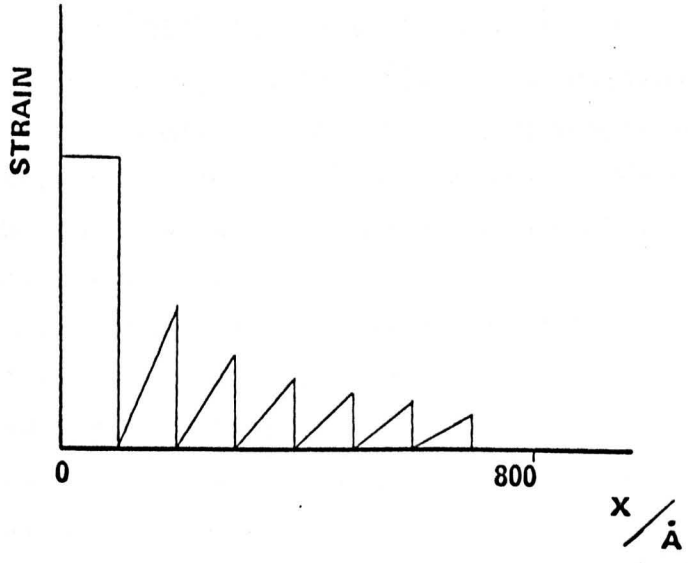

Figure 2.9 The variation of elastic strain in an island with the island width X.

2.3.3 Accommodation of Misfit by Partial Dislocations

In the preceeding sections it has been assumed that accommodation of misfit is effected by complete dislocations, i.e.a dislocation for which the Burgers vector is a complete lattice translation. This may not always be the case and it has been shown by Matthews (69) that in some circumstances it is energetically favourable for misfit to be accommodated by partial dislocations, i.e. dislocations for which the Burgers vector yields a new lattice configuration. Associated with partial dislocations in f.c.c. structures is a region of stacking fault and hence in crystals with negative stacking fault energy partial dislocations are to be expected (57,58,74,77). However accommodation of misfit by partial dislocations may be possible in certain films with positive stacking fault energy and Matthews has shown this to be the case for thin deposits of silver (69).

2.4 Comments on the Theoretical Treatments of Pseudomorphism

The basic concept of the equilibrium theory of pseudomorphism is that the state of a particular bicrystal system will be determined by minimisation of the sum of elastic strain energy and interfacial energy. It is therefore assumed that the equilibrium number of dislocations will always be present. This may not be the case, particularly for systems which exhibit layer growth, since a large stress is required to nucleate new dislocations (56). In bicrystal systems in which the misfit dislocations are produced by extension of existing dislocations there is the possibility that dislocation motion could be restricted by impurities, and again the equilibrium length of misfit dislocation would not be formed.

It has already been mentioned in section 2.2 that the use of equilibrium thermodynamics is strictly not applicable to the dynamic process of crystal growth. This limitation could be particularly serious in growth situations where the normal equilibrium conditions are not achieved, e.g. for very high deposition rates or for systems in which a metastable growth morphology occurs (chapter 5). In spite of these limitations the equilibrium theory does give results which are in reasonable agreement with experiment for thin overlayers. The predicted values of critical thickness given in Table II are, in several cases, in good agreement with the experimental determinations listed in Table I. However, the equilibrium theory predicts that a very rapid return to the bulk lattice parameter should occur once

coherence in an overgrowth is lost. This prediction is not supported by experimental evidence (36,59,73,75). The difficulty of forming the equilibrium number of dislocations could explain this discrepancy, but this additional factor could not be readily included in the theory. One other experimental finding not predicted by the equilibrium theory is that in some cases thick overgrowth films may show considerable elastic strain (36,59). Matthews (73) has suggested that this could be a result of dislocation interaction when the density of misfit dislocations becomes high. One of the initial assumptions of the equilibrium theory is that there is no interaction between dislocations and hence it seems likely that this assumption results in the poor agreement between theory and experiment for thicker films.

The alternative theory of Matthews described in section 2.3 is a much simpler approach and for the case of nickel on copper gives predictions which are in good agreement with experiment (36). The equations do however contain a term involving the core energy of a dislocation, this term being an approximation since an exact expression for the core energy is not known (56,125). This could be particularly significant since omission of this term from the equation gives a result which does not predict the occurence of pseudomorphism for nickel on copper (36). The theory does have one particular advantage, apart from its simplicity, and that is the possibility of including a term to take into account the interaction between dislocations. Inclusion of this term gives predictions for the variation of elastic strain against thickness which are in much better agreement with experimental results for thicker deposits than the predictions of the equilibrium theory. In addition Matthews has extended the theory to cases where misfit is accommodated by partial dislocations separated by a region of stacking fault and has obtained good agreement with experiment for the systems cobalt on copper (73) and silver on palladium (69).

Comparing the two different theories for cases of pseudomorphism in layer deposits it is found that both theories give predictions for h_c which are in reasonable agreement with experiment. However, the accuracy of experimental techniques, particularly with regard to thickness determination, is not sufficiently good to enable distinctions to be made. In addition, both expressions for the equilibrium elastic strain involve the interfacial shear modulus which

is not known. For cases of thicker deposits the failure of the equilibrium theory to consider interaction between dislocations could explain the considerable discrepancy between the theory and experimental results in these circumstances. In this respect the approach of Matthews is preferable since the interaction of dislocations can be included and theoretical results in agreement with experiment obtained.

Comparison of the two different approaches when applied to island deposits is more difficult because in the most recent treatments both theories predict a sawtooth dependence of the elastic strain (85,123). This sawtooth behaviour has been observed by Vincent for tin islands on tin telluride (90) and the failure of earlier investigators to obtain this dependence was probably a result of insufficient data. The treatment of Matthews does however contain the factor p, relating island height to island width. Generally p would not be known for a particular island and different values of p give rise to considerably different values of island size at which dislocations would be expected to be introduced. In this respect the treatment is unsatisfactory, although an electron microscope investigation should enable an average value of p to be obtained for a particular amount of deposited material. This will be discussed further in chapter 6. It is significant that using a value of $p = \frac{1}{4}$ Matthews predicts that the first dislocation in an island of copper on nickel should be formed when the island size is less than 100 Å. The theory of Jesser and Kuhlmann-Wilsdorf predicts complete coherency for the copper up to an island diameter of 410 Å and Matthews (85) has in fact observed completely coherent islands of copper of 350 Å diameter.

It is worthwhile considering the relevance of the theories outlined to the aim of the present work described in section 1.5. The initial experiments involved the deposition of silver on nickel, the misfit between these two materials being 14.7%. Reference to Figure 2.3 shows that one would not expect to observe complete pseudomorphism if the silver forms a two dimensional layer. Similarly reference to Table II shows that if the silver forms three dimensional islands the critical radius of such islands would be less than 20 Å making them difficult to observe. The deposition of copper on nickel was already known to exhibit pseudomorphism and experiments were performed in an attempt to discover the role of contamination in

determining the value of the critical thickness. However, the affect of contamination on the movement of dislocations cannot be readily included in the theory, although it might be more easily included as an additional term in the approach of Matthews. Nevertheless the approach of Matthews does give a clearer picture of the way in which dislocations are introduced in some systems, and intuitively one might expect the presence of impurities to have an affect on the motion of these dislocations. Finally the deposition of copper on hot nickel was known (59,85) to result in island growth of the copper. Hence a comparison of experimental results with the island theory of Matthews was possible and in particular an attempt was made to obtain values for the factor p.

CHAPTER 3

QUANTITATIVE AUGER ELECTRON SPECTROSCOPY

3.1 Introduction

The majority of applications of AES to date have been concerned with qualitative information regarding chemical species present on a surface. If AES is to realise its full potential as an analytical technique it must be made capable of yielding quantitative information. Quantitative interpretation of Auger spectra can be made most readily in cases of submonolayer deposits, in which a material A is deposited on another material B and grows uniformly flat. In this case the Auger current from A should be linear with fractional coverage θ , and is given by (104)

$$I_A = \theta I_{1A} \qquad (3.1)$$

where I_{1A} is the Auger current from a complete monolayer of A. In practice most Auger spectrometers do not measure Auger current directly, but measure $\frac{d^2I}{dE^2}$. However, Weber and Johnson (103) have pointed out that, if the shape of the Auger peak does not change with coverage, $\frac{d^2I}{dE^2}$ is proportional to I and hence may be used as a measure of I.

Investigation of the Auger signal from submonolayer deposits has been carried out for a number of systems. Weber and Johnson deposited known amounts of potassium and caesium on to germanium and silicon (111) surfaces. They were able to show that the deposit Auger signal was linear with coverage, if all spectrometer parameters were held constant. Musket and Ferrante (128) investigated the adsorption of oxygen on a tungsten (110) surface. They employed a background nulling technique which allowed N(E) (or $\frac{dI}{dE}$) to be measured directly, and the strength of the Auger signal was taken as the area under the peak. Assuming that saturation adsorption corresponded to one monolayer of oxygen they were then able to investigate the adsorption as a function of oxygen exposure. They also found that the oxygen peak shape did not change with coverage, in agreement with the assumption made by Weber and Johnson.

A similar experiment was performed by Florio and Robertson (129)

for chlorine adsorption on silicon (111). Once again saturation adsorption was taken to be one monolayer coverage, following which chlorine adsorption as a function of exposure was investigated. The experiment was repeated for several different substrate temperatures and values for the sticking coefficient obtained.

A somewhat more complex system which is also capable of quantitative interpretation is that of layer growth. In this system the deposit material A grows uniformly in layer by layer fashion on the substrate material B, as distinct from the commonly observed (2) nucleation and growth mechanism in which the initial deposit forms three dimensional islands. As described in chapter 1, this type of layer growth is expected when the surface free energy of the substrate is greater than that of the deposit plus the interface.

Investigations of the dependence of the Auger signal on deposit thickness have been carried out in a number of cases involving systems exhibiting layer by layer growth. Palmberg and Rhodin (130) investigated the growth of silver on gold and from the fact that the gold Auger signal disappeared rapidly with silver deposition concluded that layer growth was occuring. The Auger signal strength was monitored as silver was deposited in stages on to the gold, the monolayer calibration being determined from the disappearance of a feature associated with gold in the LEED pattern. In a similar experiment Ridgeway and Haneman (131) observed the thickness dependence of Auger signals as iron was condensed on to silicon (111). The deposit thickness was calibrated using a quartz crystal ratemeter.

Seah (40) used a similar ratemeter calibration to observe the thickness dependence of the Auger signals when silver, beryllium and copper were, each in turn, condensed on each other.

In a recent investigation Tang and Wehner (132) studied the dependence of the relative Auger signals with thickness as molybdenum was sputtered on tungsten, and vice versa. They calibrated the deposit thickness by optical interferometry on a thick specimen prepared under identical experimental conditions.

In the experiments referred to above some subsidiary assumption was made regarding the calibration of deposit thickness. In the case of the ratemeter determinations it is necessary to assume that the sticking coefficient on the ratemeter and substrate are equal. The use of features associated with the LEED pattern from the substrate may be uncertain in that the features may disappear before complete

coverage has been obtained. If the deposit is growing in true layer fashion then as high coverage develops the area of substrate exposed to the LEED beam may be very small. For these regions of substrate to give rise to well defined diffracted beams the size of the region must be of the order of the coherence length of the electron beam (133). The coherence length for 100 eV electrons in a typical LEED system is of the order of 250 Å (96). Therefore if the regions of substrate exposed are less than this value it is unlikely that the substrate diffraction pattern would be observed, even though complete coverage has not been obtained. Film thickness determination by optical interferometry should give a reliable value for the total film thickness (42), it does however ignore the possibility that the sticking coefficient of A on B may be different to that of A on A. This could lead to considerable error in the determination of deposit thickness in the very early stages.

A model for the growth of the deposit Auger signal with thickness has been proposed by Gallon (47) for the case of layer growth. This model is described in the next section, and it will be shown that for true layer by layer growth an absolute calibration of deposit thickness is possible, requiring no subsidiary assumptions about sticking coefficients. The only pre-requisite, apart from a system exhibiting layer growth, is a constant arrival rate of the deposit material.

3.2 The Simple Model for Layer Growth

In the model due to Gallon (47) the crystal is regarded as being made up of atomic planes labelled 1,2,3,...n, parallel to the specimen surface, n = 1 being the outermost layer. The production of a back scattered Auger current due to an incident electron beam penetrating into the crystal is described in terms of the probabilities of a primary electron reaching the n^{th} layer, of an Auger electron being produced there, and of this Auger electron escaping back through the (n - 1) layers to the vacuum. Summing the contributions gives the Auger current from n layers as

$$I_n = I_\infty \left(1 - \left(1 - \frac{I_1}{I_\infty}\right)^n\right) \qquad (3.1)$$

where I_1 is the current from one monolayer and I_∞ is the current from bulk material.

The aim of the model is to deduce the thickness of an overlayer

solely from the strength of its Auger signals, there being no prior assumption of values for sticking coefficients. In addition it should be possible to determine the mean escape depth for the particular electrons contributing to the Auger signal.

If R is the arrival rate of a material A at the surface of a material B (in monolayers. s^{-1}), S_1 is the sticking coefficient of A on B, assumed independent of coverage, and t is the time since the start of deposition, the initial Auger current is given by

$$I_A = RS_1 I_1 t \qquad (3.2)$$

where I_1 is the current from one monolayer of A. The linear increase of the Auger current with deposition time continues up to a time t_1, which corresponds to completion of the first layer. When the second layer begins to develop the Auger current will be given by

$$I_A = I_1 (1 - \theta) + I_2 \theta \qquad (3.3)$$

where θ is the fractional coverage of the second layer and I_2 is the Auger current from two layers, given by equation 3.1 with n = 2. The fractional coverage at a time t is given by $\theta = RS_2(t - t_1)$, where S_2 is the sticking coefficient of A on A, again assumed to be independent of coverage. Substituting for I_2 in equation 3.3 gives

$$I_A = I_1 \left(1 + \theta \left(1 - \frac{I_1}{I_\infty}\right)\right) \qquad (3.4)$$

so that there is a linear increase of Auger current with coverage as the second layer develops. If t_n is the time that corresponds to the completion of the n^{th} layer then the Auger current from n layers is given by equation 3.1 with $n = 1 + RS_2(t_n - t_1)$. The dependence of I_A on t from this analysis is shown in Figure 3.1, which is drawn for the hypothetical case in which $\frac{I_1}{I_\infty} = 0.4$. In addition the sticking coefficients S_1 and S_2 have been assumed equal.

The dependence is piece-wise linear, there being abrupt changes in the slope at integral values of the layer number. In cases of true layer by layer growth and with data of sufficient accuracy it should be possible to distinguish the linear portions. In practice the experimental accuracy and deviations from true layer growth may

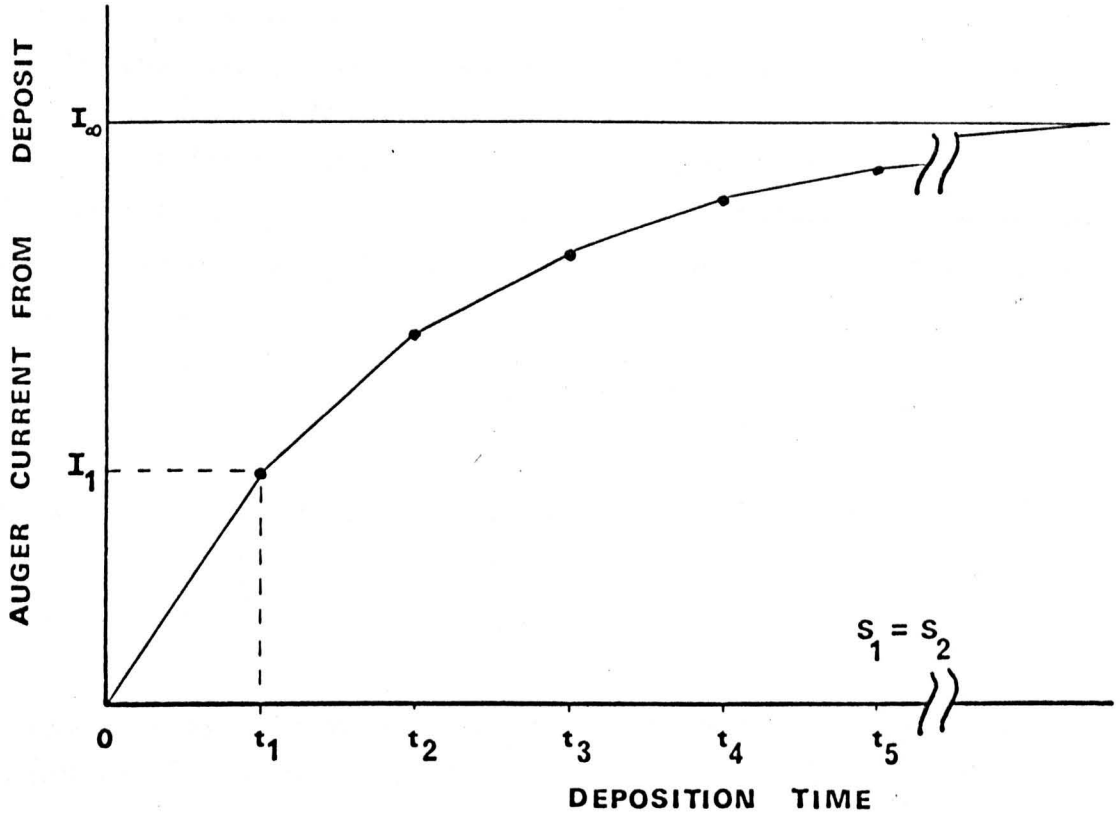

Figure 3.1 Deposit Auger signal as function of deposition time according to model.

make this difficult. It is of particular importance to be able to locate the time t_1, corresponding to completion of the first layer, and inspection of equation 3.1 shows that

$$I_{n+1} - I_n = I_1 \left(1 - \frac{I_1}{I_\infty}\right)^n \qquad (3.5)$$

which means that the most abrupt change in slope occurs at n = 1. Hence the discontinuity in the slope corresponding to completion of the first layer should be the easiest to discern. In addition the ratio of S_1 to S_2 affects the ease of location of t_1, $S_1 > S_2$ making the change of slope more abrupt, and vice versa. If t_1 can be located the current I_1 from the first layer of deposit is immediately obtained.

It is also important to obtain a value for I_∞, the Auger current from the bulk for material A. This will be determined experimentally at long deposition times when the current becomes

constant to within the experimental accuracy. The value of I_∞ so obtained should be independent of any deviations from true layer growth that might occur in the earlier stages, providing a thick continuous deposit is eventually formed.

If the accuracy of the experimental data does not allow the identification of linear portions in the I_A versus t curve beyond the initial layer then n may be treated as a continuous variable, and equation 3.1 becomes

$$I_A = I_\infty \left(1 - (1 - \frac{I_1}{I_\infty})^n\right) \qquad (3.6)$$

where $n = 1 + RS_2(t - t_1)$. Rearranging equation 3.6 gives

$$\log (1 - \frac{I_A}{I_\infty}) = 1 + RS_2(t-t_1) \log (1 - \frac{I_1}{I_\infty}) \qquad (3.7)$$

It should therefore be possible to obtain a value for t_1 from the departure of a plot of $\log (1 - \frac{I_A}{I_\infty})$ versus t from linearity, as well as from the I_A versus t data.

Reference to equation 3.2 shows that the initial slope of the I_A versus t plot equals (RS_1), and hence S_1 may be calculated if R is known. The graph of $\log (1 - \frac{I_A}{I_\infty})$ versus t for the region $t > t_1$ should give a straight line of slope $RS_2 \log(1 - \frac{I_1}{I_\infty})$, enabling S_2 to be calculated. Since (RS_1) and (RS_2) may be found the ratio of S_1 to S_2 can be calculated even if R is unknown, hence the time for growth of a monolayer of A on A can be obtained. This enables the total deposit thickness to be calculated.

Similar results may be deduced for the decay of the Auger signal from the substrate, thus

$$I_B = I_{B\infty} \left(1 - RS_1 t (1 - \frac{I_{1BA}}{I_{B\infty}})\right) \text{ for } t < t_1 \qquad (3.8)$$

where I_{1BA} is the signal from the substrate covered by one layer of A, and $I_{B\infty}$ is the signal from the clean substrate. Hence the decay of the substrate signal should be linear up to a time t_1. Similarly

$$I_B = I_{B\infty} (\frac{I_{1BA}}{I_B})^n \qquad t > t_1 \qquad (3.9)$$

where, as before, $n = 1+RS_2(t-t_1)$. Equation 3.9 may be rearranged to give

$$\log \left(\frac{I_B}{I_{B\infty}} \right) = 1+RS_2(t-t_1) \log \left(\frac{I_{1BA}}{I_\infty} \right) \qquad (3.10)$$

and hence the sticking coefficient S_2 may also be obtained from a semi-logarithmic plot of the substrate signal. The departure of the above plot from linearity yields another estimate of the value of t_1 and hence for true layer growth four values for t_1 should be possible, enabling a more confident determination.

If the growth of the overlayer is considered to be quasi-continuous, equation 3.1 may be expressed as

$$I_A = I_\infty \left(1 - \exp - \frac{x}{x_o}\right) \qquad (3.11)$$

where x is the thickness of the overlayer. The parameter x_o is often taken to be the mean escape depth (40), though to do so ignores the initial linear portion of the graph. It is shown by Gallon and Matthew (104) that in terms of the model just described, the mean escape depth is given by

$$n_o = \tfrac{1}{2} \frac{I_1}{I_\infty} + \left(1 - \frac{I_1}{I_\infty}\right) \left(1 + \frac{1}{\log \frac{I_\infty}{I_\infty - I_1}}\right) \qquad (3.12)$$

where n_o is expressed in atomic layers.

The model as described assumes that all the Auger electrons are produced by the primary beam as it passes through the overlayer and into the substrate. However some of the primary electrons may undergo large angle inelastic scattering and pass back towards the surface. If these electrons still possess sufficient energy to cause ionization of deposit or substrate atoms in the surface region this will lead to an enhancement of the Auger yield. This backscattering effect can be formally allowed for by defining a backscattering factor r, where $r>1$, such that the incident electron current I_p is replaced by rI_p. If the backscattering factor remains constant throughout the deposition of material A the model still applies, since the enhanced Auger current may be allowed for in the probability factor for production of Auger electrons (47). The backscattering factor increases with increasing atomic number (40,134) and hence systems for which the above model is likely to apply are those in which the substrate -

condensate materials are of similar atomic number. If the materials are of markedly different atomic number the model should still apply in the early stages of deposition, since the majority of back-scattering will occur in the substrate and hence will remain constant. However, as the deposit thickness increases the backscattered electrons will gradually originate from the overlayer, causing the flat portion of the curve in Figure 3.1 to have a slight upward or downward slope to a new saturation value for I_∞. A consequence of this is that use of equation 3.12 for the mean escape depth may give rise to uncertainty. However, if the backscattering factors for the deposit and substrate are known the value of I_∞ observed can be corrected, using the equation (40)

$$I_\infty^o = I_\infty^c \left(\frac{1 + r_A}{1 + r_B} \right) \qquad (3.13)$$

in which r_A and r_B are the backscattering factors of deposit and substrate respectively, I_∞^o is the saturation value observed and I_∞^c is the saturation value that would have been observed with constant backscattering factor. Values of backscattering factor for a number of elements of differing atomic number have recently been obtained by Smith and Gallon (134), and the affect of differing backscattering factors has been investigated by Tarng and Wehner (132). The results of Tarng and Wehner substantiate the discussion given above.

Finally consideration may have to be given to the electron trajectory through the overlayer. This is because Auger electrons produced a distance z below the surface and travelling at an angle θ to the surface normal have to pass through a thickness $z \sec\theta$ of material before escaping into the vacuum. It has been shown by Seah (40) that for practical spectrometers the value of n_o determined is $f \times n_o^s$, where n_o^s is the mean escape depth measured along the surface normal and f is a numerical factor less than one. The value of f for a typical retarding grid spectrometer and for a C.M.A. operated with its axis at 45° or 90° to the surface normal is between o.70 and 0.75. Hence the results obtained using these types of spectrometer are interchangeable and it is not necessary to correct the value of n_o calculated from equation 3.12 for quantitative analysis. However, if results of mean free paths are to be interchanged between other spectrometer configurations it may be necessary to correct the values of n_o obtained as above, this would also be necessary if values of n_o

were to be compared with a formal theory of electron mean free paths.

3.3 Extension of the Simple Model for Island Deposits

For many deposit-substrate systems the initial structure of the deposit is in the form of isolated three dimensional islands (2), rather than a continuous layer. As deposition proceeds the number of islands increases up to some saturation value, and subsequent deposition causes growth of already existing islands (30). Eventually the islands become so large that they begin to touch each other and coalescence between the islands occurs. Further deposition results in the filling in of holes remaining between islands which have coalesced, until eventually a continuous deposit is formed. In principle it is possible to calculate the expected Auger current from a distribution of islands and hence determine the quantity of material deposited from the strength of the Auger signal. However, at present insufficient knowledge is available about the number, shape and size of islands (48) to make such a calculation practical for the early stages of deposition. Once the saturation number of islands has been established the situation becomes less complex and by making a number of assumptions it is possible to make some predictions about the Auger current.

In the model it will be assumed that the number of islands remains fixed, that all islands are the same height and that the islands are in the form of square slabs. Making use of equation 3.11 the Auger current from unit area of deposit is given by

$$I_d = I_{d\infty} \left(1 - \exp - \frac{h}{x_o}\right) \qquad (3.14)$$

where $I_{d\infty}$ is the signal from unit area of bulk deposit and h is the thickness of the deposit. If the number of islands per unit area is N_o and the length of each island is d, then the Auger signal from unit area of specimen is

$$I_d = N_o d^2 I_{d\infty} \left(1 - \exp - \frac{h}{x_o}\right) \qquad (3.15)$$

Now $N_o d^2$ is simply the fractional coverage θ of the deposit, and hence equation 3.15 may be re-written as

$$\frac{I_d}{I_{d\infty}} = \theta \left(1 - \exp - \frac{h}{x_o}\right) \qquad (3.16)$$

As deposition continues and the thickness of the islands increases

a situation will eventually arise where $h \gg x_o$ and hence equation 3.16 becomes

$$\frac{I_d}{I_{d\infty}} = \theta \qquad (3.17)$$

The normalised Auger current is seen to be equal to the fractional coverage of the deposit. Equation 3.17 is perfectly general and applies to any shape of deposit island, provided that the thickness of the island is everywhere greater than x_o.

Similar results may be deduced for the decay of the Auger signal from the substrate, and for $h \gg x_o$ the normalised Auger current is given by

$$\frac{I_s}{I_{s_\infty}} = (1 - \theta) \qquad (3.18)$$

Hence a plot of deposit Auger signal against coverage θ should be linear once the situation $h \gg x_o$ has been obtained. For regions where $h \not> x_o$ the factor $\exp - \frac{h}{x_o}$ becomes significant and the detected Auger current should be less than the observed coverage. It ought to be possible to test the above predictions by coupling Auger measurements on a nucleating specimen with subsequent electron microscopy, electron microscopy enabling a determination of the fractional coverage of the deposit to be made.

The dependence of the Auger signal with deposition time is not straightforward and depends upon the time dependence of θ. If the sticking coefficient is S and the arrival rate of deposit material R, the thickness h is given by

$$h = \frac{RSt}{\theta}$$

Equation 3.16 may therefore be written as

$$\frac{I_d}{I_{d_\infty}} = \theta(t)\left(1 - \exp - \frac{RSt}{\theta(t)x_o}\right) \qquad (3.19)$$

Since θ is <1 until complete coverage is obtained, the growth of the deposit Auger signal with deposition time for systems which nucleate will be less rapid than for a system exhibiting layer growth.

CHAPTER 4

DESCRIPTION OF THE APPARATUS

4.1 Ultra-High Vacuum System

The experiments reported were carried out in a stainless steel UHV system known as 'Rentaport'. The system was in the form of a closed cylinder with ports arranged radially around the circumference, together with a number of ports on the upper flat surface, Figure 4.1. The system was designed so that the specimen in a suitable manipulator was mounted at the centre of the chamber. The radial ports were used to provide a range of analytical techniques so that a considerable amount of information could be obtained about any specimen without breaking the vacuum. Thus facilities were available for low energy electron diffraction, Auger electron spectroscopy, reflection high energy electron diffraction, residual gas analysis and optical absorption by means of a light path through the crystal. Two of the radial ports were used to house the vapour sources which are described in detail in section 4.2.

The system was initially rough pumped by means of sorption pumps, then finally by a Ferranti 500 litres.sec^{-1} ion pump. Following a twelve hour bake at 300^{o}C ultimate pressures in the 10^{-10} torr range were achieved.

4.2 Evaporation Sources

4.2.1 Constant Rate Source

In order to investigate AES as a quantitative technique a primary requirement was an evaporation source capable of maintaining a constant arrival rate at the substrate surface. The evaporation sources best able to fulfil this requirement are of the Knudsen cell type, described in chapter 1.

The number of molecules per second emerging from the hole in the cell is given by the Langmuir effusion equation (35)

$$\frac{dn}{dt} = \frac{PN}{\sqrt{2\pi MRT}} \frac{\pi a^2}{4} \qquad (4.1)$$

It can be shown that the arrival rate at a remote substrate is given by (135)

$$\frac{dD}{dt} = 1.46 \sqrt{\frac{M}{\rho^2 T}}\, p' \frac{a^2}{r^2} \text{ Å sec}^{-1} \qquad (4.2)$$

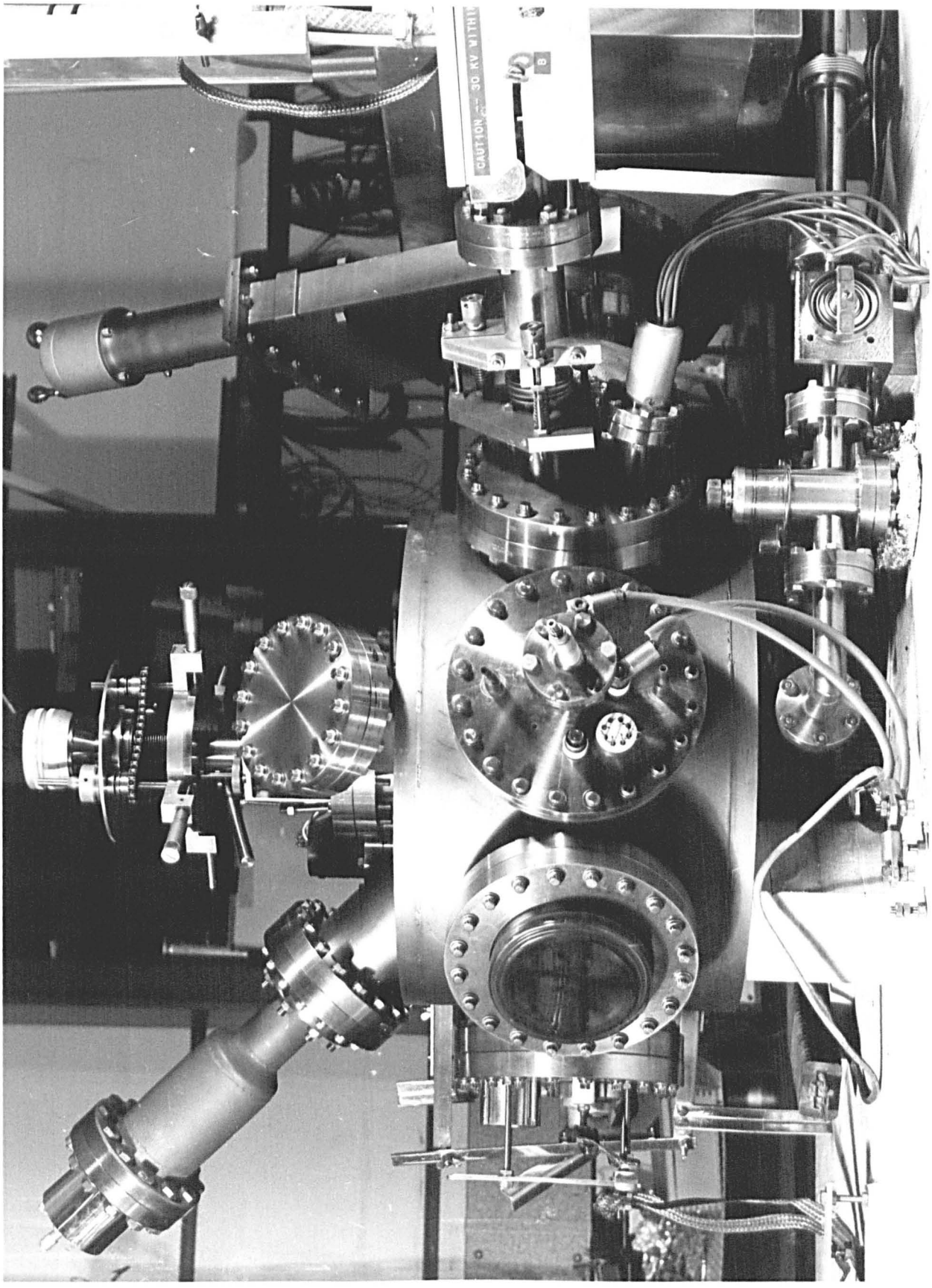

Figure 4.1 The UHV System

where
- a = diameter of the hole (cm)
- r = source to substrate distance (cm)
- P = vapour pressure (dynes.cm^{-2})
- p' = vapour pressure (micro-torr)
- T = absolute temperature
- M = atomic weight
- N = Avogadro's number
- ρ = density (gm cm^{-3})

From equation 4.2 it can be seen that providing geometric factors are kept constant, the only variables are p' and T. However, the vapour pressure p' is a unique function of T, hence if the temperature is held constant the deposition rate will also be constant. Equation 4.2 is only valid if the diameter of the effusion hole is at least ten times smaller than the mean free path of the vapour molecules inside the cell (136). The mean free path of the molecules inside a cell at typical operating temperatures is several centimetres, hence the above condition can be satisfied if the hole diameter is about a millimetre.

The practical requirements of a Knudsen source are a crucible material which does not react with the evaporant and can be machined or formed into a suitable shape, together with a method of heating and maintaining the crucible at a constant temperature. Tantalum was already known to be a suitable crucible material for copper and silver (35,137) and is readily machined. The source was designed with two crucibles which could be operated independently or simultaneously to increase the flexibility of the system. Electron bombardment was chosen as the method of heating because electrons can be focused on the crucible, so avoiding excessive heating and consequent outgassing of neighbouring components. It was found that a 15 cm length of 0.008" tungsten wire filament was sufficiently rigid and gave adequate emission current for either source, whilst keeping the total area of white hot metal to a minimum. The crucibles were machined from 0.25" diameter tantalum rod and were 1.2 cm high with an orifice 1 mm in diameter. The crucibles could be loaded with approximately 0.3 gm of copper which enabled theoretically a total film thickness of 2000 Å to be deposited. In practice the total film thickness that could be achieved would be considerably less than this because evaporant material is lost from the cell during the extensive outgassing that is necessary.

The temperature of each crucible was monitored by spot welding to the base a Pt/Pt-Rh(13%) thermocouple, the output of which

was fed to an A.E.I. proportional controller, type CRS 10X1. The controller compares the thermocouple output with a pre-set reference and limits the amount of time during each half cycle of the mains that power is let through to the load, in this case the H.T. transformer. In this way the applied H.T. was regulated according to the output from the thermocouple and it was possible to maintain a crucible temperature within $\pm 5^{\circ}C$ for long periods. At the chosen operating temperatures for copper and silver, $1230^{\circ}C$ and $1050^{\circ}C$ respectively, this fluctuation leads to a variation in vapour pressure of about $\pm 6\%$, and hence a corresponding variation in deposition rate. One additional advantage of the thermocouple was that on connecting to an x,t chart recorder whilst heating or cooling a flat region was observed in the trace, corresponding to the melting point of the metal. This served as a calibration check on the thermocouple and in addition the length of the flat portion gave some indication of the quantity of material remaining in the source.

A schematic diagram of the source is shown in Figure 4.2 and a photograph in Figure 4.3.

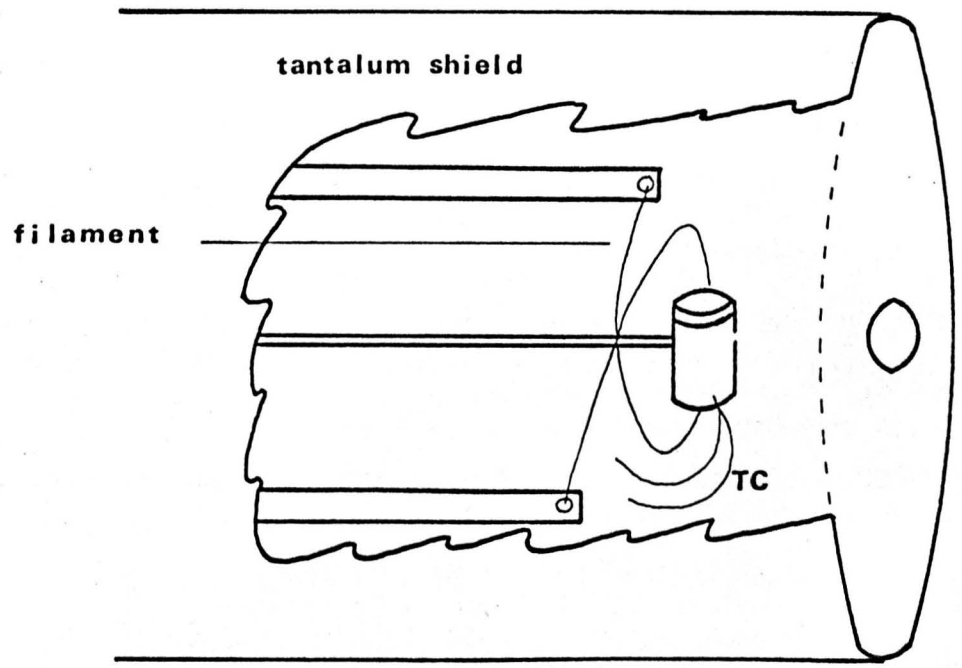

Figure 4.2 Schematic diagram of the Knudsen source.

The principle source components were constructed of tantalum and supported on Varian medium current feedthroughs, type 954-5019.

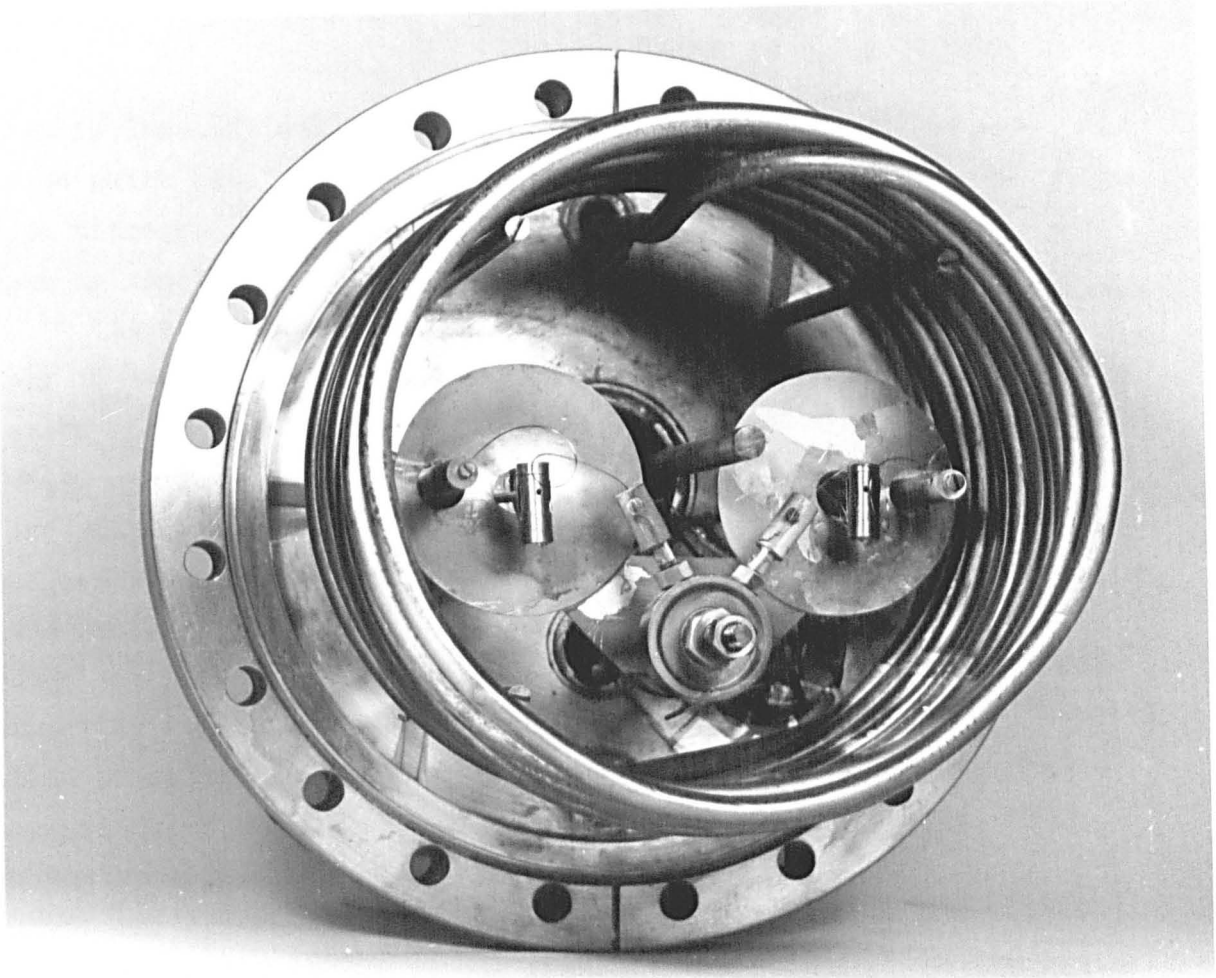

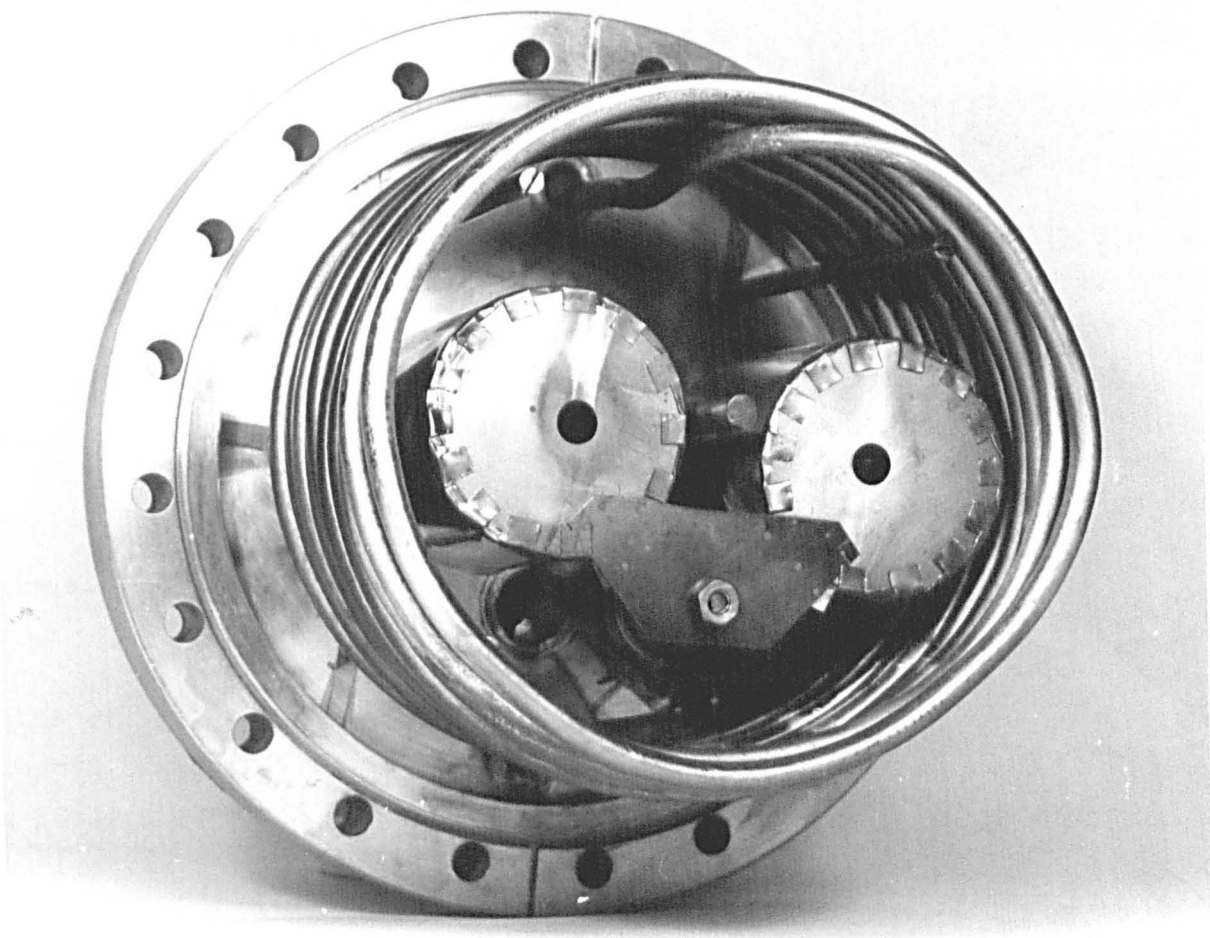

Figure 4.3 The Knudsen Source

The whole assembly was surrounded by a 0.25" copper cooling coil through which water or liquid nitrogen could be passed. Using liquid nitrogen as coolant it was possible to evaporate silver or copper in the 10^{-9} torr range.

At the operating temperature the input power from the H.T. supply to the silver and copper sources was typically 22 watts and 35 watts respectively. In addition a power requirement of about 40 watts was needed to raise the temperature of the tungsten filament to the point where adequate emission current was obtained. One consequence of using electron bombardment to heat the source was that a small current (approximately 10^{-9} A) of electrons emerged through the beam defining apertures and was incident upon the sample. However the source was fitted with a rotating shutter to allow precise control of deposition times and it was found that, since the shutter was earthed, it could be used to deflect the stray electrons away from the specimen.

The arrival rate from each Knudsen cell can be calculated using equation 4.2 if the vapour pressure and cell temperature are known. However it was felt that an experimental determination was necessary because the vapour pressure is such a rapidly varying function of temperature. The following method was used to determine the absolute arrival rate. A small pyrex tube was positioned against the final beam defining aperture as shown in Figure 4.4.

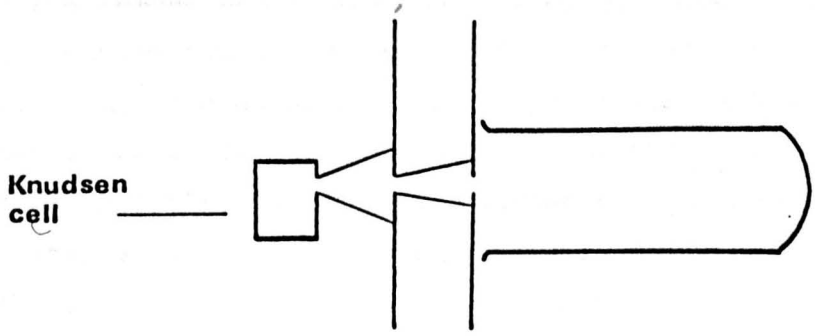

Figure 4.4 Schematic representation of the method used to determine the absolute arrival rate.

In this way all the vapour emerging from the aperture would be condensed inside the tube. The total mass of metal collected in the tube after a measured deposition time was then determined by colourimetric analysis, see section 4.8. In a separate experiment

the diameter of the deposit on an actual specimen crystal was measured by means of a travelling microscope. Hence having obtained the area of the deposit and the mass deposited in a given time, the arrival rate may be calculated. The arrival rates used in the experiments were 0.6 ± 0.1 Å min^{-1} for copper and 0.48 ± 0.1 Å min^{-1} for silver. The calculated arrival rates using equation 4.2 were 0.4 Å min^{-1} for copper and 0.7 Å min^{-1} for silver. The difference in the measured and calculated rates in each case reflects the uncertainty in the vapour pressure data (38).

4.2.2 Source for Preparation of Substrate Films

The nickel substrates used throughout the experiments were films about 1500 Å thick deposited on alkali halide crystals. The advantage of using thin film substrates rather than a bulk nickel crystal is that the final specimens, once removed from the alkali halide, are of a suitable thickness for electron microscopy. In addition the resulting surfaces are clean, providing the pressure remains low during deposition and spectroscopically pure evaporant materials are used. This means that special cleaning techniques such as ion bombardment are unnecessary. The presence of an additional vapour source has the further advantage that multiple layer films may be prepared if required.

The most significant problem encountered with designing a nickel evaporation source is that nickel alloys with refractory metals commonly used as filaments or boats. This can be overcome with Unvala or pendant drop sources described in chapter 1, but these sources are rather complicated involving L.T. and H.T. supplies and their geometries would have resulted in part of the LEED screen being obscured. Nickel does sublime at temperatures just below the melting point and a source for the controlled sublimation of nickel used by Farnsworth (37) was described in chapter 1. The major disadvantage of this source is that very low deposition rates are obtained, typically less than 1 Å min^{-1}. In order to prepare substrate films between 1000 and 1500 Å thick, deposition rates in excess of 20 Å min^{-1} were required to keep deposition times reasonable. Matthews (73) had utilized sublimation from a wire in order to deposit films of cobalt and hence a nickel source based on this idea was constructed. The nickel wire was wound into a tight helix and positioned sideways-on so that a large area of nickel was presented to the substrate crystal. In addition the electrodes supporting the nickel helix were hinged so that following deposition the source

could be lowered to the floor of the chamber, thus avoiding obstruction of the LEED optics.

The nickel helix was wound from .040" spectroscopically pure nickel wire and when in position was 10 cm from the substrate crystal. The maximum deposition rate using these filaments was about 10 $\mathring{A}\ min^{-1}$ and the life of each filament was typically as low as ten films. A significant improvement in life and deposition rate was achieved by using tungsten wire to support the nickel helix. These filaments were prepared by tightly winding 0.5 mm spectroscopically pure nickel wire on a 20 cm length of 1 mm diameter tungsten wire. The nickel-tungsten combination was then wound into a tight helix 1 cm in diameter and approximately 2 cm in length, so that it would fit between the electrodes of the evaporator. The helix was heated by passing through an alternating current, typically of about 30 $\mathring{A}$, such that the nickel wire was maintained just below its melting point. This type of filament enabled deposition rates of 20 - 25 $\mathring{A}\ min^{-1}$ to be obtained with a life of about thirty thick films.

The source was constructed of stainless steel with tantalum filament carriers and shields. The nickel helix was completely enclosed except for a short exit pipe which enabled vapour to reach the crystal and a small hole at the rear to allow a view of the filament. Nickel vapour emerging from the rear of the source condensed harmlessly on the walls of the vacuum chamber. A general view of the source is shown in Figure 4.5.

4.3 Multiple Cleavage Specimen Holder

In order to produce epitaxial metal films on alkali halide crystals it is frequently necessary to cleave the crystal in vacuum prior to deposition (14,15,16,17). It was also essential that the crystal could be translated and rotated to face each vapour source and the LEED optics. For maximum use of the RHEED facility it was necessary to be able to rotate the crystal about its surface normal, and finally it was necessary to be able to heat or cool the sample. A multiple cleavage specimen holder fulfilling these requirements was designed and built by T. E. Gallon and part of the holder is shown in Figure 4.6.

The crystal manipulator was based on a commercial design by Vacuum Generators and has rotational, lateral and vertical translational movements. The position of the crystal could be adjusted by precision micrometers in the range 0 - 1" parallel to

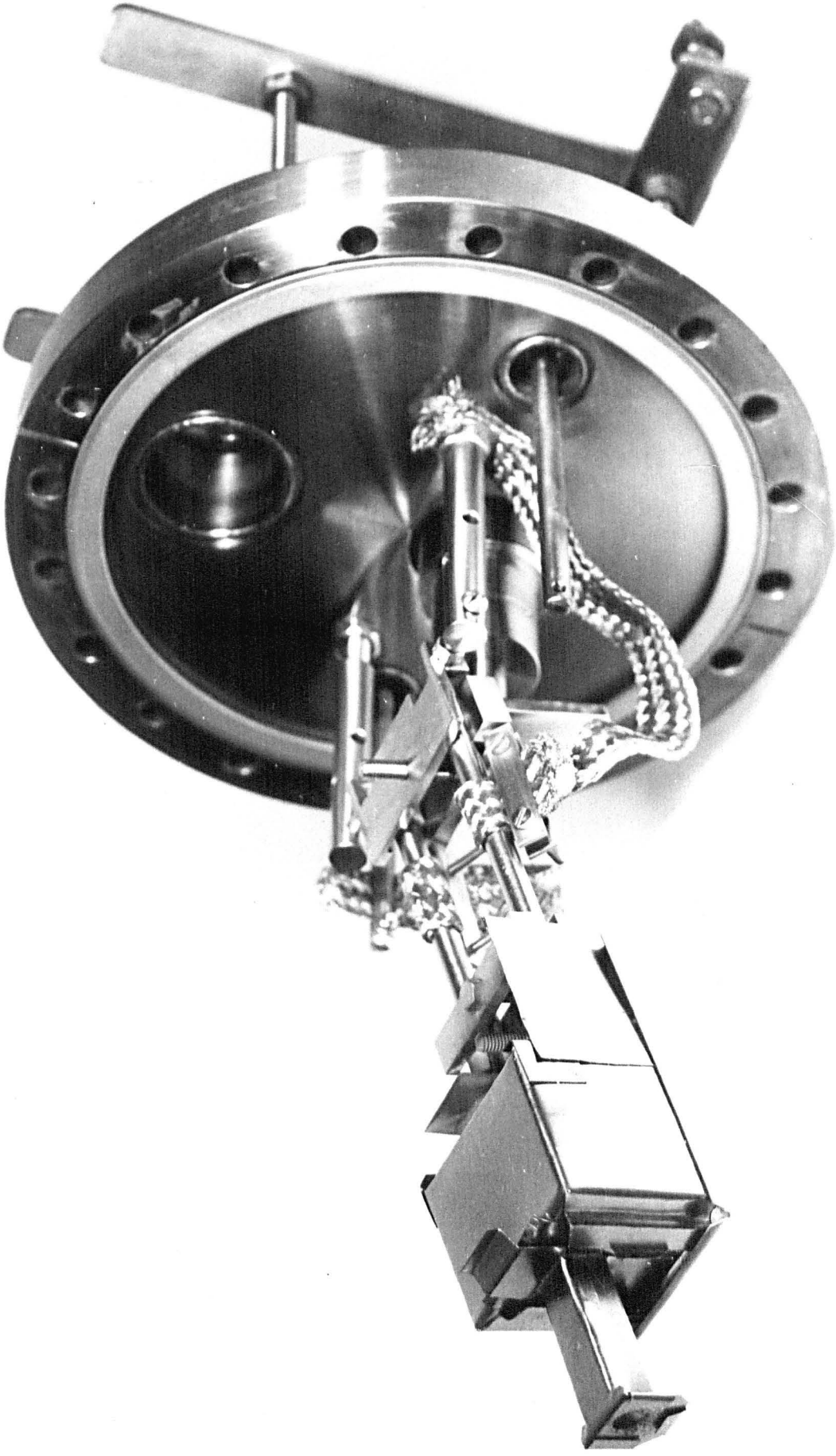

Figure 4.5 The Nickel Source

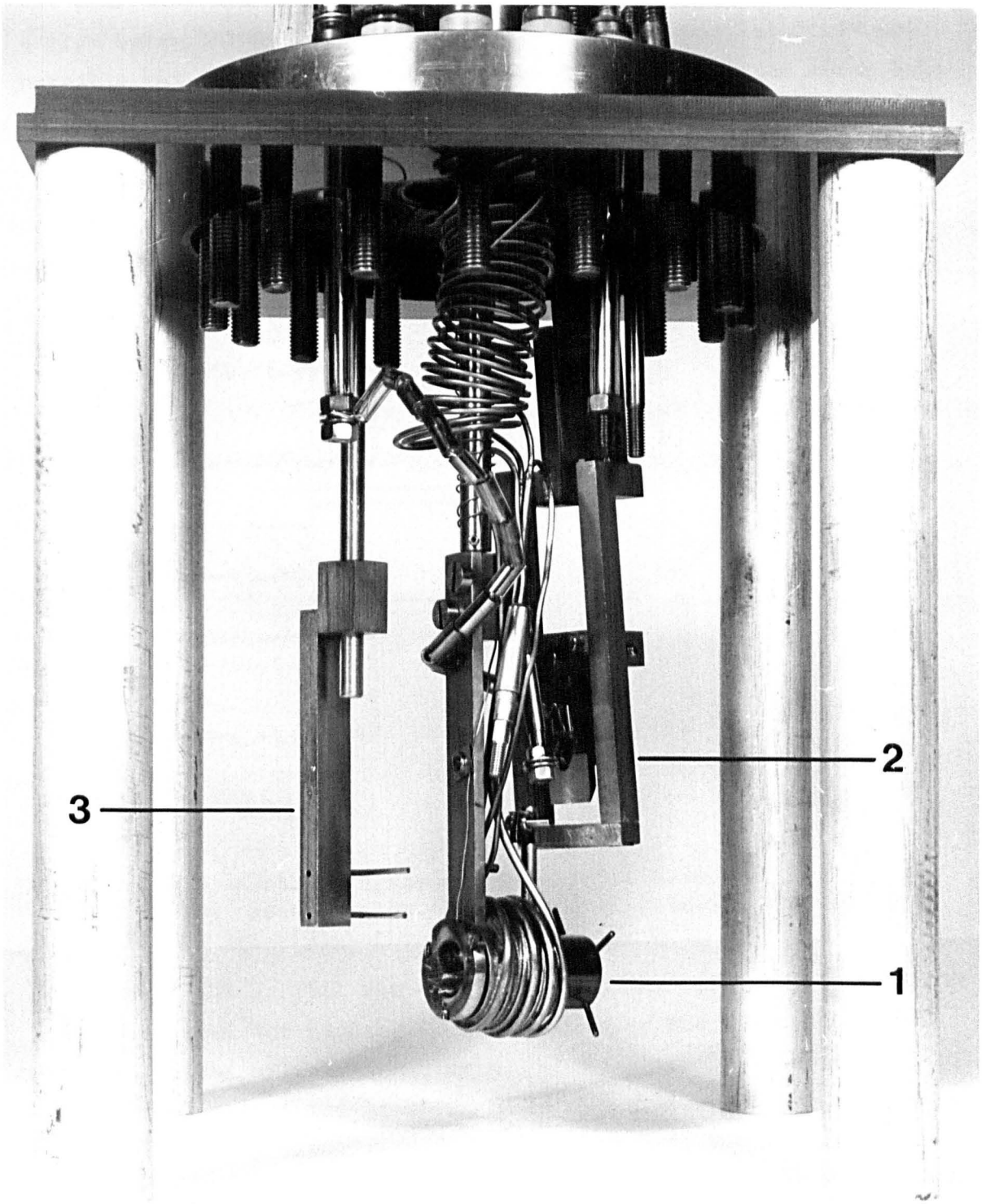

Figure 4.6 The Specimen Holder

the LEED beam and 0 - 1" perpendicular to the LEED beam, and by a coarse screw thread 0 - 1.5" vertically. The manipulator was not bakeable but could be accurately relocated on the system after bake-out.

The crystal was clamped in a stainless steel cylinder and rotated in a screw thread by means of sapphire balls, Figure 4.7a .

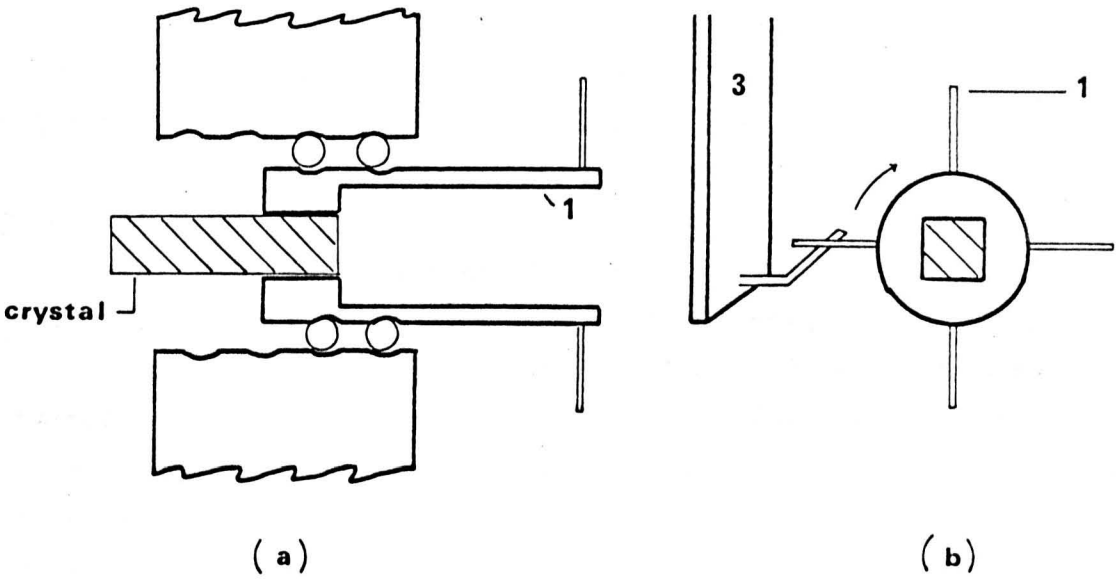

Figure 4.7 Schematic diagram of the crystal holder
a) general view b) method of rotating the crystal.

Rotation of the crystal was effected using the bellows mounted lever 3 which engaged the capstan 1, hence lowering the specimen caused rotation of the cylinder, Figure 4.7b. Rotation of the specimen allowed full use of the RHEED facility and also wound the crystal forward along the screw thread to allow multiple cleavage. The cleavage mechanism 2 consisted of a platform which could be rigidly located to support the crystal, together with a tool steel cleavage blade. The cleavage blade was operated through a bellows and the whole assembly was bellows mounted to allow vertical translation after cleavage, thereby minimising obstruction of the LEED optics.

The crystal holder assembly was surrounded by two coils of stainless steel tubing, one containing a resistive heating element and the other allowing liquid nitrogen to be passed through to cool the sample. The temperature of the sample was monitored by a thermocouple attatched to the holder, this thermocouple having been

calibrated against actual crystal temperature by comparing with a thermocouple embedded near the face of a typical NaCl crystal. Crystal temperatures between -180°C and +380°C were obtainable and for temperatures above 20°C the temperature was maintained constant by a Foster-Cambridge P130L controller. It was found that temperatures could be maintained to within $\pm$10°C at 300°C.

The specimen holder was operated successfully for NaCl, LiF, KCl, NaF and MgO crystals and with care it was possible to obtain up to six cleavage faces.

4.4 Mass Spectrometer

The mass spectrometer used in the present work was the Balzers quadrupole mass spectrometer type QMG101. The advantages of the quadrupole mass spectrometer over mass spectrometers using the deflection of ions in a magnetic field as the method of mass separation are;

a) there is no permanent magnetic field which could have serious affects on other experiments such as LEED;

b) because there is no permanent magnet the mass spectrometer is bakeable and can be made UHV compatible. (Permanent magnets may not be bakeable and the alternative, which is to remove the magnet during bakeout, has the disadvantage that precise relocation of the magnet is essential for accuracy of the spectrometer.)

In operation the output of the Balzers mass spectrometer may be conveniently displayed on an oscilloscope, x - y recorder, or for one particular mass setting on an x - t recorder. The QMG101 spectrometer was capable of detecting gases at partial pressures of 10^{-13} torr and had a resolving power ($^{m}/_{\Delta m}$) of 100 at mass 100, where Δm is the full width at 10% height of the peak due to an isotope of mass m.

Figure 4.8 shows a mass spectrometer recording of the residual gas in the system, the total pressure being about 1 x 10^{-9} torr. The traces show the presence of a small amount of chlorine (M = 35), which was also detected on the specimen surface by AES. The role of chlorine in the experiments is discussed in chapter 5.

4.5 LEED Apparatus

The LEED aparatus was of the four grid post-diffraction acceleration type manufactured by Varian Associates and mounted on a standard 8" conflat flange. The electron gun enabled a beam of electrons with energy variable between 0 and 2 kV to be obtained.

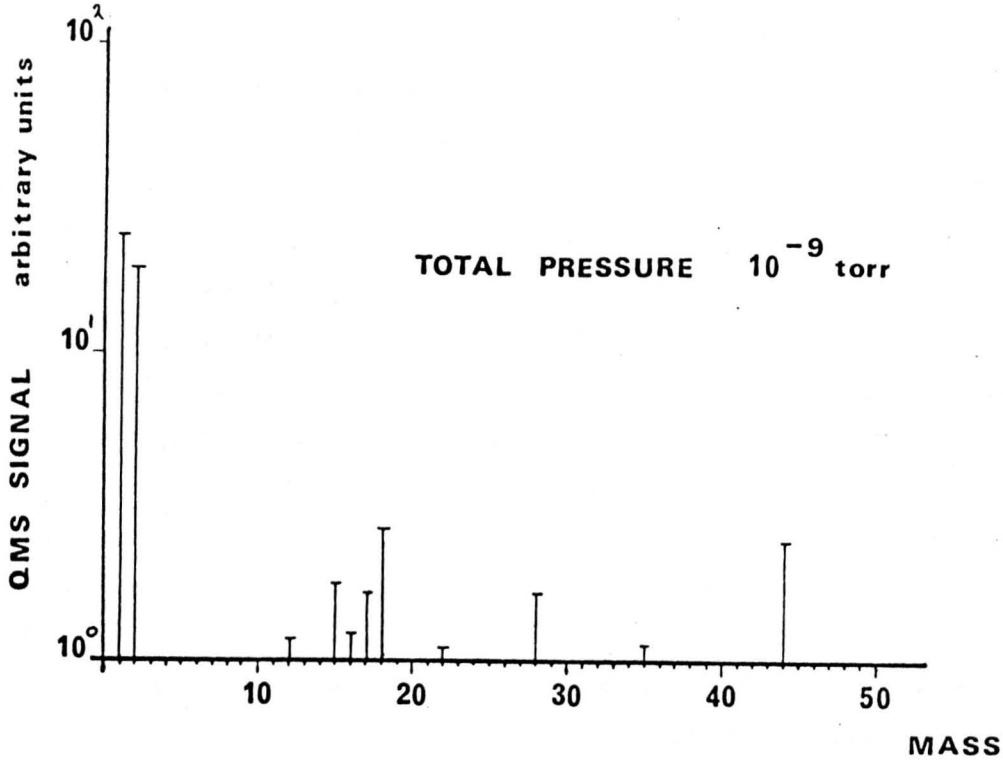

Figure 4.8 Mass spectrometer recording of the residual gas.

The beam diameter at the sample was about 1 mm and beam currents up to 1 μA were possible. The electron gun was operated by a Farnell power supply which could be switched to a constant current mode, enabling the beam current to be kept constant. Contamination of the sample by material from the electron gun cathode was not found to be a problem.

4.6 The Auger Electron Spectrometer

The Auger electron spectrometer was of the retarding field type and utilized the four grid optics of the LEED system.

The possibility of using LEED optics as an electron spectrometer was first reported by Scheibner and Tharp (140) and Weber and Peria (141). A retarding potential is applied to the centre grid (or in the case of four grid optics, to the two centre grids) so that only electrons with energy greater than this potential can pass through. The first grid is normally grounded in order that electrons leaving the sample are in field free space. The fourth grid is also grounded to prevent field penetration of the positive collector potential applied to the screen. Detection of the small currents ($\sim 10^{-11}$A) due to Auger electrons is considerably enhanced if the collected current is doubly differentiated (102). This can be achieved

by superimposing a small modulating voltage on the retarding grid and collecting the second harmonic component arriving at the screen (Appendix 1).

The detection system of the spectrometer was based on a design due to Gallon et al. (138). The design differs slightly from most analysers in that it uses a tuned load and head amplifier, instead of the resistive load normally employed. This arrangement permits a higher modulation frequency and the head amplifier (Mullard TAA 320) allows long connecting cables to be used without shunting the load.

The sensitivity of the instrument was determined by depositing silver at a known rate on a clean substrate and measuring the increase of the silver Auger peak with deposited material. The sensitivity is determined by the smallest amount of deposit material that gives rise to an Auger peak that can be positively distinguished from the noise. The experiment is described in detail in chapter 5.

The resolution of the apparatus was determined by recording the peak to peak height of the elastically reflected signal as a function of the modulation voltage. It is shown in Appendix 1 that the current in the second harmonic is proportional to the square of the modulation amplitude A, until A becomes greater than p/2, where p is the width of the peak. As A is increased beyond this limit the second harmonic current becomes less strongly dependent upon A and the point at which the departure from the square dependence occurs enables p to be determined and hence the resolution.

The resolution was determined using a 500 eV peak elastically reflected from a nickel single crystal. The departure from the square law was found to occur at a modulation of about 3V r.m.s., which implies a resolution of 1.3%. In practice the resolution is likely to be rather better than this since the above determination assumes a perfectly monochromatic beam of electrons is injected into the analyser. In general this will not be the case since the electron beam leaving the gun will have a finite breadth and this breadth will be further increased on being reflected from the target, in this case the nickel crystal.

A full discussion of the use of LEED optics as an Auger spectrometer has been given by Taylor (139).

4.7 The RHEED Apparatus

The RHEED apparatus consisted of a Marconi-Osram electrostatically focused electron gun, and a 6 cm diameter screen coated with a high efficiency P11 type phosphor supplied by E.M.I. Electronics Ltd. The electron gun was mounted on a flexible bellows system allowing mechanical steerage of the electron beam. The gun was operated with accelerating voltages in the range 10 - 15 keV and a beam current of a few microamps. Under these conditions the spot size obtained on the screen was about 1 mm in diameter. The camera length was 33 cm, although it could be varied by small amounts depending on the position of the sample manipulator.

The resolution obtainable from the RHEED apparatus was estimated using a photograph of a diffraction pattern from a flat single crystal nickel specimen. The photograph was taken using an accelerating voltage of 15 keV with the beam along a <110> azimuth. It was assumed that for a second streak to be adequately resolved the separation of the two streaks must be equal to or greater than the half width of each individual streak. A microdensitometer trace of the photograph was used to obtain the half width of the streaks and the maximum resolution found to be 6%. A similar result was obtained when the RHEED gun was operated at 10 keV. In this case the streak separation was increased but so was the half width of each streak. The resolution of the apparatus was therefore insufficient to allow the 2.6% misfit between copper and nickel to be resolved, but should adequately resolve the silver-nickel spacing. Nevertheless the RHEED apparatus was found to be useful because of its sensitivity to surface topography, providing additional evidence about the mode of growth of deposited materials.

4.8 Film Thickness Determination

4.8.1 General

The technique used for film thickness determination was photometric or colourimetric analysis (44,45). A monochromatic beam of light is passed through a cell containing a solution of the film and the concentration of the metal is determined from the intensity of light transmitted. For dilute solutions the intensity of light transmitted through the cell is given by the Lambert-Beer law (45) which may be written as

$$\log_{10} \frac{I_o}{I} = kcl \qquad (4.3)$$

I_o is the intensity of the incident light beam, I is the intensity of the transmitted light, c is the concentration of the sample and l is the length of solution traversed by the light. k is a constant called the extinction coefficient, the value of which depends upon the solvent, the temperature and the wavelength of light used. $\text{Log}_{10}\ I_o/I$ is called the extinction or optical density and a plot of extinction against concentration (for constant l) is a straight line if the Lambert-Beer law applies.

To find the concentration of an unknown solution k may be determined by measuring the extinction for a sample of known concentration and hence a knowledge of the extinction of the test sample enables c to be calculated. Alternatively a graph of extinction against concentration may be plotted and the concentration of unknown solutions found from the graph. The latter method is applicable in cases where the Lambert-Beer law does not apply providing the graph is reproducible, and was the method used in the present work.

The apparatus required for photometric analysis is a monochromatic light source, a cell in which the test solution is contained and a method of measuring the light intensity. Accurate results have been obtained using a mercury discharge lamp and filter and a simple photocell (107). In the present case a single beam scanning monochromator was available together with an E.M.I. photomultiplier. The monochromator enabled a wavelength range between 190 nm and 900 nm to be studied and either complete spectral scans could be obtained or extinction measurements made at one particular wavelength. The incident monochromatic beam was chopped at 230 Hz to allow phase sensitive detection. Consequently the affects of stray light were eliminated and additional amplification of the signal by the phase sensitive detector was obtained. The output from the phase sensitive detector was conveniently displayed on an x - t chart recorder. The test cell was constructed from a glass cylinder 6 cm in length and 1 cm in diameter. Flat silica windows were cemented to each end and a ground glass stopper used to seal the opening. The capacity of the cell was 4.5 ml and it was mounted in a light tight box between the monochromator and photomultiplier.

4.8.2 Silver Determination

Photometric determination of silver utilizes the reaction with dithizone in acid solution to form the dithizonate, which dissolves in carbon tetrachloride to form a yellow solution. In the absence of silver the dithizone solution is green and transmits little light in

the yellow region. With increasing presence of silver the reagent turns progressively more yellow and transmits a greater percentage of yellow light. The standard method for silver determination (44) is to use yellow incident light and plot values of $\log_{10}T$ against concentration, where T is the transmittance and is the ratio of light transmitted by the sample to light transmitted by the blank solution. The method used was as follows:

1) prepare the sample in about 5 ml of 0.5 N sulphuric or nitric acid and transfer to a separatory funnel;

2) add 5 ml of a 0.001% ($^{W}/v$) solution of dithizone in carbon tetrachloride;

3) shake for one minute;

4) allow the carbon tetrachloride layer to settle and run into the absorption cell;

5) obtain the intensity of light transmitted;

6) repeat the procedure using a blank solution and hence obtain the transmittance of the sample.

Using the optical system as a scanning spectrophotometer the blank dithizone solution was found to have a broad absorption maximum from 500 nm to 560 nm. Greatest sensitivity for the change from green to yellow was found using a wavelength of 560 nm.

A calibration graph was obtained by measuring the transmittance of solutions containing known amounts of silver and the graph is shown in Figure 4.9. The calibration graph was repeated many times and was found to be accurately reproducible if a fresh dithizone solution was used. If dithizone solution is left it slowly turns from green to yellow and whilst a straight line graph for transmittance against concentration was always obtained, the slope of the graph was reduced resulting in greater uncertainty.

The area of the silver deposit was found as described in section 4.2.1 and hence, assuming bulk density for the silver films, the measured concentration could be related to film thickness. The minimum amount of silver which could be detected was 0.5 μgm which in the present case corresponds to a film thickness of 40 $\mathring{A}$.

The range of concentrations which could be measured was from 0.5 μgm to greater than 30 μgm and the uncertainty of a particular determination was about $\pm$ 0.5 μgm. The accuracy obtainable using this technique for film thickness measurement is determined by the uncertainty in the concentration measurements and also by the area of the film. In the present case the area of the film was only

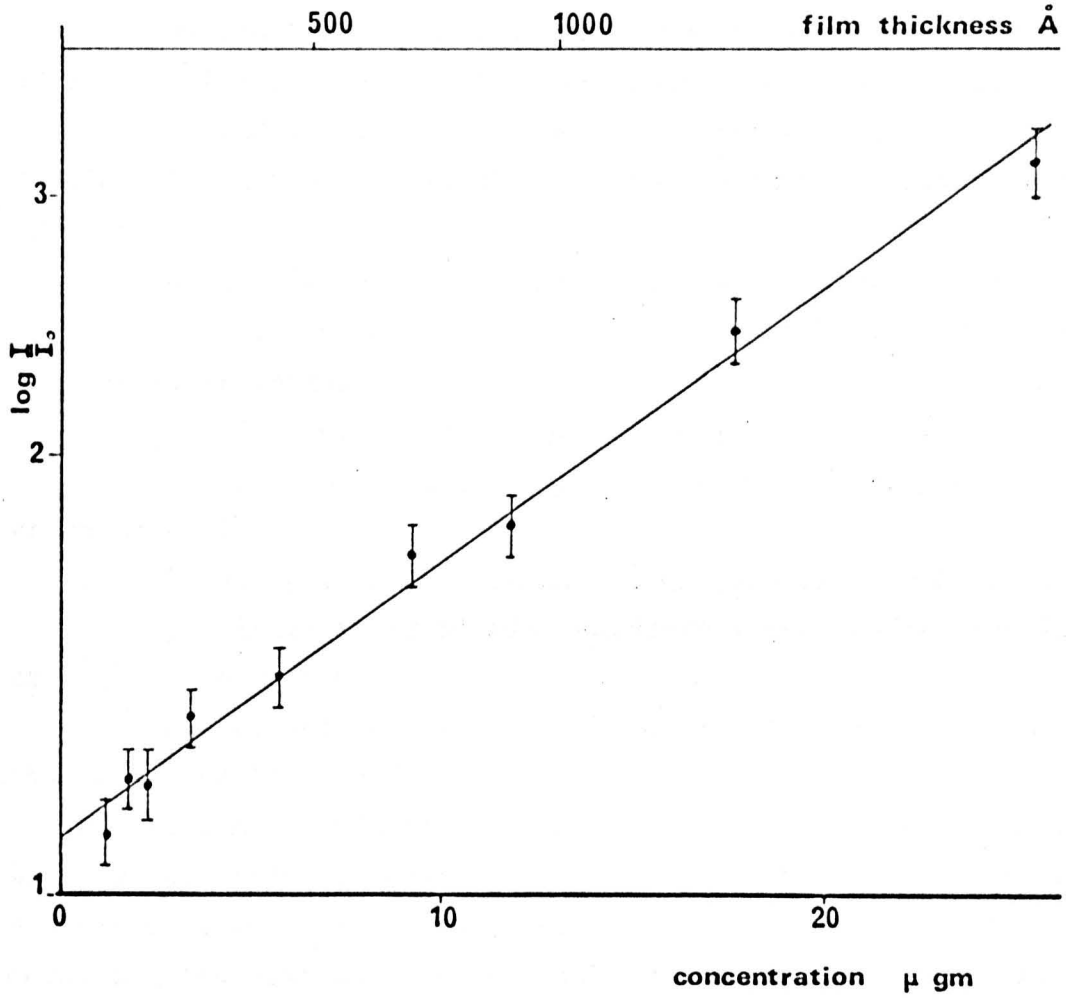

Figure 4.9 Calibration graph for silver.

1.2×10^{-1} cm^2 which gives an uncertainty of about ± 20% for film thicknesses of about 200 Å. The small area of deposit used was to make possible experiments in which silver was deposited on different regions of an alkali halide crystal surface which had been subjected to varying amounts of electron bombardment (29).

4.8.3 Copper Determination

The photometric determination of copper utilizes the yellow compound formed between copper ions and sodium diethyldithiocarbamate. The solution has an absorption maximum in the blue region and a graph of extinction against concentration may be obtained using samples of known copper concentration. The copper sample is required in a solution of pH 8.5 but generally it is simpler to prepare the copper in dilute acid solution and to adjust the final pH by addition of ammonia. If there are other metals present use may be made of the fact that copper

is soluble in concentrated ammonia and thus separation from other metals is possible. The procedure was as follows:

1) prepare 5 ml of sample solution;

2) add 2 ml of ammonium citrate solution * followed by 5 ml of a 10% ($^{w}/v$) aqueous solution of disodium ethylenediaminetetraacetate;

3) add two drops of cresol red indicator followed by concentrated ammonia until the indicator just shows its alkali colour, pH ~8.5;

4) dilute to 25 ml and transfer to a separatory funnel;

5) add 2 ml of a 0.1% ($^{w}/v$) aqueous solution of sodium diethyldithiocarbamate;

6) add 3 ml of chloroform and shake vigorously for 1 - 2 minutes;

7) allow to settle and run the chloroform layer into a 10 ml volumetric flask;

8) extract twice more with 2 ml portions of chloroform;

9) dilute to 10 ml with chloroform and measure the intensity of light transmitted;

10) repeat the procedure using a blank solution and hence obtain the extinction.

A sample solution containing copper was found to have maximum absorption between 430 nm and 450 nm and all extinction measurements were made at 435 nm. A calibration graph was obtained by measuring the extinction of solutions of known copper concentration and the graph is shown in Figure 4.10.

As with the silver determination the sodium diethyldithiocarbamate solution was not stable for more than a few days and hence a fresh solution was made before each set of measurements. Copper concentrations between 0.4 and 18 $\mu gm\ cm^{-3}$ were used and the uncertainty associated with a copper determination was about $\pm$ 0.3 $\mu gm\ cm^{-3}$. The area of the copper deposit was determined and hence concentrations could be related to film thickness and this is also shown on Figure 4.10.

* ammonium citrate - mix 210 ml of concentrated ammonia with 150 ml of water and add 200 gm of citric acid in small portions whilst stirring and cooling. Make the solution slightly ammoniacal, add a little sodium diethyldithiocarbamate and extract traces of copper with chloroform. Dilute to 500 ml.

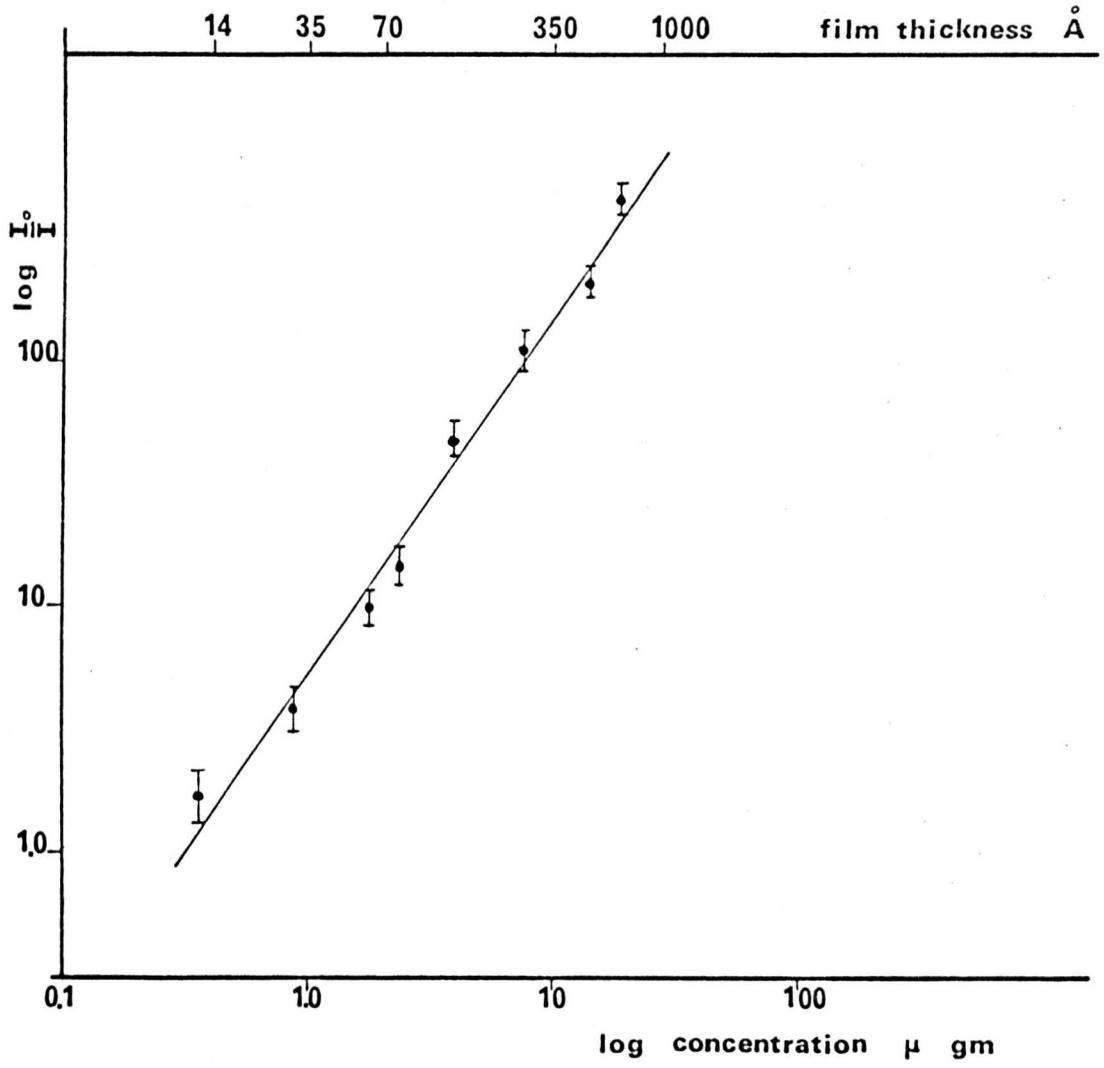

Figure 4.10 Calibration graph for copper.

The area of copper was 0.32 ± 0.04 cm^2 and this larger area enabled film thicknesses down to about 10 Å to be determined, the accuracy obtainable being about 10% for films thicker than 100 Å.

The procedure described is specific for copper and quite large concentrations of other metals may be present without causing interference (44). All chemicals used for both silver and copper determinations were of analar quality.

CHAPTER 5

SILVER ON NICKEL
EXPERIMENTAL PROCEDURE, RESULTS AND DISCUSSION

5.1 Introduction

A series of experiments was performed in which silver was deposited on clean (001) surfaces of nickel prepared inside the vacuum chamber. The Auger signals from deposit and substrate were monitored as deposition proceeded, and a comparison made with the predicted time dependence from the model described in chapter 3.

The affect of heat treatment on the silver-nickel bicrystals was investigated, and the observed changes in the Auger signals related to results obtained from subsequent electron microscopy of the specimens.

Finally, values of misfit between the silver and nickel lattices were obtained for very thin overlayers of silver.

5.2 Experimental Procedure

5.2.1 Preparation of the Nickel Substrate

A method was required to produce clean, single crystal continuous nickel films for use as substrate crystals. A series of trial experiments was performed in which nickel films of varying thickness were deposited on (001) cleavage faces of alkali halide crystals held at different temperatures. The films were examined in situ by LEED, RHEED and AES and were then removed from the UHV chamber and examined by transmission electron microscopy. Nickel films ~ 1500 Å thick, deposited on (001) faces of rocksalt obtained by cleavage immediately prior to deposition were found to be single crystal with the (001) epitaxial structure. RHEED photographs of the specimen showed streaks characteristic of a flat single crystal and subsequent electron microscopy showed the films to be continuous and completely hole free. The indicated temperature of the rocksalt was 150°C but it is thought that thermal radiation from the nearby nickel helix may have raised the surface temperature to 200 - 300°C. Figure 5.1 shows an electron micrograph of a typical nickel substrate film with the corresponding diffraction pattern shown inset, and Figure 5.2 shows a LEED and a RHEED photograph of a similar film. AES of the nickel surface showed the two nickel peaks at 60 eV ($M_{2,3}M_4M_4$) and 850 eV ($L_3M_{4,5}M_{4,5}$) and also a peak at 170 eV which was ascribed to the presence of chlorine. Electron microscopy had shown that the nickel films were hole free, therefore the chlorine signal was not due to Auger electrons

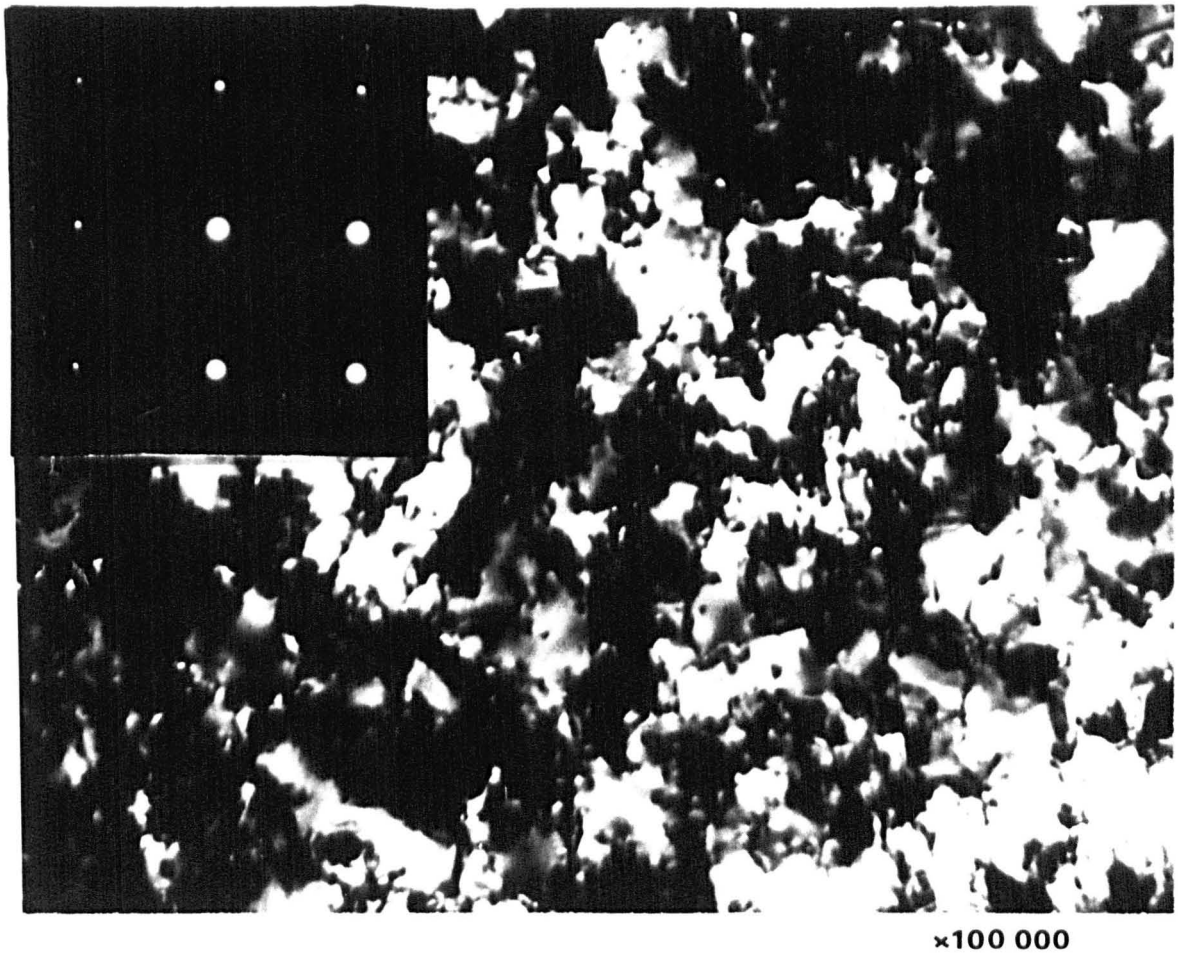

Figure 5.1 An electron micrograph of a typical nickel substrate film, with the diffraction pattern shown inset.

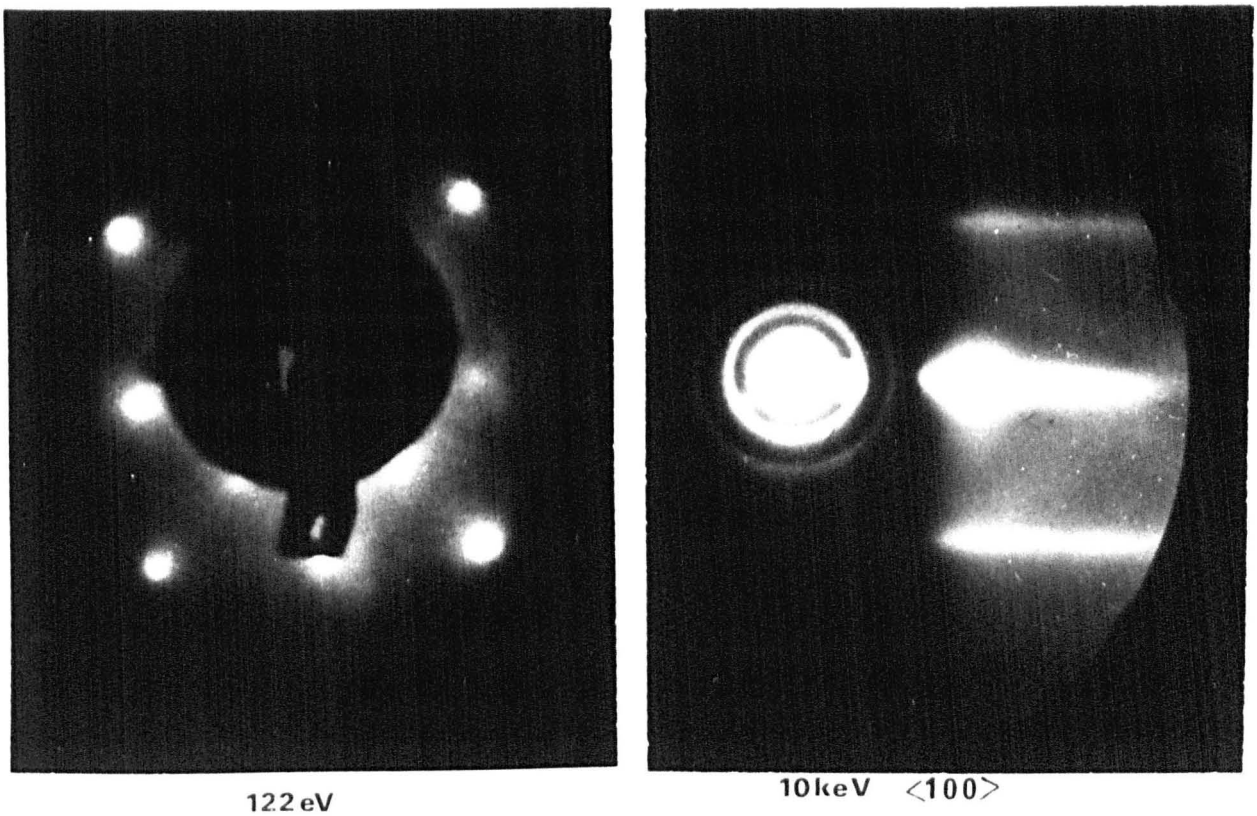

Figure 5.2 a) LEED photograph and b) RHEED photograph of a nickel film.

from the rocksalt escaping through the nickel film. In addition, care was taken to prevent the incident electron beam striking the exposed surface of the rocksalt, hence the dissociation of the rocksalt and subsequent surface diffusion of the chlorine seems unlikely. A possible explanation of the origin of the chlorine contaminant and its role during the experiment will be discussed later.

5.2.2 Deposition of Silver

Following the deposition of the nickel substrate film the rocksalt-nickel specimen was allowed to cool to room temperature. The structure of the nickel was monitored by LEED and an Auger trace obtained of the freshly deposited nickel. Silver was then deposited at normal incidence on the nickel at a rate of 0.48 ± 0.06 Å min^{-1} from the Knudsen source, the pressure during deposition being $2 - 5 \times 10^{-9}$ torr. The deposition was carried out in stages using the shutter, with the silver source turned off after each stage. Following each deposition stage the Auger spectrum of the surface was obtained and the change in the nickel and silver Auger signals recorded. Great care was taken to ensure that the Auger spectrum was obtained from the same region of the silver-nickel specimen each time, although as a result of backlash in the specimen manipulator the region sampled by the 1 mm diameter incident beam was probably about 2 mm across.

In the initial experiments the deposition of silver was continued until both the nickel Auger signals had disappeared and the silver Auger signal had reached a constant value. During the course of these experiments the RHEED facility was not used to avoid the possibility of damaging the specimen. However, at the end of each experimental run the structure of the silver overlayer was monitored by LEED, and in every case the observed diffraction pattern was characteristic of an (001) single crystal surface (130,143). Finally the specimen was removed from the UHV chamber, floated off the rocksalt and examined by transmission electron microscopy.

5.2.3 Annealing Experiments

At the conclusion of the foregoing experiments, approximately 30 Å (see later discussion) of silver had been deposited on the nickel, the nickel Auger signals were not detectable and therefore the nickel was completely covered by silver. In the following experiments the situation described above was used as a starting point for investigations using AES to study the affect of heat treatment on the specimens.

In the first experiment a silver-nickel bicrystal was left at

room temperature under vacuum (2×10^{-9} torr) for 56 hours, after which any change in the Auger spectrum was recorded. Subsequently, with the same starting conditions, a silver-nickel bicrystal was heated to 300°C. The Auger spectrum was monitored as a function of time from the point at which the specimen heater was switched on. The sample was then allowed to cool, removed from the vacuum system and examined by transmission electron microscopy.

5.3 Observations and Discussion

5.3.1 Deposition of Silver

Silver was initially deposited on the nickel in thirty second stages corresponding to an average expected thickness of 0.24 Å per deposition. A typical Auger spectrum taken after 150 seconds of deposition is shown in Figure 5.3. The peaks due to nickel and silver are clearly visible, as is the chlorine signal which remained practically constant throughout the experiment.

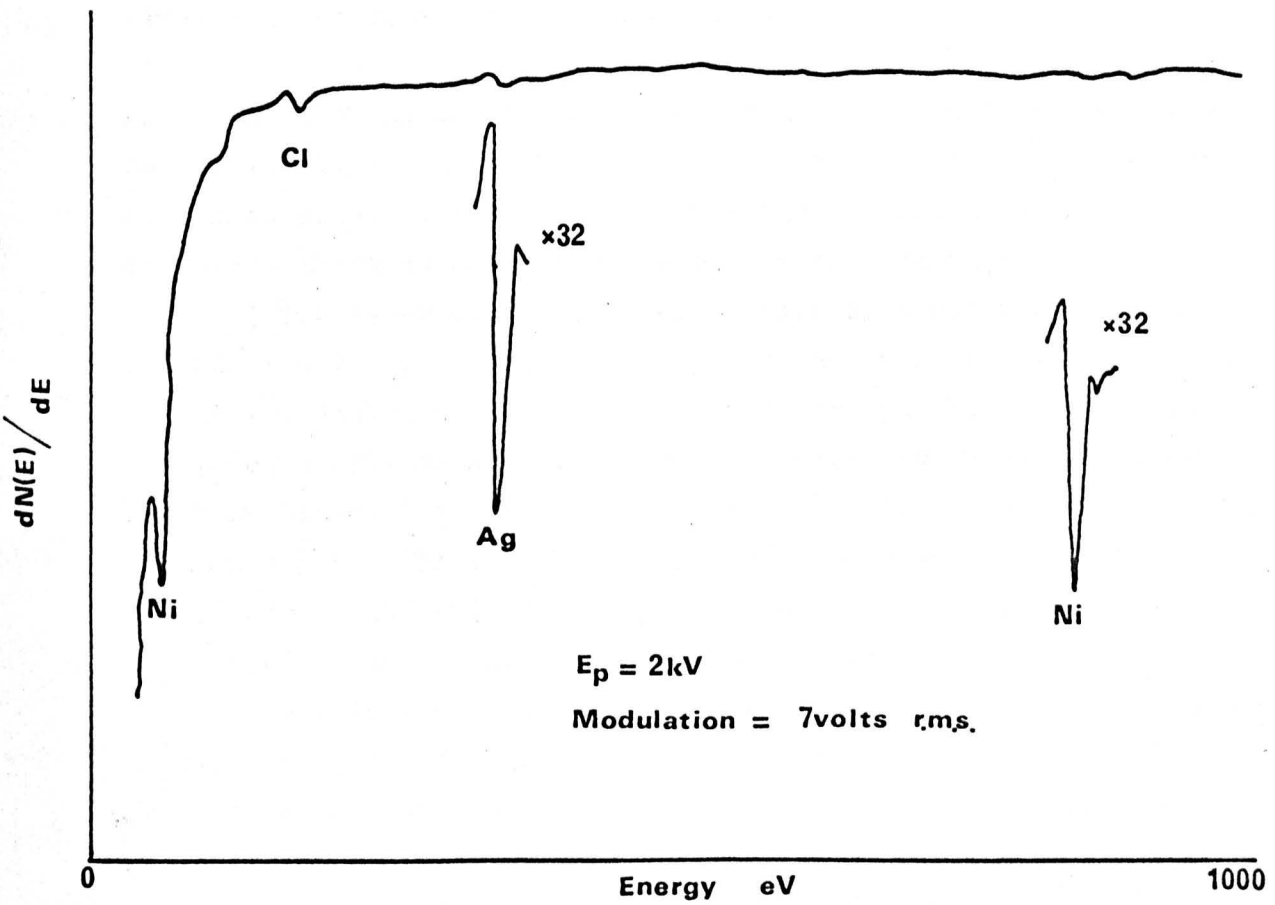

Figure 5.3 An Auger trace taken after 150 seconds of silver deposition.

The data for the growth of the silver Auger signal as a function of deposition time are shown in Figure 5.4. It is seen that the graph is initially linear and the associated experimental points show very little scatter about this line. After approximately 400 seconds there is a break from linearity, following which the strength of the Auger signal increases less rapidly with a larger scatter of the data. Eventually the signal reached a constant value which was taken as the value of I_∞ for silver.

The corresponding data for the decay of the nickel substrate signals are shown in Figure 5.5, where the inset shows the decay of the 60 eV signal on an expanded time scale. The decay of the 60 eV signal is seen to be linear, reaching a very small value after 400 seconds, the approximate time at which the silver signal broke from linearity. The 60 eV nickel signal was still present for some time beyond the 400 second stage, but the signal was very small and only detectable as a point of inflexion on the rapidly changing background of the dN(E)/dE curve. The signal was no longer present for deposition times greater than about 700 seconds.

The decay of the 850 eV nickel signal is seen to be less rapid and the signal is still present up to about 8000 seconds of deposition time. It is not possible to discern a point of discontinuity from this graph because the 850 eV nickel signal is comparitively weak and hence there is a greater scatter of the experimental points.

The experiment was repeated several times particularly in the region of 0 to 1000 seconds of deposition. The same variation of the silver and nickel signals was observed, except that in one instance the 60 eV nickel signal broke from linearity at an earlier stage than had been observed in other experiments, and is shown by the dotted line in Figure 5.5. There was no correlation between this change in the 60 eV nickel signal and either the 850 eV nickel or the 355 eV silver signals, both these plots remaining as in previous runs.

A comparison of the experimental data in Figure 5.4 with the theoretical plot of Figure 3.1 shows that in both instances there is an initial linear portion, followed by a break from linearity and a less rapid increase of the Auger signal. This suggests that monolayer growth may have been occuring, although from the discussion in section 3.3 it is evident that in some instances island growth may lead to a similarly shaped plot. That layer growth was occuring in the present case is confirmed by the linear decay of the 60 eV nickel signal in Figure 5.5

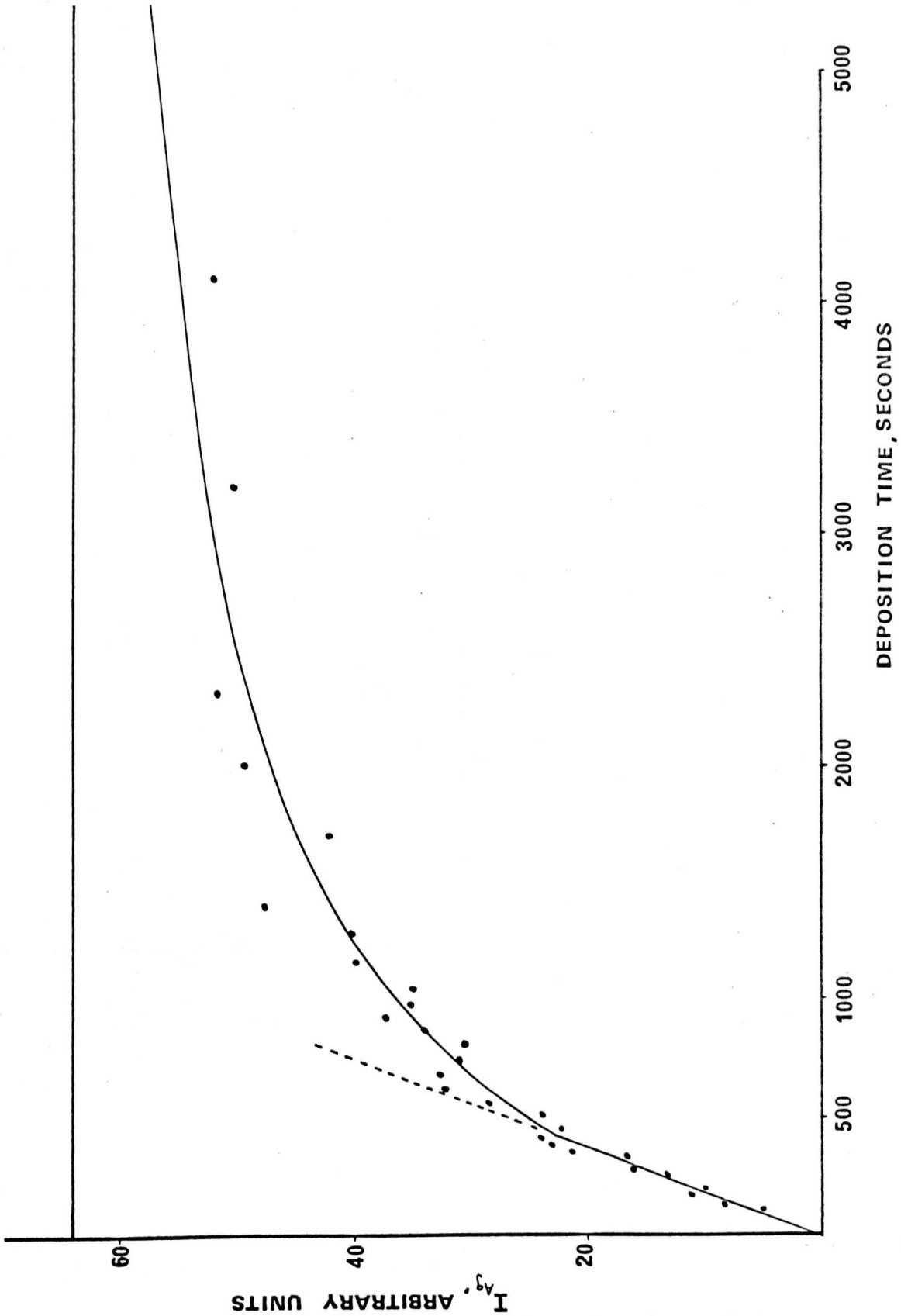

Figure 5.4 Growth of the 355 eV silver Auger signal with deposition time. Experimental points at long deposition times not shown.

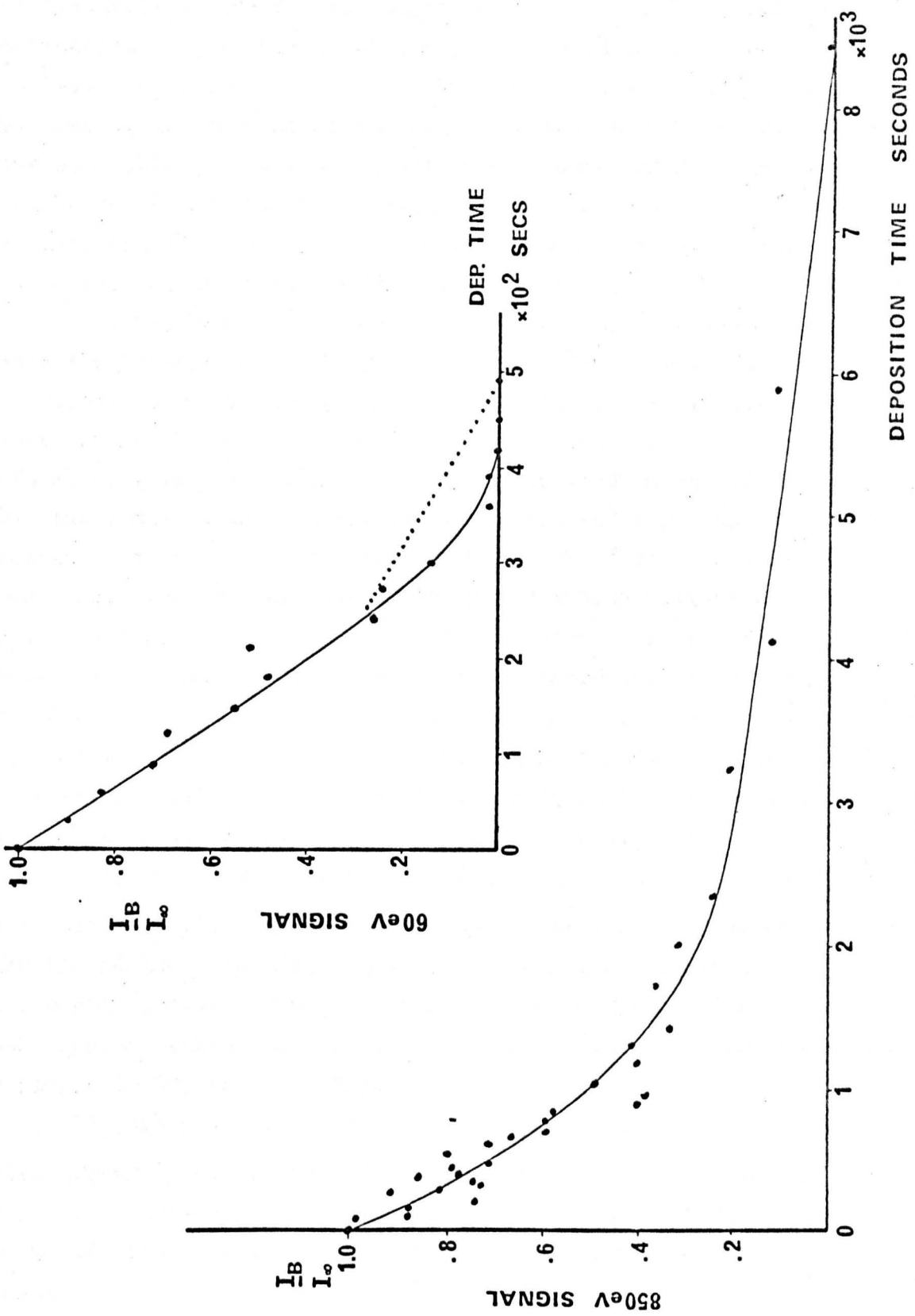

Figure 5.5 Decay of the nickel substrate Auger signal with silver coverage. Inset shows 60 eV signal on an expanded time scale.

the signal becoming exceedingly small for deposition times beyond about 400 seconds. For any other growth morphology the departure from linearity of the deposit Auger signal would not correspond to the practical disappearance of the substrate signal. Thus in the case of island growth a discontinuity may occur, corresponding to the formation of the saturation number of islands, but large areas of the substrate would remain exposed and hence a substantial Auger signal would be detected. The 60 eV nickel signal is particularly useful for the investigation since it has a small escape depth (see later discussion) and is especially surface sensitive.

It has been shown in chapter 3 that for true layer by layer growth the dependence of the deposit Auger signal is piece-wise linear with deposition time, abrupt changes in slope occuring for integral numbers of completed layers. This is also true for the decay of the substrate signal. Inspection of the graphs in Figures 5.4 and 5.5 shows that, due to the scatter of the experimental points it is not possible to identify linear regions beyond the formation of the first layer. The experimental results suggest a smooth variation with deposition time of both the 355 eV silver signal and the 850 eV nickel signal beyond about 400 seconds. One may therefore treat 'n' in equations 3.6 and 3.10 as a continuous variable and follow through the procedure outlined in chapter 3, from which it should be possible to obtain another value for t_1, the time for formation of one monolayer, and also the sticking coefficient of silver on silver.

Figure 5.6 shows a plot of $\log(1 - \frac{I_A}{I_\infty})$ against t for the 355 eV silver peak. It can be seen that, particularly for deposition times beyond 1000 seconds, there is considerable scatter in the experimental points. The graph does however suggest a discontinuity in the region between 400 and 600 seconds, which is in agreement with the discontinuity shown in Figure 5.4.

Figure 5.7 shows a plot of $\log(\frac{I_B}{I_{B\infty}})$ against t for the 850 eV nickel signal. The scatter of the results in this case make it difficult to draw any conclusions from the graph, although there does seem to be slight evidence of a change in slope in the region of 400 seconds.

The comparitively large scatter of the silver data for the region $t > t_1$ and over the whole range of deposition for the 850 eV nickel signal does not allow an accurate determination of t_1 from the logarithmic plots, Figure 5.6 and 5.7. The value for t_1 was therefore

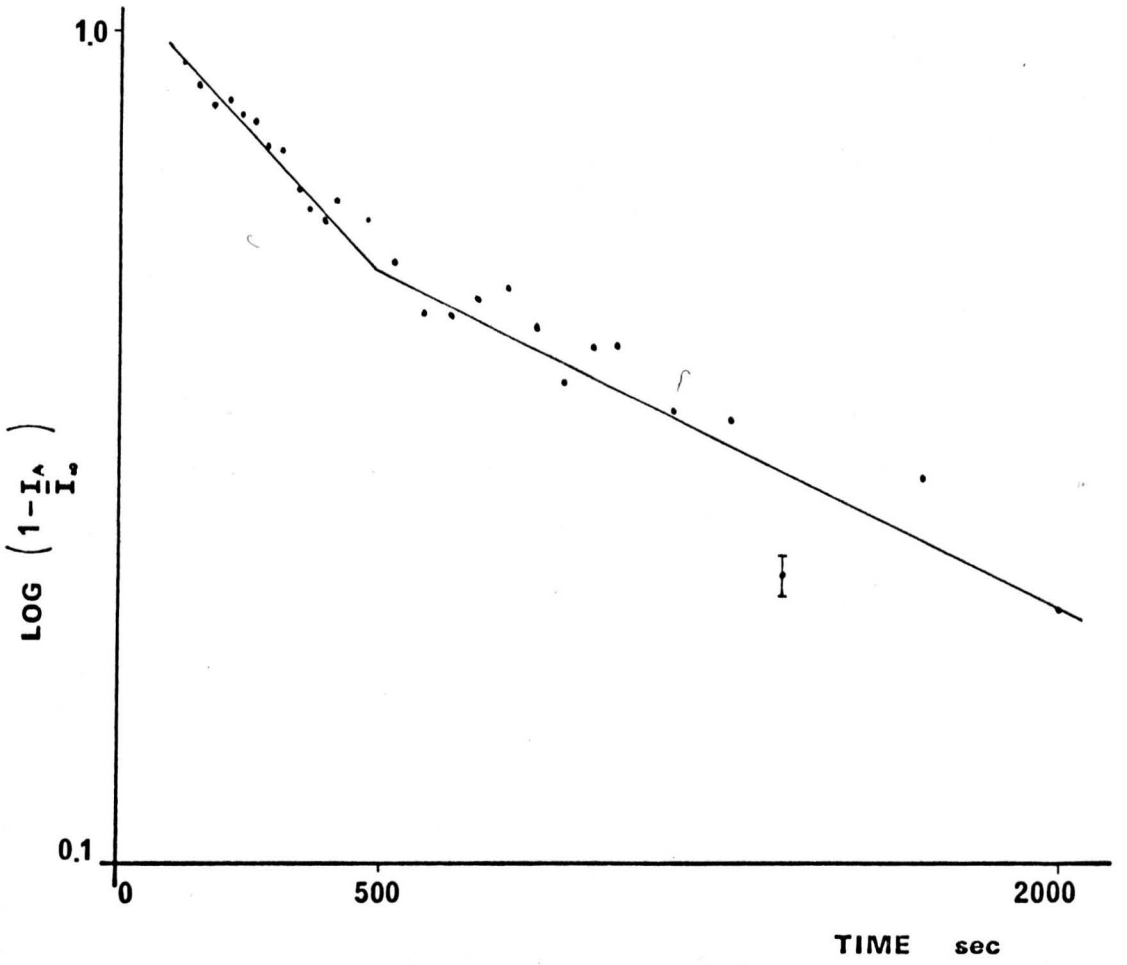

Figure 5.6 Graph of $\log(1 - \frac{I_A}{I_\infty})$ against deposition time for the 355 eV silver peak.

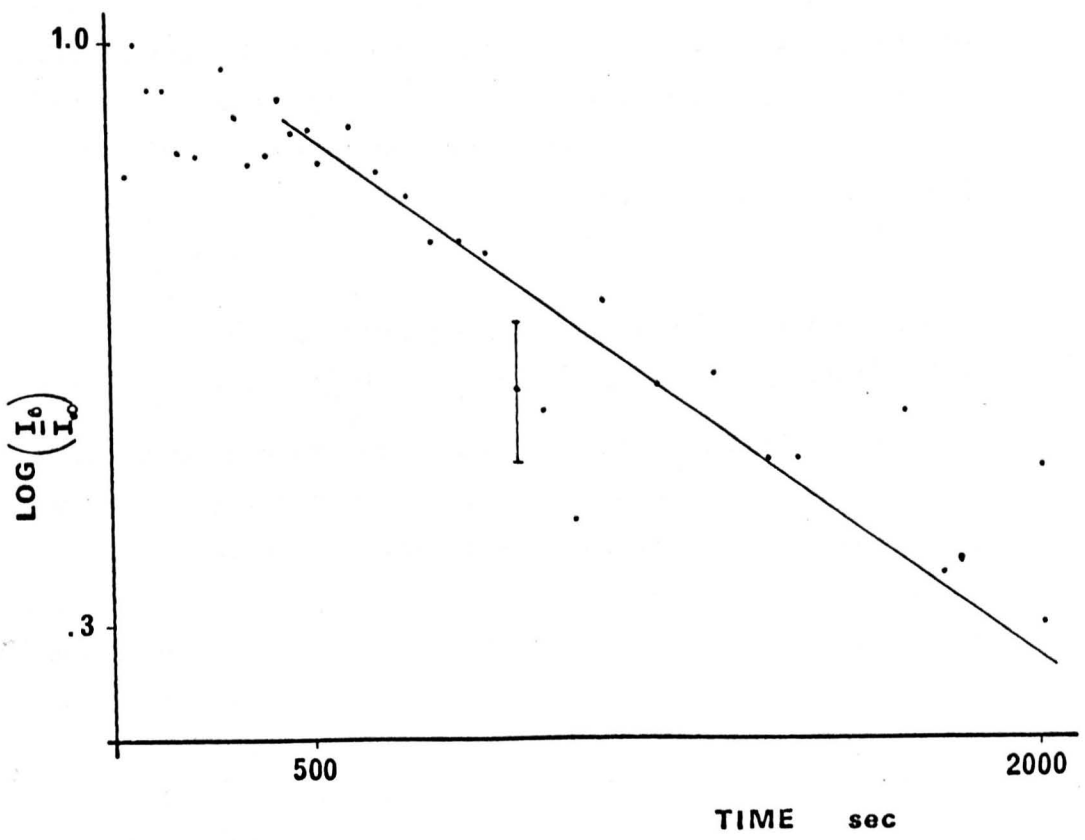

Figure 5.7 Graph of $\log(\frac{I_B}{I_{B\infty}})$ against deposition time for the 850 eV nickel peak.

deduced by inspection of the 355 eV silver and 60 eV nickel data (Figures 5.4 and 5.5) to be 400 ± 50 seconds, a value which is substantiated by Figure 5.6.

The associated value of I_1 for silver gives the ratio $I_1/I_\infty = 0.32 \pm 0.04$, which substituted into equation 3.12 gives the mean escape depth for 355 eV Auger electrons in silver as 5.4 ± 0.6 Å. This is not in agreement with the value of 8 Å found by Palmberg and Rhodin (130), even though I_1/I_∞ obtained from their Figure 9 is also 0.32.

The reasons for this difference in the estimate of n_o lie in the treatment of the data. The definition of the mean escape depth n_o is

$$n_o = \frac{\int_o^{I_\infty} n \, dI}{\int_o^{\infty} dI} = \int_o^{I_\infty} n \frac{dI}{I_\infty} \qquad (5.1)$$

dI is the Auger current generated at a depth of n layers which passes through the (n-1) layers above to the vacuum, without significant energy loss. Relating equation 5.1 to experimentally determined quantities, $\int_o^{I_\infty} n \, dI$ is the area bounded by the I (signal) axis, the experimental curve of I against t and the line I_∞. The line I_∞ is the tangent to the experimental curve at $n = n_\infty$, the total number of layers which contribute to the observed Auger current. The quantity n_o may be estimated in three ways:

(i) By direct integration of the area $\int_o^{I_\infty} n dI = A$, from which $n_o = \frac{A}{I_\infty}$

(ii) By fitting an exponential curve of the form $I = I_\infty \left[1 - \exp\left(\frac{-n}{n_o}\right)\right]$ to the data, see for example Seah (40). This procedure ignores the initial linear rise of the deposit signal and in addition assumes equality of the sticking coefficients S_1 and S_2.

(iii) By using an expression such as equation 3.12, obtained by applying the definition of equation 5.1 to a model like the one described in chapter 3. In this case n_o is a function of I_1 and I_∞ only, it being unnecessary to know n_∞.

Procedure (iii) appears to be less reliable because it involves the assumption of a model. However the advantages of procedure (iii) are that n_∞ need not be known, and providing I_1 can be determined the detailed growth morphology after the first layer is not important. In particular the measured value of I_∞ will be

substantially independent of the final morphology, although as mentioned later, some correction for differing backscattering factors may be necessary. In addition procedure (iii) does not ignore the initial linear region or the possibility of differing sticking coefficients. Therefore in circumstances where the experimental data are more reliable in the early stages and a linear portion is obtained, deduction of n_o by procedure (iii) is preferable.

The data shown in Figure 5.4 can be used to obtain a value for n_o using procedure (i), but it is necessary to know the number of layers contributing to the bulk signal. The thickness of silver that gave rise to the bulk signal I_∞ in the present case was found to be about 27 Å (see later discussion), which gives a value for n_∞ of about 13 layers. Using this value and the area $\int_o^{I_\infty} n dI$ obtained from Figure 5.4 gives a value for the mean escape depth n_o = 5.9 Å. This is within the limits of experimental error of the result obtained using procedure (iii) and hence the use of equation 3.12 based on the model of Gallon appears to be justified in the present case.

Procedure (iii) was used to estimate the mean escape depth of 850 eV electrons through silver and gives a value of 6.7 $\pm$ 0.5 Å. The form of the decay for the 60 eV nickel signal does not allow the procedure described above to be used. However the signal was very small at the one monolayer stage and had completely disappeared before two monolayers were formed. Hence the mean escape depth for 60 eV electrons through silver is about one atomic layer. The use of background nulling techniques (128) would enable a more accurate value to be obtained, since in the present case the rapidly sloping background in the low energy region of the Auger traces made it difficult to assign values for the strength of the 60 eV nickel signal.

The values quoted for the mean escape depth are the values which apply for the retarding grid spectrometer used. It was stated in chapter 3 that these values must be corrected if they are to be used for other spectrometers or in a theory of electron mean free paths. Seah (40) has shown that the correction factor for a typical retarding grid spectrometer is 1/0.7, which will lead to correspondingly larger values for n_o than those quoted.

The affect of differing backscattering factors on the values for the mean escape depths must be considered. The decay of the substrate Auger signal with deposit thickness will be unaffected in the early stages of deposition. This is because the backscattered electrons that give rise to Auger electrons from the substrate would

not be significantly altered by the presence of a thin overlayer. As the overlayer builds up the backscattering factor for the substrate will remain the same, but attenuation of the primary beam will occur. This would be most significant in cases where the electron mean free path in the overlayer is less than that in the substrate. Silver on nickel falls into this category, since the electron mean free path decreases with increasing atomic number (40). Experimentally this would cause the Auger signal from the substrate to disappear at a somewhat earlier stage than would otherwise be the case. However, if equation 3.12 is used to determine the mean escape depth then the affect of differing backscattering factors may be ignored. In this case the two parameters required are $I_{B\infty}$, the signal from the clean substrate, and I_{1BA}, the signal covered by one layer of deposit, and for the reasons given above these will be unaffected.

The affect of differing backscattering factors on the Auger signal from the overlayer is more significant. In cases such as silver on nickel it has been shown by Tarng and Wehner (132) that the signal from the overlayer rises more rapidly than it would for a constant backscattering factor. If I^c_∞ is the saturation Auger signal that would have been observed with constant backscattering factor, then the signal actually observed is given by equation 3.13. Hence the value of I_∞ used to determine n_o may be in error to the extent of the factor in brackets in equation 3.13. A knowledge of the backscattering factors would enable the value of I^o_∞ to be corrected, but at present the backscattering factor is known only for a few elements. The backscattering factor has been determined for silver, and although values are not available for nickel there are values for selenium which is close to nickel in the periodic table. Using the results for silver and selenium obtained by Smith and Gallon (134) gives $r_A = 1.5$ and $r_B = 1.3$, under the experimental conditions used. Hence using equation 3.13 to correct the value of I^o_∞ and then substituting into equation 3.12 gives the mean escape depth for 355 eV electrons in silver as 5.2 Å. This is not very different from the value obtained using the observed value of I_∞ and is well within the limits of experimental error.

The sticking coefficient S_1 for silver on nickel is obtained from the slope of the linear portion of Figure 5.4, together with equation 3.2 and the known arrival rate, and was found to be $S_1 = 0.7 \pm 0.2$, under the conditions of the experiment. The sticking coefficient of silver on silver S_2 can be found using equation 3.7 and

the slope of the log $(1 - \frac{I_A}{I_\infty})$ versus t plot (Figure 5.6) for $t > t_1$. This gives the result $S_2 = 0.37 \pm 0.15$. S_2 can also be obtained from the slope of the log $(\frac{I_B}{I_{B\infty}})$ versus t plot (Figure 5.7) for $t > t_1$ which gives the result $S_2 = 0.3 \pm 0.1$. These results are in reasonable agreement considering the large scatter of the data in Figure 5.7. This result is suprisingly low, since for metal-metal combinations the sticking coefficient is often nearer unity (107). However in cases where layer by layer growth occurs one would expect to find $S_1 \geq S_2$, since the occurrence of layer growth implies strong bonding in the initial stages of deposition.

Having obtained the two sticking coefficients S_1 and S_2 the total deposit thickness may be calculated from the known arrival rate and the total deposition time. For a total deposition time of 9000 seconds this gives a deposit thickness of 27 ± 7 Å. The uncertainty arises predominantly from the value of the sticking coefficient S_2 which itself is subject to large uncertainty.

For any deposition of silver in which layer growth occurs and substantially more than one monolayer is deposited, the sticking coefficient S_2 of silver on silver is the dominating one. A separate experiment was performed to measure the mean sticking coefficient for a prolonged deposition to see if the value obtained was in agreement with the value found from the Auger data. In the subsidiary experiment silver was deposited from the Knudsen source at the same rate as in previous experiments, the substrate being a typical (001) nickel film at room temperature. Silver was deposited for 400 minutes and then the mass of silver present found by photometric analysis. The mean sticking coefficient is given by the ratio of the mass detected to the expected mass, calculated assuming unity sticking coefficient. The photometric analysis was complicated in the present case because it was essential to remove the nickel prior to the silver determination, as the presence of nickel would affect the result (44). The nickel was removed by dissolving in dilute sulphuric acid, which should not affect the silver layer. The value of the mean sticking coefficient was found to be less than 0.5, which is in reasonable agreement with the previous value of 0.37. It is not possible to be more precise because of large errors involved due to the very small mass of silver (less than 1 μ gm) and the possibility of nickel contamination.

The sensitivity of the Auger electron spectrometer under the operating conditions described may be determined once the time for

formation of the first monolayer is known. Starting with a clean nickel substrate the 355 eV silver signal was just distinguishable from the background noise after thirty seconds deposition. The time for deposition of one monolayer was found to be 400 $\pm$ 50 seconds which means that 0.08 of a monolayer of silver was just detectable.

Finally consideration must be given to the role of the chlorine contaminant in the experiment. Residual gas analysis had shown that there was a small ($\sim 10^{-12}$ torr) partial pressure of chlorine in the system throughout the experiment. It therefore seems likely that the chlorine detected on all the surfaces under investigation was a result of adsorption from the gas. This would be consistent with its substantially constant value throughout. However, no trace of chloride structures could be found in transmission electron diffraction patterns, suggesting that the adsorption was only temporary.

5.3.2 Thermal Treatment

The Auger trace taken after a silver-nickel sample had been left in the vacuum for 56 hours at room temperature was identical to the trace obtained from the freshly deposited surface. The silver peak was the same size and neither nickel signals had reappeared. This means that substantial alloying between the two films or a change of morphology does not occur at room temperature. If any change had occured whose net result was to bring nickel closer to the surface then the 850 eV nickel peak would have reappeared, since at 9000 seconds of silver deposition the 850 eV nickel peak was only just extinguished.

When a similar silver-nickel specimen was heated to 300°C a change was observed in the Auger trace after about 30 minutes. This was before 300°C was reached, since the specimen holder took approximately 1 hour to reach 300°C. The two nickel signals reappeared and the size of the silver signal was reduced. The behaviour of the Auger signals as a function of time after the specimen had reached 300°C is shown in Figure 5.8. The 355 eV silver peak is seen to drop to below half its initial value, this change being accompanied by a reappearance of the 850 eV nickel signal. The 60 eV nickel signal shows a very gradual increase in strength throughout the anneal, never reaching a value above 0.15 of the bulk value. This last result is of particular importance because of the small escape depth of 60 eV electrons through silver. For the signal to reappear at all implies the presence of nickel within one or two atomic layers of the surface. However, since the size of the nickel signal was never greater than 0.15 of the bulk value it is unlikely that large areas of the nickel substrate were

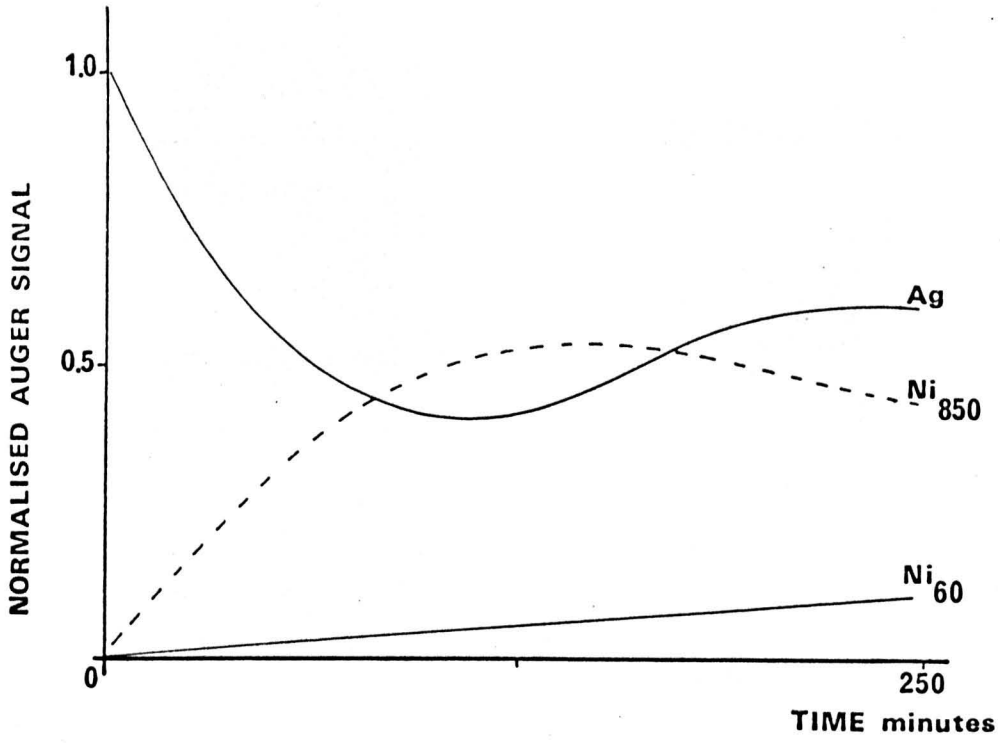

Figure 5.8 Time dependence of the normalised Auger signals during a 300°C anneal.

being uncovered.

It is worth noting that the silver-nickel bicrystal underwent a change in appearance following the anneal. Specimens prior to the anneal had a smooth mirror-like appearance, but on heating developed a 'crazed' appearance. Figure 5.9 shows a photograph of a typical specimen before and after heating.

This behaviour indicated that the silver-nickel combination had alloyed or undergone some change in morphology. That a change of morphology had occured was subsequently shown by electron microscopy and diffraction, the results of which are shown in Figures 5.10 and 5.11a, 5.11b. Figure 5.10 shows the transmission diffraction pattern taken at 100 keV. The bright spots are due to the (001) nickel substrate film. Just inside the low index spots, faint but sharp spots with no streaking can be seen. Accurate measurement of the diffraction pattern, using a microdensitometer trace of the image plate, identified the spots as having the same spacing as would be expected from bulk silver. Hence the silver was not detectably strained, which is in agreement with the predictions of pseudomorphism theory. In addition,

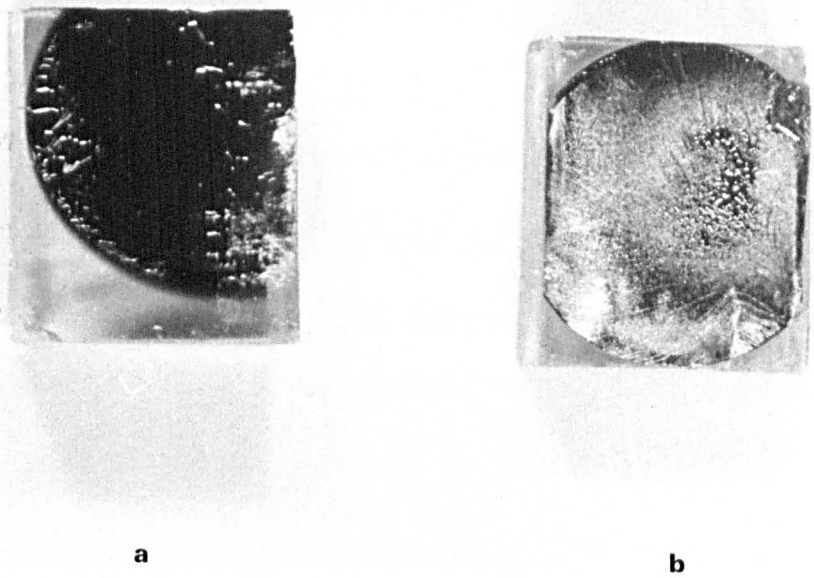

a b

Figure 5.9 Appearance of the silver-nickel bicrystals a) before heating b) following a 300°C anneal.

since the silver spots were sharp with no evidence of streaking the silver-nickel crystals were not alloying. A bright field micrograph is shown in Figure 5.11a. The dark regions were shown to be silver islands by dark field microscopy using the (220) diffracted beam from the silver, giving the micrograph of Figure 5.11b.

The existence of silver islands on the nickel is interesting with reference to the strength of the Auger signals shown in Figure 5.8. If the silver overlayer was becoming mobile at the increased temperature and forming into islands then large areas of nickel substrate would be exposed between the islands. This would give rise to a substantial 60 eV Auger peak from the nickel, which was not observed. In a similar fashion if the silver present was in the form of large islands whose thickness was in excess of the escape depth of Auger electrons, then the strength of the silver Auger signal as a fraction of the bulk signal should be approximately equal to the fractional coverage of the silver islands. In the present case the islands are certainly thicker than the escape depth of the relevant Auger electrons, as evidenced by their

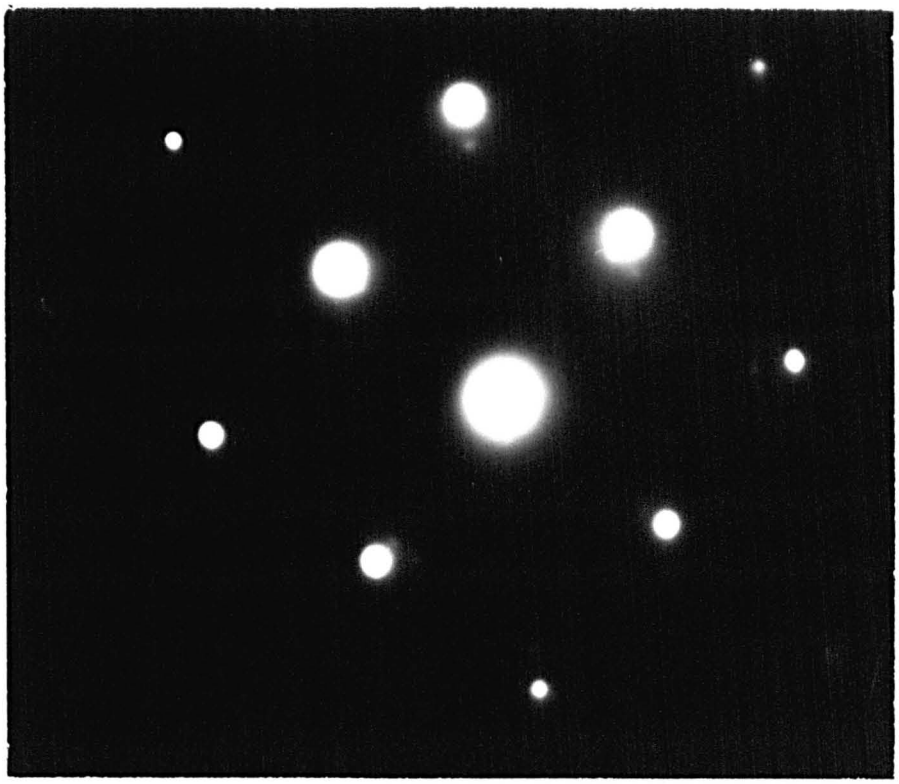

Figure 5.10 Transmission electron diffraction pattern at 100 keV of a Ag - Ni specimen annealed at 300°C in vacuum.

opacity to 100 keV electrons under microscopy. The strength of the silver Auger signal at the end of the experiment would indicate between 60% and 70% silver coverage. Reference to Figure 5.11b shows that the actual coverage of the islands is much lower than this, in the region of 20%.

A possible explanation of this discrepancy is the existence of a monolayer of silver strongly bonded to the nickel substrate. On heating this layer does not undergo significant diffusion, but subsequent layers of silver not bonded to nickel may diffuse and form into islands. The net result of this process is shown schematically in Figure 5.12. A structure of this type would give rise to a very large Auger signal from the silver and would also allow a substantial 850 eV nickel signal to be detected. The 60 eV nickel signal would however be very weak since few 60 eV electrons would be able to escape through the monolayer of silver. A structure of this type is not inconsistent with the results obtained from electron microscopy because the single layer of silver would not scatter sufficiently strongly for its presence to be detected in dark field.

It is also worth noting that silver bonds very strongly to nickel is implied by the results for the sticking coefficients in which it was found that $S_1 > S_2$.

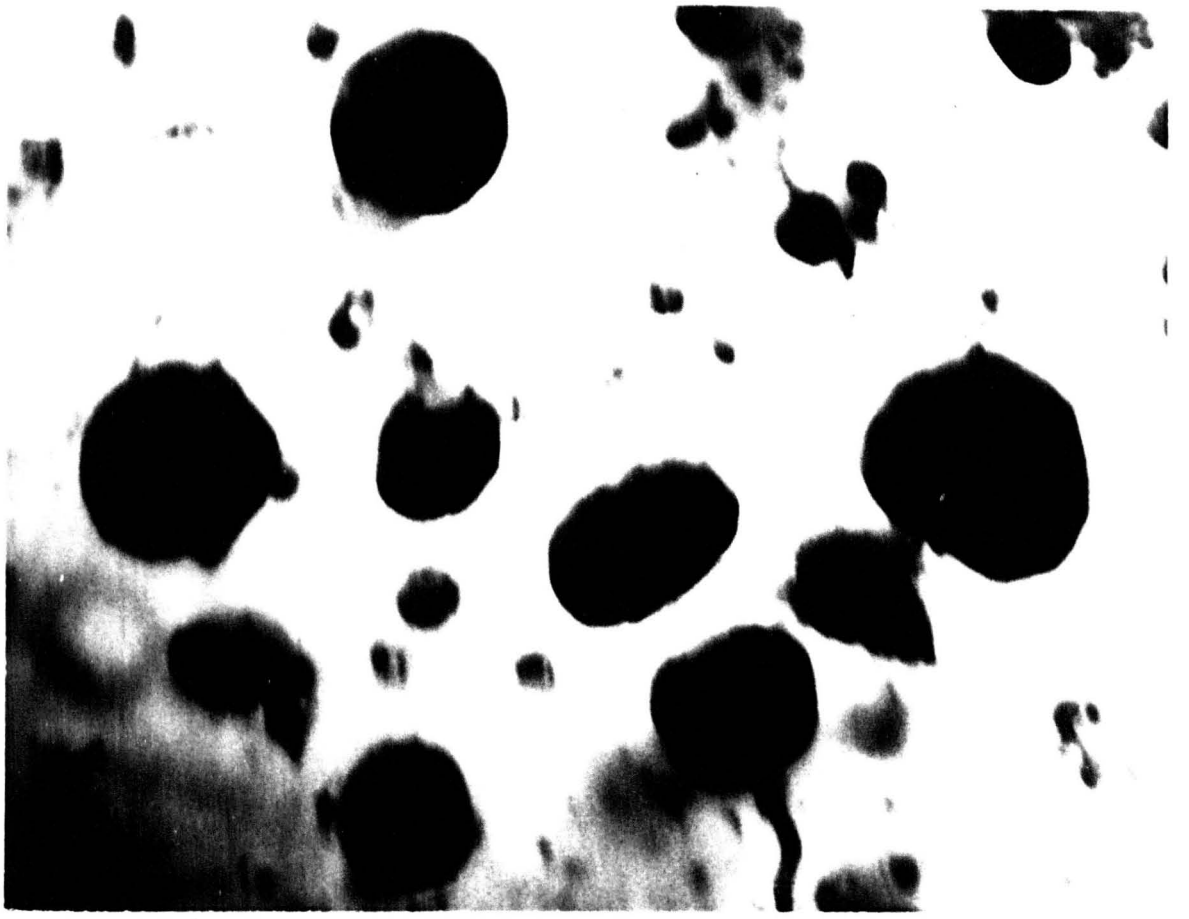

a

b

Figure 5.11 Electron micrographs of the annealed Ag - Ni specimen a) bright field b) dark field on (220) silver spot.

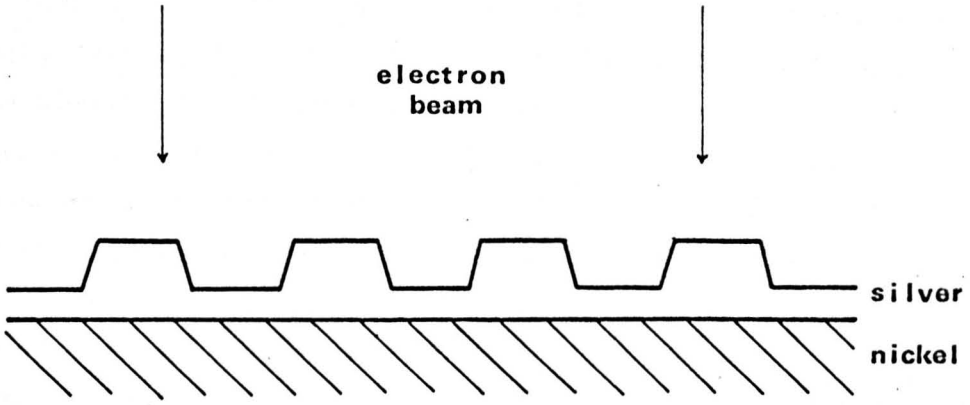

Figure 5.12 Schematic representation of the possible structure of the silver-nickel specimen following heat treatment.

The changes that would occur in the strength of the Auger signals when rearrangement of the atoms on the surface occurs are interesting with respect to the scatter of experimental results obtained for silver on nickel at room temperature. It was a feature of all the runs made that considerably lower scatter of the data for the 355 eV silver peak was observed for $t<t_1$ than for $t>t_1$, and it seems unlikely that this increased scatter was due to instrumental instability. In fact for the region between 500 and 1200 seconds of deposition there are three more or less equally spaced dips in the curve. A possible explanation of this is that regions of the $(n+1)^{th}$ layer were being formed from the existing n^{th} layer as a result of surface mobility of the silver atoms. Such an uncovering process between measurements could lead to a reduction in the strength of the total signal. The three dips in the plot of the silver data could not be correlated with any change in the 850 eV nickel signal but this was primarily due to the larger scatter of all the experimental points for this particular Auger signal. If an uncovering process was occuring in the silver overlayer one would expect the dips in the silver data to be correlated with an increase in the strength of the signal from the substrate. The dotted curve of Figure 5.5 obtained for the 60 eV nickel data may have been evidence of a similar phenomenon occuring during the growth of the initial layer. That irregularities of this sort were only observed once for the region between 0 and 400 seconds might be a result of the stronger bonding of silver atoms to nickel than of silver to silver. Thus the first silver atoms to arrive might undergo comparatively little surface diffusion and form a stable layer

strongly bonded to the nickel. Subsequent silver atoms arriving on top of other silver atoms may not bond so strongly and undergo surface diffusion, leading to irregularities in the plot of the Auger data. This possibility is supported by the results of the annealing experiments in which depositions at room temperature resulted in a two dimensional morphology which was apparently stable. However on heating the silver very rapidly formed three dimensional islands, suggesting that the two dimensional morphology may be metastable, and kinetic effects may occur even at room temperature. Such conversion of a metastable to a stable structure has been observed for platinum deposited on gold (62).

5.3.3 Misfit Determination

Measurement of relative lattice constants following the 300°C anneal had shown that the silver islands were not strained to fit the nickel substrate. However no information had been obtained on the misfit of the silver when in the form of a thin layer. Experiments were performed to measure the misfit with silver overlayers of two and six monolayers in thickness. The misfit in each case was measured from a microdensitometer trace of the image plate, obtained by transmission electron diffraction of the composite silver-nickel film. In both cases the silver was found to have the bulk lattice spacing and hence pseudomorphism does not occur for the system of silver on nickel (001), which is in agreement with the predictions of theory. Unfortunately as a result of low beam intensities it was not possible to image misfit dislocations in either specimen. Misfit dislocations were visible in micrographs of the silver islands from samples which had undergone a thermal anneal and a typical micrograph is shown in Figure 5.13. The dislocations form a crossed grid, the direction of the dislocations being along $[110]$ and $[1\bar{1}0]$. Because of insufficient beam intensity it was not possible to determine the Burgers vectors of the dislocations and hence verify the prediction of Matthews (69) that misfit dislocations in silver should be partial dislocations for low deposit thicknesses.

5.4 Summary

The experiments described, in which silver was deposited on clean nickel surfaces and the change in strength of the Auger signals monitored, did not show complete agreement with the theory outlined in chapter 3. There was well defined layer growth in the initial stages, but following the completion of the first layer the precise variation predicted by theory was not obtained. The silver did however form a

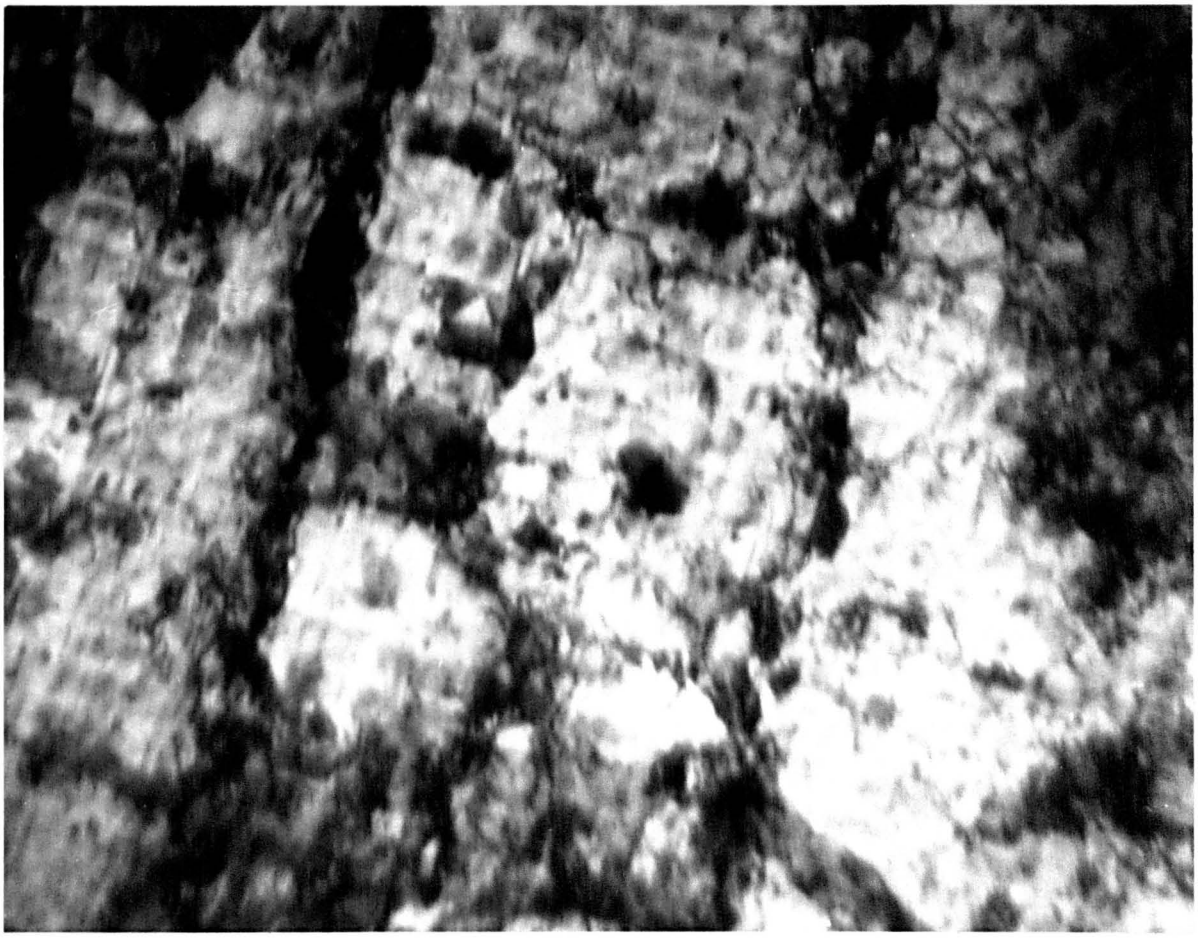

Figure 5.13 Electron micrograph of silver on nickel showing a crossed grid of dislocations.

continuous deposit and the deviations from theory are thought to be due to surface mobility. It is possible that experiments at lower temperatures would show better agreement. Close agreement between theory and experiment would enable an absolute calibration of the Auger intensities for this combination of materials. Nevertheless the Auger data does show unambiguously that layer growth was occuring in the initial stages and enables an absolute calibration for this restricted region. This information would enable precise starting conditions to be set up in situ for a surface diffusion experiment, in which for example, a quantity of silver could be deposited in a localised region on the nickel and its subsequent surface diffusion monitored. The 60 eV nickel signal would be particularly useful for such an investigation because of its sensitivity to small coverages of silver.

Despite the lack of complete agreement between theory and experiment the results do allow the sticking coefficients for silver on nickel and silver on silver to be obtained, together with values for the mean escape depth of Auger electrons in silver. In addition

the two values of sticking coefficient together with the known arrival rate and the deposition time enable the total deposit thickness to be calculated.

The annealing experiments show that, as is the case for the bulk materials, nickel and silver do not alloy when in thin film form. Also the rapid change from a two dimensional to a three dimensional morphology on heating indicates that the two dimensional structure may be metastable.

Finally it may be noted that silver deposits epitaxially on (001) nickel at room temperature, but no evidence could be found to show that the misfit between nickel and silver lattices is either totally or partially accommodated by elastic strain.

CHAPTER 6

COPPER ON NICKEL

EXPERIMENTAL PROCEDURE, RESULTS AND DISCUSSION

6.1 Introduction

A series of experiments was performed in which copper was deposited on (001) surfaces of nickel prepared inside the vacuum chamber. In the first set of experiments the nickel substrate was at room temperature and copper was deposited in stages from the Knudsen source. After each deposition stage the Auger signals from the specimen were recorded and their dependence on deposition time obtained. In a second set of experiments, still with the nickel substrate at room temperature, various amounts of copper were deposited. The composite copper-nickel films were then removed from the vacuum chamber and transferred to the electron microscope, where misfit measurements were obtained. This experimental procedure was then repeated, except that the nickel substrates were exposed to the residual gas for several hours and an attempt was made using AES to detect adsorption of gas.

Following the experiments at room temperature the experimental procedures were repeated for a nickel substrate temperature of $300 \pm 20^{\circ}C$.

6.2 Experimental Procedure for Depositions at Room Temperature

6.2.1 Preparation of the Substrate

Single crystal nickel films about 1500 Å thick with an (001) face were used as substrate crystals. They were prepared in an exactly similar fashion to that already described in section 5.1.1 for the deposition of silver on nickel.

6.2.2 Deposition of Copper

Following the deposition of the nickel substrate the rocksalt-nickel specimen was allowed to cool to room temperature. The structure of the nickel was confirmed to be single crystal with an (001) face, using the LEED facility, and an Auger trace of the nickel surface was obtained.

Copper was then deposited at normal incidence on the nickel at an arrival rate of 0.6 ± 0.1 Å. min^{-1} from the Knudsen source, the pressure during deposition being between 5×10^{-9} torr and 3×10^{-8} torr. In the first experiment the copper was deposited in two minute stages using the shutter, with the copper source turned off after each stage. Following each deposition stage the Auger spectrum of the surface was

obtained, and in the initial experiment the deposition was continued until the copper Auger signal had reached a constant value. The Auger spectrometer parameters were the same as those used for the silver-nickel experiment, namely a primary energy of 2 keV and a modulation of 7 volts r.m.s.. In subsequent experiments the first stages of copper deposition were studied in greater detail by reducing the deposition time for each stage to 30 seconds.

With the system copper on nickel it is not possible to observe the decay of the substrate signal directly because the 850 eV $L_3M_{45}M_{45}$ nickel signal is coincident with the $L_3M_3M_{45}$ copper signal. Hence the signal observed at 850 eV is a combination of a signal from the nickel which decays with deposition time and a signal from the copper which increases with deposition time. A method of estimating the contribution from the nickel substrate will be described in section 6.3.1. During the course of these experiments RHEED photographs were not taken to avoid the possibility of damage to the copper-nickel specimen. In a subsequent experiment RHEED was used to gain information on the morphology of the copper deposit in the early stages. Copper was deposited on the clean nickel substrate in two minute stages and a series of 15 keV, <110> azimuth RHEED photographs obtained.

In a second set of experiments, with identical starting conditions, various expected thicknesses of copper ranging from 3 Å to 97 Å were deposited on nickel substrates. The copper-nickel specimens were then removed from the vacuum chamber, floated off the rocksalt and caught on copper grids. These specimens were examined in the electron microscope and misfit measurements obtained by a combination of THREED, Moiré, and dislocation techniques.

6.3 Experimental Results and Discussion

6.3.1 Auger Investigation

The data for the growth of the copper 920 eV $L_3M_{45}M_{45}$ Auger signal as a function of deposition time are shown in Figure 6.1. In the early stages the copper signal is seen to rise linearly up to about eight minutes of deposition, following which the increase becomes progressively less rapid and eventually approaches a constant signal. The value of I_∞^{Cu} used is the signal obtained at long deposition times, which could not be conveniently shown in the Figure. The general shape of the graph is seen to be very similar to that of Figure 5.4 for the growth of the silver Auger signal with deposition time. Figure 6.2 shows an Auger trace taken after 60 minutes of copper deposition.

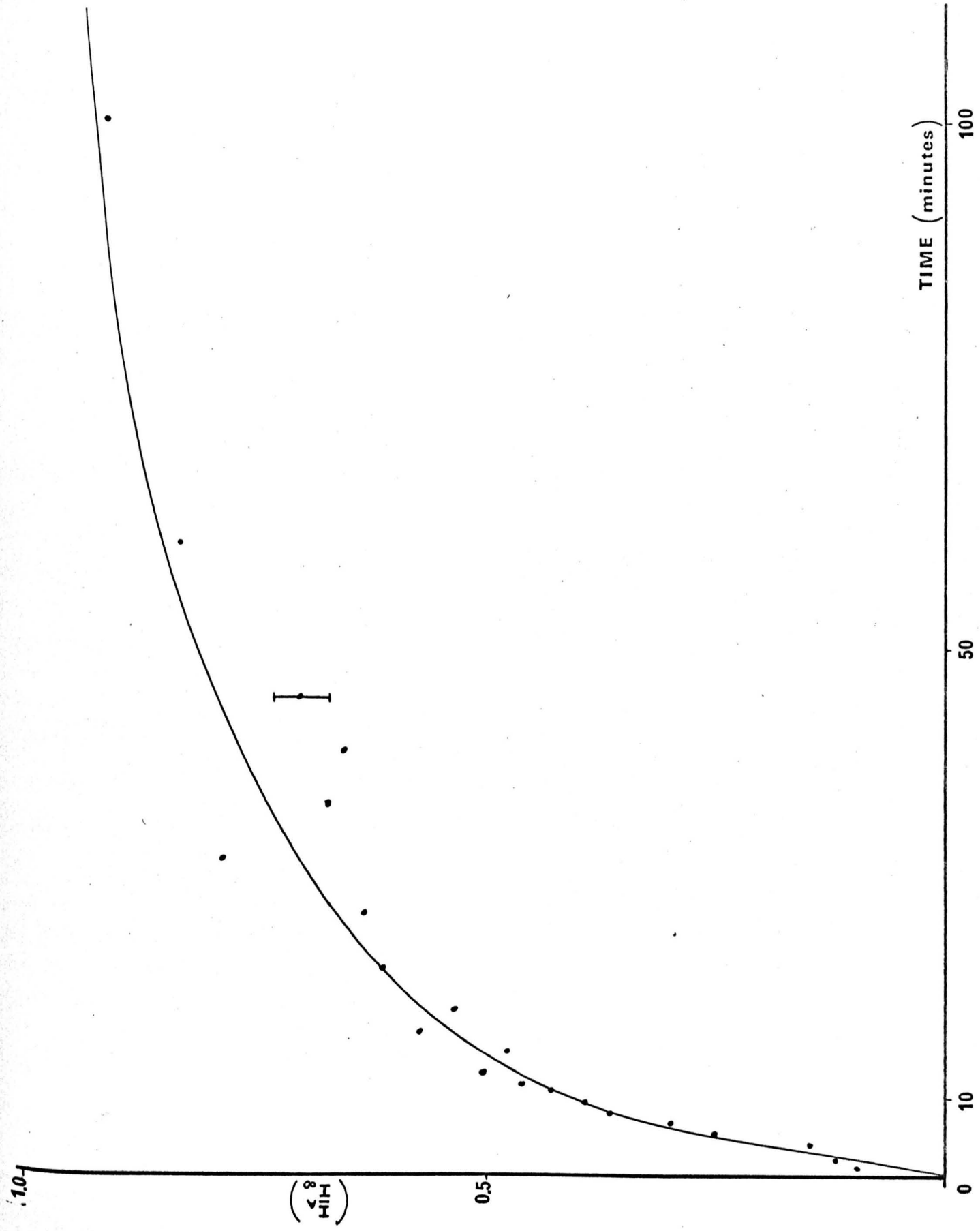

Figure 6.1 Growth of the 920 eV copper Auger signal with deposition time.

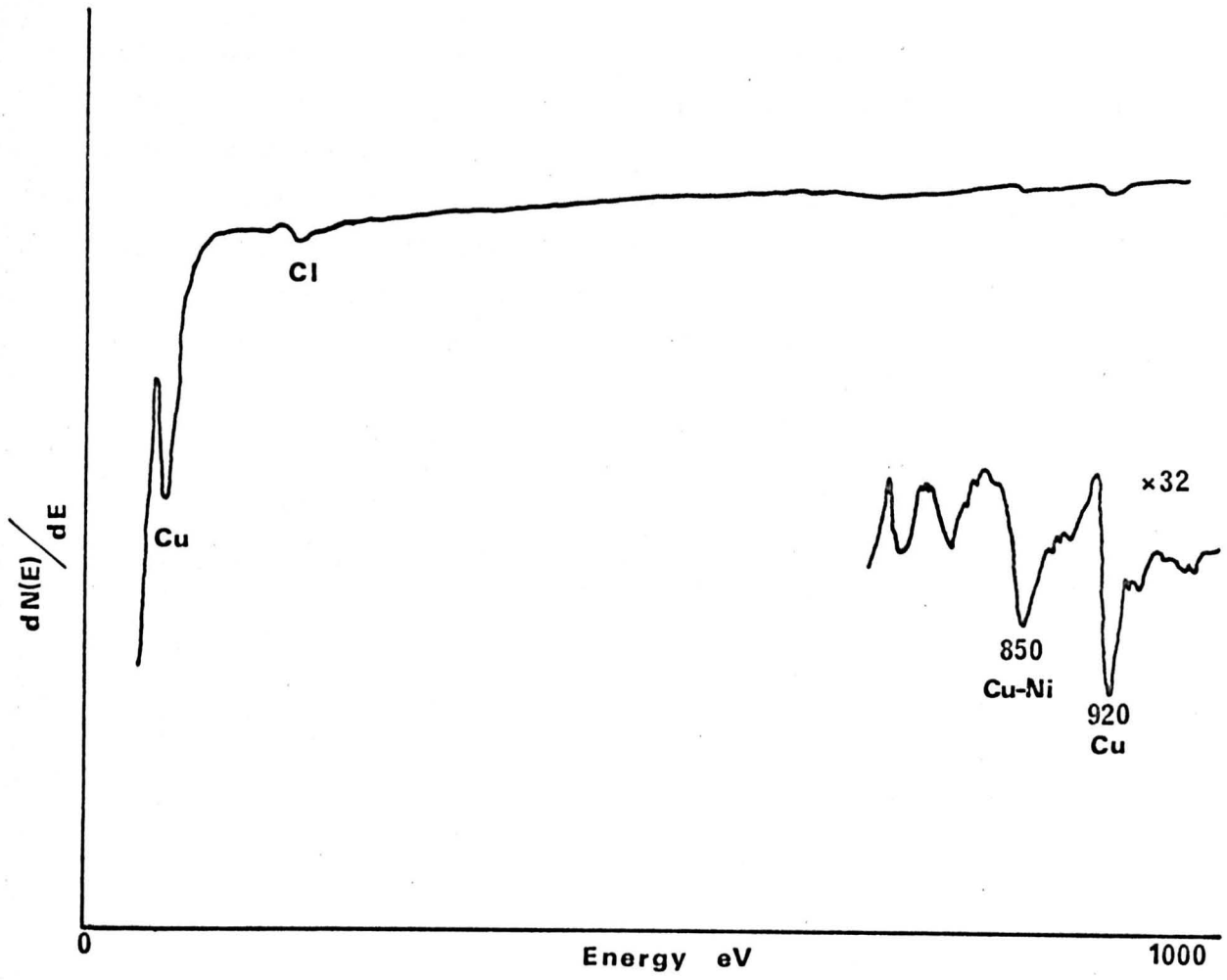

Figure 6.2 An Auger trace taken after 60 minutes of copper deposition.

The 920 eV copper peak and the composite copper-nickel peaks can be clearly seen, together with the peak due to chlorine.

The 850 eV $L_3M_{45}M_{45}$ signal from the nickel substrate could not be obtained directly because of the presence of a copper peak at the same energy. The contribution to the total observed signal at 850 eV which originated from the nickel substrate was estimated in the following way. An Auger trace of a clean, thick (~1000 Å) film of copper was obtained, revealing the larger $L_3M_{45}M_{45}$ peak at 920 eV and the subsidiary $L_3M_3M_{45}$ peak at 850 eV. The ratio of peak to peak heights of the 850 eV signal to the 920 eV signal was then determined and found to be 0.47. It was then assumed that whenever a 920 eV copper peak of X units was observed there would be associated with it a peak at 850 eV of 0.47 X units. Hence by subtraction, the contribution to the total 850 eV signal originating from the nickel may be obtained. This procedure may only be used when the two Auger signals of interest are very close together in energy, otherwise differences in escape depth would alter the ratio of the two signals as deposition proceeds.

Even in cases where the two signals of interest are very close together in energy the procedure will inevitably lead to increased uncertainty in the experimental results.

The decay of the 850 eV nickel signal obtained by the above method is shown in Figure 6.3.

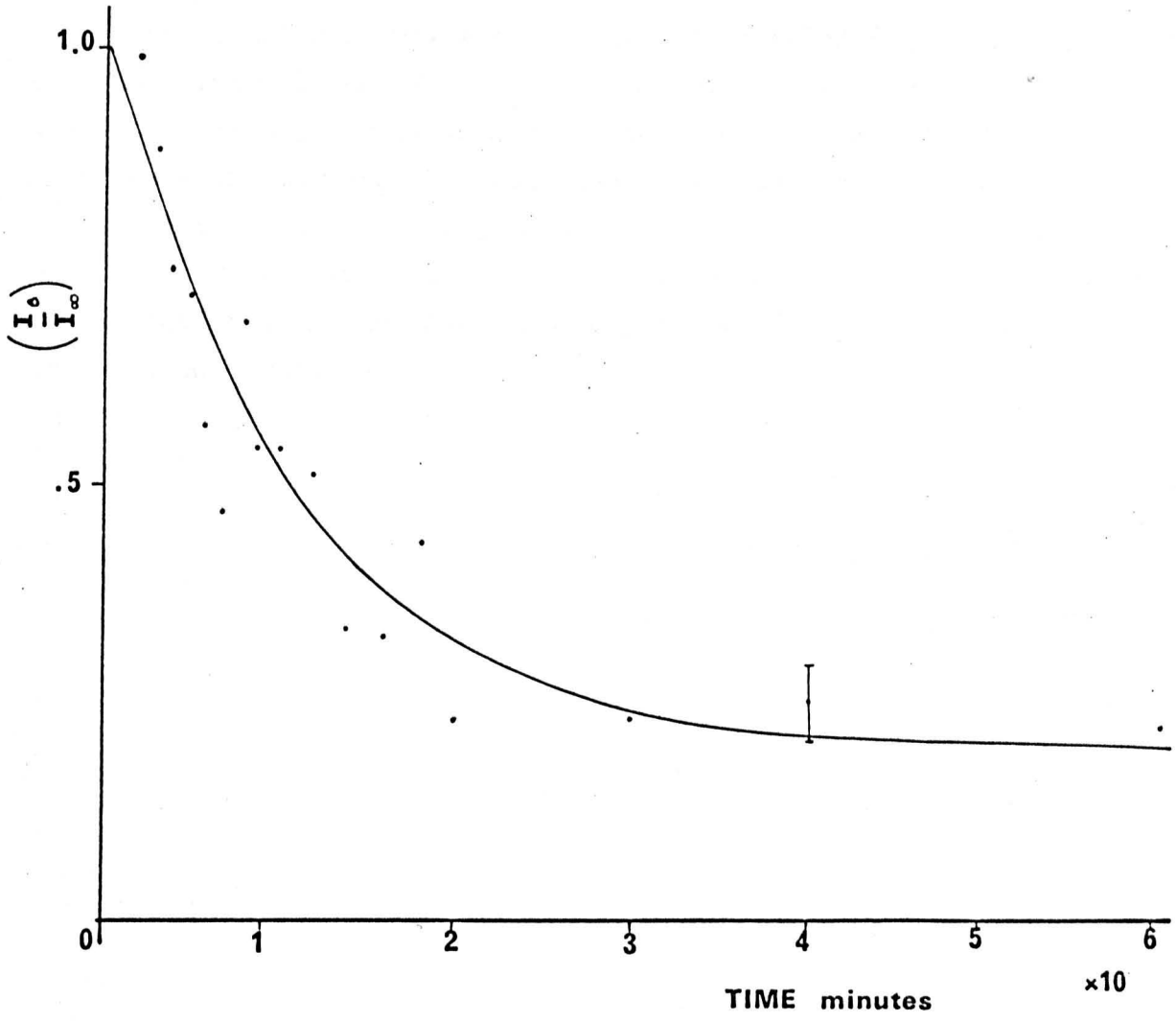

Figure 6.3 Decay of the 850 eV nickel signal with deposition time.

The signal is seen to decay rapidly during the first ten minutes of deposition, after which the decay becomes considerably less rapid. As a result of the large scatter and the error involved in the determination of each point it is not possible to discern linear regions on the graph.

The similarity between Figure 6.1 and Figure 5.4 suggests that layer by layer growth may be occuring in the present system of copper on nickel. In the case of silver on nickel the rapid decay of the low energy $M_3M_4M_4$ peak at 60 eV from the nickel provided conclusive evidence for layer growth. In the present case the low energy nickel peak could not be recorded because of the $M_3M_4M_4$ peak from copper within 1 eV of

the nickel signal. The procedure described previously for separating the two contributions was thought to be invalid in this case because of the difference in escape depths for 920 eV and 60 eV electrons. However, the four grid Auger spectrometer used should be able to resolve two peaks near 60 eV separated by about 1 eV. This was attempted, the modulation and primary beam energy used for AES being reduced to 1 volt r.m.s. and 1 keV respectively, to increase resolution and ionization cross-section. It was found impossible to resolve the signals adequately to allow measurement of their individual strengths, and frequently the two signals could not be resolved at all.

If the copper was growing in layer by layer fashion then beyond the first layer the time dependence of the copper signal should be exponential. A semi-logarithmic graph of $(1 - \frac{I_A}{I_\infty})$ against deposition is shown in Figure 6.4.

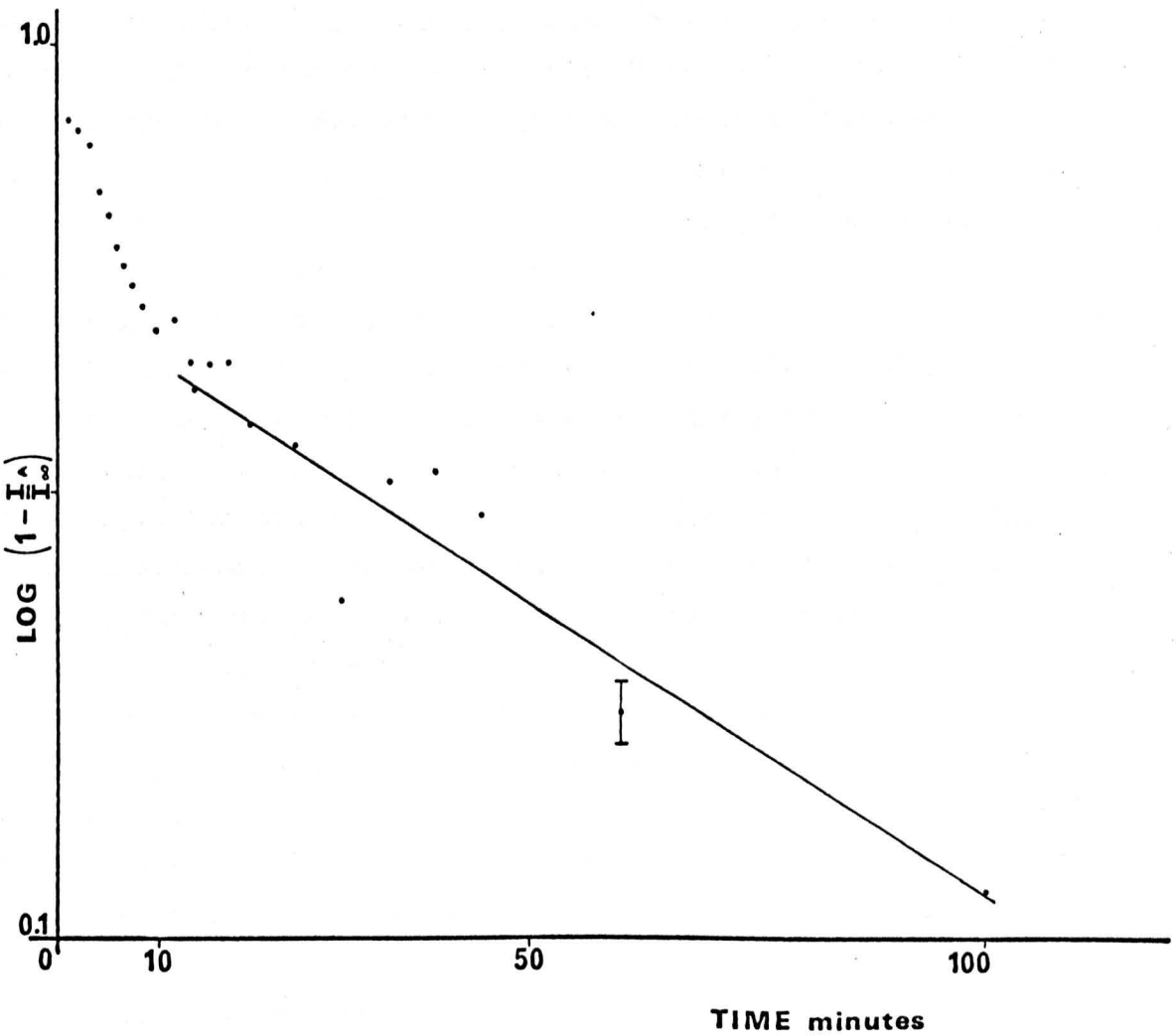

Figure 6.4 Graph of log $(1 - \frac{I_A}{I_\infty})$ against deposition time for the 920 eV copper signal.

For deposition times beyond about ten minutes the experimental points do seem to indicate a straight line, though the evidence was not conclusive.

It was therefore decided to perform an independent experiment using RHEED to study the early stages of copper deposition. A nickel substrate was prepared in an identical manner to that already described and after it had cooled to room temperature RHEED photographs of the surface were obtained. Copper was then deposited at the same constant rate in two minute stages. Following each deposition stage the crystal was rotated to the RHEED position and a 15 keV <110> azimuth photograph taken. The photographs obtained are shown in Figure 6.5. The photograph of the nickel substrate shows streaks characteristic of a flat single crystal. After two minutes of copper deposition the RHEED pattern has begun to change, having a less streaked appearance.

The reciprocal lattice of an infinite two dimensional mesh (e.g. a perfectly flat single crystal surface) consists of a set of parallel rods of infinite extent normal to the crystal face. If, however, the electron beam samples more than one lattice plane the reciprocal lattice rods begin to alter in shape, becoming more 'balloon-like' (96). The intensity maxima in the rods occur at angles corresponding to Bragg reflections and also at positions corresponding to maxima in the shape transform of the thickness of crystal being sampled. In the present case the change in appearance of the RHEED pattern indicates that the electron beam is sampling additional crystal planes. As copper deposition continues this change in appearance, i.e. loss of streaking, becomes progressively more pronounced and is most evident after about eight to ten minutes of deposition. Further deposition of copper yields RHEED patterns which show some tendency for a return to the streaked pattern. The appearance of the RHEED photographs in the range two - ten minutes of copper deposition indicates that the copper was not growing in true layer by layer fashion. The fact that the electron beam samples more crystal planes following the copper deposition can best be explained if the copper was in island form. However, the diffraction patterns did not show at any stage the sharp spots which can sometimes be seen as a result of transmission diffraction through hemispherical islands, and hence it seems likely that the islands were fairly flat.

The evidence from the Auger investigation together with the RHEED experiment indicates that the copper was not growing in true layer by layer fashion. In the early stages the copper appears to form islands, although it is thought the islands were flat. As deposition continued

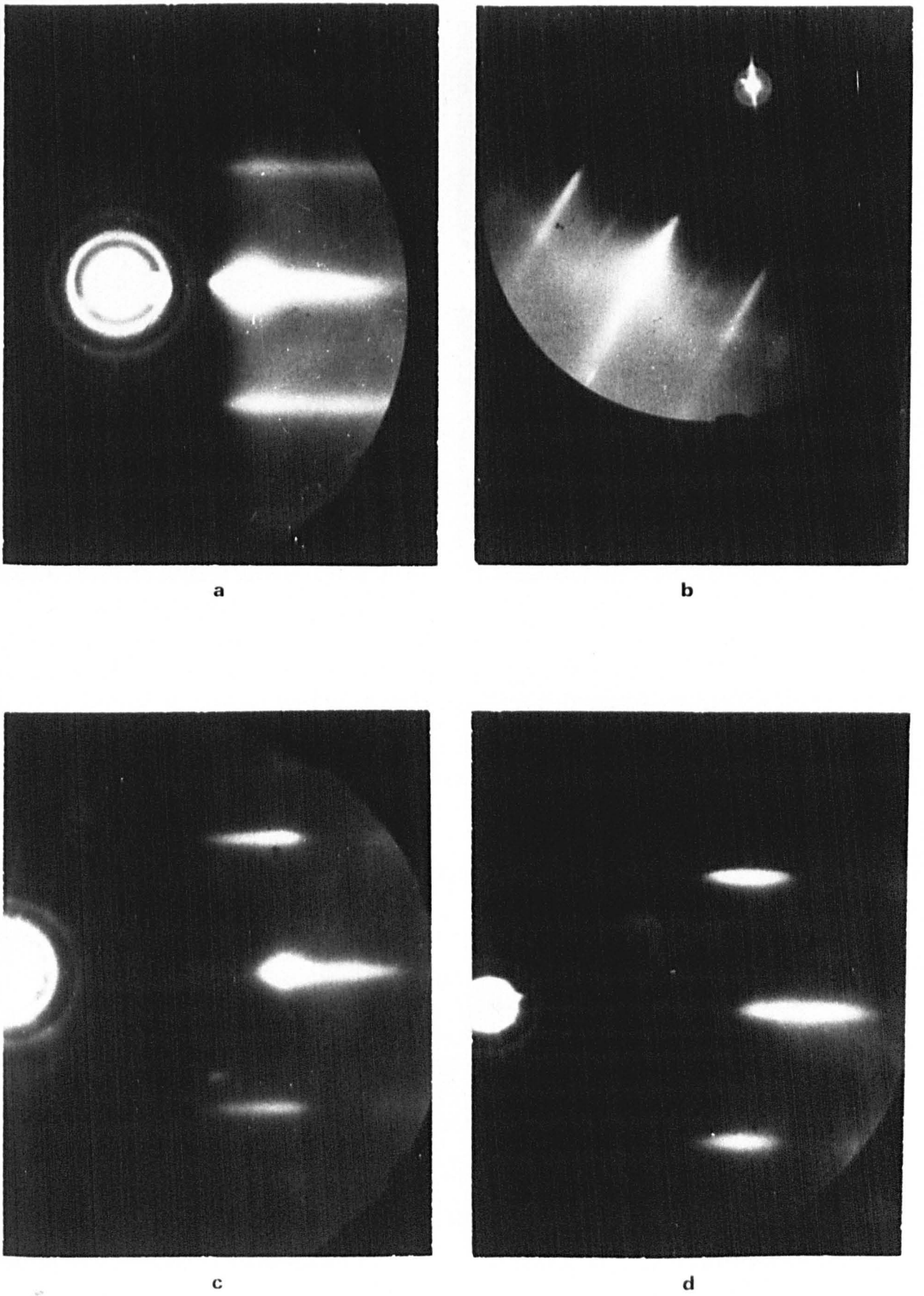

Figure 6.5 RHEED photographs of the growth of copper on nickel
a) clean nickel <100> 10 keV b) clean nickel <110> 15 keV
c) 2 minutes of copper d) 4 minutes of copper.

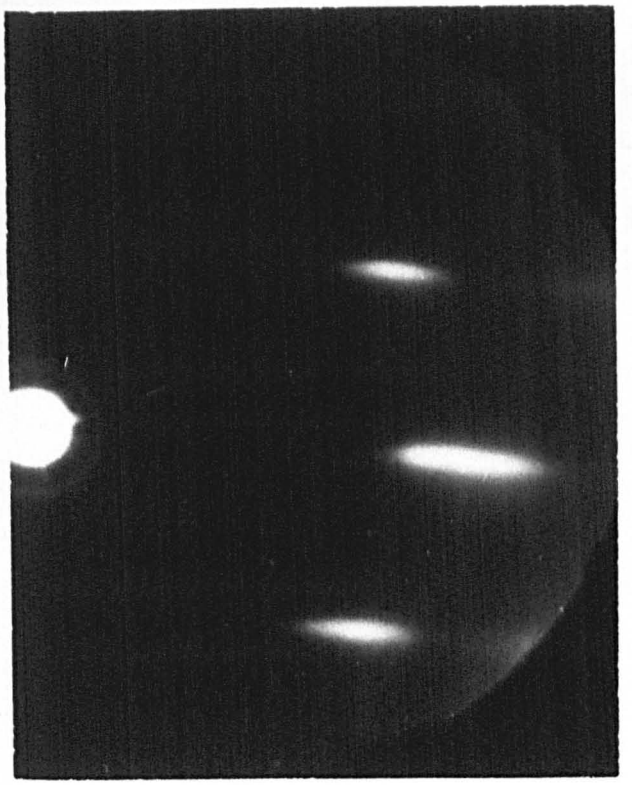

e

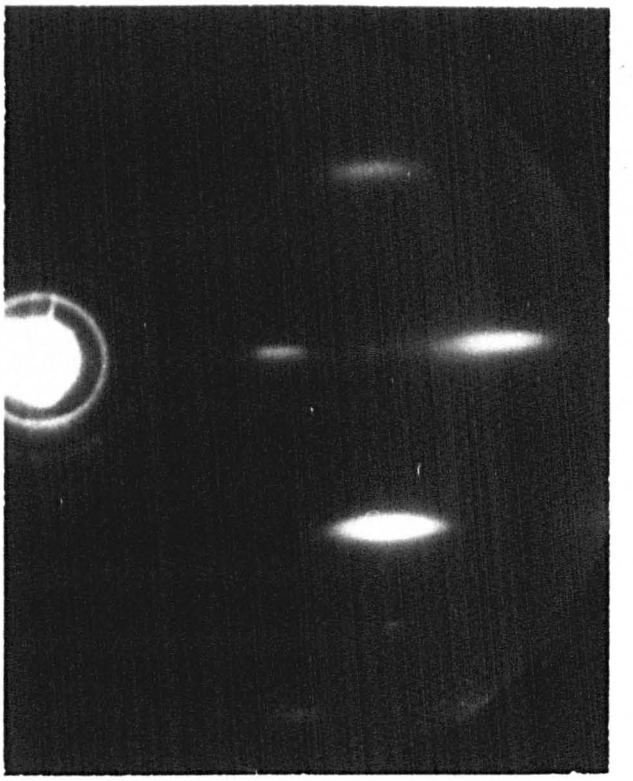

f

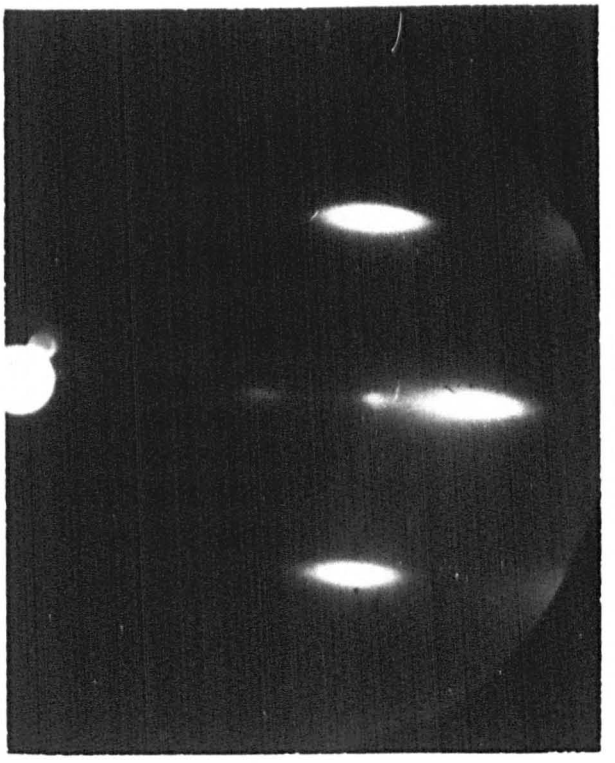

g

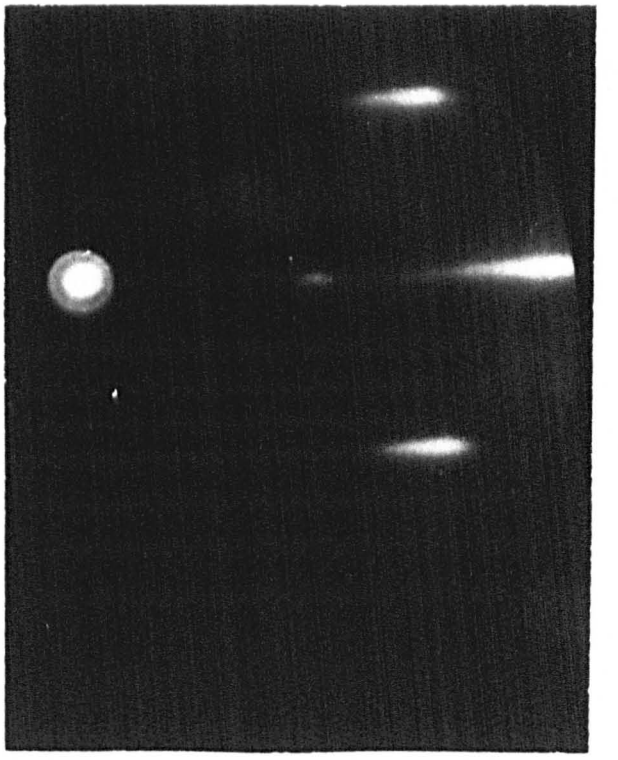

h

e) 6 minutes of copper
g) 10 minutes of copper

f) 8 minutes of copper
h) 20 minutes of copper

(e) - (h) <110> 15 keV

the copper coverage becomes relatively large, as evidenced by the strong copper Auger signal (greater than 0.5 I_∞ for t = 20 minutes) and by the tendency for the RHEED features to return to the streaked pattern. Once high coverage had been obtained the following growth would be predominantly copper on copper, and would approximate to layer growth. This could give rise to the approximately exponential form of the Auger data observed for larger values of t.

The experiment described above shows that it is not always possible to identify layer by layer growth solely from the Auger data. This is particularly difficult in the absence of a low energy signal from the substrate. In the present case it was found necessary to perform an additional experiment before a conclusion could be reached. Further evidence on the mode of growth of the copper was obtained from electron microscopy of copper-nickel specimens described in the next section.

In the absence of true layer by layer growth it was not possible to use the procedures described in chapter 3 to determine mean escape depths or sticking coefficients. This was particularly unfortunate in the present case because copper and nickel are next to each other in the periodic table and hence should have very similar backscattering factors. Therefore the uncertainty in determining n_o described in chapter 3 does not exist. Experiments at lower temperatures might show true layer by layer growth and the corresponding Auger data should yield a reliable value for the mean escape depth of 920 eV electrons in copper.

Finally the time dependence of the recorded Auger traces was investigated. In the first experiment copper was deposited on nickel for 160 minutes, this deposition time resulting in a specimen which recorded an Auger trace identical to that obtained from thick copper films (~1000 Å). The specimen was then left overnight at room temperature and in a vacuum of 1×10^{-9} torr, after which an Auger trace was obtained. The trace was identical, within the limits of experimental uncertainty, with the trace from the freshly deposited copper. In a second experiment copper was deposited on nickel in two minute stages and an Auger trace taken after each deposition. However in this case the time between completing each deposition stage and obtaining the Auger trace was 15 minutes, whereas in previous experiments the Auger trace had been obtained within two minutes of deposition. If alloying was occuring between the thin deposits of copper and the nickel substrate then the graph of Auger current against deposition time should show a less rapid time dependence than those previously

obtained. It was found that the variation of the copper Auger signal with deposition time was identical, within the limits of experimental uncertainty, to the results from the previous experiments. It therefore seems unlikely that significant surface rearrangement or alloying occurs in either thick or very thin copper films on nickel at room temperature. This is of particular importance in pseudomorphic investigations of copper on nickel, since an interfacial alloy would significantly affect pseudomorphism in the specimen. It must however be emphasised that the above conclusion is based upon observation of the high energy copper Auger peak which may not be sensitive to small amounts of surface rearrangement. Observation of the nickel and copper low energy $M_3M_4M_4$ peaks using a high resolution Auger spectrometer would allow a more definite conclusion to be drawn. In addition the present experimental arrangement would not detect alloying if the time for the interfacial alloy to form was very small. This is a result of the finite time required to move the crystal from the deposition position to the position for AES.

6.3.2 Electron Microscopy

Figure 6.6 shows a series of micrographs of typical areas of copper-nickel specimens in which various amounts of copper were deposited on clean nickel surfaces at room temperature. The micrograph taken after five minutes of deposition does not reveal copper islands, nor is there conclusive evidence of Moiré fringes or misfit dislocations. The only evidence of copper is a slight granularity in parts of the surface. An Auger trace of the specimen taken whilst still in the UHV chamber positively revealed the presence of copper and hence the copper must have been completely pseudomorphic. The micrograph taken after 20 minutes of deposition is interesting in that it shows patches of copper which, judging from their near transparency, are fairly thin. Furthermore the coverage of copper is high, in accordance with the conclusions from the AES and RHEED experiment. Figure 6.6c shows the appearance of the copper after 60 minutes of deposition. The copper has become fairly thick with a high coverage, and Moiré fringes can be seen in places. Finally Figure 6.6d shows 80 minutes of copper deposition. There is very nearly complete coverage and Moiré fringes can be readily seen.

Before a graph of misfit against film thickness could be plotted it was necessary to relate deposition times to actual film thickness. The sticking coefficient could not be found from the Auger data in this case and hence an independent determination was required. The absolute

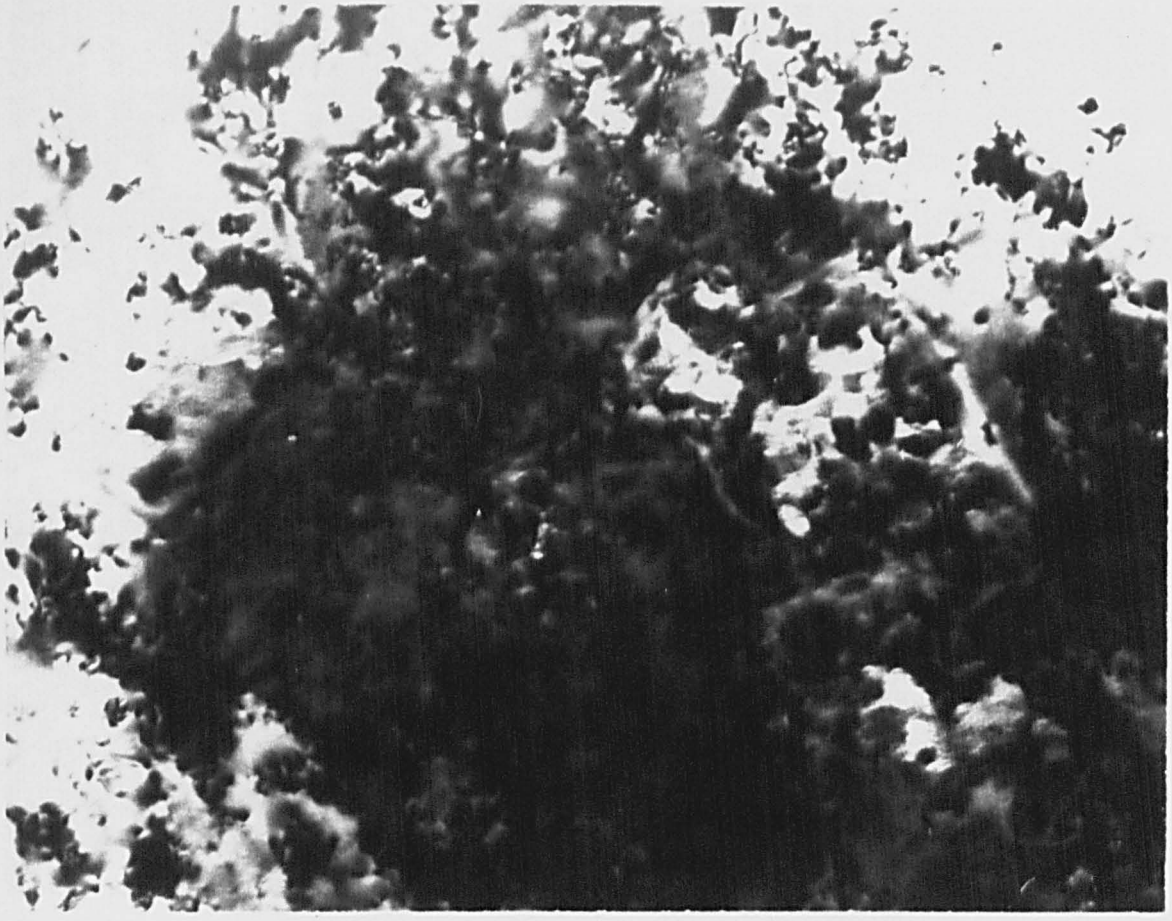

a

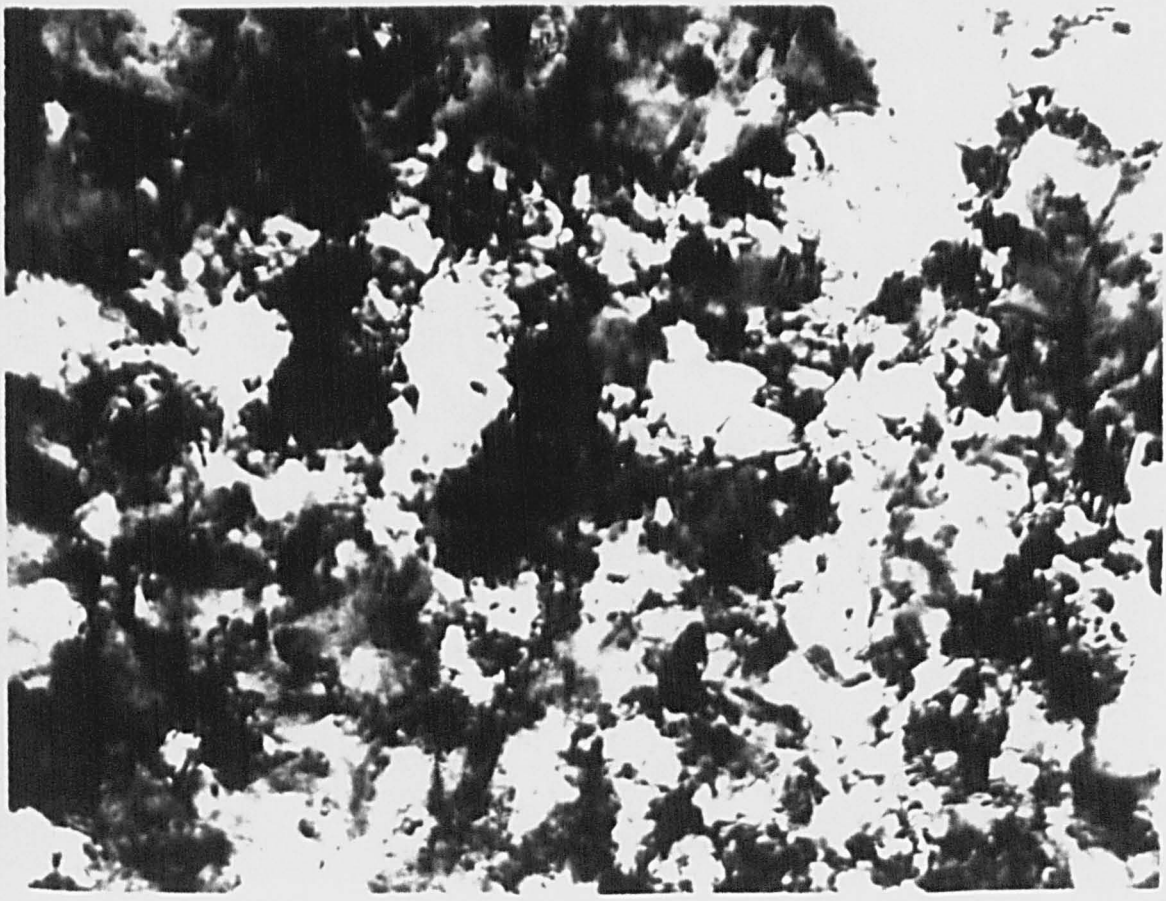

b

Figure 6.6 Electron micrographs of various amounts of copper on nickel a) 5 minutes of copper b) 20 minutes of copper.

c

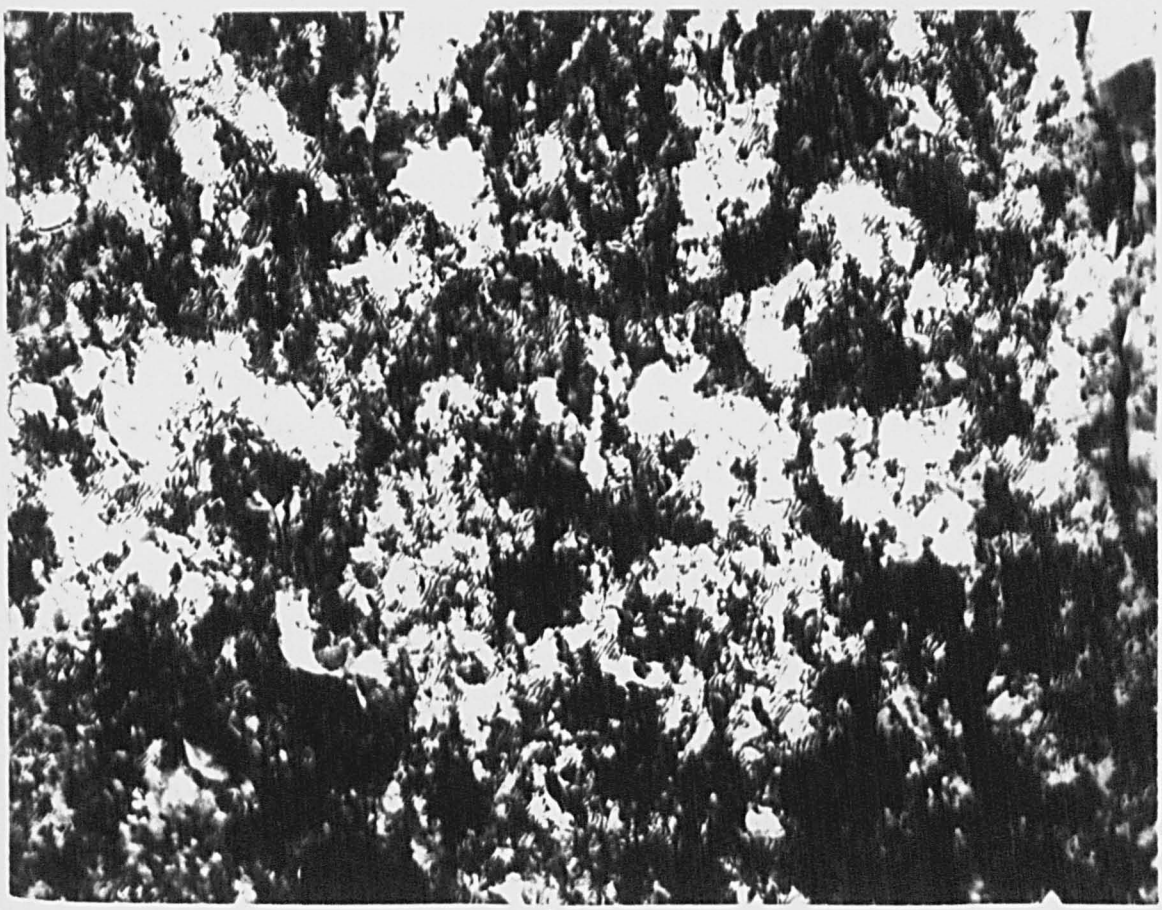

d

c) 60 minutes of copper d) 80 minutes of copper (approximately x 100,000)

arrival rate from the Knudsen source had been determined by photometric analysis and was found to be 0.6 ± 0.1 Å min^{-1}. The mean sticking coefficient was found initially for deposition of copper on nickel at 300°C, since the result was required for later experiments. The value was obtained by depositing copper for a known time and then determining the mass of copper actually present by photometric analysis. Assuming bulk density for the copper the mean sticking coefficient was found to be $1.02 \pm .05$ i.e. unity. The experiment was not repeated at room temperature since the sticking coefficient is unlikely to be less at the lower temperature; hence a sticking coefficient of unity was assumed throughout for depositions of copper on nickel.

Figure 6.7 shows a plot of the measured elastic strain in the overgrowth against mean deposit thickness. The values were obtained from the spacing of Moiré fringes for thinner films and from both Moiré fringes and THREED measurements for thicker deposits. The values obtained are shown in Table III for comparison between the THREED and Moiré results. The values of misfit obtained by THREED are thought to be accurate to about 2% of the value quoted, whereas the Moiré technique is uncertain to about 15%. The Moiré fringe determinations were made by photographing regions of the sample where fringes could be clearly seen. In regions where the fringes were approximately parallel the fringe spacing was obtained from a microdensitometer trace across several fringes. Each value of misfit shown in Table III is an average value obtained from the spacing of several fringes in one particular area. A typical microdensitometer trace is shown in Figure 6.8. THREED is not readily applicable in cases of very small misfit or for low deposit thicknesses. In the case of low deposit thickness the intensity of the diffracted spot from the overlayer is weak in comparison to the spot from the substrate, and the two diffracted spots cannot be separated. For this reason THREED measurements were not obtained for deposit thicknesses below 27 Å. It was not possible in any of the specimens to obtain clear images of misfit dislocations, and hence misfit determination from the spacing of dislocation lines was not made.

Figure 6.7 also shows the predicted values of elastic strain against film thickness for copper on nickel. The values were calculated using equation 2.8, originally taken from Matthews and Crawford (36). The shear modulus of the interface G_i was put equal to the shear modulus of copper, which is lower than the value for nickel. A higher value of interfacial shear modulus would lead to a correspondingly larger prediction of elastic strain.

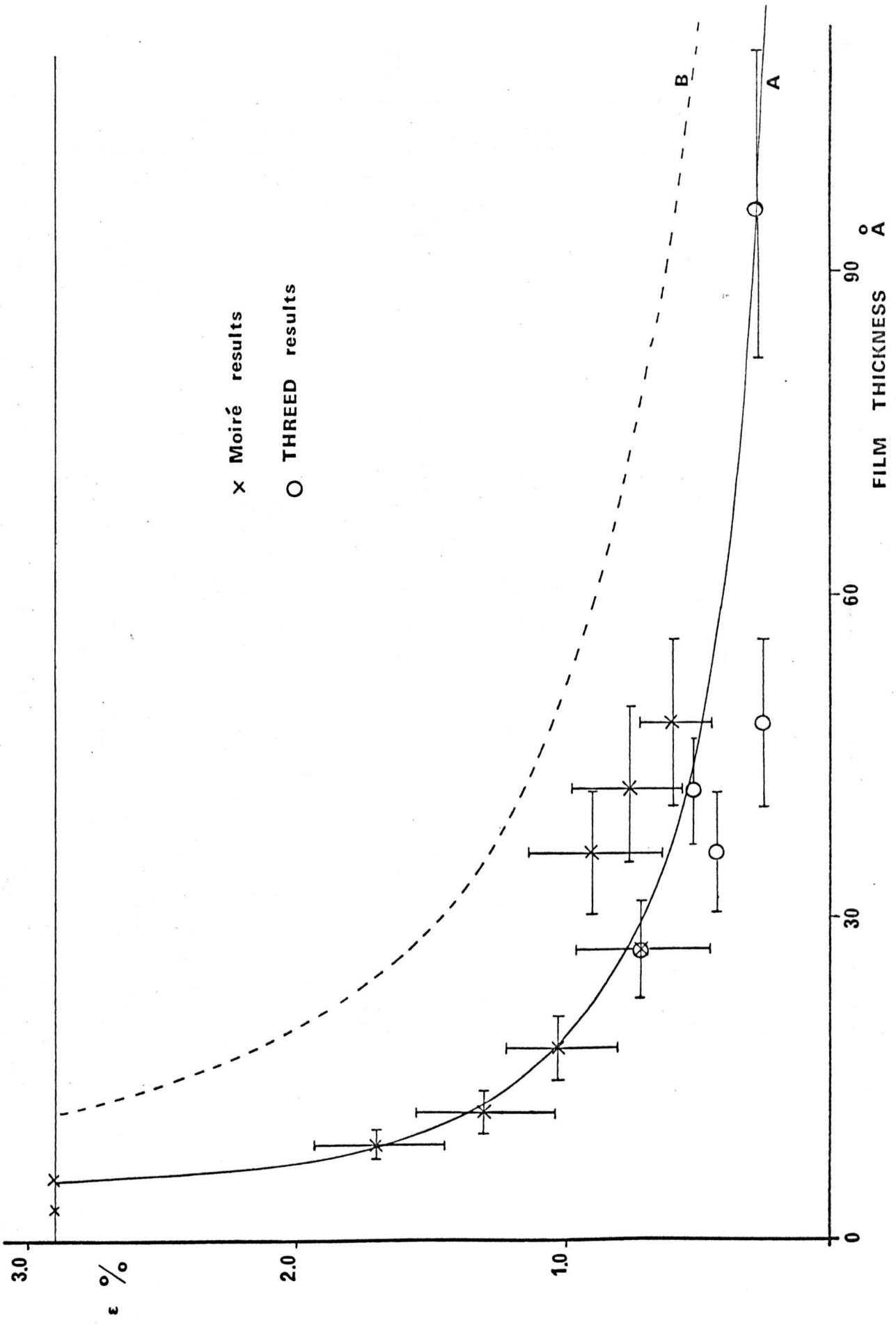

Figure 6.7 Variation of elastic strain with deposit thickness; curve A experimental results, curve B theoretical predictions.

TABLE III

Film Thickness Å	Misfit (Moiré) %	Average strain %	Misfit (THREED) %	Strain %
3		2.90		
6		2.90		
9	1.30	1.70		
12	1.60 1.66 1.52	1.31		
18	1.70 2.05	1.03		
27	2.39 2.75 2.37 2.00	0.52	2.40	0.51
36	1.99	0.91	2.47	0.43
42	2.15 2.11	0.77	2.39	0.51
48	2.3	0.6	2.64	0.26
96			2.62	0.28

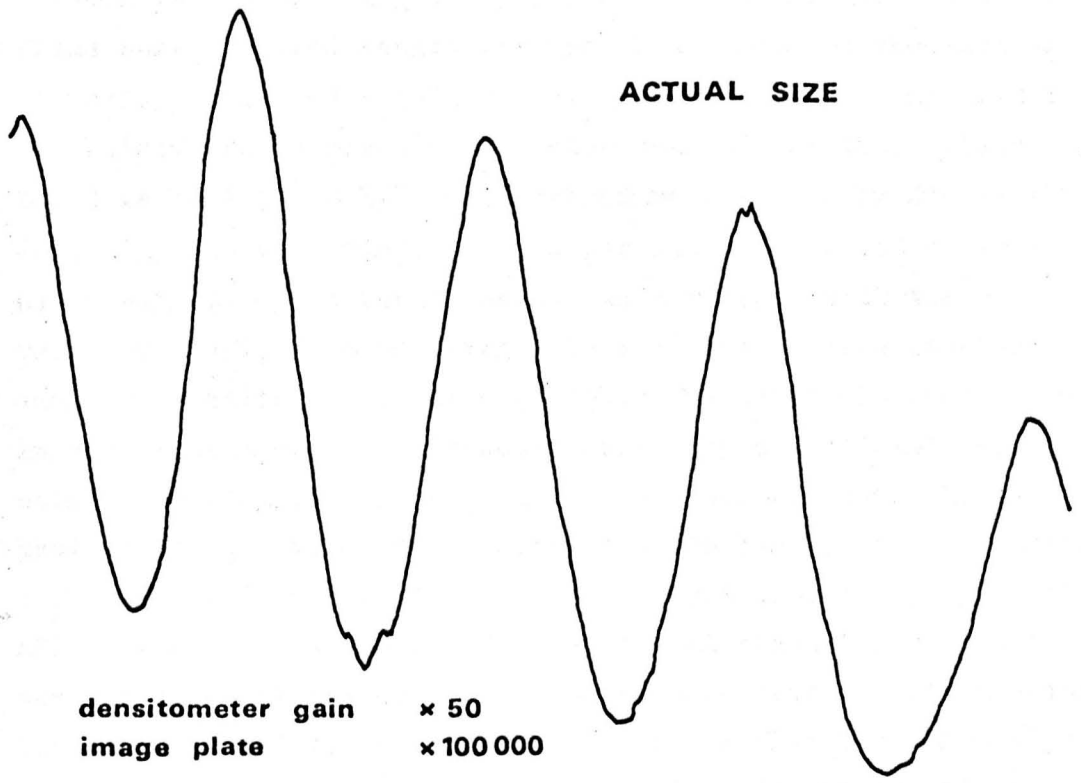

Figure 6.8 Microdensitometer trace of Moiré fringes.

The experimental results and the predictions of theory appear to be in reasonable agreement. It is however unusual for the observed strain to be lower than the theoretically predicted value. Normally the observed elastic strain is greater than expected and this has been interpreted in terms of dislocation interaction (36) or interference from oxide layers (75,107). However the theoretical treatments of pseudomorphism assume the overlayer to be of constant thickness and uniformly strained. This was not the case in the experiments reported, particularly in the early stages of film growth. Thus the values plotted as abscissae are average values of film thickness and the actual film thickness may have been considerably greater in parts. In addition, the Moiré and THREED results from the same specimen were not always in agreement, even if the large error associated with the Moiré determination is allowed for. The reason for this discrepancy is probably because the THREED method averages the misfit throughout the whole region of the specimen sampled by the electron beam, whereas the Moiré technique determines misfit in a localized area. The discrepancy does show however that the copper film was not strained uniformly, since if that were the case the THREED and Moiré results would agree within the limits of experimental error.

The value of ε_o shown was obtained from the bulk misfit between two thick, single crystal copper and nickel films. The two films were prepared separately and then placed on the same electron microscope grid and a THREED photograph obtained. The bulk misfit was determined from a microdensitometer scan of the image plate, and was found to be $2.9 \pm 0.1\%$. This procedure was used by Kuntze (107) to determine the bulk misfit for copper and nickel, and a similar result was obtained. This result is not in agreement with the calculated value of 2.59%, obtained from values of the lattice constants (146) and the equation for lattice misfit. The materials used by Kuntze and in the present work were spectroscopically pure nickel and grade I copper supplied by Johnson, Matthey and Co. Limited. Kuntze suggested that the larger value of M_o reflected the purity of the materials and the possible incorporation of residual gas into the growing film. AES of the present samples did not reveal significant impurities, with the exception of the chlorine peak already discussed in chapter 5. Nevertheless reference to Figure 4.8 shows that the largest partial pressure of gas in the system was due to hydrogen and it has been shown (147) that inclusion of hydrogen in f.c.c. metals can lead to significant changes in the lattice parameter. Thus complete occupation of the

octahedral voids in the f.c.c. structure can lead to a 5% change in the lattice parameter for copper, with proportionate changes for lower values of interstitial hydrogen occupation. If inclusion of hydrogen was occuring in the present set of experiments then the suggestion of Kuntze could explain the observed value of M_o. Reference to Figure 6.7 shows that the average film thickness at which complete pseudomorphism was lost in the present case was between 6 and 9 Å. This is in reasonable agreement with the prediction of 11 Å from theory, although it must be remembered that true layer growth did not occur in the present case. There was never any indication of thicker films showing large values of elastic strain and it seems likely that true layer by layer growth of copper on (001) nickel in UHV would yield results in close agreement with theory.

6.3.3 Gas Contamination

In the experiments described so far the nickel substrate films were kept as clean as possible, with the minimum time delay between growing the nickel film and commencing deposition of copper. In a subsequent experiment a nickel substrate crystal was prepared in an identical manner to those used previously. Following the nickel deposition the nickel-rocksalt specimen was allowed to cool to room temperature and then left in the residual vacuum (1×10^{-9} torr) for five hours. At the end of this period an Auger trace of the specimen was found to be identical to the trace obtained from freshly deposited nickel. Following this, copper was deposited for 90 minutes, corresponding to a film thickness of 54 ± 9 Å. An Auger trace taken after copper deposition revealed the 920 eV copper peak, the composite copper-nickel peaks and the small chlorine peak only. A RHEED photograph of the copper surface was obtained and then the copper-nickel specimen removed from the UHV chamber and examined in the electron microscope. Figure 6.9 shows the RHEED photograph of the copper-nickel surface and Figure 6.10 shows a micrograph of the composite copper-nickel film. The RHEED photograph shows that the surface of the copper overlayer was flat. The micrograph shows the copper overlayer to be continuous, and also reveals a crossed grid of widely spaced misfit dislocations with lines parallel to <110> type directions. A THREED photograph of the specimen did not reveal a split low order diffracted spot which means that the misfit was close to zero. Before the misfit can be calculated from the spacing of misfit dislocations it is necessary to know the magnitude of the Burgers vector in the plane of the film. The possible Burgers vectors of dislocations in an f.c.c.

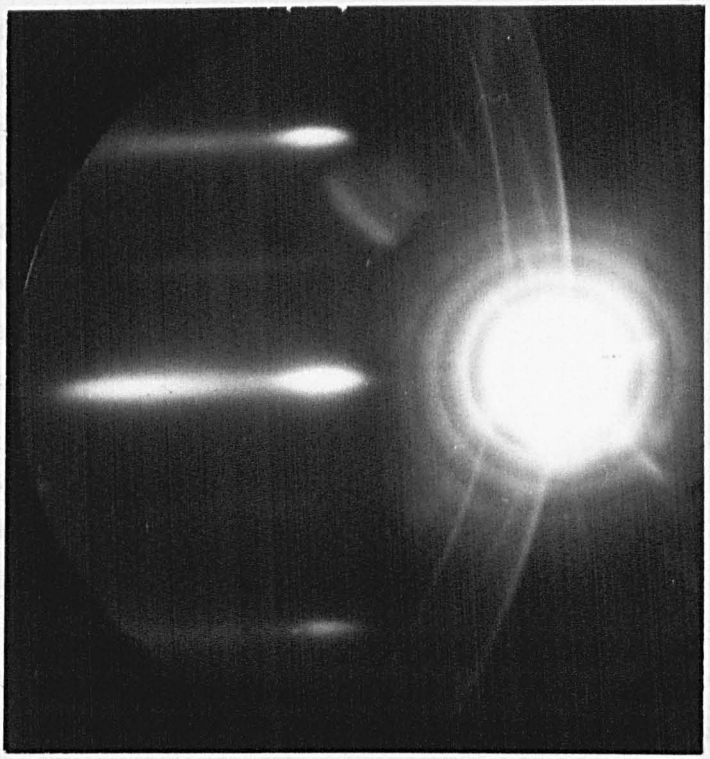

Figure 6.9 15 keV <100> RHEED photograph of 54 Å of copper on nickel.

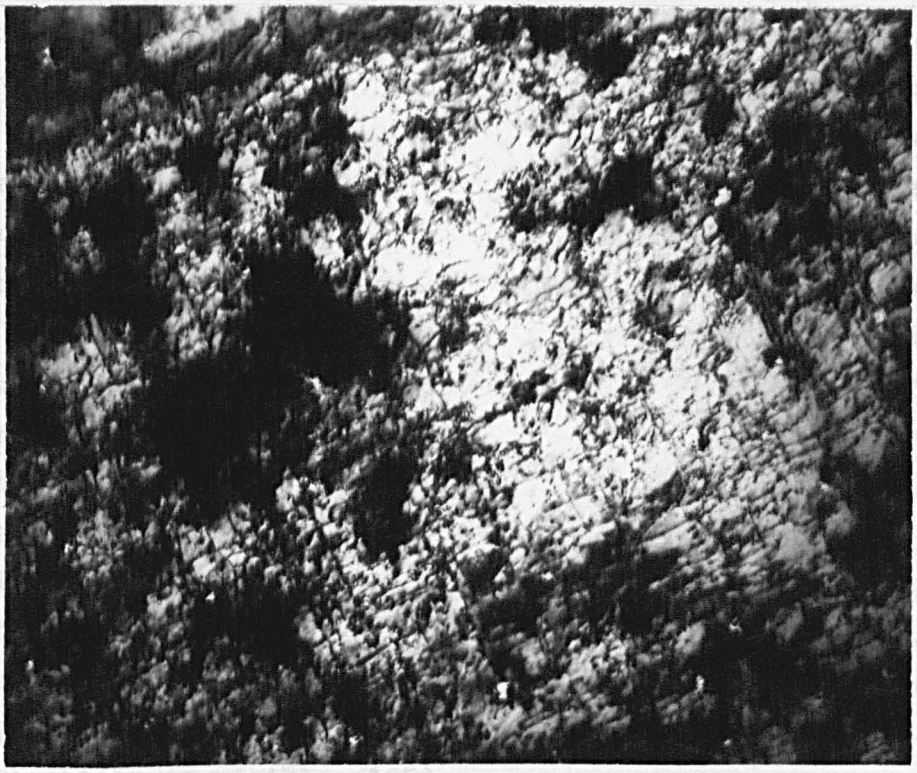

× 50,000

Figure 6.10 Electron micrograph of the copper-nickel specimen in which the substrate was exposed to the residual gas for five hours.

crystal which could accommodate misfit in an (001) plane are the pure edge type $b = \frac{1}{2}a[110]$, or the mixed type with inclined Burgers vectors, $b = \frac{1}{2}a[101]$. The Burgers vector of a dislocation may be determined by dark field microscopy (105), using the condition that the dislocation is invisible if $\underline{g}.\underline{b} = 0$, where $\underline{g}$ is the operating reciprocal lattice vector and $\underline{b}$ is the Burgers vector. In the present case, dislocations with Burgers vectors of the type $\frac{1}{2}a[110]$ would be out of contrast in $(2\bar{2}0)$ type reflections, whereas dislocations with $b = \frac{1}{2}a[101]$ would be invisible in (020) type reflections. Dark field microscopy using $(2\bar{2}0)$ type reflections revealed all the dislocations, indicating that the dislocations were not of the pure edge type. Figure 6.11a shows a region of bright field micrograph in which the lengths of dislocation circled are visible. Figure 6.11b shows a dark field (020) micrograph of the same area in which the lengths of dislocation are out of contrast. The Burgers vectors of these dislocations are therefore of the type $\frac{1}{2}a[101]$. This type of dislocation is inefficient for reducing elastic strain, it is however the type of dislocation formed by glide of existing dislocations and hence this mechanism would seem to be operating in the present case.

The dark field investigations were carried out in two ways. In the first instance the electron beam was tilted so that the diffracted beam of interest travelled down the axis of the microscope. Figure 6.11b was obtained in this manner. In the second case the electron beam was in the normal position and the specimen was tilted until dislocations were seen to go out of contrast. On reverting to the diffraction pattern the operating reflection was identified as being the most intense diffracted spot (149). Throughout the dark field investigations it was not possible to obtain diffraction conditions such that half the crossed grid of misfit dislocations became invisible. This may however have been due to the fact that edge dislocations give rise to two displacements of the crystal lattice (150), one parallel to the Burgers vector (R_1), and one normal to the slip plane (R_2). The condition $\underline{g}.\underline{b} = 0$ is satisfied when the displacement R_1 is parallel to the reflecting planes and hence does not give rise to contrast. However, the displacement R_2 may not be parallel to the reflecting planes, and if this is the case will give rise to image contrast and the dislocation is visible (105).

Having obtained the type of dislocation present the misfit was calculated from the spacing of dislocation lines. The maximum value of misfit obtained (corresponding to the minimum separation of

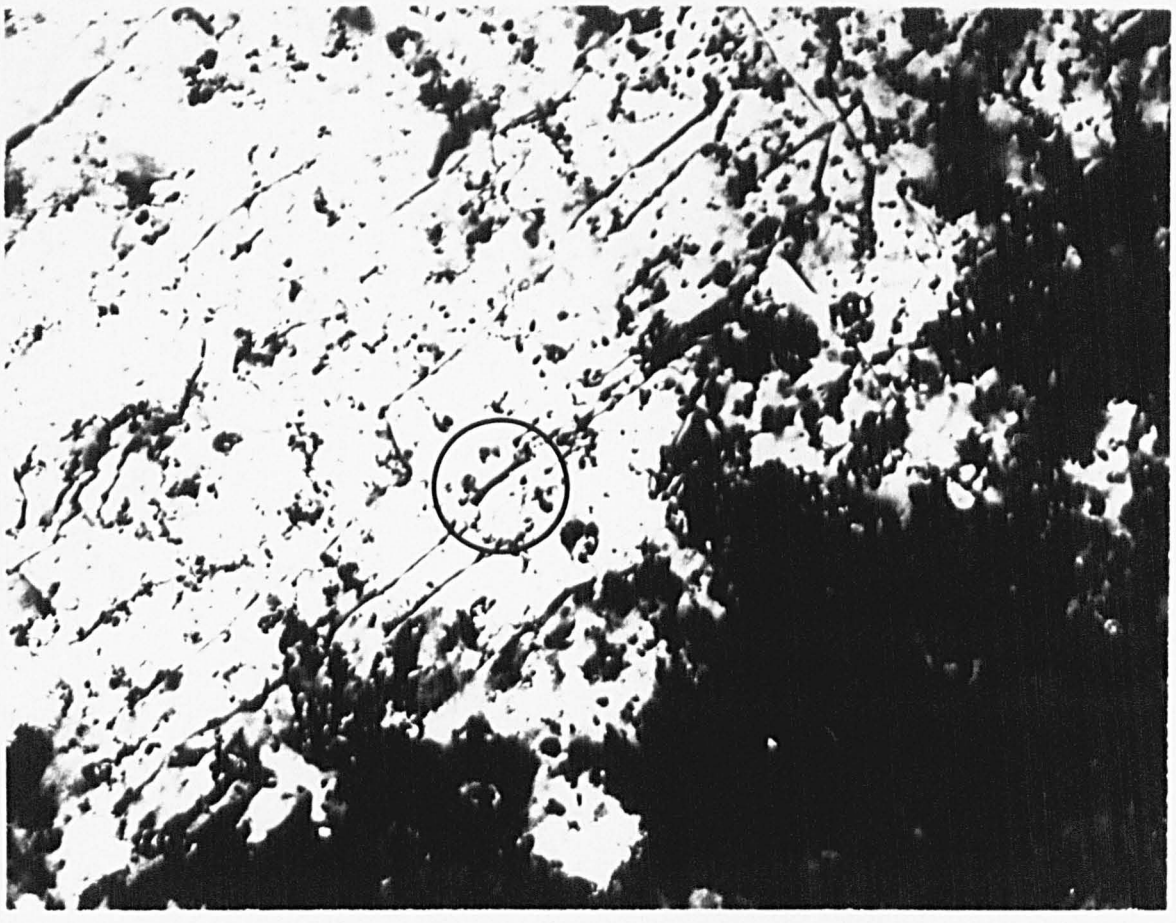

a

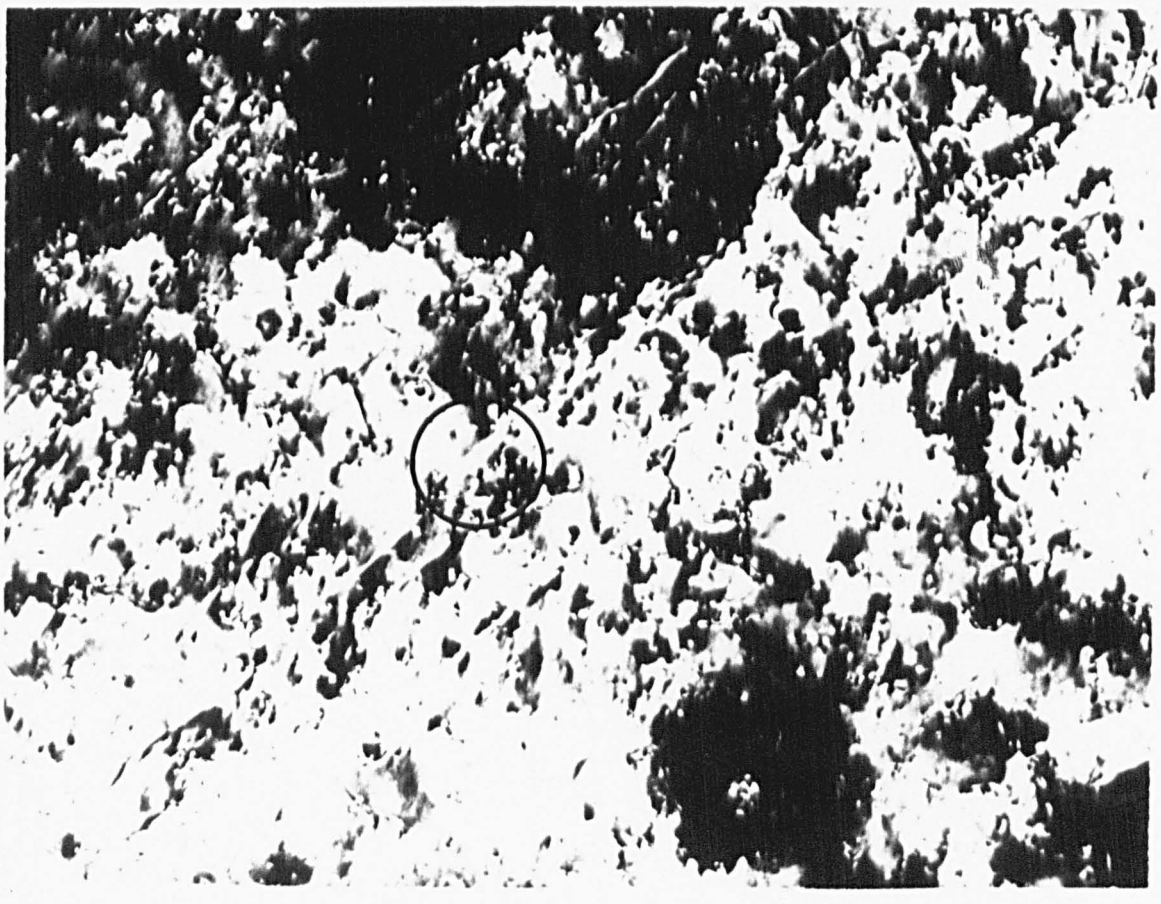

b

Figure 6.11 a) Bright field electron micrograph and
b) corresponding (020) dark field micrograph of the copper-nickel specimen (x 100,000).

dislocations) was 0.3%. The misfit in general was rather less than this, and misfits less than 0.1% were observed. The specimen therefore was very nearly completely pseudomorphic, which was not in agreement with the predictions of theory or with the previous experimental results. The only way in which the specimen differed from the previous set was that the substrate had been exposed to the residual gas for five hours prior to copper deposition.

A subsequent experiment was performed in which a more careful attempt was made to identify any surface contaminant using AES. A nickel substrate crystal was prepared in exactly the same manner as before and allowed to cool to room temperature. The crystal was then exposed to the residual gas for five hours and an Auger trace taken. Once again there was no sign of additional Auger peaks, indicating that surface contamination was below the level of detection, or that the incident electron beam was desorbing any gas present. The sensitivity of the Auger spectrometer was unknown for gases, although it had been shown capable of detecting about 0.08 of a monolayer of silver. The same nickel surface was then exposed to the residual gas for twelve hours, after which additional Auger traces were obtained. The first trace revealed a small signal at 500 volts, which is thought to be due to oxygen. A second trace taken only a few minutes after the first did not record a signal at 500 volts. Figure 6.12 shows two consecutive Auger traces taken after the nickel surface had been exposed to the residual gas for twelve hours.

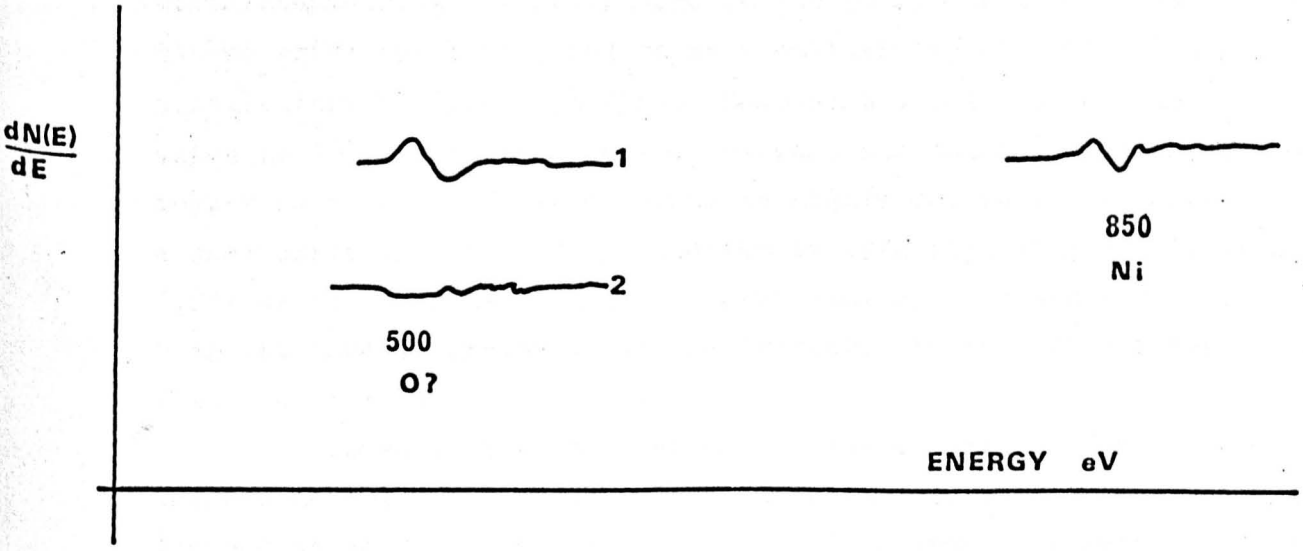

Figure 6.12 Two consecutive Auger traces of the nickel surface after twelve hours under vacuum.

The traces were taken using low amplifier gain to enable maximum scan rates to be achieved. The traces shown were taken within one minute of each other, and the size of the nickel peak obtained from a separate trace is shown for comparison. The experiment was repeated except that the energy of the incident electron beam for AES was reduced to 1 keV. The same result was obtained, i.e. the initial trace revealed a small signal at 500 volts, but later traces did not. This result suggests that oxygen was adsorbed on the nickel surface but desorbed by the electron beam. The residual gas composition during these experiments was similar to that shown in Figure 4.8, the partial pressure of oxygen being approximately 10^{-12} torr. The desorption of gases by the incident electron beam has been observed by Tracy and Palmberg (151). In their case carbon monoxide adsorbed on the surface of palladium was so rapidly removed that they were unable to detect its presence by AES. LEED of the nickel surfaces gave the 1 x 1 pattern identical to that obtained from freshly deposited nickel, with one exception. In the case of a specimen left under vacuum for twelve hours a LEED observation at 122 eV showed slight evidence of fractional order spots. The intensity of these spots was very weak and it was not possible to photograph them. In addition LEED observations were difficult because of the stray magnetic field from the ion pump, which at the time was inadequately screened.

As a result of the inability to detect adsorbed gases with AES and the experimental difficulty associated with LEED, the gas contamination experiments were not pursued further. Nevertheless it is worth considering the literature on the (001) surface of the nickel. Nickel oxide has been found to grow epitaxially on (001) nickel in parallel orientation (153,154). However the lattice constant of nickel oxide is 18% larger than that of nickel, and hence pseudomorphism of copper on a layer of nickel oxide is highly unlikely. In addition nickel oxide may be readily detected by LEED (153,154) and despite the difficulties with LEED in the present case some evidence should have been obtained if nickel oxide was present. It therefore seems unlikely that the true oxide was formed.

However, LEED observations of the oxidation of a clean nickel surface have shown that an intermediate structure is formed which is thought to be Ni_3O (155,156,157,159). A schematic diagram of the (001) face of the Ni_3O is shown in Figure 6.13.

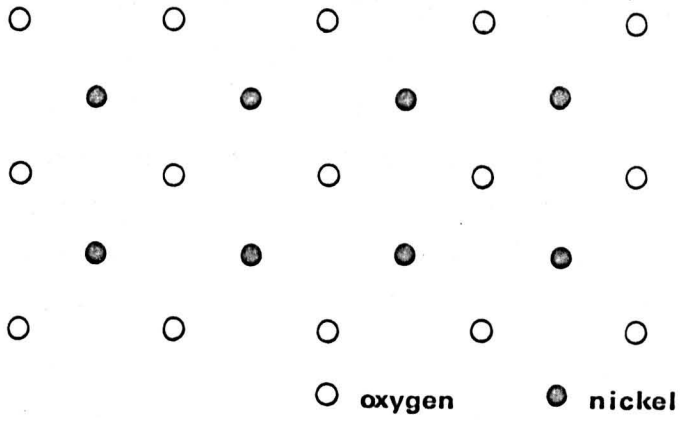

Figure 6.13 The (001) face of Ni_3O (from Farnsworth 159).

There are several important points about the structure of Ni_3O, the first being that Farnsworth (159) has observed an expansion of the nickel lattice of between 2 and 5% on the formation of Ni_3O. Such an expansion could well result in there being near zero misfit between the substrate and the deposited copper, which would considerably affect pseudomorphism. Secondly the displaced nickel atoms are thought to form a layer on the surface of the sub-oxide (159) and hence the deposited copper may condense on a nickel surface, with the oxide layer underneath. The trapped layer of oxide could impede the motion of dislocations at the interface and hence an increase in critical thickness would be observed. Finally the sub-oxide was found to be extremely stable (156,157) and was not decomposed by heating to 850°C.

The relevant literature on adsorption of other gases on nickel surfaces shows that nitrogen (160), carbon monoxide (156) and water vapour (161) are not readily adsorbed. Carbon dioxide is adsorbed at room temperature (162) but is readily desorbed by heating (163). Hence the two possibilities in the present case appear to be formation of the sub-oxide or the adsorption of carbon dioxide. If adsorption of carbon dioxide had been occuring then the relative ease with which it can be desorbed could explain the fact that there was never any sign of a carbon Auger peak at 270 eV. Because of the difficulty of observing adsorbed gas using AES it was not possible to decide which of the two possibilities was occuring. However there was evidence of oxygen adsorption whereas a carbon Auger peak was never observed and hence it seems likely that some oxygen adsorption was occuring, presumably resulting in formation of the sub-oxide.

It was shown by Kuntze (107) that an increased partial pressure of hydrogen could lead to a higher degree of pseudomorphism, probably as a result of inclusion of the gas. In the present case the nickel and copper depositions were performed under similar conditions, and although inclusion of gas may have occured, it could not have been the cause of the increase in elastic strain. The presence of chlorine on the nickel could not have caused the increase in elastic strain since, as with the silver experiment, the amount of chlorine detected was substantially constant throughout all the experiments.

The reduction of elastic strain in the present system appears to be effected by extension of already existing dislocations. This leads to misfit dislocations with inclined Burgers vectors. The presence of oxygen at the interface might impede the motion of these dislocations in the way that solute atoms cause hardening in crystals (56,150). As a result the equilibrium length of misfit dislocation would not be formed and a larger elastic strain observed in the overgrowth. This conjecture is supported by observations of cobalt on copper made by Federenko and Vincent (75), in which abnormally large strains were interpreted in terms of interference from an oxide layer between substrate and overgrowth. This result also supports the hypothesis of interference from oxide layers put forward by Kuntze (107) to explain the abnormally large elastic strain observed for deposits of nickel on copper.

6.4 Experimental Procedure - Depositions at 300°C

6.4.1 Preparation of the Substrate

The nickel substrates were prepared in exactly the same way as in previous experiments, with the exception that following deposition of the nickel the nickel-rocksalt specimen was heated to $300 \pm 20^{\circ}C$. An Auger trace of the hot nickel is shown in Figure 6.14. The chlorine peak is no longer evident but a peak at about 150 volts has appeared. This is probably the $L_3M_{23}M_{23}$ sulphur peak and could be a result of diffusion of sulphur from the bulk of the nickel.

6.4.2 Deposition of Copper

In the first set of experiments copper was deposited from the Knudsen source at normal incidence and in stages. Following each deposition stage an Auger trace of the copper-nickel specimen was obtained, deposition being continued up to the point where the Auger signal from the deposit had reached a constant value. As an additional part of the Auger investigation of the growth of copper on hot nickel, the time dependence of the Auger traces following deposition was studied.

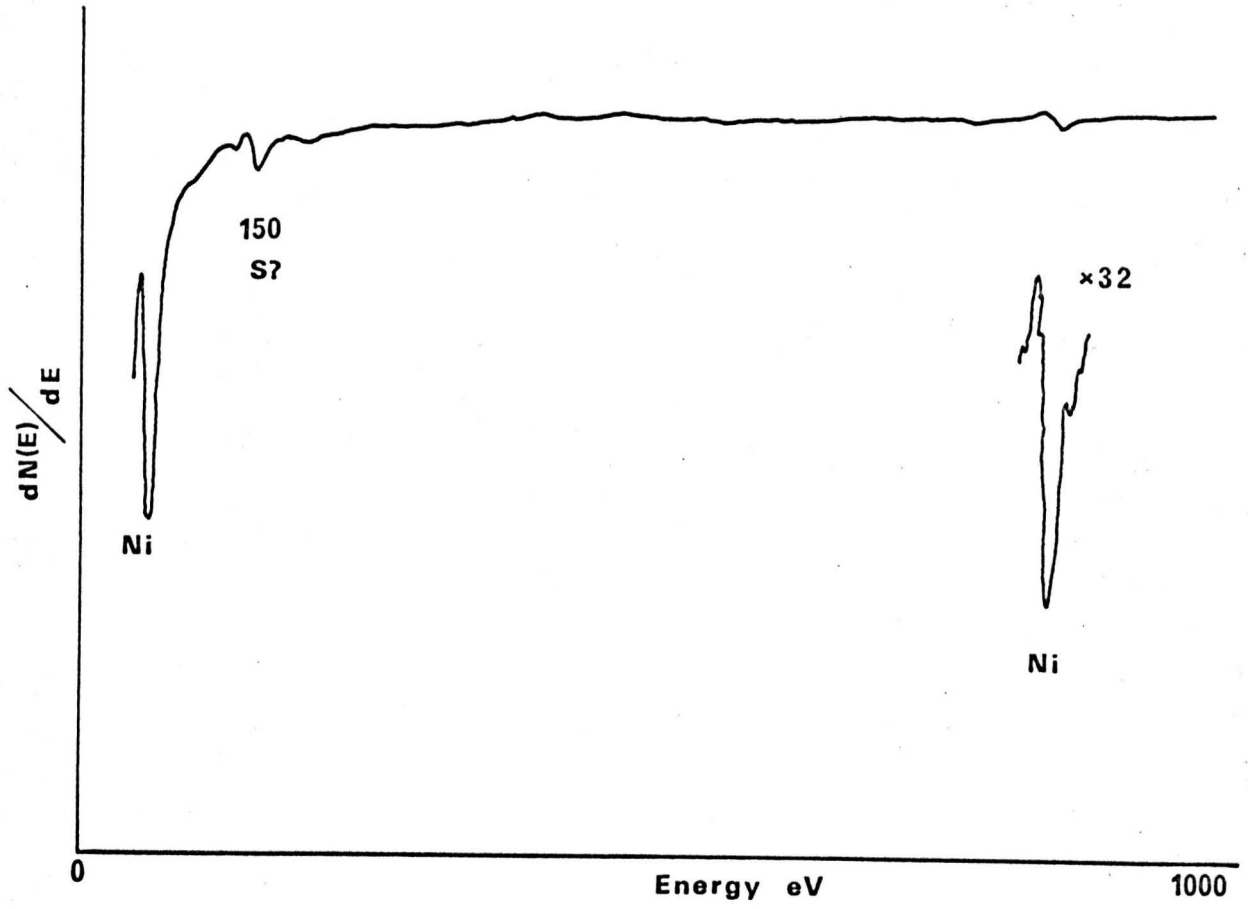

Figure 6.14 An Auger trace of a nickel substrate at 300°C.

In a second set of experiments, nickel substrates were prepared in an identical manner and following preparation were heated to 300°C. Various thicknesses of copper were then deposited on the nickel, after which the copper-nickel specimen was allowed to cool to room temperature. The samples were then removed from the UHV chamber and transferred to the electron microscope for misfit measurements.

6.5 Experimental Results and Discussion

6.5.1 Auger Investigation

The growth of the 920 eV copper Auger signal as a function of deposition time is shown in Figure 6.15. The dashed line on Figure 6.15 is the Auger signal as a function of deposition time for copper on nickel at room temperature. Comparison of the two curves shows that throughout deposition the signal from the copper deposited on hot nickel was smaller than that observed for depositions at room temperature. The Auger signal from the nickel substrate was estimated in the manner described in section 6.2.1 and is shown in Figure 6.16. Again the corresponding signal for deposition at room temperature is

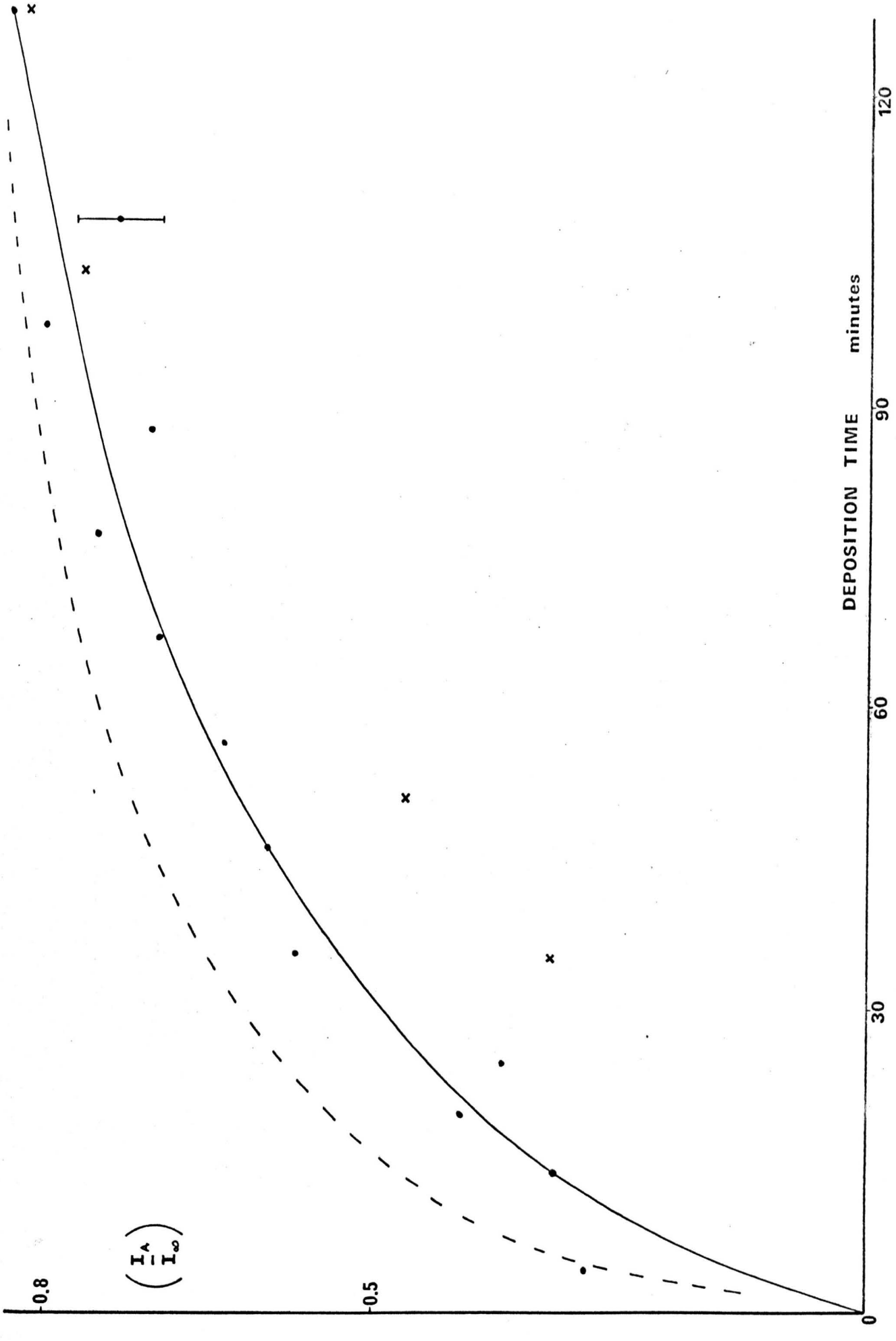

Figure 6.15 ____ Growth of the 920 eV copper signal for depositions at 300°C

_ _ _ Growth of the 920 eV copper signal for depositions at room temperature

x Coverage data for the copper from electron microscopy

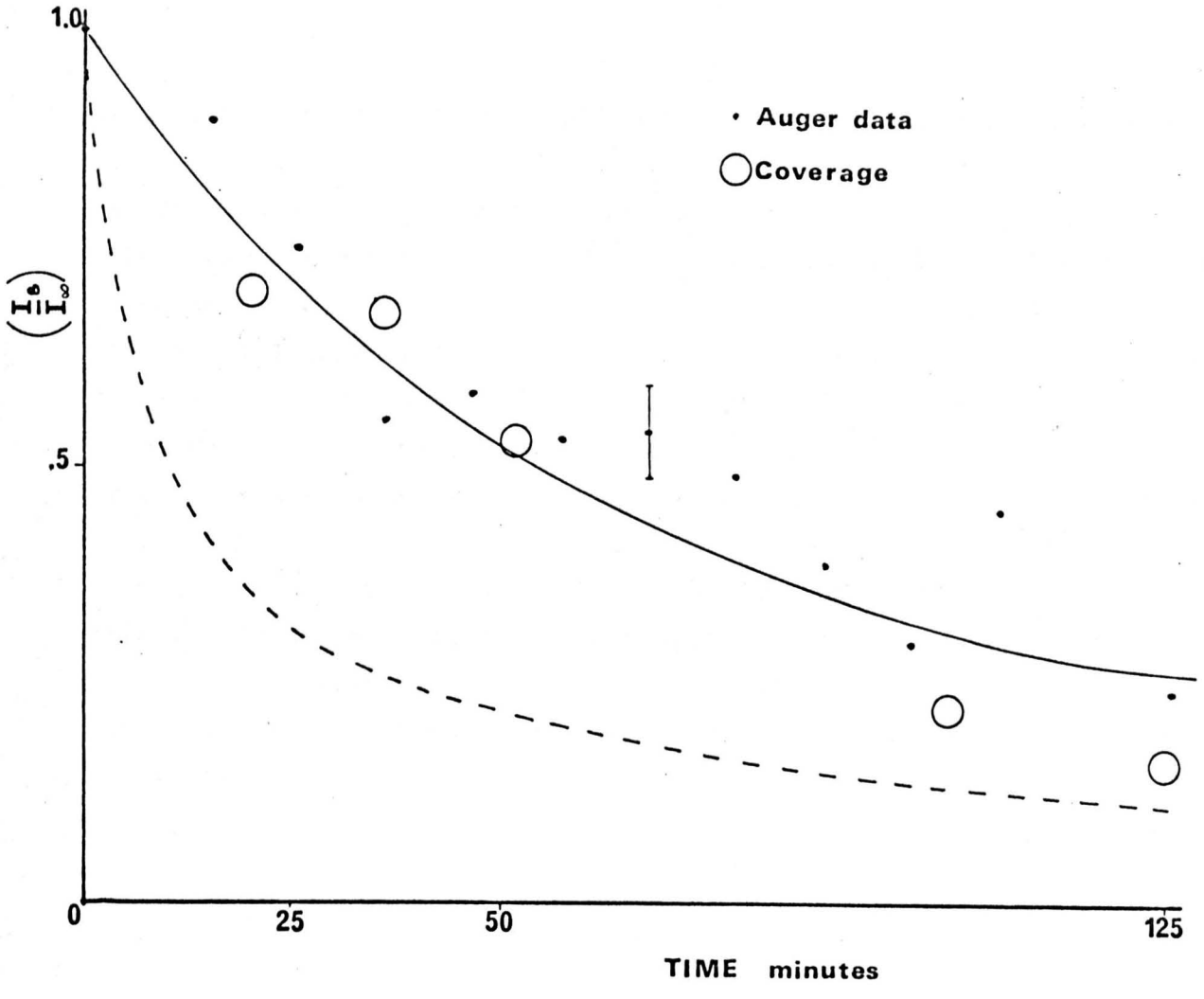

Figure 6.16 Decay of the 850 eV signal with deposition time
——— at 300°C _ _ _ _ at room temperature
○ coverage data from electron microscopy

shown as a dashed line. The decay of the substrate signal for deposition at 300°C can be seen to be somewhat slower than for the room temperature depositions.

Possible events which could give rise to the observed change in the time dependence of the Auger signals are:

i) a different growth morphology

ii) alloying between the copper and nickel films.

The Auger results are consistent with island growth of the overlayer as distinct from layer by layer growth, since as described in chapter 3, island growth should lead to a less rapid time dependence of both deposit and substrate Auger signals. Island growth is also consistent with the results obtained by Kuntze (107) and Matthews (85) for deposition of copper on nickel at elevated temperatures. Confirmation of island growth was obtained from electron microscopy of similar specimens, to be described in the next section.

The possibility of alloying still remains, since alloying across the interface between the nickel substrate and the copper islands is unlikely to be detected by electron microscopy. A separate experiment

was performed using AES in an attempt to decide whether alloying was occuring. In the experiment, 12 Å of copper was deposited on a nickel substrate at 300°C. An Auger trace was taken and then the copper-nickel specimen maintained at 300°C for ten hours. At the end of this period the Auger signal from the copper had decreased by about 30%, whereas the signal from the nickel had increased by nearly 60%. However, the Auger signals from thick copper films obtained at the end of the Auger signal versus deposition time experiments had not shown any significant change with time. The change in strength of the Auger signals for the thin copper deposit may have been due to alloying, or could have been a result of surface mobility and rearrangement of the copper. It was not possible to decide which of the above alternatives was in fact occuring. The fact that thicker deposits did not show this change indicates that alloying, if occuring, must be limited to a few layers only.

6.5.2 Electron Microscopy

a) General

Micrographs of typical areas of various thicknesses of copper deposited on clean nickel substrates at 300°C are shown in Figure 6.17. The shape of the islands is particularly striking, most islands having very straight edges. Even when coalescence of the islands begins to occur, as in Figure 6.17c, the islands still retain their regular shape. Superposition of the diffraction pattern on a micrograph showed the edges of the islands to be parallel to <100> type directions.

The good contrast of most of the copper islands in Figure 6.17 indicates that the islands are fairly thick. In fact the average height of the islands can be calculated from the fractional coverage and the mean deposit thickness. For the micrographs shown, the average height of the islands is in the region of 70 - 120 Å. This is relevant to the results of the Auger investigation, since as has been shown in chapter 3, if the thickness of the islands is substantially greater than the mean escape depth for the relevant Auger electrons, the normalised Auger signal from the deposit should equal the fractional coverage θ. Similarly the normalised Auger signal from the substrate should equal $(1 - \theta)$. Figure 6.15 also shows the calculated value of the Auger current using values of θ obtained from electron microscopy, and assuming the thickness of the islands to be considerably greater than the mean escape depth. The two values for high coverage are seen to be in good agreement with the results of the AES experiment. The results for lower coverage are not in such good agreement and in fact are on the wrong side of the

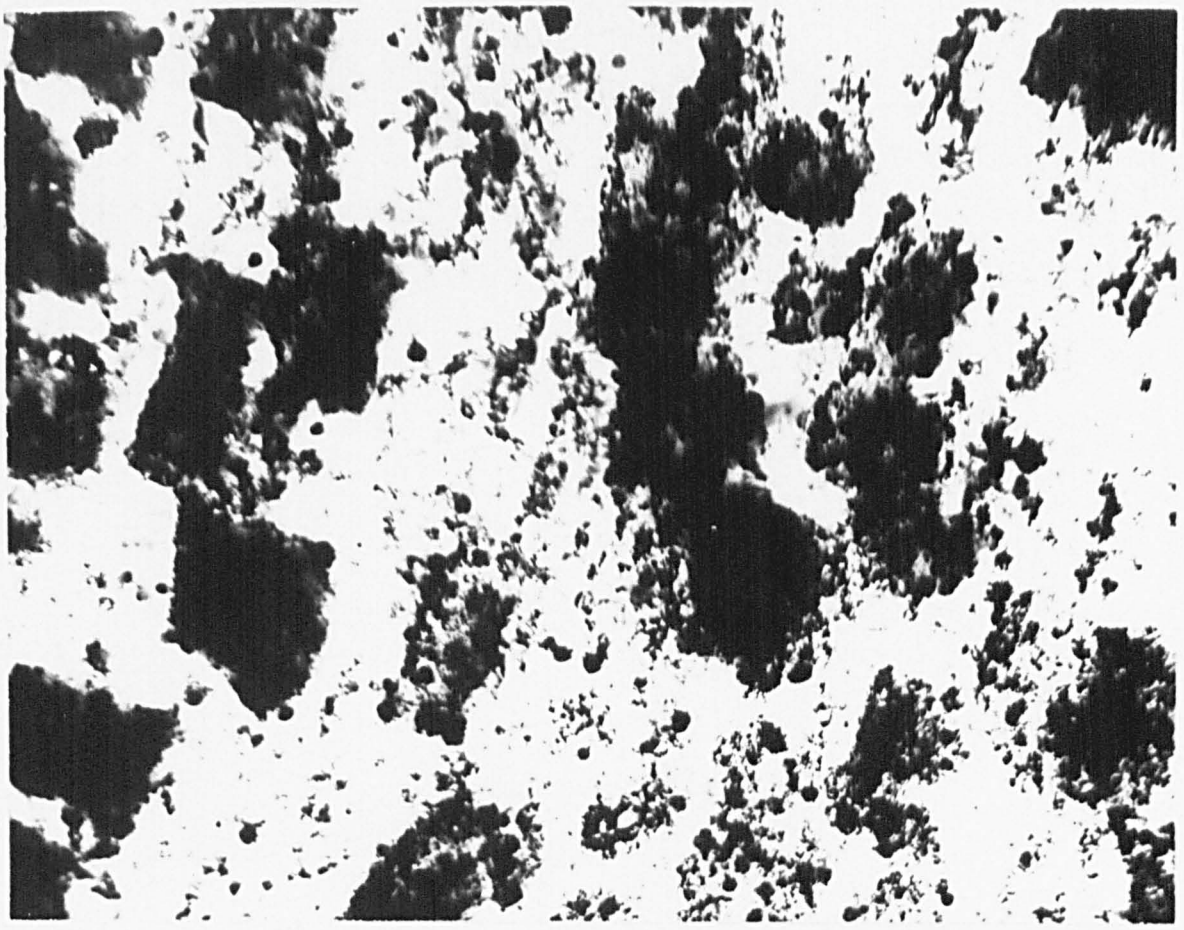

a

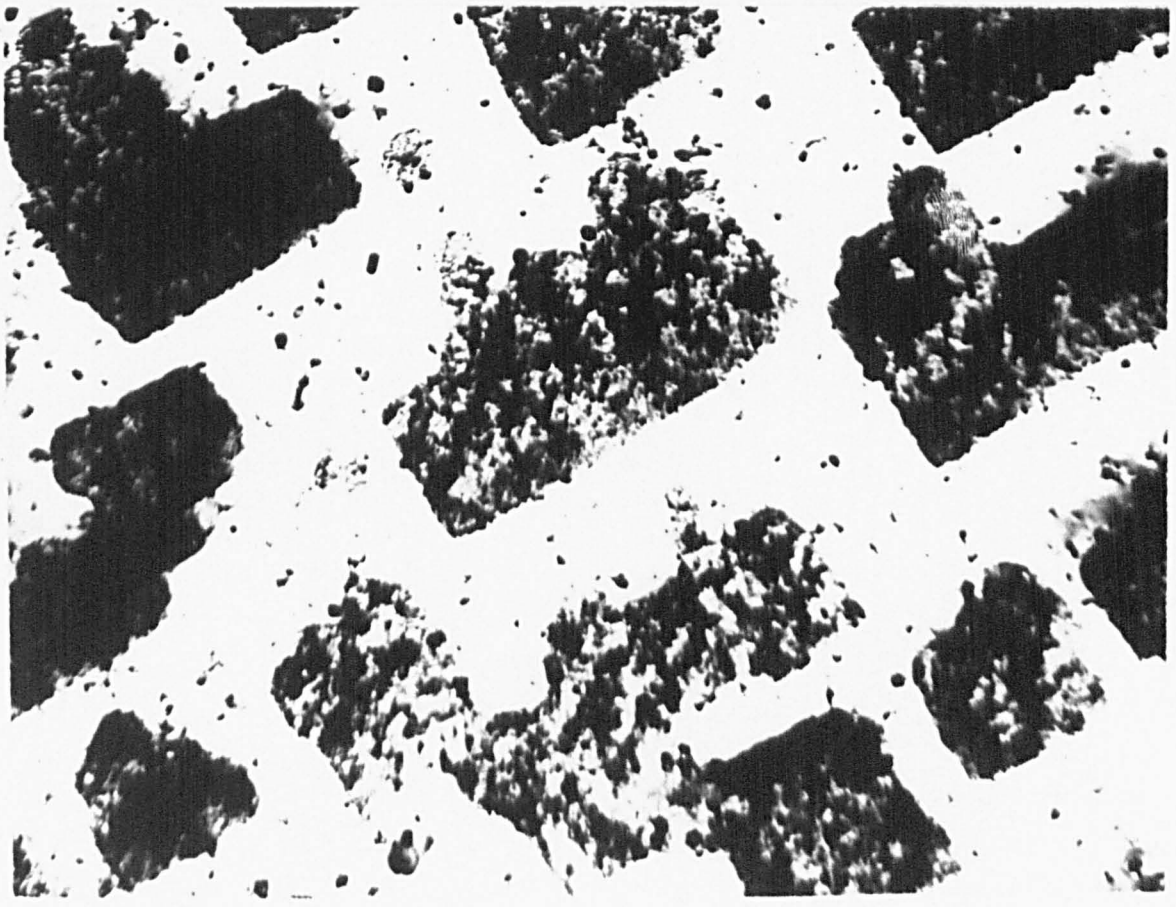

b

Figure 6.17 Electron micrographs of various amounts of copper deposited on nickel at 300°C (x 30,000)
a) 35 minutes - 21 Å b) 50 minutes - 30 Å

c

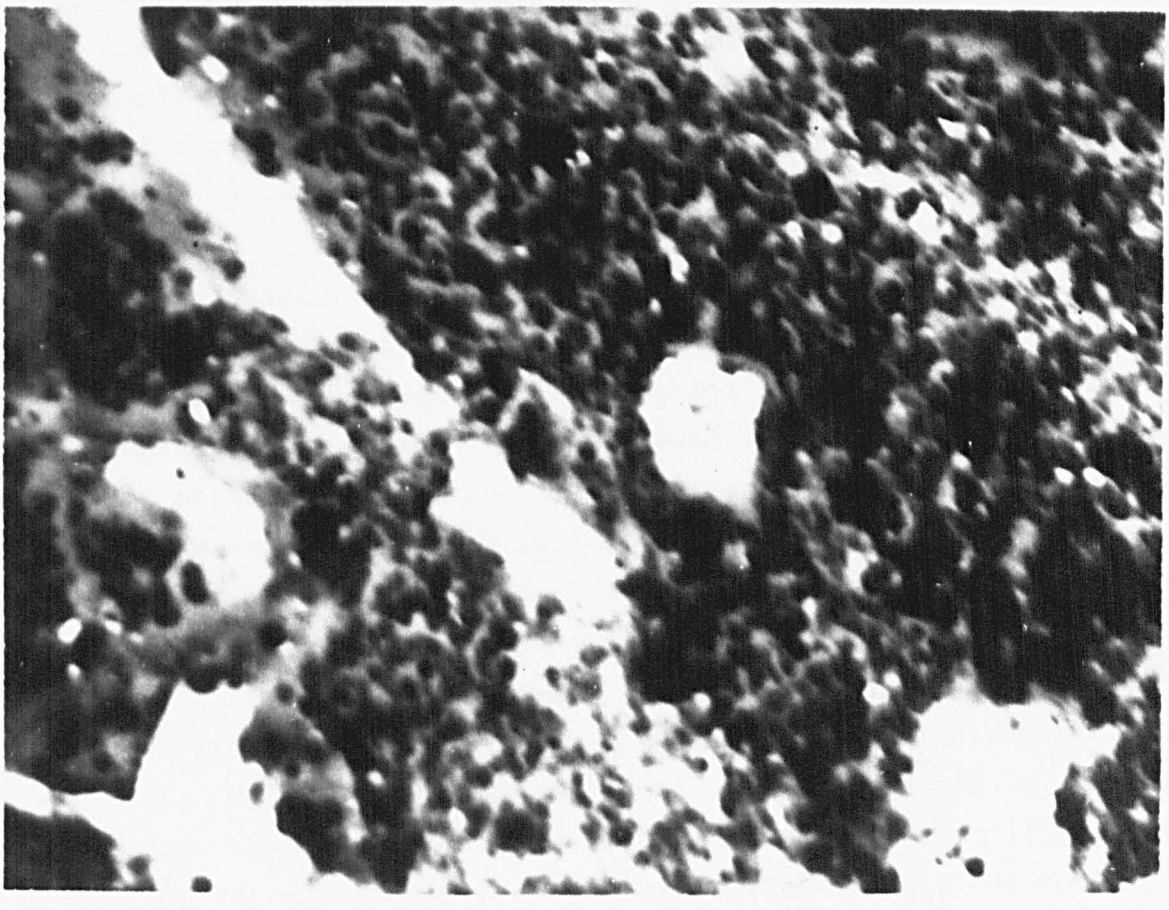

d

c) 100 minutes - 60 Å d) 125 minutes - 75 Å

Auger signal versus time curve. For low island thicknesses the normalised Auger signal is given by $I = \theta (1 - \exp - \frac{\bar{h}}{\bar{x}_o})$, and hence the Auger signal should always underestimate the coverage. The discrepancy in the present case is probably due to deposited material between the islands which was not detected by electron microscopy. Hence the discrepancy in Figure 6.15 is most likely due to an underestimate of coverage θ, rather than a significantly oversize Auger signal. The corresponding calculated values of $(1 - \theta)$ against t are plotted on Figure 6.16 and are seen to be in reasonable agreement with the Auger data for decay of the substrate signal.

The results of electron microscopy described above, when coupled with the AES results, do seem to show that AES could be a useful calibration tool over a limited range for deposits which nucleate. Until more is known about nucleation density and island size and shape for deposits which nucleate, it is not possible to determine the amount of material present from the strength of the Auger signal. Nevertheless it does seem to be possible to determine the fractional coverage of the deposit, particularly in the region approaching complete coverage. The discrepancy between the Auger results and fractional coverage in the early stages is thought to be primarily a result of material between the islands which was not detected by electron microscopy. As coverage increases the material between the islands becomes less significant and agreement is considerably better.

b) Misfit and Pseudomorphism

The micrographs of Figure 6.17 show that a large number of the copper islands were regularly shaped, and hence were suitable as an experimental test of the theory proposed by Matthews (85) relating elastic strain to island size for rectangular islands. The THREED method was unsuitable for misfit measurements because it averages the misfit over the whole area of specimen sampled by the electron beam. In the investigation described here methods were required for determining the misfit of individual islands. Misfit determinations by spacing of Moiré fringes and from the separation of misfit dislocations were employed. As in previous results, the spacing of Moiré fringes was determined from a microdensitometer trace of the image plate. This technique was also found to be useful for determining the spacing between dislocation lines, since magnifications of up to x 50 were available. However, before a value of the misfit could be obtained from dislocation spacing it was necessary to determine the Burgers vector of the dislocations.

A series of dark field investigations was carried out using both the beam tilting technique and the specimen tilt stage. With the tilt stage it was possible to get some dislocations out of contrast when (020) type reflections were operating. As has already been described in section 6.3.2 this means that the Burgers vectors are of the inclined $\frac{1}{2}a[101]$ type. It was not possible with either technique to get dislocations out of contrast when (220) type reflections were operating. Electron micrographs showed the dislocations to have formed a crossed grid at right angles, and superposition of the diffraction pattern revealed the dislocations to be along $\langle 110 \rangle$ type directions. If the dislocations were of pure edge type, then using the criterion $\underline{g}.\underline{b} = 0$, possible combinations of Burgers vectors cannot give rise to both sets of dislocations being visible in (220) type reflections. The dark field results therefore suggest that pure edge type dislocations were not present. However comparison of misfit results from Moiré fringes and dislocation spacing, in islands where both could be seen, were only in agreement in some instances if pure edge dislocations were assumed. It therefore seems likely that both types of dislocation were present and the failure to obtain invisibility for dislocations under (220) type reflections was a result of the displacement R_2 described in section 6.3.2.

The presence of mixed dislocations in islands is interesting, since this type of dislocation is inefficient for accommodating misfit. It is normally assumed (57,152) that pure edge dislocations would be formed, because it is relatively easy to introduce dislocations at the edge of a growing island. However mixed dislocations have been observed by Jesser and Matthews (77) in island deposits of iron on copper and a formation mechanism involving extension of existing dislocations was proposed, operating in a similar fashion to the mechanism for producing dislocations in a continuous film.

A plot of measured elastic strain against mean island length is shown in Figure 6.18. The results were obtained using islands which were approximately square since these correspond to the theoretical treatment given by Matthews. The results shown are in agreement with similar results obtained by Kuntze (107) for copper on nickel at 360°C. It can be seen that the island size at which a particular elastic strain is observed is much larger than the thickness at which a continuous film shows the same strain.

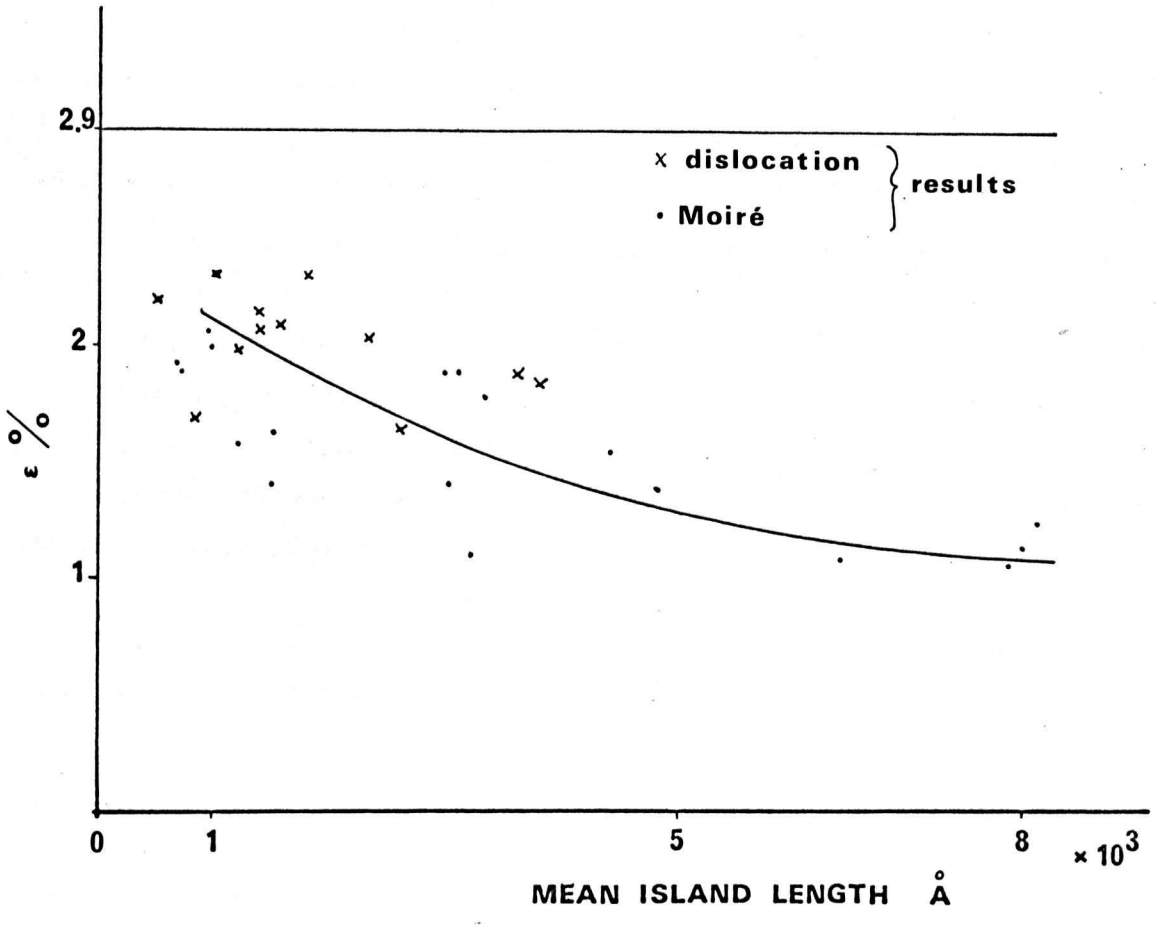

Figure 6.18 Measured values of elastic strain against mean island length for copper islands on nickel.

Before considering individual islands it is worthwhile to take an overall look at Figure 6.18 and compare the shape of the curve with theoretical predictions. As described in chapter 2, the theoretical treatments of island growth can be divided into two classes, the first applying to hemispherical islands and using the results of the equilibrium theories (55,122), and the second considering the motion of individual dislocations (85). The dislocation theory of Matthews refers to deposits in which the islands are rectangular, and judging from the micrographs of Figure 6.17 this would appear to be more applicable to the present case. Matthews does however give an equation for the variation of elastic strain with island size which neglects the discrete nature of the relaxation of strain. The resulting expression $\varepsilon = \frac{b(1 - \nu)}{4 p X}$, in which b is the magnitude of the Burgers vector, ν is Poisson's ratio, X is the island dimension and p is the ratio of island height to island width, can be compared directly with Figure 6.18. In the original paper Matthews took $p = \frac{1}{3}$, $\nu = \frac{1}{3}$ and $b = 2.5$ Å. If this is done in the present case the resulting graph of

ε against X is in total disagreement with the experimental observations, predicting a strain of less than 0.4% for X = 1000 Å. The value of p used was presumably an arbitrary choice and hence it is worthwhile trying to fit the equation above to the experimental results by adjusting the value of p. If this is done a value of $p \sim \frac{1}{50}$ gives a reasonable fit for X<1500 Å, whilst progressively smaller values of p are necessary as X increases beyond 2000 Å. Adjustment of the parameter p might at first sight seem a dubious procedure since, as the strain ε is inversely proportional to p, suitable values of p could be found to fit any observed value of ε. However an independent estimate of the average value of p can be obtained from electron microscopy and these results will be discussed later.

Final reference to Figure 6.18 reveals considerable scatter of the experimental results. In many cases islands of approximately the same size show a large range of elastic strain. This effect was investigated extensively by Vincent (90) and the large scatter attributed to the discrete nature of relaxation of strain.

The theoretical treatment of elastic strain with island size, due to Matthews and described in chapter 2, was applied to the case of small rectangular islands of copper on nickel. Figure 2.6 shows the island size at which the first and subsequent misfit dislocations should be introduced. An attempt was made to obtain micrographs of small copper islands which contained few misfit dislocations, so that a comparison with theory could be made.

Figure 6.19 shows four micrographs of various sizes of copper islands containing misfit dislocations. In all cases the number of dislocations present for a given island size was considerably less than that predicted by Matthews. The equation used for these predictions, (equation 2.4.8) does however contain the factor p which, using the value assumed by Matthews has already been seen to give results not in agreement with experiment. Equation 2.4.8 was therefore used to obtain a value of p which would fit the islands seen in electron microscopy. Table IV shows the values obtained for island size, number of misfit dislocations and the corresponding value of p. The results include observations taken from micrographs obtained by Kuntze (107) and a result quoted by Matthews (85). Once again the values of p required to make theory fit the experimental results are significantly different to the values assumed by Matthews.

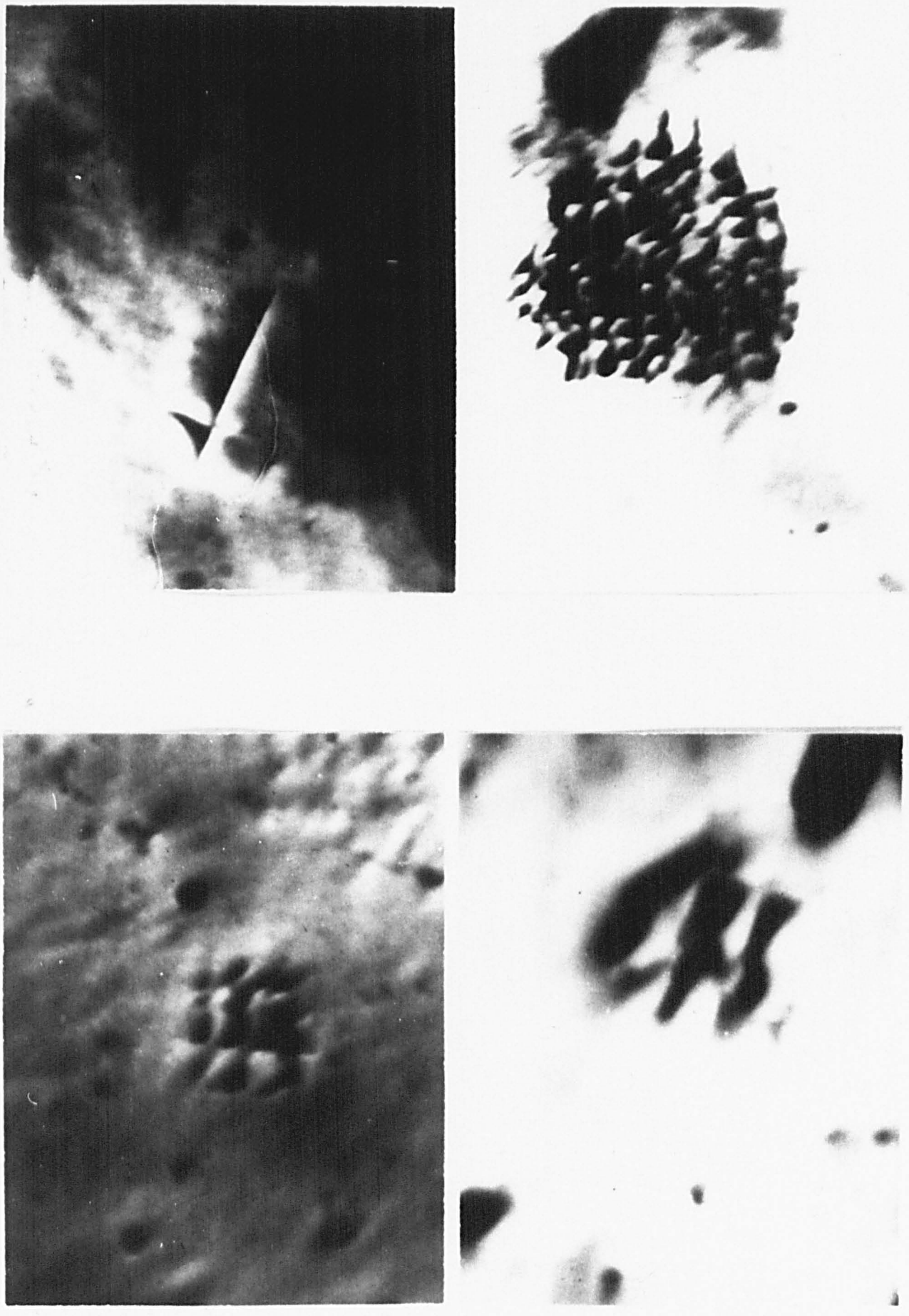

Figure 6.19 Electron micrographs of small islands of copper on nickel (x 300,000).

TABLE IV

Island Width / Å	Number of Dislocations	p
700	7	1/43
840	6	1/47
1000	4	1/67
1000	2	1/78
1200	5	1/77
1500	16	1/60
1800	11	1/120
2600	35	1/140
* 500	5	1/31
1340	10	1/88
1500	11	1/98
2320	21	1/145
# 350	1	1/27

* Results taken from reference (107)
# Result taken from reference (85)

An independent determination of p for the copper islands was therefore required. The mean value of p for islands like those shown in Figures 6.17a and b can be found quite simply once the coverage θ has been determined. If the number of islands per unit area is N and the average island width $\bar{X}$, then $N\bar{X}^2 = \theta$, hence $\bar{X}$ can be found. The average height of the islands $h = \frac{t}{\theta}$, where t is the mean deposit thickness, and hence $\bar{p} = \frac{h}{\bar{X}}$. This procedure cannot be used once coalescence has started since N becomes uncertain. Three values obtained for p were 1/118, 1/96 and 1/90, for islands of average dimensions 8300, 6600 and 7200 Å respectively. The island dimensions are seen to be considerably greater than those listed in Table IV, but the resulting values of p are of the same order of magnitude.

The results show that the island dimensions given by Matthews at which misfit dislocations should be introduced are not in agreement with experiment in the present case. Much better agreement can be obtained if smaller values of the factor p are used, and the evidence

from electron microscopy indicates that such values of p are more realistic in the present case. In fact the evidence from electron microscopy indicates that once the islands are of such a size as to be easily visible in the electron microscope their height does not increase very rapidly. Matthews introduced the factor p to take into account the increase in elastic strain energy of an island of length X as the height of the island increased. In the present case it would appear that this additional complication is unwarranted and better results are obtained by assuming the island height to be approximately constant. It is interesting that the experimental result quoted by Matthews for the introduction of the first dislocation in a copper island can only be reconciled with theory if p = 1/27 is assumed.

Finally it is worth noting that the critical radius for complete pseudomorphism of hemispherical copper islands on nickel calculated by Jesser and Kuhlmann-Wilsdorf (55) is 205 Å. If the circular base of such an island is approximated to a square, the island dimension becomes 410 Å. This is of the same order as the results for smaller islands shown in Table IV.

6.6 Summary

Copper was deposited on single crystal (001) faces of nickel at both room temperature and 300°C. The time dependence of the relevant Auger signals was monitored as deposition proceeded.

In the case of deposition at room temperature the copper did not build up in layer by layer fashion and a structure intermediate between true layer growth and isolated islands was thought to exist. Thus in the early stages of deposition the copper formed fairly flat islands, with a relatively high coverage. As deposition proceeded the coverage increased, until a situation very close to layer growth existed. The absence of a readily identifiable low energy Auger signal from the substrate made it necessary to perform an independent RHEED experiment before a conclusion on the mode of growth could be made.

Electron microscopy of similar copper-nickel specimens enabled misfit measurements to be obtained. A graph of elastic strain in the copper against mean deposit thickness was in fair agreement with the predictions of theory, although somewhat less elastic strain was observed than predicted which is unusual. The disagreement present was thought to be primarily a result of the non-uniformity of the deposited layer and it is thought that true layer by layer growth of the copper would give results in close agreement with theory.

A copper-nickel specimen, in which the nickel substrate had been exposed to the residual gas (1×10^{-9} torr) for five hours prior to copper deposition, showed almost complete pseudomorphism. The thickness of copper was 54 Å and similar films deposited on clean nickel had shown only 0.5% elastic strain. AES of similar nickel surfaces detected some oxygen but the oxygen signal very rapidly disappeared. There was no sign of any other contaminant, with the exception of chlorine which was present throughout all the room temperature studies. Hence it seems likely that oxygen contamination caused the observed increase in pseudomorphism, although it is thought that the true oxide was not formed and that a sub-oxide of the type observed by Farnsworth (159) may have been present. The presence of contamination between the copper and nickel crystals may impede the motion of dislocations, which would result in an increased amount of elastic strain.

Copper deposits on nickel substrates held at 300°C were found to be in the form of islands. The theory outlined in chapter 3 for the dependence of deposit and substrate Auger signals with coverage for deposits which nucleate appears to be in agreement with experimental results for high values of coverage. The agreement was not good for lower coverages but this was thought to be due to material between the islands which was not detected by electron microscopy. A graph of elastic strain in individual islands against island size was of the general form observed by Kuntze (107) in a similar experiment. However, measurement of the number of misfit dislocations in an island as a function of island width was not in agreement with the theoretical predictions of Matthews (85). Agreement was better if the ratio of island height to island width, the factor p, was modified to the range 1/50 - 1/100. Evidence obtained from electron microscopy indicates that a value of p in this range is more realistic in the present system.

Finally experiments using AES show that significant alloying does not occur between copper and nickel films at room temperature. Similar experiments at 300°C were not so conclusive and whilst thick copper deposits did not show time dependent Auger traces this was observed for thin copper layers. It was not possible to decide whether alloying or surface rearrangement was occuring for the thin deposits, but it is thought that if alloying does occur it is limited to a few layers only.

CHAPTER 7

SUMMARY, CONCLUSIONS AND FINAL COMMENTS

7.1 Summary

A Knudsen source was designed and built to enable controlled deposition of copper and silver in UHV. The source was calibrated using photometric chemical analysis and enabled either copper or silver to be deposited at pressures in the 10^{-9} torr range. In addition a sublimation source for nickel was built to enable the deposition of thick nickel films for use as substrate crystals.

In the initial experiments silver was deposited in stages on single crystal nickel films and the growth of the silver monitored by AES. The Auger data alone enabled the occurrence of layer by layer growth to be ascertained. The dependence of the growth of the silver Auger signal with deposition time was in good agreement with the predictions of Gallon (47) for the early stages of deposition. The agreement was not so good at longer deposition times and this was thought to be due to deviations from true layer growth. Nevertheless the experimental results enabled values for the mean escape depths for 355, 850 and 60 eV electrons in silver to be obtained, together with values of sticking coefficients. The values of sticking coefficients and the known arrival rate enabled the total deposit thickness to be calculated.

It was found that the Auger spectrum from silver-nickel specimens changed rapidly if the specimens were heated to 300°C. Subsequent electron microscopy showed that the silver was forming into large islands, with the bulk lattice parameter. The relative strength of the Auger signals following the thermal anneal was interesting in that the silver signal indicated about 60% coverage of the surface. Electron microscopy had shown the silver islands to occupy about 20% of the surface and the additional Auger signal was thought to be due to a layer of silver strongly bonded to the nickel.

Finally misfit determinations for thin layers of silver on nickel showed the silver to have its bulk lattice constant and hence silver does not grow pseudomorphically on (001) nickel.

In a second set of experiments copper was deposited on single crystal (001) nickel surfaces at both room temperature and 300°C. An examination of the growth and decay of the relevant Auger signals for deposition at room temperature did not allow the mode of growth

to be determined. This was primarily a result of the proximity of many of the Auger signals for this combination of materials, which increased the experimental uncertainty of the data.

An investigation of elastic strain against deposit thickness for depositions at room temperature was in reasonable agreement with theoretical predictions. However, the observed elastic strain was generally lower than the theoretical value which is unusual in pseudomorphic investigations. The discrepancy in the present case is thought to be due to deviations from true layer growth. No evidence was found in which thick copper films showed large values of elastic strain.

In an experiment in which the nickel substrate was exposed to the residual gas for five hours, a 54 Å thick copper film showed almost complete pseudomorphism. Further investigation of nickel substrates which had suffered prolonged exposure to the residual gas showed oxygen to be present on the surface. The oxygen was detected using AES, although it was found that the signal very rapidly disappeared, probably as a result of desorption by the electron beam. It was not possible to determine the structure of any adsorbed species.

The experimental procedure was repeated for the deposition of copper films in which the nickel substrate was held at 300°C. It was found that the copper deposit was in the form of large islands, often rectangular in shape. There was a limited amount of evidence to show that coverage information can be obtained from the relative strength of the deposit Auger signal. An examination of the number of misfit dislocations in copper islands showed that the predicted values of island dimensions for introduction of dislocations given by Matthews (85) were not in agreement in the present case. Much better agreement could be obtained if the island height was assumed to be a small fraction of the width and evidence from electron microscopy indicated that this was the case.

Finally it is worth noting that at room temperature Auger traces of copper deposits on nickel did not show time variation. At 300°C thick copper deposits were stable with time but this was not the case for fairly thin deposits. It therefore appears that alloying does not occur at room temperature, and while it may occur at 300°C it is limited to a few layers only.

7.2 Conclusions

The results obtained from an Auger electron spectroscopy study of the growth of silver on nickel were in good agreement with the model of Gallon (47) for the early stages of deposition. As the deposit thickness increased there was not complete agreement and this was thought to be due to deviations from true layer by layer growth. Nevertheless it is thought that in a system where true layer by layer growth occurred it would be possible to obtain an absolute calibration of deposit thickness over a limited range simply from the strength of the Auger signal. The restriction on the range is due to the finite number of layers which contribute to the Auger signal and once this number of layers has been exceeded the Auger signal remains constant. In a system exhibiting true layer growth the useful range, depending on mean escape depth, would appear to be between zero and about twenty layers. This is a range for which other methods of thickness measurement are not well suited, particularly for in-situ determinations. Even if calibration were only possible up to one monolayer, as in the experiment reported, AES could be particularly useful for surface diffusion experiments, especially if the substrate has a low energy Auger peak, since such signals have been shown to be very sensitive to the quantity of deposit.

A study of pseudomorphism of copper on nickel at room temperature produced results which were in fair agreement with theory. There was no evidence of thick copper films with large values of elastic strain and the discrepancy with theory was thought to be due to deviation from true layer growth. Contamination of the substrate by prolonged exposure to the residual gas produced a copper-nickel biorystal in which the 54 Å thick copper film was almost completely pseudomorphic. There was some evidence that oxygen was present on the surface but it is not certain whether this was the only contaminant. In addition it was not possible to determine the structure of any contaminant. This was the most unsatisfactory part of the present work and in view of the significant affect on pseudomorphism it would be particularly worthwhile to determine the exact nature of the contaminant. The difficulty of gas desorption experienced with AES might be overcome by using a more sensitive spectrometer so that the incident beam current could be substantially reduced, or alternatively by using photoelectron spectroscopy as the method of surface chemical analysis.

7.3 Final Comments

Throughout the experiments described the substrate crystal was itself a thin film prepared by deposition of nickel on rocksalt. The sublimation source used to deposit nickel suffered from the defect of many types of evaporation source described in chapter 1, namely the difficulty of controlling the evaporation rate. Consequently the thickness of the nickel film was difficult to control and this frequently lead to nickel substrates which had to be discarded because they were not quite continuous. To avoid this the thickness of the nickel films was increased but this lead to difficulties with electron microscopy, since nickel films much thicker than about 1500 Å result in very low beam intensities. This frequently made dark field microscopy impossible and even bright field microscopy difficult. For reasons already discussed in chapter 1 Knudsen sources are not suitable for repeated deposition of thick films, and could not be used in any case for materials which alloy, such as nickel. It is desirable to be able to produce substrate films of constant thickness and hence the best solution would probably be to include a quartz crystal ratemeter in the apparatus. This would enable films of constant thickness to be produced even if there were fluctuations in the evaporation rate.

One other consequence of producing thin film substrates is that they generally contain large numbers of dislocations. In pseudomorphic systems such as copper-nickel where accommodation of misfit is effected by existing dislocations it would be interesting to study the affect of variations in the density of dislocations in the substrate. It would however be difficult to vary the density of dislocations in a thin film substrate and the use of specially prepared bulk single crystals would probably be necessary.

The Auger investigation of the growth of silver on nickel when coupled with the theory due to Gallon (47) enabled the mean escape depths for the relevant Auger electrons to be obtained. If AES is to realise its full potential as a quantitative technique then electron mean escape depths will be required for a large range of materials. It would therefore be worthwhile to repeat experiments like the silver on nickel investigation for as wide a range of materials as possible.

Finally it was found that when both the silver and copper deposits were in island form the relative strength of their Auger signals generally indicated a much higher coverage than that observed in electron microscopy. This was thought to be due to a thin layer of deposit

material between the islands. It would be interesting to study the growth of silver on hot nickel to see if this thin layer was formed initially and then subsequent material grew in the form of islands. It should be possible to decide if this were occuring from the strength of the Auger signal, providing the Auger signal from one monolayer of deposit is known. It is unlikely that the presence of an initial monolayer would be detected by electron microscopy since it would not scatter sufficiently strongly to be detected under dark field conditions.

APPENDIX

PRODUCTION OF THE SECOND DERIVATIVE CURVE

The analysis of Bishop and Rivière (142) is followed in order to show that the second harmonic component of the electron current reaching the screen in a retarding field analyser is proportional to the second derivative of the current with respect to the analysing energy.

If the analysing voltage is V and the total collected current is i(V) then expanding the function i(V) in a Taylor series about a point V_o

$$i(V) = i(V_o) + \left[\frac{di(V)}{dV}\right]_{V=V_o} (V-V_o) + \tfrac{1}{2}\left[\frac{d^2i(V)}{dV^2}\right]_{V=V_o} (V-V_o)^2 + \ldots\ldots \quad (A1)$$

The voltage $(V-V_o)$ is the sinusoidal modulation A sin ωt and $\frac{di(V)}{dV}$ is the electron energy distribution N(E). Therefore substituting into equation A1 gives

$$i(V) = i(V_o) + A\,N(E)\sin\omega t + \frac{A^2}{4}\left[\frac{dN(E)}{dE}\right]_{E=E_o} (1 - \cos 2\omega t)$$

$$+ \frac{A^3}{24}\left[\frac{d^2N(E)}{dE^2}\right]_{E=E_o} (3\sin\omega t - \sin 3\omega t) + \ldots\ldots \quad (A2)$$

Rearranging equation A2 gives

$$i(V) = \left[i(V_o) + \frac{A^2}{4} N'(E_o) + \ldots\ldots\right]$$

$$+ \left[A\,N(E_o) + \frac{A^3}{8} N''(E_o) + \ldots\ldots\right] \sin\omega t$$

$$- \left[\frac{A^2}{4} N'(E_o) + \frac{A^4}{48} N'''(E_o) + \ldots\ldots\right] \cos 2\omega t$$

$$+ \ldots\ldots \quad (A3)$$

The current collected at frequency 2ω (the second harmonic) is

$$\frac{A^2}{4} N'(E_o) + \frac{A^4}{48} N'''(E_o) + \ldots\ldots \qquad (A4)$$

which will be proportional to $N'(E_o)$ providing the other terms in equation A4 are negligible compared to the first. This requirement will be satisfied if the modulation amplitude $A < \frac{p}{2}$, where p is the width of the Auger peak. Hence if $A < \frac{p}{2}$ the current in the Auger peak will be proportional to the square of the amplitude of modulation. This fact may be used to estimate the resolution of the Auger spectrometer.

References

(1) K L Chopra Thin Film Phenomena M^{c}Graw-Hill New York 1969

(2) D W Pashley Recent Progress in Surface Science 3 (1970) 23

(3) J F Pócza, A Barna and P B Barna J. Vac. Sci. and Technol. 6 (1969) 472

(4) L Royer Bull. Soc. Franc. Mineral 51 (1928) 7

(5) D W Pashley Advan. Physics 5 (1956) 173

(6) L G Schulz Acta. Cryst. 4 (1951) 487

(7) L G Schulz Acta. Cryst. 5 (1952) 130

(8) G A Bassett and D W Pashley J. Inst. Metals 87 (1959) 449

(9) L Bruck Ann. Phys. Leipzig 26 (1936) 233

(10) J W Matthews App. Phys. Letters 7 (1965) 131

(11) J W Matthews Phil. Mag. 12 (1965) 1143

(12) E W Dickson, M H Jacobs and D W Pashley Phil. Mag. 11 (1965) 575

(13) J W Matthews Phil. Mag. 7 (1962) 915

(14) M H Jacobs, D W Pashley and M J Stowell Phil. Mag. 13 (1966) 129

(15) G A Bassett in Proceedings of the European Regional Conference on Electron Microscopy Delft 1960 (eds. A L Houwink and B J Spits)

(16) C Sella and J J Trillat in Single Crystal Films p231 (eds. M H Francombe and H Sato) Pergamon Press New York 1964

(17) S Ino, D Watanake and S Ogawa J. Phys. Soc. Japan 17 (1962) 1074

(18) B Persson and H Norden Phys. Stat. Sol. 22 (1967) 632

(19) T Honma and C M Wayman J. Appl. Phys. 36 (1965) 2791

(20) G A Bassett Phil. Mag. 3 (1958) 1042

(21) H Bethge and V Schmid Z. Naturforschg. 14A (1959) 307

(22) H Bethge and W Keller Z. Naturforschg 15A (1960) 271

(23) G R Hennig Appl. Phys. Letters 4 (1964) 52

(24) G A Bassett, J W Menter and D W Pashley in Structure and Properties of Thin Films p11 (eds. Neugebauer, Newkirk & Vermilyea) John Wiley and Sons 1959

(25) J W Matthews J. Vac. Sci. and Technol. 3 (1966) 133

(26) D J Stirland Appl. Phys. Letters 8 (1966) 326

(27) A Chambers and M Prutton Thin Solid Films 1 (1968) 393

(28) T E Gallon, I G Higginbotham, M Prutton and H Tokutaka Surface Science 21 (1970) 224

(29) D G Lord Thin Solid Films 7 (1971) R39

(30) C A Neugebauer in Handbook of Thin Film Technology chapter 8 (eds. L I Maissel and R Glang) McGraw-Hill New York 1970

(31) O S Heavens J. Sci. Instr. 36 (1959) 95

(32) L Holland British Patent 754 102 1951

(33) B A Unvala and G R Booker Phil. Mag. 9 (1964) 691

(34) L Holland Vacuum Deposition of Thin Films Wiley New York 1958

(35) R Glang in Handbook of Thin Film Technology chapter 1 (eds. L I Maissel and R Glang) McGraw-Hill New York 1970

(36) J W Matthews and J L Crawford Thin Solid Films 5 (1970) 187

(37) C A Haque and H E Farnsworth Surf. Sci. 4 (1966) 195

(38) R E Honig R.C.A. Review 23 (1962) 567

(39) W A Pliskin and S J Zanin in Handbook of Thin Film Technology chapter 11 (eds. L I Maissel and R Glang) McGraw-Hill New York 1970

(40) M P Seah Surf. Sci. 32 (1972) 703

(41) C A Neugebauer J. Appl. Phys. 35 (1964) 3599

(42) O S Heavens Optical Properties of Thin Solid Films Butterworths 1955

(43) R E Reason Physics Bulletin 24 (1973) 587

(44) E B Sandell Colorimetric Metal Analysis Interscience New York 1959

(45) R Belcher and A J Nutten Quantitative Inorganic Analysis Butterworths London 1960

(46) P L Clegg and A N Crook J. Sci. Instru. 29 (1952) 201

(47) T E Gallon Surface Science 17 (1969) 486

(48) J W Matthews Physics of Thin Films 4 (1967) 137

(49) F C Frank and J H Van der Merwe Proc. Roy. Soc. (London) A198 (1949) 216

(50) F C Frank and J H Van der Merwe Proc. Roy. Soc. (London) A198 (1949) 205

(51) F C Frank and J H Van der Merwe Proc. Roy. Soc. (London) A200 (1949) 125

(52) G I Finch and A G Quarrell Proc. Roy. Soc. (London) A141 (1933) 398

(53) J W Matthews Phil. Mag. 6 (1961) 1347

(54) N Cabrera Surf. Sci. 2 (1964) 320

(55) W A Jesser and D Kuhlmann-Wilsdorf Phys. Stat. Solidi 19 (1967) 95

(56) A H Cottrell Dislocations and Plastic Flow in Crystals Oxford 1953

(57) J W Matthews Phil. Mag. 13 (1966) 1207

(58) W A Jesser and J W Matthews Phil. Mag. 17 (1968) 595

(59) R Kuntze, A Chambers and M Prutton Thin Solid Films 4 (1969) 47

(60) U Gradmann Phys. Kondens Materie 3 (1964) 91

(61) P W Palmberg and T N Rhodin J. Chem. Phys. 49 (1968) 134

(62) W A Jesser and J W Matthews Acta. Met. 15 (1967) 595

(63) W A Jesser, J W Matthews and D Kuhlmann-Wilsdorf App. Phys. Letters 9 (1966) 176

(64) H Poppa Z. Naturforschg 19A (1964) 835

(65) M Cahoreau and M Gillet Physique des Solides Serie B t271 (1970) 425

(66) E F Wasserman and H P Jablouski Surf. Sci. 22 (1970) 69

(67) W A Jesser and D Kuhlmann-Wilsdorf J. Appl. Phys. 38 (1967) 5128

(68) W A Jesser and D Kuhlmann-Wilsdorf Acta. Met. 16 (1968) 1325

(69) J W Matthews J. Appl. Phys. 42 (1971) 13

(70) G O Krause Surf. Sci. 3 (1965) 421

(71) R Wubbenhorst, K Hartig and R Neidermayer J. Vac. Sci. and Technol. 6 (1969) 865

(72) E Grunbaum Proc. Phys. Soc. (London) 72 (1958) 451

(73) J W Matthews Thin Solid Films 5 (1970) 369

(74) J W Matthews and W A Jesser Phil. Mag. 17 (1968) 461

(75) A I Fedorenko and R Vincent Phil. Mag. 24 (1971) 50

(76) J W Matthews and W A Jesser Phil. Mag. 17 (1968) 475

(77) J W Matthews and W A Jesser Phil. Mag. 15 (1967) 1097

(78) G H Olsen and W A Jesser Acta. Met. 19 (1971) 1009

(79) U Gradmann and J Muller Phys. Stat. Solidi 27 (1968) 313

(80) U Gradmann Ann. der Phys. 17 (1966) 91

(81) U Gradmann Surf. Sci. 13 (1967) 498

(82) E R Thompson and K R Lawless App. Phys. Letters 9 (1966) 138

(83) G O Krause J. Appl. Phys. 37 (1966) 3694

(84) B Borie, C J Sparks and J V Cathcart Acta. Met. 10 (1962) 691

(85) J W Matthews Surf. Sci. 31 (1972) 241

(86) J W Matthews and W A Jesser Phil. Mag. 20 (1969) 999

(87) J W Matthews and W A Jesser Acta. Met. 16 (1968) 1307

(88) F Portele Z. Naturforschg 24A (1969) 1268

(89) K Yagi, K Takayanagi, K Kobayashi and G Honjo J. Cryst. Growth 9 (1971) 84

(90) R Vincent Phil. Mag. 19 (1969) 1127

(91) S Sugita, Tamura and Sugawara J. Appl. Phys. 40 (1969) 3089

(92) J W Matthews, S Mader and T B Light J. Appl. Phys. 41 (1970) 3800

(93) G O Krause and E C Teague App. Phys. Letters 10 (1967) 251

(94) E Grunbaum and J W Mitchell in Single Crystal Films p221 (eds. M H Francombe and H Sato) Pergamon Press New York 1964

(95) R L Park and H E Farnsworth Rev. Sci. Instru. 35 (1964) 1592

(96) M Prutton Met. Rev. 152 (1971) 57

(97) P J Estrup in Modern Diffraction and Imaging Techniques in Materials Science p377 (eds. S Amelinckx, R Gevers, G Remault and J Van Landuyt) North Holland Amsterdam 1970

(98) P W Palmberg, G K Bohm and J C Tracy App. Phys. Letters 15 (1969) 254

(99) W Meltihorn Z. Physik 208 (1968) 1

(100) P J Bassett, T E Gallon and M Prutton J. Phys. E 5 (1972) 1008

(101) K Maeda and T Ihara Rev. Sci. Instru. 42 (1971) 1480

(102) L A Harris J. Appl. Phys. 39 (1968) 1419

(103) R E Weber and A L Johnson J. Appl. Phys. 40 (1969) 314

(104) T E Gallon and J A D Matthew Rev. Phys. Technol. 3 (1972) 31

(105) P B Hirsch, A Howie, R B Nicholson, D W Pashley and M J Whelan Electron Microscopy of Thin Crystals chapter 7 Butterworths London 1965

(106) H Brooks Metal Interfaces (Cleveland: American Society for Metals) p20 1952

(107) R Kuntze D. Phil thesis University of York 1970

(108) E W Muller in Modern Diffraction and Imaging Techniques in Materials Science p711 (eds. S Amelinckx, R Gevers, G Remault and J Van Landuyt) North Holland Amsterdam 1970

(109) D W Turner Molecular Photoelectron Spectroscopy Wiley Interscience London 1970

(110) W C Price Physics Bulletin 23 (1972) 87

(111) A E Jenkinson and A R Lang Direct Observation of Imperfections in Crystals p47 Interscience New York 1962

(112) R V Culver and F C Tompkins Advanc. Catalysis 11 (1959) 67

(113) C J Smithells Metals Reference Book Butterworths London 1967

(114) E R Funk, H Udin and J Wulff J. Metals, J. Petrol. Technol. and Mining Eng. 191 (1951) 1206

(115) J H Van der Merwe J. Appl. Phys. 31 (1963) 117

(116) J H Van der Merwe Proc. Phys. Soc. A63 (1950) 616

(117) J H Van der Merwe in Single Crystal Films p139 (eds. M H Francombe and H Sato) Pergamon London 1964

(118) C A B Ball and J H Van der Merwe Phys. Stat. Solidi 38 (1970) 335

(119) C A B Ball and J H Van der Merwe Phys. Stat. Solidi 42 (1970) 357

(120) J H Van der Merwe Surf. Sci. 31 (1972) 198

(121) J H Van der Merwe in Surfaces and Interfaces I p361 (eds. J Burke, N Reed and V Weiss) Syracuse University New York 1967

(122) W A Jesser and J H Van der Merwe Phil. Mag. 24 (1971) 295

(123) W A Jesser and J H Van der Merwe Surf. Sci. 31 (1972) 229

(124) J W Matthews Phil. Mag. 18 (1968) 1149

(125) J W Christian The Theory of Transformations in Metals and Alloys p252 Pergamon Oxford 1965

(126) E Grunbaum, G Kremer and C Raymond J. Vac. Sci. and Technol. 6 (1969) 475

(127) U Gradmann Ann. der Phys. 13 (1964) 213

(128) R G Musket and J Ferrante J. Vac. Sci. and Technol. 7 (1969) 14

(129) J V Florio and W D Robertson Surf. Sci. 18 (1969) 398

(130) P W Palmberg and T N Rhodin J. Appl. Phys. 39 (1968) 2425

(131) J W T Ridgway and D Haneman Surf. Sci. 24 (1971) 451

(132) M L Tarng and G K Wehner J. Appl. Phys. 44 (1973) 1534

(133) R D Heidenreich Fundamentals of Transmission Electron Microscopy Wiley New York and London 1964

(134) D M Smith and T E Gallon to be published

(135) H Tokutaka D. Phil Thesis University of York 1970

(136) M Knudsen Ann. der Phys. 28 (1909) 999

(137) M Prutton and H Tokutaka Thin Solid Films 3 (1969) 411

(138) T E Gallon, I G Higginbotham and M Prutton J. Phys. E 2 (1969) 894

(139) N J Taylor Rev. Sci. Instru. 40 (1969) 792

(140) E J Scheibner and L N Tharp Surf. Sci. 8 (1967) 247

(141) R E Weber and W T Peria J. Appl. Phys. 38 (1967) 4355

(142) H E Bishop and J C Riviere J. Appl. Phys. 40 (1969) 1740

(143) A M Mattera, R M Goodman and G A Somorjai Surf. Sci. 7 (1967) 26

(144) K Jacobi and J Holzl Surf. Sci. 26 (1971) 54

(146) International Tables of X-ray Crystallography Kynoch Press Birmingham England 1968

(147) B Baranowski, S Majchrzak and T B Flanagan J. Phys. F. 1 (1971) 258

(149) S Amelinckx The Direct Observation of Dislocations Academic Press New York 1964

(150) D Hull Introduction to Dislocations p75 Pergamon Press 1965

(151) J C Tracy and P W Palmberg J. Chem. Phys.51(1969)4852

(152) F R N Nabarro Phil. Mag. 22 (1970) 178

(153) A U MacRae Surf. Sci. 1 (1964) 319

(154) H E Farnsworth and J Tuul J. Phys. Chem. Solids 9 (1958) 48

(155) R L Park and H E Farnsworth J. Appl. Phys. 35 (1964) 2220

(156) R L Park and H E Farnsworth J. Chem. Phys. 40 (1964) 2354

(157) R L Park and H E Farnsworth Appl. Phys. Letters 3 (1963) 167

(158) J W Matthews Phil. Mag. 18 (1968) 1149

(159) H E Farnsworth Appl. Phys. Letters 2 (1963) 199

(160) J E Fisher and J Goddard J. Phys. Soc. Japan 25 (1968) 413

(161) W H J Vernon Nature 167 (1951) 1037

(162) J A Dillon Jr. and H E Farnsworth J. Chem. Phys. 22 (1954) 1601

(163) R L Park and H E Farnsworth J. Chem. Phys. 43 (1965) 2351

Acknowledgements

I should like to express my sincere thanks to the following:

my supervisor, Dr A Chambers, for his help, advice and encouragement throughout the course of this work;

Dr D G Lord with whom I shared the apparatus, for his generosity regarding the amount of time during which I had sole use of the equipment;

all members of the thin films and surfaces group for many helpful discussions;

and the Science Research Council for financial support.

I should also like to thank the technical staff and in particular Messrs J C Dee, A Gebbie and P Durkin for their skilled assistance.

Finally I thank my wife for typing the manuscript and more important, for her encouragement and patience whilst I have been writing this thesis.

Publications

A model for the Auger electron spectroscopy of systems exhibiting layer growth, and its application to the deposition of silver on nickel.

Surface Science 36 (1973) 381

SURFACE SCIENCE 36 (1973) 381–394 © North-Holland Publishing Co.

A MODEL FOR THE AUGER ELECTRON SPECTROSCOPY OF SYSTEMS EXHIBITING LAYER GROWTH, AND ITS APPLICATION TO THE DEPOSITION OF SILVER ON NICKEL

D. C. JACKSON, T. E. GALLON and A. CHAMBERS
Physics Department, University of York, Heslington, York Y01 5DD, England

Received 20 October 1972; revised manuscript received 1 January 1973

The dependence of Auger intensities on deposition time for deposits which grow in layer-by-layer fashion is analysed in terms of a simple model. It is shown that it is possible in principle to calibrate the Auger signals as a function of thickness absolutely with no prior assumption of values for sticking coefficients. The extent to which theory and experimental data for the deposition of silver on nickel are in agreement is examined, and values deduced for sticking coefficients and escape depths of Auger electrons in silver. It is also found that silver grows epitaxially on nickel at room temperature, and that silver/nickel bicrystals do not alloy after heat treatment.

1. Introduction

The value of Auger Electron Spectroscopy as a sensitive tool for qualitative analysis of surface chemical composition has long been recognised. However it has not yet been possible to determine the concentration of a surface species from its Auger signal, except in the case of sub-monolayer deposits. Even in this restricted case, some subsidiary assumption has to be made. Thus for the deposition of iron on silicon[1]) equality of the sticking coefficients of iron on silicon and on the quartz crystal of a ratemeter was assumed and for the deposition of silver on gold[2]) the disappearance of a feaure associated with gold in the LEED pattern was taken as an indication of monolayer coverage of silver.

The purpose of this paper is to present an extension of a model already developed by one of us[3]), which describes the dependence of Auger intensities on specimen thickness, to the analysis of layer-by-layer growth of a deposit on a substrate, and to compare the results of the analysis with experimental data we have obtained for the deposition of silver on the (100) surface of nickel.

2. Theory

In the model referred to above[3]), the crystal is regarded as being made up

of atomic planes labelled 1, 2, ..., n, parallel to the surface, $n=1$ being the outermost layer. The production of a back-scattered Auger current due to an incident electron beam penetrating into the crystal is described in terms of the probabilities of a primary electron reaching the nth layer, of an Auger electron being produced there, and of this Auger electron escaping back through $(n-1)$ layers to the vacuum. Summing the contributions gives the Auger current from n layers as

$$I_n = I_\infty \left[1 - \left(1 - \frac{I_1}{I_\infty} \right)^n \right], \tag{1}$$

where I_1 is the current from one monolayer and I_∞ is the current from bulk material.

The application of this model to the growth of a depositing material A which arrives at a constant rate at the surface of material B, and grows in layer-by-layer fashion on it, is as follows. The aim is to deduce the thickness of the A overlayer solely from its Auger signal, there being no prior assumption of values for sticking coefficients.

Let R = arrival rate of material A at surface of B in monolayers $\sec^{-1}$, S_1 = sticking coefficient of A on B (assumed independent of coverage), t = time elapsed from start of deposition.

The initial Auger current is given by

$$I_A = RS_1 I_1 t, \tag{2}$$

where I_1 is the current from a monolayer of A. This dependence continues up to a time t_1 which corresponds to the deposition of a monolayer. As the second layer develops the current is given by

$$I_A = I_1 (1 - \theta) + I_2 \theta, \tag{3}$$

where $\theta = R S_2 (t - t_1)$ is the fractional coverage of the second layer, S_2 is the sticking coefficient of A on A, assumed to be independent of coverage, and I_2 is given by eq. (1) with $n=2$. Substituting in (3) for I_2 leads to the expression

$$I_A = I_1 \left[1 + \theta \left(1 - \frac{I_1}{I_\infty} \right) \right], \tag{4}$$

so that, as expected, there is a linear increase of Auger current with coverage as the second layer develops. For an integral number n of deposited layers the Auger current is given by eq. (1) with $n = 1 + RS_2 (t_n - t_1)$, where t_n is the particular time that corresponds to the completion of the nth layer. The dependence of I_A on t indicated by this analysis is shown in fig. 1, which is drawn for a hypothetical case in which $I_1/I_\infty = 0.4$ and the equality of the

time interval $(0\text{–}t_1)$ to subsequent intervals implies equality of the sticking coefficients S_1 and S_2.

One notes that the dependence is piece-wise linear, there being abrupt changes in slope at integral values of the layer number. It is clearly of particular importance to be able to locate the time t_1 corresponding to monolayer coverage of A on B. With data of sufficient accuracy it should be possible to distinguish the linear portions. However in practice the experimental accuracy may make this difficult, and also there may be deviations

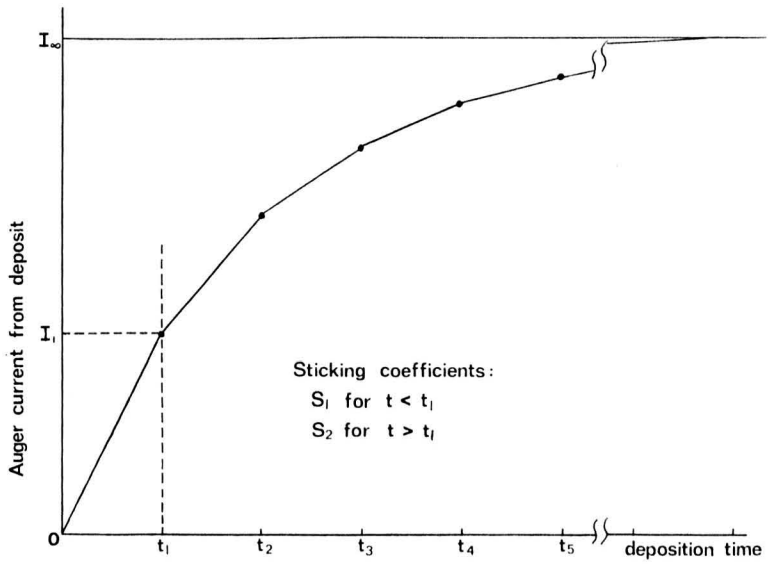

Fig. 1. Deposit Auger signal as function of deposition time according to model. I_1 and I_∞ correspond to monolayer coverage and bulk respectively. t_n = deposition time corresponding to completion of nth layer. Drawn for $S_1 = S_2$.

from true layer growth in that the $(n+1)$th layer may start to develop on top of the nth before the nth is complete. If either or both of these circumstances arise then the data will approximate to a smoothed curve having the general form of fig. 1. It may however be deduced from eq. (1) that the quantity

$$I_{n+1} - I_n = I_1\left(1 - \frac{I_1}{I_\infty}\right)^n,$$

so that the most abrupt change in slope occurs at $n=1$, and therefore the discontinuity in slope at the time corresponding to the completion of the first layer should be the easiest to discern. In addition the ratio S_1/S_2 affects the ease of location of t_1, $S_1/S_2 < 1$ and $S_1/S_2 > 1$ making the change of slope

less and more abrupt respectively. If by inspection of the data t_1 can be located, the current from the first layer of the deposit, I_1 is immediately deduced.

The other quantity of importance for the theory, I_∞, will be determined experimentally at long deposition times, when the Auger current becomes constant to within the experimental accuracy. Although, as noted previously, there may be deviations from true layer growth, the value of I_∞ deduced is independent of these deviations provided a continuous deposit is eventually formed.

If the accuracy of the experimental data does not allow the identification of linear portions in the I_A versus t curve for $t > t_1$, but nevertheless suggests a smooth variation of I_A with t up to a constant value I_∞ then it is permissible to treat n as a continuous variable and write

$$I_A = I_\infty \left[1 - \left(1 - \frac{I_1}{I_\infty} \right)^n \right], \tag{5}$$

where $n = 1 + RS_2(t - t_1)$. Rearranging (5) gives

$$\log\left(1 - \frac{I_A}{I_\infty} \right) = [1 + RS_2(t - t_1)] \log\left(1 - \frac{I_1}{I_\infty} \right). \tag{6}$$

Hence it should be possible to estimate a value for t_1 from the departure of a plot of $\log(1 - I_A/I_\infty)$ versus t from linearity as well as from the I_A versus t data.

Having obtained I_1 the initial slope of the I_A versus t plot gives (RS_1) from eq. (2) and hence S_1 if R is known. The graph of $\log(1 - I_A/I_\infty)$ versus t for the region $t > t_1$ should give a straight line of slope $RS_2 \log(1 - I_1/I_\infty)$ and hence S_2 if R is known. Even if R is unknown the time for the growth of a monolayer of A on A can be determined from the value of t_1 and the ratio S_1/S_2 obtained by dividing (RS_1) by (RS_2), (RS_2) being obtained from the slope of the $(1 - I_A/I_\infty)$ versus t plot. Thence $t_2 - t_1 = (S_1/S_2)\, t_1$ and the deposit thickness may be calibrated.

Similar results may be deduced for the decay of the Auger signal from the substrate. Thus

$$I_B = I_{B\infty} \left[1 - RS_1 t \left(1 - \frac{I_{1BA}}{I_{B\infty}} \right) \right], \quad t < t_1, \tag{7}$$

where I_{1BA} is the signal from the substrate covered by one layer of A and

$$I_B = I_{B\infty} \left(\frac{I_{1BA}}{I_\infty} \right) RS_2 t, \quad t > t_1, \tag{8}$$

It is shown in ref. 4 that in terms of this model the mean escape depth of

Auger electrons, expressed as a number n_0 of atomic layers is given by

$$n_0 = \frac{1}{2}\frac{I_1}{I_\infty} + \left(1 - \frac{I_1}{I_\infty}\right)[1 + 1/\log\{I_\infty/(I_\infty - I_1)\}]. \quad (9)$$

This model assumes that the backscattering factor remains constant during the growth of the overlayer. In the inital stages, the distribution of backscattered electrons will be determined by the substrate and this assumption will probably hold good. However, as the deposit increases in thickness the backscattered electrons will gradually originate from the overlayer. For deposit/substrate systems of markedly different scattering properties this may affect the shape of the curve of Auger signal vs. time, probably causing the flat portion of the curve to have a slight upward or downward slope to a new saturation value.

The application of this model to experimental data for the depostion of silver on nickel is described in subsequent sections.

3. Experiment

The deposition of silver on nickel has been monitored as a function of time by Auger Electron Spectroscopy, hereafter referred to as AES.

3.1. Apparatus and technique

The apparatus consists of an ultra-high vacuum system which contains facilities for the deposition of silver and nickel, for analysis of surface structure by LEED and RHEED, for AES, and for residual gas analysis. The crystal manipulator and holder allows multiple-cleavage of crystals, typically rocksalt, of initial dimensions $8 \times 8 \times 30$ mm, enabling about four (100) crystal faces 8 mm square of such materials to be prepared in-situ. The crystal temperature may be varied between about -180°C and 380°C by liquid nitrogen cooling and radiation heating respectively. The base pressure of the system is about 8×10^{-10} torr. Other facilities of the plant, which are described elsewhere[5]), are not relevant to this investigation.

The nickel substrate on which silver is deposited is prepared by deposition of nickel on rocksalt. The nickel source consists of a helix of nickel wire which is resistance heated to a temperature at which its vapour sublimes at an appreciable rate. The helix is formed by winding a nickel wire 0.02 inch in diameter round a length of straight tungsten wire 0.04 inch in diameter so that its turns touch, and then forming the composite wire into a helix with closely-spaced turns. The nickel is Grade I material supplied by Johnson–Matthey Ltd. The helix is housed in a tantalum box from which a short pipe permits the vapour to emerge. As viewed from this exit pipe the

helix is sideways on so that its close winding presents a large evaporating area. In operation the source is raised to a position such that the open end of the pipe almost touches the crystal face on which a film is to be deposited, thus localising the deposition region to a circle of 6 mm. diameter, and the helix–crystal distance is then 5 cm. The helix may be viewed through a small hole in the tantalum box, and the vapour which emerges from here condenses harmlessly in a region remote from the crystal. The power supplied to the source is manually controlled and nickel films ~ 1500 Å thick, as judged from subsequent electron microscopy, may be deposited in about 1 hour. In operation the source causes the pressure in the system to rise initially to about 4×10^{-8} torr, but the pressure improves progressively as the source outgasses so that eventually depositions are possible in an ambient pressure of about 5×10^{-9} torr.

Silver is evaporated from a Knudsen source consisting of a closed tantalum crucible from which silver vapour emerges through a 1 mm orifice. Subsequent apertures define a horizontal beam path to the crystal which is 22 cm. distant. A shutter may be interposed in the beam. The crucible is heated by electron bombardment and its temperature sensed by a Pt/Pt – Rh thermocouple whose signal regulates the heating power to maintain a constant crucible temperature and therefore a constant pressure of silver vapour in the Knudsen cell. For this experiment the temperature was set to give an expected arrival rate of 0.7 Å min^{-1} of silver at the crystal face, as deduced from an analysis of the geometry of the source and the vapour pressure data for silver[6]). Colorimetric metal analysis[7]) of a silver film deposited in an auxiliary experiment enabled the actual arrival rate to be measured unambiguously. The result was 0.48 ± 0.06 Å min^{-1}, the difference between this and the predicted value reflecting uncertainty in the vapour pressure data. Expressed in monolayers per minute, the arrival rate is $R = 0.23 \pm 0.03$, the lattice constant of silver being 4.17 Å. During operation of the source, the pressure in the system does not exceed 5×10^{-9} torr.

AES is carried out using the electron gun and optics of a four-grid LEED system, together with external circuitry described in ref. 8. The peak-to-peak height of the second differential of the modulated Auger current is taken as the measure of the current in the Auger peak, as proposed by Weber and Johnson[9]). The signals measured in the course of the experiment were the silver signal at 355 eV due to the unresolved $M_{4,5}\,N_{4,5}\,N_{4,5}$ transitions and the nickel signals at 60 and 850 eV due to $M_{2,3}\,M_4\,M_4$ and $L_3\,M_{4,5}\,M_{4,5}$ transitions respectively.

3.2. Preparation of nickel substrates

Nickel films ~ 1500 Å thick were deposited in the manner previously

described on to (100) faces of rocksalt obtained by cleavage immediately prior to deposition. The rocksalt crystal was held at an indicated temperature of 150°C, but thermal radiation from the incandescent nickel helix may have raised the surface temperature to 200–300°C. This prescription for preparing nickel substrates was arrived at after a series of trial experiments in which films of various thickness were examined by LEED, RHEED at 15 keV, AES and subsequent transmission electron microscopy. After cooling the as-deposited films LEED and RHEED showed that the deposits were monocrystalline with the (100) epitaxial structure, and the streaking of features in RHEED patterns indicated that films were flat. Microscopy showed that films 1500 Å thick were continuous and completely hole-free. This last result was important because AES of the deposited nickel surfaces, in which great care was taken to prevent the incident electron beam striking the adjacent rocksalt substrate, revealed the presence of a small amount of chlorine. AES revealed no other contaminant on the nickel surface. The origin and behaviour of the chlorine contaminant during the experiment will be discussed later.

3.3. Procedure and results for silver deposition on Ni(100)

Silver was deposited at normal incidence and at a constant rate of 0.48 Å/min on to the nickel surface at room temperature. The deposition was carried out in stages, using the shutter, and with the source turned off during the measurement period. After each stage an Auger spectrum of the surface was taken, and the progressive decline of the nickel Auger signals (at 60 and 850 eV) and the growth of the silver signal (at 355 eV) recorded as a function of deposition time. The deposition of silver was continued to the point when the nickel signals were no longer detectable and the silver signal had reached a constant value. The chlorine signal remained substantially constant throughout the experiment.

The data for the growth of the silver signal as a function of deposition time are shown in fig. 2. One notes the linear rise of the plot initially and the low scatter of the associated experimental points, followed by a break from linearity after approximately 450 sec and a gradual increase, with larger scatter of data, to a constant signal. The I_∞ value drawn takes into account a number of experimental points at long deposition times which could not conveniently be displayed in the figure.

The corresponding data for the decay of the nickel substrate signals are shown in fig. 3, where the insert shows the decay of the 60 eV signal on an expanded time scale to aid clarity. One notes here the linear decay of the 60 eV signal which reaches a very small value after 400 sec, the approximate time at which the silver signal in fig. 2 broke from linearity. The decay of the

850 eV signal is more gradual and ceases to be detectable at 8000 sec deposition time.

The experiment was repeated several times. The same variation of silver and nickel signals was observed, with the exception that in one run the decay of 60 eV signal broke from linearity at an earlier stage than in other runs, falling thereafter at a slower rate, as shown by the dotted line in fig. 3.

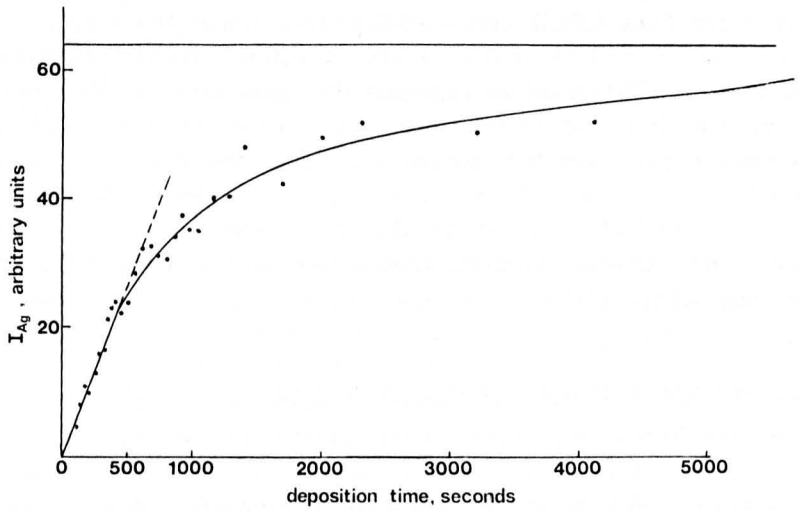

Fig. 2. Growth of 355 eV silver Auger signal with deposition time. Experimental points at long deposition times off scale.

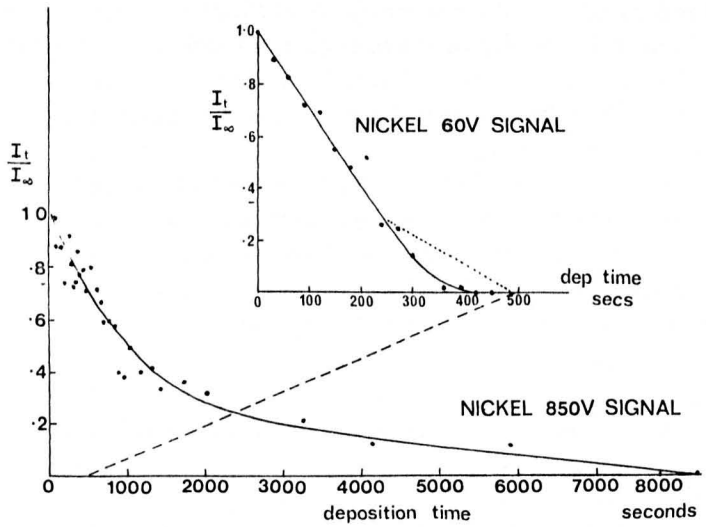

Fig. 3. Decay of nickel substrate Auger signals with silver coverage. Inset shows 60eV signal on expanded scale for clarity. Dashed line connects corresponding times.

3.4. Annealing experiments

At the conclusion of the foregoing experiments, approximately 30 Å (see later discussion) of silver had been deposited on the nickel, nickel Auger signals were not detectable and therefore the nickel was completely covered by silver. Further experiments using AES and heat treatment were carried out on such deposits.

In one experiment, having recorded the final Auger trace of the deposition sequence, the sample was left at room temperature in the vacuum (2×10^{-9} torr) for 56 hr. The Auger spectrum taken after this interval was identical

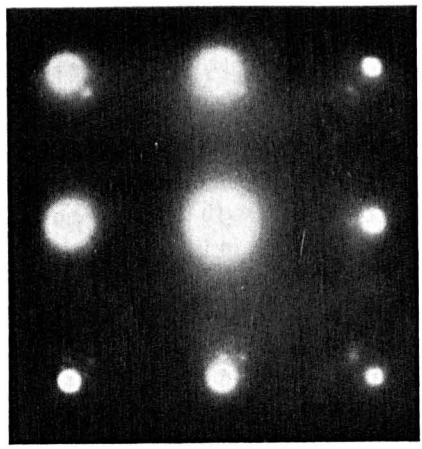

(a)

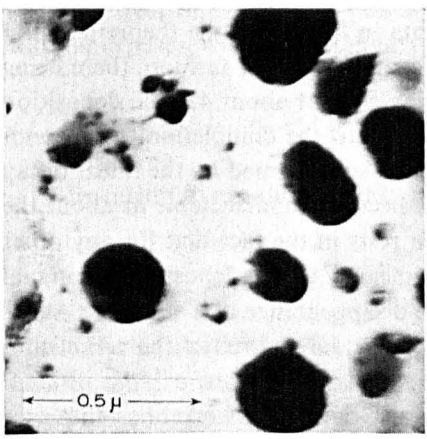

(b)

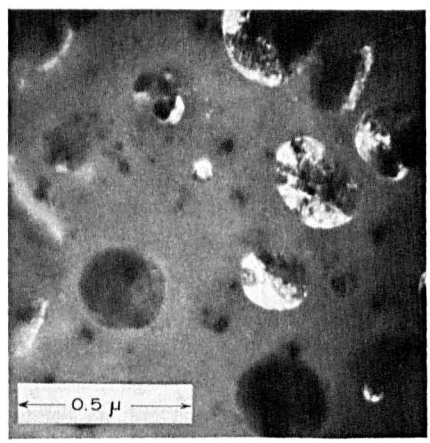

(c)

Fig. 4. Electron microscopy and diffraction at 100 kV of Ag/Ni bicrystal annealed at 300°C in vacuum: (a) transmission diffraction pattern at 100 kV; (b) bright field micrograph; (c) dark-field micrograph on (220) silver spot.

to the previous one – the silver signal had the same strength and neither of the nickel signals had reappeared.

In a second experiment, with the same starting conditions as those above, the silver–nickel bicrystal was heated at 300°C for 17 hr. After thirty minutes heating, even before 300°C was reached, changes started to occur in the Auger spectrum. The nickel signals reappeared and the size of the silver signal was reduced. This behaviour indicated that the nickel/silver combination had either alloyed, thus bringing some nickel to the surface, or that some change in morphology had occurred. The dilemma was resolved by subsequent electron microscopy and diffraction of the stripped film, the results of which are shown in fig. 4. Fig. 4a shows the transmission diffraction pattern taken at 100 kV of the composite film after heat treatment. The bright spots are due to the epitaxial (100) nickel film. Just inside the low index spots faint but sharp spots with no streaking can be discerned. By accurate measurement of the pattern using microdensitometer traces of the image plate these were identified as silver spots having the same spacing as would be expected from bulk data, so that the silver is not detectably strained. A bright field micrograph is shown in fig. 4b. The fact that the dark regions are silver islands is shown by dark field microscopy using the (220) silver diffracted beam, which gives the micrograph of fig. 4c. It is thus proved that nickel and silver do not mix to form an alloy as a result of this heat treatment, but rather that a change of morphology occurs.

4. Discussion

A comparison of the experimental data in fig. 2 with the theoretical plot in fig. 1 suggests that the silver may be growing in layer fashion, there being a well-defined initial linear portion which ends at about 450 sec deposition time corresponding, in terms of the model, to the completion of a monolayer. The correctness of this interpretation is confirmed by the linear decay of the 60 eV nickel signal (fig. 3) which becomes undetectable at about the same deposition time. The confirmation rests in the fact that for any other growth morphology, a departure from linearity of the deposit Auger signal would not occur at the same time as the disappearance of a substrate Auger signal. Thus if the silver had been nucleating, large areas of the nickel substrate would at this stage be left uncovered resulting in a large residual substrate signal. It is fortuitous for the investigation that nickel has an Auger peak at the low energy of 60 eV, for this presumably has a small escape depth which makes it especially surface sensitive.

The comparatively large scatter of the silver data for the region $t > t_1$, and over the whole range of deposition time for the 850 eV signal, do not allow

the procedures based on eqs. (6) and (7) to yield meaningful values for t_1, the monolayer formation time for silver on nickel. t_1 is therefore deduced by inspection of the Ag and 60 eV Ni data to be 400 ± 50 sec. The associated value of I_1 gives $I_1/I_\infty = 0.32 \pm 0.04$ for silver. Using the known arrival rate ($R = 0.48 \pm 0.06$ Å/min) and eq. (2) gives the sticking coefficient of Ag on Ni as $S_1 = 0.7 \pm 0.2$ under the prevailing conditions. Putting the value of I_1/I_∞ in eq. (9) gives the mean escape depth for 355 eV Auger electrons in silver as 5.4 ± 0.6 Å which differs from the value of 8 Å found by Palmberg and Rhodin [2]) even though I_1/I_∞ deduced from their fig. 9 is also 0.32.

The reasons for this difference in the estimate of n_0 lie in the treatment of the data, and are as follows. The elementary definition of mean escape depth is

$$n_0 = \int_0^{I_\infty} n \, \mathrm{d}I / \int_0^{\infty} \mathrm{d}I = \int_0^{I_\infty} n \, \mathrm{d}I / I_\infty ,$$

and in the quantity $n \, \mathrm{d}I$, $\mathrm{d}I$ is to be interpreted as that part of the Auger current generated at a depth of n layers which passes through the overlying layers to reach the vacuum without loss of energy. The eq. (9) quoted previously results from applying this definition to the layer-by-layer model. In terms of experimental intensity versus coverage data $\int n \, \mathrm{d}I$ is the area bounded by the I axis, the experimental curve, and a line $I = I_\infty$ which touches the experimental curve tangentially at $n = n_\infty$ this being the total number of layers which contribute to the observed Auger current. The quantity n_0 may be estimated in three ways:

(i) By direct integration of this area, and by comparison of it, for calibration purposes, with the rectangular area $n_\infty I_\infty$. Then

$$n_0 = n_\infty \times \text{a ratio of two areas} .$$

(ii) By fitting an exponential curve of the form

$$I = I_\infty [1 - \exp(-n/n_0)]$$

to the data. This procedure involves the assumption of equal sticking coefficients in the pre- and postmonolayer stages. The curve is fitted to the data using only one experimental point, typically I_1, in addition to the I_∞ value and the initial linear rise of a deposit signal would be ignored.

(iii) By using an expression such as eq. (9) based on a simple model, in which case n_0 is a function only of the ratio I_1/I_∞, and it is not necessary to know n_∞.

Procedure (iii) appears to be less reliable because it involves the assumption of a model whereas the other two use the data more or less directly. However the advantages of procedure (iii) are that n_∞ need not be known, and provided I_1 can be determined, the detailed growth morphology after the first monolayer coverage, which for reasons discussed previously is subject to greater uncertainty, is not important. In particular the measured value of I_∞ will be substantially independent of the final morphology. Therefore, in circumstances where the experimental data seems to be more reliable in the stage up to monolayer coverage than it does in later stages, which is the case in our measurements, the deduction of n_0 by procedure (iii) is preferable.

When applied to both our data and that of Palmberg and Rhodin[2]) procedure (iii) yields 5.4 Å for the escape depth of 355 eV Auger electrons in silver, because I_1/I_∞ is the same in both cases. Procedure (i) applied to Palmberg and Rhodin's data and taking $n_\infty = 15$ yields their value of 8 Å. The same procedure applied to our data gives 6 Å but with large uncertainty ~ 2.4 Å.

The escape depth of 850 eV electrons through silver estimiated byprocedure (iii) is 6.7 ± 0.5 Å. The form of the Ni 60 eV signal decay indicates that the escape depth of electrons of this energy through silver is about 1 atomic layer.

The considerably lower scatter of the data for $t < t_1$ compared with that for $t > t_1$, which was a feature of all the runs made, suggests that the data for $t > t_1$ may represent a true surface effect rather than the onset of instrumental instability. There are indeed certain regularities in the variation of the data between 500 and 1200 sec, viz: three dips in the curve more or less equally spaced in deposition time. This might be due to bits of $(n+1)$th layer being formed from existing nth layers between individual measurements, due to surface mobility of the silver atoms. Such an un-covering process could lead to a reduction of the total signal. The dotted curve of fig. 3 for the 60 eV nickel decay may be evidence of this phenomenon, but there was no clear correlation with the silver data. Such speculation is supported in a general way by the results of annealing experiments. Although thick as-deposited layers seem to be stable at room temperature the rapidity with which this overlayer transforms to a thermodynamically stable island structure at 300 °C suggests that the as-deposited overlayer at room temperature may be metastable, so that kinetic effects might occur in thin overlayers even at room temperature. Such conversions of a metastable to a stable structure have been observed for platinum deposited on gold[10]).

Despite these uncertainties about what is happening in detail for $t > t_1$, the fact that the deposit layer is continuous makes it worthwhile to plot a smoothed curve through the experimental points for $t > t_1$, as has been done

in fig. 2 and to follow the procedure based on eq. (6) to estimate an approximate sticking coefficient for silver on silver at room temperature. This has been done and the result is $S_2 = 0.37 \pm 0.15$.

The situation for $t > t_1$ might be clarified by repeating the investigation with a lower substrate temperature, when atomic mobilities would be much reduced, and making greater use of the experimental facilities to study surface structure.

The role of the chlorine contaminent in the experiment is difficult to assess. Residual gas analysis showed that there was a small ($\sim 10^{-12}$ torr) partial pressure of chlorine in the system in the system during the experiment, and it seems most likely that the origin of chlorine on the surfaces under investigation was adsorption from the gas phase, which would be consistent with its substantially constant value throughout. That its stay on the surface was temporary, involving an adsorption stay time, is also suggested by the fact no traces of chloride structures etc. could be found in transmission electron diffraction patterns.

5. Conclusion

The agreement between the theory of the development of Auger intensities for deposits growing in layer fashion and the experimental data for silver depositing on nickel is only partial. There is well defined layer growth initially up to a monolayer thickness of silver but thereafter, although a continuous overlayer is produced, the precise variation expected from the theory is not followed. Experiments at a lower temperature might show better agreement. Close agreement between theory and experiment would afford an absolute calibration of the Auger intensities for this combination of materials, thus enabling precise starting conditions to be set up in situ for, e.g., a surface diffusion experiment. Nevertheless the agreement of theory and experiment for the sub-monolayer stage of deposition indicates unambiguously that layer growth is occurring initially, affords an absolute calibration for this restricted region, and yields the sticking coefficient for Ag on Ni under the prevailing conditions together with data on the escape depth of Auger electrons. The annealing experiments show that, as is the case for the bulk materials, nickel and silver do not alloy when in thin film form. Finally may be noted that siver deposits expitaxially on (100) nickel at room temperature.

Acknowledgments

The authors wish to thank Dr. D. G. Lord for helpful discussions during the course of the work and Dr. M. Prutton and Mr. J. C. Dee for their contributions to the design and development of the apparatus.

References

1) J. W. T. Ridway and D. Haneman, Surface Sci. **24** (1971) 451.
2) P. W. Palmberg and T. N. Rhodin, J. Appl. Phys. **39** (1968) 2425.
3) T. E. Gallon, Surface Sci. **17** (1969) 486.
4) T. E. Gallon and J. A. D. Matthew, Rev. Phys. Technol. **3** (1972) 31.
5) D. G. Lord and T. E. Gallon, Surface Sci. **36** (1973) 605.
6) R. E. Honig, RCA Rev. **23** (1962) 574.
7) E. B. Sandell, *Colorimetric Metal Analysis* (Interscience, New York, 1959).
8) T. E. Gallon, I. G. Higginbotham and M. Prutton, J. Phys. E **2** (1969) 894.
9) R. E. Weber and A. L. Johnson, J. Appl. Phys. **40** (1969) 314.
10) J. W. Matthews and W. A. Jesser, Acta Met. **15** (1967) 595.